

REPORT DOCUMENTATION PAGE			Form Approved OMB NO. 0704-0188		
<p>The public reporting burden for this collection of information is estimated to average 1 hour per response, including the time for reviewing instructions, searching existing data sources, gathering and maintaining the data needed, and completing and reviewing the collection of information. Send comments regarding this burden estimate or any other aspect of this collection of information, including suggestions for reducing this burden, to Washington Headquarters Services, Directorate for Information Operations and Reports, 1215 Jefferson Davis Highway, Suite 1204, Arlington VA, 22202-4302. Respondents should be aware that notwithstanding any other provision of law, no person shall be subject to any penalty for failing to comply with a collection of information if it does not display a currently valid OMB control number.</p> <p>PLEASE DO NOT RETURN YOUR FORM TO THE ABOVE ADDRESS.</p>					
1. REPORT DATE (DD-MM-YYYY) 31-10-2014		2. REPORT TYPE Final Report		3. DATES COVERED (From - To) 1-Aug-2012 - 31-Jul-2014	
4. TITLE AND SUBTITLE Final Report: Integrated Photonic Orbital Angular Momentum Multiplexing and Demultiplexing on Chip			5a. CONTRACT NUMBER W911NF-12-1-0311		
			5b. GRANT NUMBER		
			5c. PROGRAM ELEMENT NUMBER		
6. AUTHORS Ryan P. Scott, Roberto Proietti, Binbin Guan, S.J.B. Yoo			5d. PROJECT NUMBER		
			5e. TASK NUMBER		
			5f. WORK UNIT NUMBER		
7. PERFORMING ORGANIZATION NAMES AND ADDRESSES University of California - Davis 1850 Research Park Drive Suite 300 Davis, CA 95618 -6153			8. PERFORMING ORGANIZATION REPORT NUMBER		
9. SPONSORING/MONITORING AGENCY NAME(S) AND ADDRESS (ES) U.S. Army Research Office P.O. Box 12211 Research Triangle Park, NC 27709-2211			10. SPONSOR/MONITOR'S ACRONYM(S) ARO		
			11. SPONSOR/MONITOR'S REPORT NUMBER(S) 62313-PH-DRP.8		
12. DISTRIBUTION AVAILABILITY STATEMENT Approved for Public Release; Distribution Unlimited					
13. SUPPLEMENTARY NOTES The views, opinions and/or findings contained in this report are those of the author(s) and should not be construed as an official Department of the Army position, policy or decision, unless so designated by other documentation.					
14. ABSTRACT The work on this project focused on the design, fabrication, and demonstration of photonic integrated circuits (PICs) which create, multiplex, and demultiplex light beams with orbital angular momentum (OAM). Initial work on devices that manipulate the azimuthal OAM states included 2D silicon PICs for OAM state MUX/DEMUX that supported up to 65 OAM states and 2D silicon nitride PICs for OAM state MUX/DEMUX that supported up to 9 OAM states. Further, we fabricated and demonstrated hybrid devices based on 3D waveguide PICs coupled with 2D silicon PICs that support 15 OAM states and both polarization states. We also developed devices that					
15. SUBJECT TERMS Coherent communications, Optical vortices, Integrated photonics, Multiplexing					
16. SECURITY CLASSIFICATION OF:			17. LIMITATION OF ABSTRACT UU	18. NUMBER OF PAGES	19a. NAME OF RESPONSIBLE PERSON S. J. Ben Yoo
a. REPORT UU	b. ABSTRACT UU	c. THIS PAGE UU			19b. TELEPHONE NUMBER 530-752-7063

## Report Title

### Final Report: Integrated Photonic Orbital Angular Momentum Multiplexing and Demultiplexing on Chip

#### ABSTRACT

The work on this project focused on the design, fabrication, and demonstration of photonic integrated circuits (PICs) which create, multiplex, and demultiplex light beams with orbital angular momentum (OAM). Initial work on devices that manipulate the azimuthal OAM states included 2D silicon PICs for OAM state MUX/DEMUX that supported up to 65 OAM states and 2D silicon nitride PICs for OAM state MUX/DEMUX that supported up to 9 OAM states. Further, we fabricated and demonstrated hybrid devices based on 3D waveguide PICs coupled with 2D silica PICs that support 15 OAM states and both polarization states. We also developed devices that manipulated the radial OAM states using two different technologies; 3D stacking of 2D silicon nitride PICs and multi-ring 3D waveguide PICs coupled to two-layer 2D silicon nitride PICs. Multiple transmission link experiments were conducted using the fabricated OAM devices including free-space coherent communication link demonstrations utilizing polarization, frequency, quadrature and space dimensions to achieve a 1.68-Tb/s link bandwidth and a 9.6-b/s/Hz spectral efficiency. At the same time, photon-efficiency beyond 10 bpp is projected by combining the demonstrated 65 number of OAM states per ring and multi-ring 2D-3D OAM Mux/Demux technologies, while maintaining or suppressing the currently achieved 5~6 dB loss in the 2D-3D OAM Mux/Demux pair. We also demonstrated OAM state switching experiments and formulations of conceptual schemes for generating arbitrary spatial modes and including arbitrary waveform generation and detection in time, space, and spectral domains.

---

**Enter List of papers submitted or published that acknowledge ARO support from the start of the project to the date of this printing. List the papers, including journal references, in the following categories:**

**(a) Papers published in peer-reviewed journals (N/A for none)**

<u>Received</u>	<u>Paper</u>
08/28/2013	1.00 Tiehui Su, Ryan P. Scott, Stevan S. Djordjevic, Nicolas K. Fontaine, David J. Geisler, Xinran Cai, S. J. B. Yoo. Demonstration of free space coherent optical communication using integrated silicon photonic orbital angular momentum devices, Optics Express, (04 2012): 0. doi: 10.1364/OE.20.009396
10/30/2014	4.00 Binbin Guan, Ryan P. Scott, Chuan Qin, Nicolas K. Fontaine, Tiehui Su, Carlo Ferrari, Mark Cappuzzo, Fred Klemens, Bob Keller, Mark Earnshaw, S. J. B. Yoo. Free-space coherent optical communication with orbital angular, momentum multiplexing/demultiplexing using a hybrid 3D photonic integrated circuit, Optics Express, (12 2013): 0. doi: 10.1364/OE.22.000145
<b>TOTAL:</b>	<b>2</b>

**Number of Papers published in peer-reviewed journals:**

---

**(b) Papers published in non-peer-reviewed journals (N/A for none)**

<u>Received</u>	<u>Paper</u>
-----------------	--------------

**TOTAL:**

Number of Papers published in non peer-reviewed journals:

(c) Presentations

Number of Presentations: 0.00

Non Peer-Reviewed Conference Proceeding publications (other than abstracts):

Received Paper

TOTAL:

Number of Non Peer-Reviewed Conference Proceeding publications (other than abstracts):

Peer-Reviewed Conference Proceeding publications (other than abstracts):

Received Paper

08/28/2013	2.00	Ryan P. Scott, Nicolas K. Fontaine, Tiehui Su, Carlo Ferrari, Mark Cappuzzo, Fred Klemens, Binbin Guan, Bob Keller, Mark Earnshaw, S. J. Ben Yoo. Integrated Optical Orbital Angular Momentum Multiplexing Device using 3-D Waveguides and a Silica PLC, CLEO: Science and Innovations. , San Jose, California. : ,
08/28/2013	3.00	Ryan P. Scott , Binbin Guan , Chuan Qin , Nicolas K. Fontaine , Tiehui Su , Carlo Ferrari , Mark Cappuzzo , Fred Klemens , Bob Keller , Mark Earnshaw, S. J. B. Yoo. Free-Space Coherent Optical Communication Demonstration using a 3D Photonic Integrated Circuit Device for Orbital Angular Momentum Multiplexing/Demultiplexing, European Conference on Optical Communication. 22-SEP-13, . : ,
10/30/2014	5.00	Chuan Qin, Binbin Guan, Ryan P. Scott, Roberto Proietti, Nicolas K. Fontaine, Tiehui Su, Carlo Ferarri, Mark Capuzzo, Fred Clemens, Bob Keller, Mark Earnshaw, S.J.Ben Yoo. Demonstration of Orbital Angular Momentum State Conversion using Two Hybrid 3D Photonic Integrated Circuits, Optical Fiber Communication Conference. 09-MAR-13, San Francisco, California. : ,
10/30/2014	6.00	Binbin Guan, Chuan Qin, Ryan P. Scott, Nicolas K. Fontaine, Tiehui Su, Roberto Proietti, S. J. Ben Yoo. Polarization-Diversified, Multichannel Orbital Angular Momentum (OAM) Coherent Communication Link Demonstration using 2D-3D Hybrid Integrated Devices for Free-Space OAM Multiplexing and Demultiplexing, CLEO: Science and Innovations. 08-JUN-13, San Jose, California. : ,
10/30/2014	7.00	Ryan P. Scott, S.J.B. Yoo. 3D waveguide technologies for generation, detection, multiplexing/ demultiplexing orbital angular momentum optical waves, OECC/ACOFT 2014. 06-JUL-14, . : ,

TOTAL: 5

Number of Peer-Reviewed Conference Proceeding publications (other than abstracts):

(d) Manuscripts	
<u>Received</u>	<u>Paper</u>
TOTAL:	

Number of Manuscripts:

Books	
<u>Received</u>	<u>Book</u>
TOTAL:	
<u>Received</u>	<u>Book Chapter</u>
TOTAL:	

Patents Submitted

Patents Awarded

Awards



---

**Graduate Students**

<u>NAME</u>	<u>PERCENT SUPPORTED</u>	Discipline
Burcu Ercan	0.01	
Philip A. Garcia	0.01	
Binbin Guan	0.25	
Guangyao Liu	0.01	
Chuan Qin	0.22	
Kuanping Shang	0.09	
Tiehui Su	0.21	
Runxiang Yu	0.30	
Stanley Cheung	0.10	
<b>FTE Equivalent:</b>	<b>1.20</b>	
<b>Total Number:</b>	<b>9</b>	

---

**Names of Post Doctorates**

<u>NAME</u>	<u>PERCENT SUPPORTED</u>	
Shaoqi Feng	0.08	
Roberto Proietti	0.21	
Wook Jae Lee	0.14	
Ryan P. Scott	0.21	
Domenico Tulli	0.03	
<b>FTE Equivalent:</b>	<b>0.67</b>	
<b>Total Number:</b>	<b>5</b>	

---

**Names of Faculty Supported**

<u>NAME</u>	<u>PERCENT SUPPORTED</u>	National Academy Member
S. J. Ben Yoo	0.10	No
<b>FTE Equivalent:</b>	<b>0.10</b>	
<b>Total Number:</b>	<b>1</b>	

---

**Names of Under Graduate students supported**

<u>NAME</u>	<u>PERCENT SUPPORTED</u>	Discipline
Patrick Huynh	0.10	Electrical and Computer Engineering
<b>FTE Equivalent:</b>	<b>0.10</b>	
<b>Total Number:</b>	<b>1</b>	

### Student Metrics

This section only applies to graduating undergraduates supported by this agreement in this reporting period

The number of undergraduates funded by this agreement who graduated during this period: ..... 1.00

The number of undergraduates funded by this agreement who graduated during this period with a degree in science, mathematics, engineering, or technology fields:..... 1.00

The number of undergraduates funded by your agreement who graduated during this period and will continue to pursue a graduate or Ph.D. degree in science, mathematics, engineering, or technology fields:..... 1.00

Number of graduating undergraduates who achieved a 3.5 GPA to 4.0 (4.0 max scale):..... 1.00

Number of graduating undergraduates funded by a DoD funded Center of Excellence grant for Education, Research and Engineering:..... 0.00

The number of undergraduates funded by your agreement who graduated during this period and intend to work for the Department of Defense ..... 0.00

The number of undergraduates funded by your agreement who graduated during this period and will receive scholarships or fellowships for further studies in science, mathematics, engineering or technology fields: ..... 0.00

### Names of Personnel receiving masters degrees

NAME

**Total Number:**

### Names of personnel receiving PHDs

NAME

0.3 Runxiang Yu

0.1 Stanley Cheung

**Total Number:** 2

### Names of other research staff

NAME

PERCENT SUPPORTED

Victor S. Yeh 0.05

**FTE Equivalent:** 0.05

**Total Number:** 1

### Sub Contractors (DD882)

### Inventions (DD882)

### Scientific Progress

Please See Attachment.

### Technology Transfer

**FINAL TECHNICAL PROGRESS REPORT**

**DARPA DSO Inpho – Integrated Photonic Orbital Angular Momentum Multiplexing and  
Demultiplexing on Chip**

Award # W911NF-12-1-0311

**Report Period:** August 1, 2012 – July 31, 2014

**Technical Point of Contact**

Professor S. J. Ben Yoo  
University of California  
Dept. of Electrical and Computer Engineering  
Kemper Hall, Rm 3179  
Davis, California 95616  
Tel: 530-752-7063  
Fax: 530-752-8428  
E-mail: sbyoo@ucdavis.edu

## Table of Contents

Table of Contents .....	2
List of Figures .....	4
II.A. ABSTRACT.....	9
II.B. TECHNICAL APPROACH AND RESULTS.....	9
II.B.1. Report Summary .....	9
II.B.2. Integrated silicon photonic orbital angular momentum devices <a href="#">Equation Chapter 1 Section 1</a> .....	10
II.B.2.a. Integrated Silicon Photonic OAMv1 Device design and fabrication .....	11
II.B.2.b. Integrated Silicon Photonic OAMv1 Device characterization .....	12
II.B.2.c. Integrated Silicon Photonic OAMv1 Free-Space-Optical Transmission .....	13
II.B.2.d. Integrated Silicon Photonic OAMv2 Design, fabrication and characterization .....	15
II.B.2.e. Integrated silicon-nitride orbital angular momentum devices.....	19
II.B.2.f. Summary of 2D integrated silicon photonic and silicon-nitride orbital angular momentum devices .....	20
II.B.3. Hybrid integrated silica orbital angular momentum devices <a href="#">Equation Chapter 1 Section 1</a> .....	20
II.B.3.a. Integrated silica OAM device concept.....	21
II.B.3.b. 3D-Integrated Photonic Silica OAM device implementation .....	21
II.B.3.c. 3D-Integrated Photonic Silica OAM device characterization overview .....	22
II.B.3.d. Phase characterization of the 3D-Integrated Photonic Silica OAM devices .....	31
II.B.3.e. Integrated 3D-Integrated Photonic Silica OAM device coherent transmission .....	36
II.B.3.f. Packaging of Hybrid 3-D PIC and 2D Silica PLC.....	37
II.B.3.g. Multi-device 15 OAM MUX/DEMUX + 20 Gb/s QPSK optical communication experimental arrangement.....	38
II.B.4. Arbitrary Spatial Waveform Generation and Detection including the Radial Component 41	
II.B.4.a. 3D waveguide writing to add a radial component .....	41
II.B.4.b. Multilayer 2D photonic integrated circuit.....	42
II.B.4.c. Grating simulation.....	44
II.B.4.d. Coupling Simulation .....	46
II.B.4.e. Mask layout.....	46
II.B.5. Multilayer SiN fabrication process .....	48
II.B.6. Arbitrary Spatial Waveform Transformer.....	50
II.B.7. Arbitrary Waveform Shaping in Time, Space, Spectral Domain.....	51
II.B.8. Transmission and switching experiment based on OAM 3D-Integrated Photonic Silica OAM device 56	
II.B.8.a. OAM State Switching .....	56
II.B.8.b. Crosstalk Reduction by Phase Error Correction (PEC) .....	56
II.B.8.c. Crosstalk measurement .....	58
II.B.8.d. Switching experiment setup and BER curve measurement .....	59
II.B.9. OAM based High speed and high spectral efficiency WDM based DP-QPSK transmission experiment .....	62
II.B.10. Multi-ring hybrid 2D-3D OAM devices using multilayer silicon nitride PLCs and 3D waveguide blocks.....	63
II.B.10.a. 3D Waveguide Device Design .....	63
II.B.10.b. 3D Waveguide Fabrication at UC Davis.....	65
II.B.10.c. Multilayer silicon nitride 2D PLC for multi-ring OAM.....	68

II.B.10.d.	Multi-ring 3D Waveguide Block for Multi-ring OAM .....	68
II.B.11.	Multilayer Silicon Nitride Orbital Angular Momentum Devices <a href="#">Equation Chapter 1 Section 1</a> .....	69
II.B.11.a.	Multilayer orbital angular momentum (OAM) device fabrication .....	69
II.B.12.	Multilayer Silicon Nitride Orbital Angular Momentum Device Fabrication.....	74
II.B.13.	Multilayer Silicon Nitride Waveguide Coupler Design.....	77
II.B.13.a.	Design and Simulation: .....	77
II.B.13.b.	Conclusion.....	80
II.B.14.	Investigation of bonding of $\text{LiNbO}_3$ and $\text{SiO}_2$ .....	80
II.B.14.a.	$\text{LiNbO}_3$ material.....	80
II.B.14.b.	Wafer bonding procedures .....	80
II.B.15.	OAM Silica PLC Design.....	83
II.B.16.	Foundry fabricated 2D silica PLC chip loss characterization for both polarizations.....	84
II.B.17.	Publications.....	86
II.B.18.	References.....	86

## List of Figures

Figure 1. (a) Visualization of the electric field of OAM beams. (b) Illustration showing how a beam encoded with an OAM state is sampled and demultiplexed by a circular arrangement of apertures, length-matched waveguides and a star coupler.....	11
Figure 2. Converting azimuthally varying phase to a linear spatial phase.....	11
Figure 3. (a) Waveguide layout of silicon OAM device for multiplexing five OAM modes ( $\ell = +2, +1, 0, -1, -2$ ). (b) Fabricated silicon OAM device. Inset shows SEM photo of grating.....	12
Figure 4. Intensity of near-field output from the OAM device (input port 0) from (a) a simulation and (b) measurement. Intensity of far-field output from OAM device for $\ell = 0$ for (c) a simulation, (d) measured without phase-error correction (PEC), and (e) with PEC. ....	12
Figure 5. Stage setup of OAM Device Characterization by Retro-Reflection.....	13
Figure 6. (a) Experimental arrangement using two silicon PICs to achieve OAM multiplexing and demultiplexing for up to two simultaneous channels.(b) Photo of OAM PICs and optics. ....	14
Figure 7. (a) Single-channel BER performance of the OAM mux/demux 10 Gb/s for BPSK and 20 Gb/s for QPSK. The legend lists the device input port number (i.e., $\ell$ ). (b) BER performance for the $\ell = -2$ and $\ell = +1$ channel without, and with, an interferer with 10 Gb/s BP.....	15
Figure 8. Simulation of silicon OAM device with 64 apertures. a) Near field intensity. b) Far field intensity for OAM charge of 5. c) Near Field phase for OAM charge of 5.....	16
Figure 9. Waveguide layer layout for silicon OAM v2. ....	16
Figure 10. Silicon OAM chips in $10 \times 10 \text{ mm}^2$ die. ....	17
Figure 11. Microscope pictures of silicon OAM v2. a) circular grating emitter b) zoom-in picture of circular grating emitter c) star coupler and array arms. d) electrode, heater and isolation trench.....	17
Figure 12. Stage setup for interference measurement.....	18
Figure 13. a) Near field intensity of 32 apertures on IR camera b) Near field intensity after linearization c) Intensity pattern after interfering the two beams d) phase pattern after interfering the two beams. ....	19
Figure 14. Designed (left) and fabricated (right) silicon-nitride OAM devices.....	20
Figure 15. (a) Integratable OAM multiplexer/demultiplexer concept. ....	21
Figure 16. (a) Illustration of the silica PLC coupled to the 3-D PIC. (b) 3-D waveguide output face detail. (c) Photo of fabricated silica PLC. (d) Photo of unpolished 3-D PIC output face.....	22
Figure 17. (a) Measured excess loss for the silica PLC and 3-D waveguides. (b) Measured intensity and phase of the device's output waveguides without PEC, (c) with PEC. (d) Measured average azimuthal phase at each output waveguide. (e) Unwrapped azimuthal phase for each OAM mode. (f) Calculated OAM mode purity. (g-i) The measured intensity and phase for three OAM modes ( $\ell = +1, -1, +6$ ).....	23
Figure 18. The measured phase for OAM mode $\ell = 0$ .....	23
Figure 19. The measured phase for OAM mode $\ell = 1$ .....	24
Figure 20. The measured phase for OAM mode $\ell = 2$ .....	24
Figure 21. The measured phase for OAM mode $\ell = 3$ .....	24
Figure 22. The measured phase for OAM mode $\ell = 4$ .....	24
Figure 23. The measured phase for OAM mode $\ell = 5$ .....	25
Figure 24. The measured intensity and phase for OAM mode $\ell = 6$ . ....	25
Figure 25. The measured phase for OAM mode $\ell = 7$ .....	25
Figure 26. The measured phase for OAM mode $\ell = -1$ .....	25
Figure 27. The measured phase for OAM mode $\ell = -2$ .....	26
Figure 28. The measured phase for OAM mode $\ell = -3$ .....	26
Figure 29. The measured phase for OAM mode $\ell = -4$ .....	26
Figure 30. The measured phase for OAM mode $\ell = -5$ .....	26
Figure 31. The measured phase for OAM mode $\ell = -6$ .....	27
Figure 32. The measured phase for OAM mode $\ell = -7$ .....	27

Figure 33. The measured intensity and phase for OAM mode $\ell = 0$ .	27
Figure 34. The measured intensity and phase for OAM mode $\ell = -1$ .	28
Figure 35. The measured intensity and phase for OAM mode $\ell = -2$ .	28
Figure 36. The measured intensity and phase for OAM mode $\ell = -3$ .	28
Figure 37. The measured intensity and phase for OAM mode $\ell = -4$ .	28
Figure 38. The measured intensity and phase for OAM mode $\ell = -5$ .	29
Figure 39. The measured intensity and phase for OAM mode $\ell = -6$ .	29
Figure 40. measured intensity and phase for OAM mode $\ell = -7$ .	29
Figure 41. The measured intensity and phase for OAM mode $\ell = 1$ .	29
Figure 42. The measured intensity and phase for OAM mode $\ell = 2$ .	30
Figure 43. The measured intensity and phase for OAM mode $\ell = 3$ .	30
Figure 44. The measured intensity and phase for OAM mode $\ell = 4$ .	30
Figure 45. The measured intensity and phase for OAM mode $\ell = 5$ .	30
Figure 46. The measured intensity and phase for OAM mode $\ell = 6$ .	31
Figure 47. The measured intensity and phase for OAM mode $\ell = 7$ .	31
Figure 48. The measured unwrapped phase for OAM mode $\ell = -7 \sim 7$ .	31
Figure 49. Shearing interferometry arrangement. The collimated beam is the reference.	32
Figure 50. Simulation of shearing interferometry to show the process of phase retrieval.	33
Figure 51. Shearing interferometry measurement results.	33
Figure 52. Verification of shearing interferometry method.	34
Figure 53. Scanning delay-line interferometry arrangement.	34
Figure 54. Measurement results from the scanning delay-line interferometer method.	35
Figure 55. Verification of the scanning delay-line interferometry method.	35
Figure 56. (a) Retrieved near-field pattern amplitude. Phase retrieval from (b) shearing interferometry and (c) scanning delay-line interferometry. (d) The difference in phase between (b) and (c).	35
Figure 57. Retrieved phase of the hybrid silica OAM device without phase-error correction (PEC) and with PEC.	36
Figure 58. Schematic of the 10GBd QPSK OAM transmission experiment. (ECL: external cavity laser, PC: polarization controller, I/Q Mod: I/Q modulator, eAWG: electrical arbitrary waveform generator, ATT: optical attenuator, AOM: acousto-optic modulator, WSS: wavelength selective switch.)	36
Figure 59. (a) BER performance of the different OAM modes for the hybrid OAM device (10 GBd DQPSK, SE = 1.67 b/s/Hz for a single channel). (b) DQPSK constellation at two different OSNRs.	37
Figure 60. Photos of optical packaging station. (a) Overview of arrangement showing input fiber in lower left corner, 6-axis alignment stages in the center and IR imaging camera in upper right. Upper left is the high resolution microscope. (b) Photo showing silica PLC and 3D waveguide block on aluminum carrier (center of photo) before curing.	38
Figure 61. Schematic diagram of the multi-device 15 OAM MUX/DEMUX + 20 Gb/s DQPSK optical communication experimental arrangement.	38
Figure 62. Photo of the multi-device 15 OAM MUX/DEMUX + 20 Gb/s DQPSK optical communication experimental arrangement. The first OAM device is shown in forefront and the second OAM device toward the back.	39
Figure 63. Experimental arrangement of the multichannel OAM free space coherent communication link testbed. ECL: external cavity laser. EDFA: erbium-doped fiber amplifier. PC: polarization controller. ATT: attenuator. BPF: bandpass filter. AOM: acousto-optic modulator.	40
Figure 64. (a) BER performance for single channel OAM state transmission. (b) BER performance for multichannel OAM state transmission (OAM state $-1$ with, and without other states (interferer) present). (c) Constellation plots at 8-dB and 16-dB OSNR for OAM state $-1$ transmission without	

other states. Constellation plots at 14-dB OSNR for OAM state -1 with (d) OAM state +3 present, (e) OAM state +3, -5 present and (f) OAM state +3, -5, -7 present. ....	41
Figure 65. Arbitrary waveform shaper using 3D waveguide writing technique.....	42
Figure 66. The apertures of the 3D waveguides arranged in concentric cylindrical symmetry.....	42
Figure 67. Stacking of multiple 2D layers for arbitrary waveform shaping. (a) Layer 1, (b) Layer 2, (c) Layer 3, (d) Layer 4, (e) Layer 5, and (f) stacked device consisting of Layer 1-5. ....	44
Figure 68 Schematic of grating coupler design .....	44
Figure 69 Table for grating period for different grating etch depth.....	45
Figure 70 Grating simulation for grating pitch 0.897um and etch depth 200nm.....	45
Figure 71 Grating simulation for grating pitch 0.923um and etch depth 300nm.....	46
Figure 72 Coupling between different layer of SiN waveguide for layer gap of 1um, 2um, 3um, 4um ....	46
Figure 73 Overall layout of one die .....	47
Figure 74 Triple layer 16 arm OAM device .....	47
Figure 75 Test structures on the layout.....	48
Figure 76 Microscope picture of the fabricated waveguide layer.....	48
Figure 77 Cross Section of the triple layer SiN device.....	49
Figure 78 SEM picture of the fabricated triple layer device .....	49
Figure 79 SEM picture of the waveguide side wall .....	50
Figure 80. Functional steps for generating orbital angular momentum states starting with (a) linear phase variation, (b) conversion of linear phase variations to azimuthal phase variations to generate (c) OAM states. ....	51
Figure 81. Functional diagram for multiplexing OAM states $ l = -m\rangle,  l = -(m-1)\rangle, \dots  l = +m\rangle$ with coefficients $a_{-m}, a_{-(m-1)}, \dots a_0, \dots a_m$ to create coherent ensemble state $ \Psi\rangle = \sum_i a_i  l = i\rangle$ .....	51
Figure 82. Reverse process of Figure 81 illustrating a functional diagram for demultiplexing the coherent ensemble state $ \Psi\rangle = \sum_i a_i  l = i\rangle$ into OAM states $ l = -m\rangle,  l = -(m-1)\rangle, \dots  l = +m\rangle$ with coefficients $a_{-m}, a_{-(m-1)}, \dots a_0, \dots a_m$ .....	52
Figure 83. Using a new basis $b$ to generate the same coherent ensemble state in Figure 81 which can be now rewritten as $ \Psi\rangle = \sum_j b_j  y = j\rangle = \sum_i a_i  l = i\rangle$ .....	52
Figure 84. OAM state converter.....	52
Figure 85. 10-GBd QPSK link experiment testbed for OAM state conversion using two OAM hybrid devices with ~1.6m round-trip free-space transmission. EDFA: erbium-doped fiber amplifier. PC: polarization controller. ATT: attenuator. BPF: bandpass filter. AOM: acousto-optic modulator. ....	53
Figure 86. (a) BER performance for OAM state -1 as the input and switched to +3, -4 and -5. (b) Constellation plots for each case at OSNR of 12dB and 20dB.....	53
Figure 87 Similarly to Figure 83 and Figure 82, the demultiplexing can utilize the new basis $ \Psi\rangle = \sum_j b_j  y = j\rangle = \sum_i a_i  l = i\rangle$ .....	54
Figure 88. Dynamic optical arbitrary waveform generation techniques using coherent optical frequency combs. ....	54
Figure 89. Dynamic optical arbitrary waveform generation and measurement schemes in symmetry. ....	55
Figure 90. Simplified generation schemes of arbitrary waveforms in time, space, and spectral domains..	55
Figure 91. Simplified detection schemes of arbitrary waveforms in time, space, and spectral domains....	55
Figure 92. OAM state converter .....	56
Figure 93. Verification of Shearing Interferometry Method for Phase Error Measurements .....	56
Figure 94. Verification of Scanning Delay-Line Interferometer Method for Phase Error Measurements..	57
Figure 95. Comparison of Shearing Interferometry and Scanning Delay-Line Interferometer Methods. ...	57



Figure 96 Phase error correction setup. ....	57
Figure 97 Setup for reflection measurement. ....	57
Figure 98. Chip to chip setup. ....	58
Figure 99. Forward crosstalk. ....	58
Figure 100. Backward crosstalk. ....	59
Figure 101. Transmission experiment setup. ....	59
Figure 102. Transmission BER curves ....	60
Figure 103. Switching experiment setup. ....	60
Figure 104. Switching experiment BER curves. ....	61
Figure 105 (a) Concept of the OAM photonic integrated circuit. (b) Conceptual view of the 2D-3D hybrid integrated device for OAM mux/demux. (c) Normalized transmission of the OAM mux/demux pair. (d) Experimental arrangement of the multichannel OAM polarization-diversified free-space communication link testbed. FPR: free-propagation region; ECL: external cavity laser; OFC: optical frequency comb; WSS: wavelength-selective switch; EDFA: erbium-doped fiber amplifier; ATT: attenuator; PC: polarization controller; PBC: polarization beam combiner; BPF: bandpass filter. EAWG: electrical arbitrary waveform generator. ....	62
Figure 106. (a) BER performance for the multichannel OAM link with 14×10-GBd, DP-QPSK WDM channels. (b) Averaged BER for three OAM states (0, -3 and -6) for two received orthogonal polarizations (x-pol and y-pol not necessarily the same as device TE and TM). ....	63
Figure 107. Targeted optical mode generations using multi-ring OAM MUX/DEMUXes. (a) Laguerre-Gaussian/Ince-Gaussian/Hermite Gaussian modes (figure courtesy of kb-en.radiantzemax.com). (b) Linear Polarization modes (figure courtesy of SPIE.org). ....	64
Figure 108. (a) Auto-routing and optical-path-length-matched multi-ring 3D waveguide design. (b) Output facet view. ....	64
Figure 109. Path-length matched 3D waveguide design flow chart. ....	65
Figure 110. Optimization of 3D waveguide inscription technology by adjusting the femtosecond laser power and repetition rates. ....	66
Figure 111. (a) Mode profile for a single scan waveguide. (b) x and y cross section for the mode profile. ....	67
Figure 112. (a) Mode profile for small MFD waveguide (6.5 $\mu\text{m}$ × 5.8 $\mu\text{m}$ ). (b) Large MFD waveguide (11.5 $\mu\text{m}$ × 11.34 $\mu\text{m}$ ). ....	67
Figure 113. (a) Si <sub>3</sub> N <sub>4</sub> device mask layout. (b) Photo of fabricated azimuthal and radial index Si <sub>3</sub> N <sub>4</sub> OAM device. ....	68
Figure 114. Fabricated 3D waveguide multi-ring OAM device. (a) Input facet view showing some of the 64 input waveguide array. (b) Close-up showing input waveguide separation in the center section where the upper and lower layers overlap. (c) Output facet view showing the two concentric output circular patterns (32 waveguides in each ring). ....	69
Figure 115. Fabrication process flow: a) silicon dioxide deposition b) first silicon nitride film deposition c) alignment mark patterning (photolithography and etch) d) grating and waveguide patterning of first layer e) silicon dioxide deposition f) chemical mechanical polishing for planarization g) second silicon nitride film deposition h) grating and waveguide patterning of second layer i) silicon dioxide deposition and chemical mechanical polishing for planarization j) third silicon nitride film deposition k) grating and waveguide patterning of third layer l) top silicon dioxide deposition. Each color describes the materials. ....	70
Figure 116. SEM images of grating and waveguide structures. They show the well-defined feature dimension. ....	71
Figure 117. Microscope images of fabricated silicon nitride OAM devices. Gratings with different shape and various width of the tapered waveguide between waveguides and gratings are designed: a) centric arc b) parallel with narrow tapered waveguide c) centric ring gratings d) parallel with broad tapered waveguide. Mask layouts of gratings are shown in the inset. ....	72

Figure 118. Mask layout (left) and fabricated wafer with silicon nitride devices (right). .....	73
Figure 119. Stacking of multiple 2D layers for arbitrary waveform shaping. (a) Stacked device consisting of Layer 1-5. (b) Fabricated three layer silicon nitride/silicon dioxide OAM device. Image of the three layer silicon nitride/silicon dioxide OAM device when the (c) bottom (layer 1), (d) middle (layer 2), and (e) top (layer 3) are illuminated. ....	73
Figure 120. CMP results: a) scanned waveguide region b) surface profile before CMP c) surface profile after CMP. ....	74
Figure 121. Integrated Multilayer silicon nitride OAM PLC cross section. ....	74
Figure 122. Schematic picture of the multilayer device .....	75
Figure 123 Top view of the fabricated device .....	75
Figure 124. Microscope picture of the grating layers. ....	76
Figure 125. Grating emission of a) lowest layer b) middle layer c) top layer .....	76
Figure 126. Schematic diagram of the multi-layer inverse taper coupling. ....	77
Figure 127: 2D top view of the multi-layer inverse taper coupling. ....	77
Figure 128. Simulated field profile of a multi-layer inverse taper coupling. ....	78
Figure 129. Variation of the simulated transmission with overlap length. ....	79
Figure 130. Variation of the simulated Loss with taper length. ....	79
Figure 131. Misalignment between layers. ....	80
Figure 132 :left) Bonded 3 inches $\text{LiNO}_3$ wafer to a 3 inches $\text{SiO}_2$ wafer [4]; right) SEM cross sectional image of the hybrid substrate. ....	81
Figure 133 Spin curves for various commercially available BCB formulations. ....	81
Figure 134 BCB degree of polymerization as a function of temperature and time. ....	82
Figure 135 SEM image of ultra-thin BCB bonding layer between Si and InP wafers, obtained using 1:12 BCB: mesitylene solution. ....	82
Figure 136. Waveguide mode design and simulation results. (a) Index profile (1.5% index contrast). (b) Calculated optical mode profile. (c). Optical mode profile computed using the effective index method. (d) Index contour map of waveguide and cladding. (e) Simulated optical mode profile. ....	83
Figure 137. Fabrication process of the silica device. ....	83
Figure 138 Layout of the OAM silica PLC. ....	84
Figure 139. Loss characterization setup. ....	84
Figure 140. Loss measurement for a fixed central input and different outputs, for both polarizations. ....	85
Figure 141. Loss measurement for a fixed central output and different inputs, for both polarizations. ....	85

## II.A. ABSTRACT

The work on this project focused on the design, fabrication, and demonstration of photonic integrated circuits (PICs) which create, multiplex, and demultiplex light beams with orbital angular momentum (OAM). Initial work on devices that manipulate the azimuthal OAM states included 2D silicon PICs for OAM state MUX/DEMUX that supported up to 65 OAM states and 2D silicon nitride PICs for OAM state MUX/DEMUX that supported up to 9 OAM states. Further, we fabricated and demonstrated hybrid devices based on 3D waveguide PICs coupled with 2D silica PICs that support 15 OAM states and both polarization states. We also developed devices that manipulated the radial OAM states using two different technologies; 3D stacking of 2D silicon nitride PICs and multi-ring 3D waveguide PICs coupled to two-layer 2D silicon nitride PICs. Multiple transmission link experiments were conducted using the fabricated OAM devices including free-space coherent communication link demonstrations utilizing polarization, frequency, quadrature and space dimensions to achieve a 1.68-Tb/s link bandwidth and a 9.6-b/s/Hz spectral efficiency. At the same time, photon-efficiency beyond 10 bpp is projected by combining the demonstrated 65 number of OAM states per ring and multi-ring 2D-3D OAM Mux/Demux technologies, while maintaining or suppressing the currently achieved 5~6 dB loss in the 2D-3D OAM Mux/Demux pair. We also demonstrated OAM state switching experiments and formulations of conceptual schemes for generating arbitrary spatial modes and including arbitrary waveform generation and detection in time, space, and spectral domains.

## II.B. TECHNICAL APPROACH AND RESULTS

### II.B.1. Report Summary

This report summarizes progress on the project *Integrated Photonic Orbital Angular Momentum Multiplexing and Demultiplexing on Chip* during the period from August 1, 2012 to July 31, 2014. A bullet list of progress is listed below.

- 2D Silicon Photonic Integrated Circuits for OAM state MUX/DEMUX
  - 5 OAM state silicon PLC designed, fabricated, and characterized
  - Chip-to-Chip 5 OAM MUX/DEMUX + 10 Gb/s BPSK/QPSK/8PSK optical communication demonstration achieved low bit-error-rate performance
  - 33 OAM state silicon PLC designed, fabricated, and initial characterization
  - 65 OAM state silicon PLC designed and fabricated
- 2D Silicon Nitride Photonic Integrated Circuits for OAM state MUX/DEMUX
  - 9 OAM state silicon nitride PLC designed, fabricated, and initial characterization completed.
- 3-D Photonic Integrated Circuit (PIC) with 2D Silica PLC phase control
  - 2D Silica PLC designed, fabricated and tested
  - 3-D waveguide designed, fabricated and tested
  - Phase control successfully achieved for phase error correction
  - Retro-reflected device 15 OAM MUX/DEMUX + 20 Gb/s DQPSK optical communication demonstration with error-free performance
  - Hybrid packaging of 3-D PIC and 2D Silica PLC successfully developed and demonstrated
  - Multi-device 15 OAM MUX/DEMUX + 20 Gb/s DQPSK optical communication experiment completed.
- Spatial Phase Measurement System
  - Shearing interferometry method successfully developed and demonstrated
  - Scanning delay-line interferometry method successfully developed and demonstrated
- Radial and Azimuthal Control of Phase and Amplitude of the Waveform
  - Conceptual design using 3D photonic integrated circuits

- Conceptual design using 2D photonic integrated circuits
- Arbitrary Spatial Waveform Generation and Detection
  - Formulation of a conceptual scheme for generating arbitrary spatial modes
  - Successful fabrication development for multi-layer fabrication processes.
- Arbitrary Waveform Generation and Detection In Time, Space, and Spectral Domains.
  - Formulation of a conceptual scheme for generating arbitrary waveforms in time, space, and spatial domains by cascading OAWG and the above spatial waveform shaper
  - Formulation of a conceptual scheme for detecting arbitrary waveforms in time, space, and spatial domains by cascading OAWM and the above spatial waveform shaper.
- Combined OAM & OAWG transmission experiments using 3D-Integrated Photonic Silica OAM device
  - 15 OAM state transmission with QPSK at 10 Gb/s
  - Phase error correction (PEC) and crosstalk measurements for improved transmission performance
- OAM state switching experiments using on 3D-Integrated Photonic Silica OAM device
  - Three state simultaneous switching from 15 OAM state with QPSK at 10 Gb/s
  - Phase error correction (PEC) and crosstalk measurements for improved transmission performance
- Investigation of LiNbO<sub>3</sub> based electro-optical devices on SiO<sub>2</sub> for 2D OAM PLC
  - Investigated BCB wafer bonding of LiNbO<sub>3</sub> on SiO<sub>2</sub> for OAM devices with low power consumption and faster reconfiguration by using electro optical effects instead of thermo-optical effects.
- Multi-ring hybrid 2D-3D OAM devices using multilayer silicon nitride PLCs and 3D waveguide blocks
  - Created 3D waveguide device design software and algorithms including path-length matching
  - Developed 3D waveguide device fabrication at UC Davis
  - Multilayer silicon nitride PLCs for multi-ring OAM designs and fabrication
  - Designed and fabricated multi-ring 3D waveguide device at UC Davis
- 3D stacking of 2D Silicon Nitride Photonic Integrated Circuits for OAM state MUX/DEMUX
  - Three layer 9 OAM state silicon nitride PLC design, fabrication, and characterization
  - Improved multi-layer fabrication to achieve lower losses
  - Multilayer coupler design for low loss multi-layer coupling
- Commercial Foundry 2D silica PLC chip loss characterization for both polarizations

### II.B.2. Integrated silicon photonic orbital angular momentum devices

In this section, we describe and demonstrate a photonic integrated circuit (PIC) that is capable of demultiplexing (or multiplexing) free-space optical beams with multiple OAM states near 1550 nm into (or from) single-mode waveguides. As such, it easily connects with high-speed telecommunication components like modulators and photodetectors. Further, the device is fabricated using a CMOS-compatible silicon fabrication process, allowing future integration with on-chip modulators, detectors and possibly even lasers.

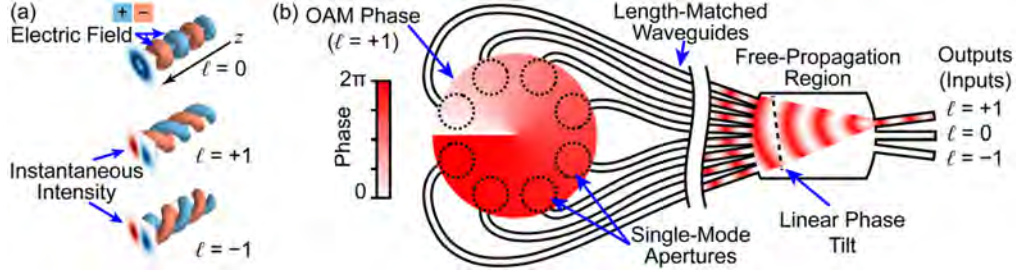


Figure 1. (a) Visualization of the electric field of OAM beams. (b) Illustration showing how a beam encoded with an OAM state is sampled and demultiplexed by a circular arrangement of apertures, length-matched waveguides and a star coupler.

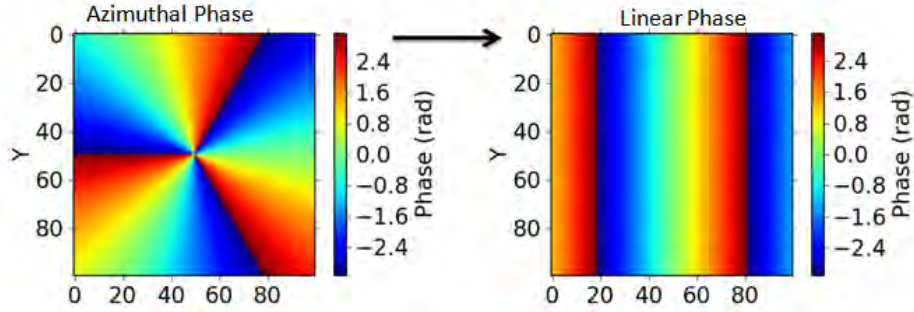


Figure 2. Converting azimuthally varying phase to a linear spatial phase.

Working as a demux (i.e., OAM state decoder), Figure 1(b) shows how a circular array of waveguide grating couplers are used to sample areas (dashed circles) of an incoming beam encoded with an OAM state (e.g.,  $\ell = 1$ ) into a corresponding array of single-mode waveguides. Careful waveguide layout ensures that they have identical optical path lengths. Thus, at the input of the free-propagation region (FPR), the azimuthally varying phase of the OAM state is converted into a linear phase front with a tilt angle determined by the incoming beam's topological charge, as indicated in Figure 2. The circular placement of the array waveguides at the input of the FPR focuses the light, and the tilt of the linear phase front directs it to a corresponding output. Using the PIC as a mux is as simple as reversing the light's propagation direction. This paper demonstrates a full coherent optical communication link including a pair of silicon photonic OAM mux/demux devices.

### II.B.2.a. *Integrated Silicon Photonic OAMv1 Device design and fabrication*

Figure 3 (a) shows the device's waveguide layout which is designed for a silicon-on-insulator (SOI) material platform, is optimized for TE polarization, and uses a 1  $\mu\text{m}$  wide silicon rib waveguides (effective index of 3.27). The upper inset of Figure 3(a) shows a quarter of the circular grating which is formed by concentric etched circles that have a grating period of 0.47  $\mu\text{m}$ , a 50% duty cycle, and an outer radius of 25  $\mu\text{m}$ . The circular grating converts the vertically incident optical beam (azimuthal polarization) into a horizontally propagating beam. Sixteen tapered waveguides surround and capture the light from the grating and send it to length-matched waveguides (20 mm long) that terminate at the FPR [lower inset of Figure 3(a)]. Depending on the OAM state of the input beam, the 16 guided modes will have a specific linear phase variation. Since the FPR is designed based on the Rowland circle principle, it focuses the 16 beams onto five waveguide outputs according to the linearly varying phase associated with the five different OAM states (labeled as  $\ell = +2, +1, 0, -1, -2$ ). The five waveguide outputs are tapered to a 3  $\mu\text{m}$  width at the edge of the chip and have 250  $\mu\text{m}$  spacing. The device also includes aluminum contact pads and traces that connect to sixteen Ti/Pt heaters. The heaters, located just above the waveguides, thermo-

optically change the local index of refraction to compensate for optical phase errors ( $< \pi$  rad) in the waveguides.

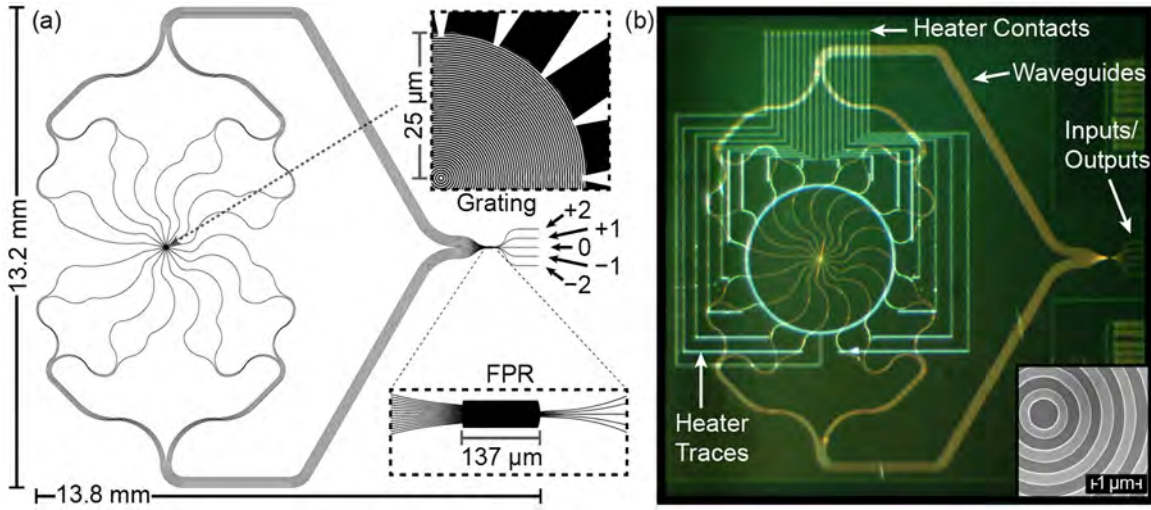


Figure 3. (a) Waveguide layout of silicon OAM device for multiplexing five OAM modes ( $\ell = +2, +1, 0, -1, -2$ ). (b) Fabricated silicon OAM device. Inset shows SEM photo of grating.

Figure 3 (b) shows the OAM device fabricated on a 6 inch silicon-on-insulator (SOI) wafer with a top silicon layer thickness of  $0.5 \mu\text{m}$ , and buried oxide (BOX) layer thickness of  $3 \mu\text{m}$ . The waveguide layer was patterned using deep-UV ASML stepper with  $248 \text{ nm}$  KrF excimer source and 4:1 reduction, then transferred to the silicon layer by a  $250 \text{ nm}$  deep highly anisotropic HBr TCP reactive ion etch. The subsequent stepper lithography and etching process was similar to the previous steps and defined the circular grating layer with an etching depth of  $200 \text{ nm}$ . The inset of Figure 3(b) shows a scanning electron microscope (SEM) image of the fabricated grating. Next, the wafer was clad with  $1 \mu\text{m}$  thick  $\text{SiO}_2$  by low pressure chemical vapor deposition (LPCVD) and then annealed for densification at  $900^\circ\text{C}$  for 40 minutes in an inert atmosphere. The LPCVD  $\text{SiO}_2$  coating isolates the waveguide mode from the surface metal layer, eliminating the loss due to metal absorption. Ti/Pt heaters were deposited with an e-beam evaporator and defined through liftoff. The heaters provide phase control on the length-matched waveguides. As a final step, aluminum electrodes were deposited and defined with another liftoff process.

### II.B.2.b. Integrated Silicon Photonic OAMv1 Device characterization

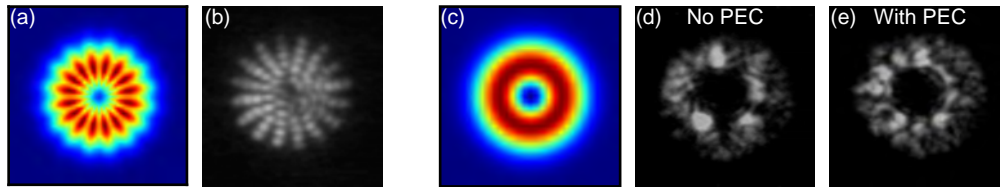


Figure 4. Intensity of near-field output from the OAM device (input port 0) from (a) a simulation and (b) measurement. Intensity of far-field output from OAM device for  $\ell = 0$  for (c) a simulation, (d) measured without phase-error correction (PEC), and (e) with PEC.

Initial device characterization was performed on straight waveguides fabricated on the same silicon chip. The Fabry-Pérot resonance measurement method yielded the straight waveguide loss of  $1.9 \text{ dB/cm}$ . Figure 4 (a) shows a simulation of the near-field intensity pattern of the circular grating output when light is coupled into the  $\ell = 0$  input. Figure 4(b) is the near-field intensity pattern imaged by an infrared vidicon camera for comparison. The 16 radial stripes indicate that the beam coupled from the waveguides to air as



expected. Each radial stripe shows a periodic dark-bright pattern which is caused by interference from light that leaks across the center of the grating from the opposing waveguides. Figure 4(c) shows a simulation of the far-field intensity pattern for  $\ell = 0$ . For comparison, Figure 4(d) shows the measured far-field pattern with no phase-error correction (PEC) and Figure 4(e) shows the more evenly distributed far-field pattern after applying appropriate PEC.

As an initial test of a single OAM device's performance, we used an objective [20 $\times$ , 0.57 numerical aperture (NA)] to collect the light from the grating output, followed by a gold-coated mirror that retro-reflected the OAM mode back through the objective and into the OAM device. The stage setup is showed in Figure 5. Thus, the same OAM device acts as both a transmitter and a receiver. In this retro-reflection configuration, when light is coupled into the +1 port, the reflected beam is directed to -1 port; similarly the input on the +2 port gives output on the -2 port. Using this configuration to measure the crosstalk performance, we coupled light into the +2 port and measured output ports -2, -1, and 0. The crosstalk without PEC from the -2 port to the -1 port was only -3 dB and -5 dB for the 0 port. After PEC was applied, the crosstalk improved significantly, the -2 port to the -1 port was -10.5 dB and -12 dB for the 0 port.

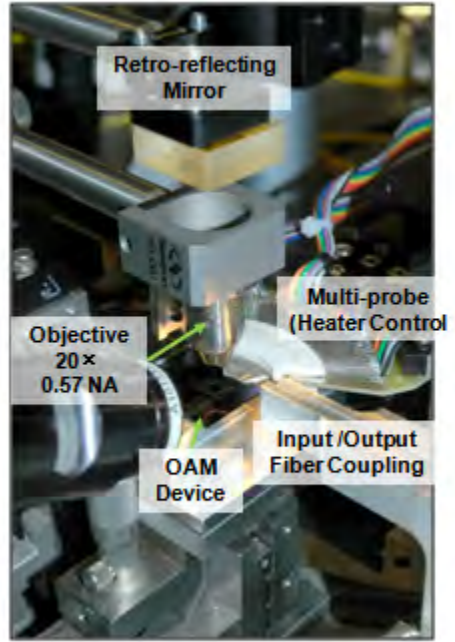


Figure 5. Stage setup of OAM Device Characterization by Retro-Reflection.

### II.B.2.c. *Integrated Silicon Photonic OAMv1 Free-Space-Optical Transmission*

Figure 6(a) shows the experimental arrangement for a SDM coherent optical communication link using two OAM devices as an OAM mux/demux. The digital coherent transmitter consists of a continuous-wave (cw) laser centered at 1540 nm, followed by an erbium-doped fiber amplifier (EDFA), an I/Q modulator, and another EDFA. The I/Q modulator was driven by an electronic arbitrary waveform generator at 12 GSa/s (5.5 GHz of analog bandwidth). Using digital signal processing (DSP) implemented in MATLAB, the digital coherent transmitter created data waveforms in either a 1 b/s/Hz, 10 Gb/s binary phase shifted keying (BPSK) format or a 2 b/s/Hz, 20 Gb/s quadrature phase shifted keying (QPSK) format. Both data waveform formats consisted of a pseudorandom bit sequence (PRBS) of length  $2^7-1$ . An acousto-optic modulator frequency shifted a sample of the unmodulated cw laser by 35 MHz to provide a reference (LO) signal for the digital coherent receiver. An EDFA amplified the signal before it

was split and sent to the OAM mux (OAM #1). The output beam from OAM #1 was then collected with an objective (20 $\times$ , 0.57 NA) and directed to OAM demux (OAM #2), where a second identical objective was used to focus the beam onto the 50  $\mu\text{m}$  diameter grating. Figure 6(b) shows a photo of the free-space optics and OAM devices, where the total beam path length was 0.5 m. An EDFA and 1 nm bandpass filter (BPF) immediately amplified the demuxed signal from OAM #2 before an attenuator and power meter tap that were used to measure the bit-error-rate (BER) performance. The signal passed through a second EDFA and 1 nm BPF before the return fiber link and detection by the digital coherent receiver. Offline DSP enabled computing the BER performance. All measurements used TE-polarization, which is transformed into azimuthal polarization by the OAM devices.

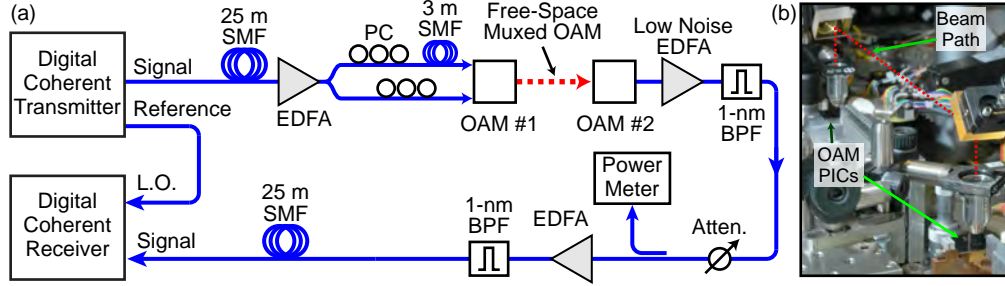


Figure 6. (a) Experimental arrangement using two silicon PICs to achieve OAM multiplexing and demultiplexing for up to two simultaneous channels.(b) Photo of OAM PICs and optics.

The BER performance for both BPSK and QPSK data were separately measured on each of the five OAM channels ( $\ell = -2, -1, 0, 1, 2$ ) by removing the power splitter and sending only one input signal to OAM #1. Figure 5(a) presents the BER versus received power at the input of the link EDFA. A total of 14,986 bits, limited by the memory, were recorded and analyzed at each power level. The back-to-back data were taken without the OAM devices and instead a fiber attenuator provided an output power of  $-45$  dBm (i.e., the highest OAM device output). For the 10 Gb/s BPSK data, all OAM channels in repeated experiments were error free for the 14,986 bits tested. The 3 to 6 dB power penalty with respect to the back-to-back case likely arises from fiber coupling loss variations for each port. For the 20 Gb/s QPSK data, there is a  $\sim 6$  dB power penalty ( $\text{BER} = 10^{-3}$ ) for the back-to-back case (with respect to BPSK back-to-back) and an error floor at a BER of  $\sim 10^{-4}$ . Since the symbol rates are the same for the BPSK and QPSK data, 3 dB of the power penalty is expected. However, the origin of the excess 3 dB penalty is not understood at this time. The error floor is likely due to the limited signal-to-noise ratio of the amplified  $-45$  dBm signal from OAM #2. Figure 5(b) shows the 10 Gb/s BPSK BER performance in the presence of a second active channel (interferer) with equal power. Due to the additional loss from the splitter, the single-channel BER has a  $\sim 4$  dB power penalty ( $\text{BER} = 10^{-3}$ ) compared to Figure 7(a). The addition of an interferer when  $\ell = -2$  only impacts the BER below  $\sim 10^{-3}$ , while the introduction of an interferer when  $\ell = -1$ , causes a  $\sim 7$  dB power penalty. This is likely due to the difference in crosstalk between the OAM channels used in the two measurements ( $-10$  dB versus  $-6$  dB). Preliminary measurements made by imaging the outputs onto an IR vidicon camera indicate that the crosstalk of the adjacent channels are not particularly worse than the other channels.



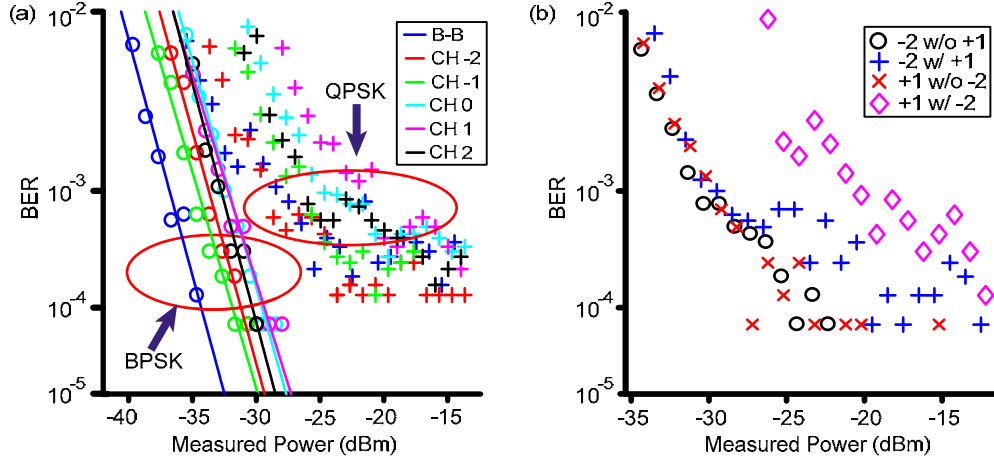


Figure 7. (a) Single-channel BER performance of the OAM mux/demux 10 Gb/s for BPSK and 20 Gb/s for QPSK. The legend lists the device input port number (i.e.,  $\ell$ ). (b) BER performance for the  $\ell = -2$  and  $\ell = +1$  channel without, and with, an interferer with 10 Gb/s BP

The fiber-to-fiber loss for the free-space communication link was estimated at  $\sim 55$  dB which included (a) 8 dB fiber coupling loss comprised of 1 dB silica fiber tip reflection, 5 dB mode mismatch, and 2.4 dB silicon facet reflection, (b) 4 dB waveguide propagation loss, (c) 4.5 dB grating-to-air loss, (d) 2 dB objective lens loss (non-optimal AR coating designed for visible), (e) repeat of (d), (f)  $\sim 21$  dB air-to-grating loss from wavefront errors (spherical aberration, residual quadratic spatial phase, etc.) and mode mismatch for the beam as it enters the circular grating, repeat of (b) and (a) for the demux device. Using a true  $4f$  imaging system is expected to reduce (f), but a full analysis of the beam relay optics is necessary. Additional device optimizations include reducing the fiber-to-waveguide coupling loss with an inverse taper at the waveguide outputs, reducing crosstalk across the grating center with a trench, and decreasing the grating-to-air loss by increasing the grating diameter and the total number of grating periods. A larger grating diameter also allows more waveguides around the grating to support multiplexing OAM states with a larger topological charge.

Although not investigated here, similar to most free-space OAM implementations, misalignments between the demonstrated OAM device pair result in increased signal losses and increased crosstalk between demultiplexed states. A full analysis of the free-space beam and optics will provide insight into the specific sensitivities of these OAM devices in a realistic free-space communications system.

## II.B.2.d. *Integrated Silicon Photonic OAMv2 Design, fabrication and characterization*

### II.B.2.d.i. *Device design and layout*

One of the major advantage of PLC based OAM is that it can be scaled to mux/demux higher order OAM mode without adding extra components in the setup. Figure 8 shows simulation of a silicon OAM device with 64 apertures. In theory, such device can mux/demux OAM stage  $-32 \sim +32$ .

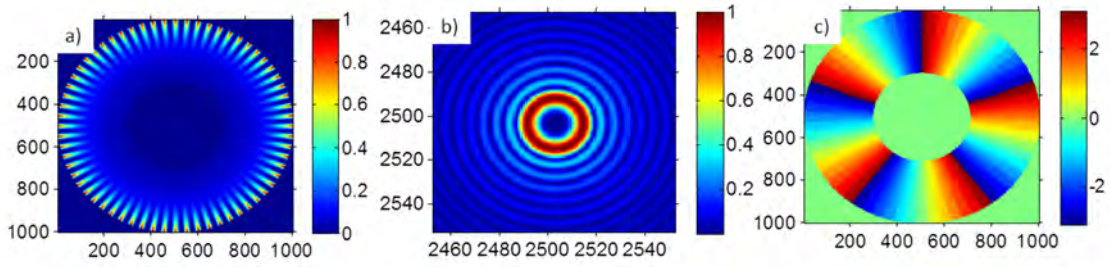


Figure 8. Simulation of silicon OAM device with 64 apertures. a) Near field intensity. b) Far field intensity for OAM charge of 5. c) Near Field phase for OAM charge of 5.

Figure 9 shows the waveguide layout of silicon OAM device version 2. Four devices are included. Two small devices ( $3.6\text{ mm} \times 3.6\text{ mm}$ ) support OAM state  $-4 \sim +4$ . Two larger devices ( $4.2\text{ mm} \times 5.6\text{ mm}$ ) support OAM state  $-16 \sim +16$ .

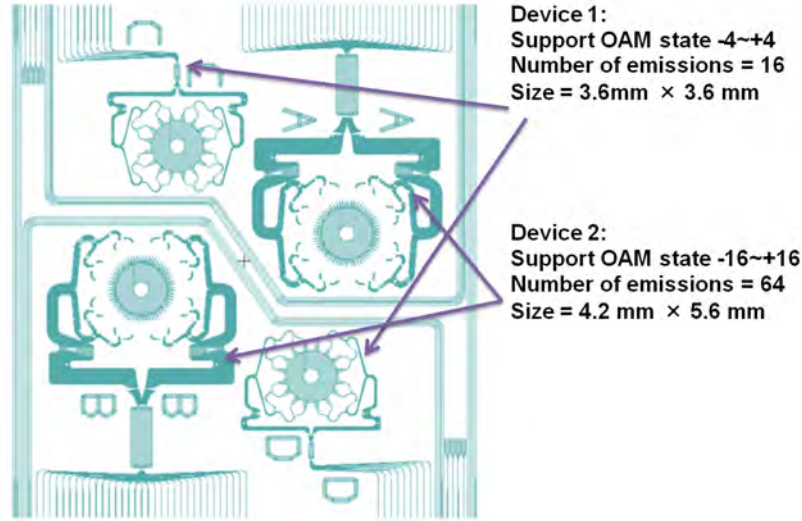


Figure 9. Waveguide layer layout for silicon OAM v2.

#### II.B.2.d.ii. *Fabricated Integrated Silicon Photonic OAMv2 device*

Figure 10 shows the actual fabricated device comparing to an U.S. currency dime. The fabrication process of the device is the same as the OAM device version 1. Each device die is  $10 \times 10\text{ mm}^2$  in size.

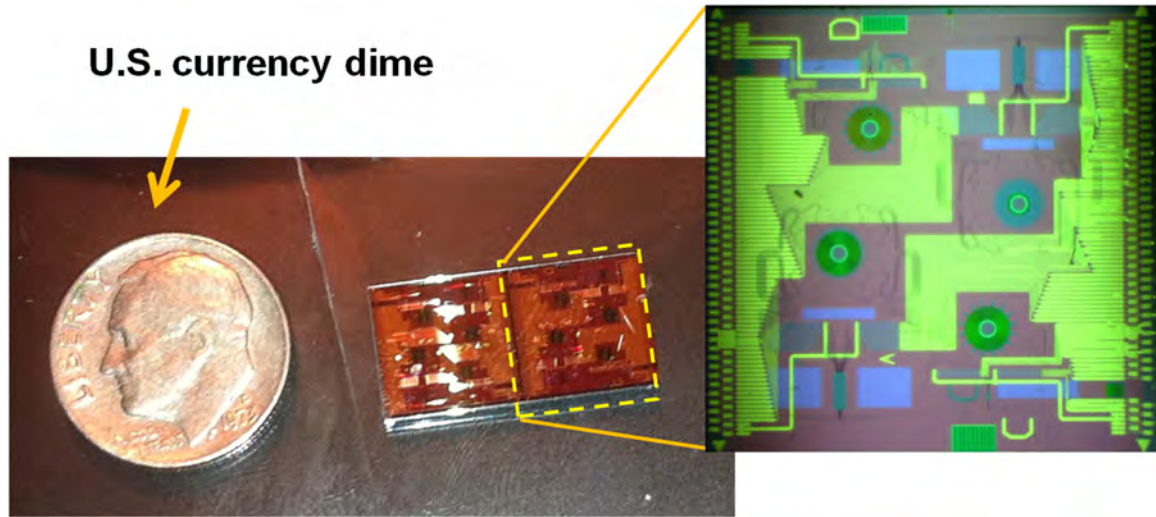


Figure 10. Silicon OAM chips in  $10 \times 10 \text{ mm}^2$  die.

Figure 11 shows microscope picture of the fabricated silicon OAM v2. The microscope picture is an important step to check the fabrication goes well. Figure 11 a) and b) shows the circular grating structure, which is the finest feature on the device. The image shows that the gratings are even and uniform. Figure 11 c) shows the junction between array arms and free propagation region, and the openings are clear during etch process. Figure 11 d) shows the metal layer. Trenches are put between heaters to improve heating efficiency and reduce crosstalk. The metal deposition and lift-off process went well, and no electrical shorts or opens were noticed.

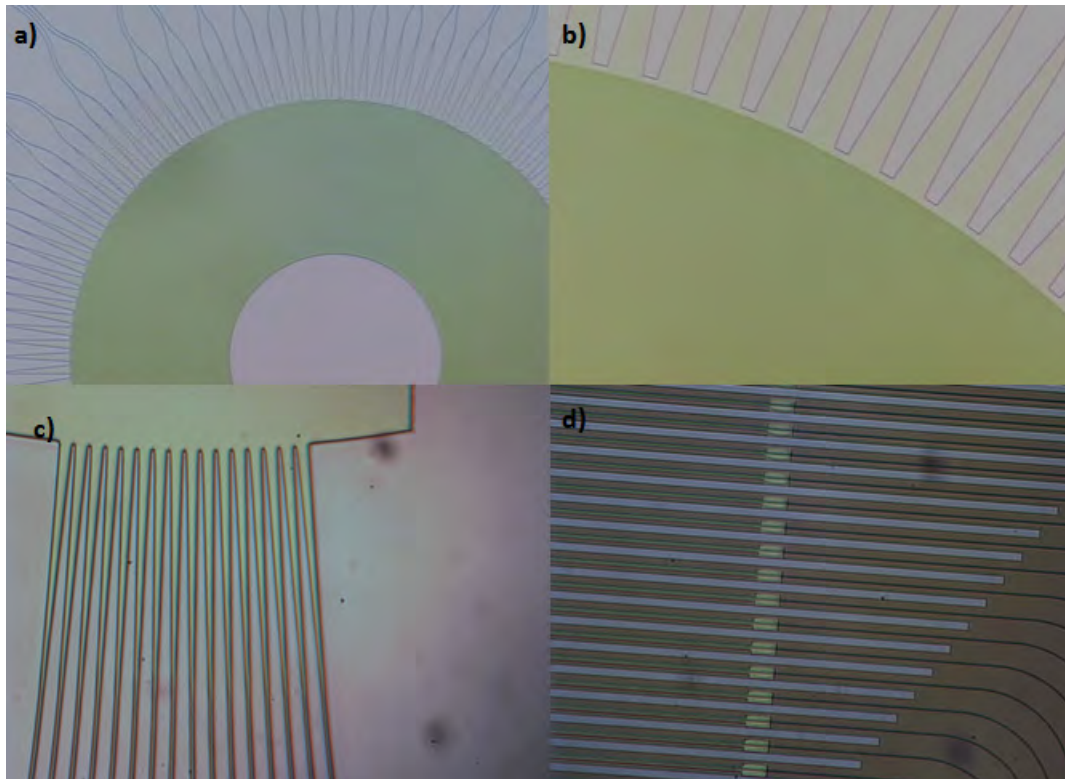


Figure 11. Microscope pictures of silicon OAM v2. a) circular grating emitter b) zoom-in picture of circular grating emitter c) star coupler and array arms. d) electrode, heater and isolation trench.

### II.B.2.d.iii. *Characterization of Integrated Silicon Photonic OAM v2*

An interference measurement stage was setup to characterize the device, as shown in Figure 12. A 1550 nm beam passes through a polarization controller, and it is then amplified by an EDFA. The beam is then split into two parts. 98% of the split beam is launched into the OAM device, and an objective focuses the field from OAM device to an IR camera (Vidicon). The other 2% of the split passes through a collimator to form a collimated beam, then a half-wave plate to create circular polarization. The two beams are combined using a 50:50 beam splitter. The interference pattern on the IR camera shows the phase of each aperture. This technique is still being developed.

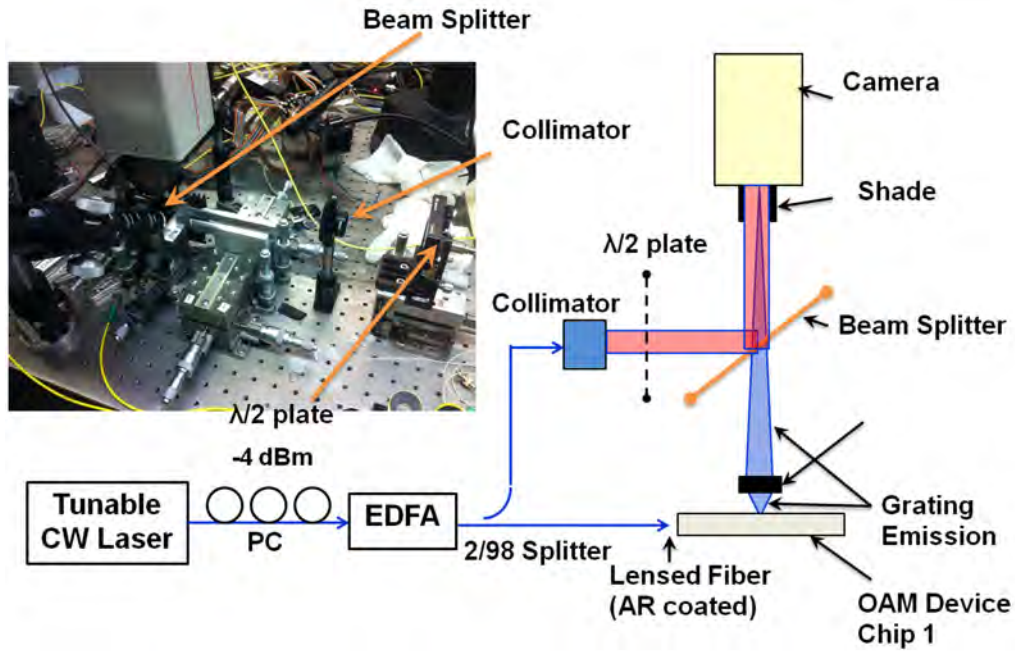


Figure 12. Stage setup for interference measurement.



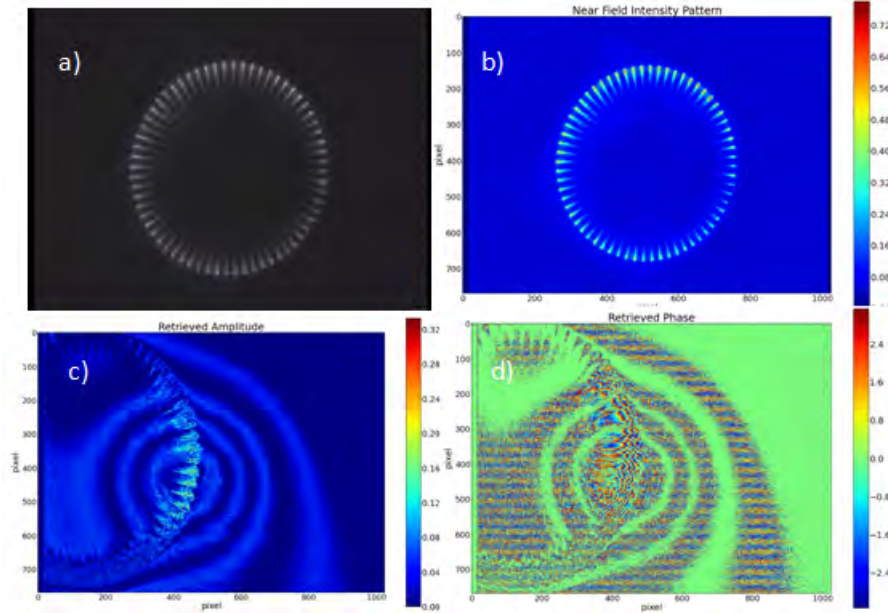


Figure 13. a) Near field intensity of 32 apertures on IR camera b) Near field intensity after linearization c) Intensity pattern after interfering the two beams d) phase pattern after interfering the two beams.

#### II.B.2.e. *Integrated silicon-nitride orbital angular momentum devices*

In an effort to reduce optical losses in integrated OAM devices, we have investigated silicon nitride on silicon oxide devices. State-of-the-art silicon nitride or silicon oxynitride waveguides can achieve optical losses below 0.1 dB/cm, and even below 0.01 dB/cm in thin core (<200 nm) devices. Further, the optical modes can be tailored to couple directly to cleaved fibers with low coupling losses. However, this loss values depend greatly on the quality of silicon nitride and fabrication. In particular, we spent dedicated efforts on improving fabrication processes of the silicon nitride waveguides with various thicknesses. While all the fabrication steps including silicon nitride deposition, lithography, and annealing are satisfactory, the dry-etching tools in UC Davis and UC Berkeley appear to cause sidewall roughness that limits optical waveguide propagation losses to > 1 dB/cm. Since our silicon photonic waveguide devices have lower propagation losses (~0.3 dB/cm) and because the 3D waveguide structures discussed below can achieve < 0.1 dB/cm losses, we are currently concentrating on 2D silicon photonic devices and 3D silica photonic devices while we further improve the silicon nitride etching processes and seek external foundry services for etching silicon nitride. Figure 14 shows (left) device design layout with (1) five 9 state OAM devices, (2) four straight waveguide and etch depth test structures, (3) all the waveguides are connected to inverse taper coupler for low loss fiber interfaces, and (right) a fabricated wafer.

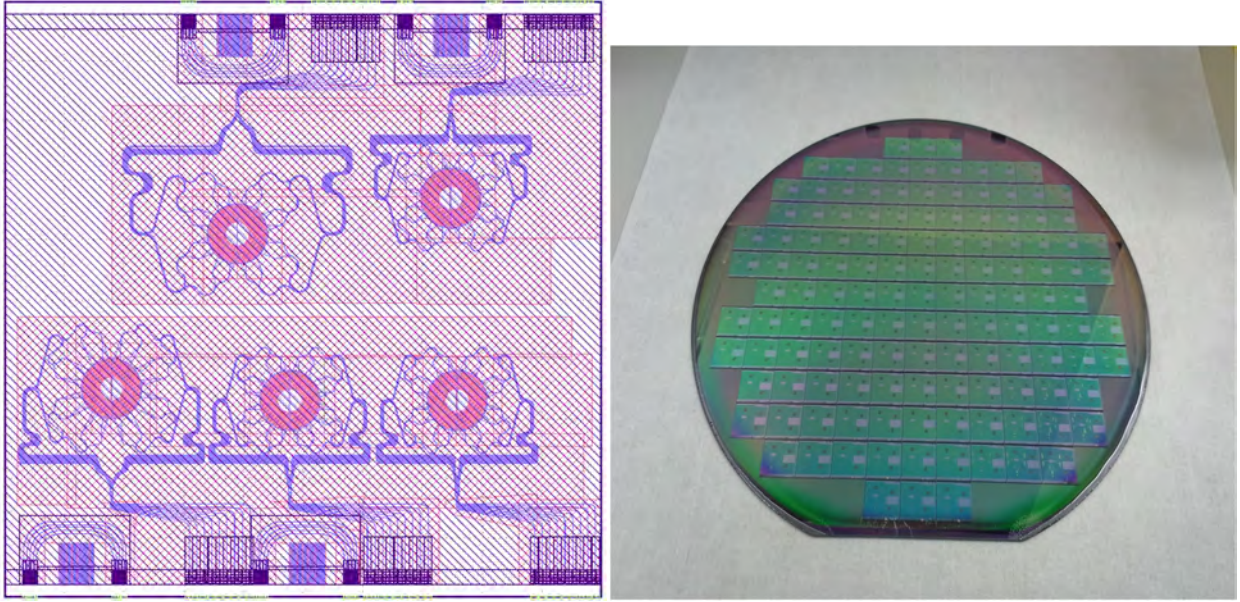


Figure 14. Designed (left) and fabricated (right) silicon-nitride OAM devices

### ***II.B.2.f. Summary of 2D integrated silicon photonic and silicon-nitride orbital angular momentum devices***

We fabricated silicon PICs and demonstrated free-space SDM coherent optical transmission using OAM state multiplexing and demultiplexing. The device design allows operation as either an OAM multiplexer or demultiplexer for a topological charge range of  $-2$  to  $+2$  and easily interfaces with fiber-pigtailed components. The single-channel BER statistics for both 10-Gb/s BPSK data and 20-Gb/s QPSK data indicated similar performance for all topological charges. In all cases, the BER was well below the forward error correction (FEC) limit of  $2 \times 10^{-3}$  (RS(255,239) coding), even for the two simultaneous channels with crosstalk suffering a significant power penalty. Future work includes reducing coupling and on-chip losses, increasing the addressable number of OAM states, and improving the free-space optical system used to relay the OAM encoded beam between devices.

### **II.B.3. Hybrid integrated silica orbital angular momentum devices**

As discussed earlier, SDM has recently generated significant interest because, like polarization-division multiplexing and wavelength-division multiplexing, it may be used to increase the photon efficiency or spectral efficiency of free-space and fiber-optic links. Although there are many approaches to SDM, we focus on using optical OAM (e.g., beams with azimuthally varying optical phase) to provide orthogonal information channels. The inherent orthogonality of OAM modes is attractive since it may require less digital signal processing (e.g., MIMO) when compared to other SDM approaches, such as multicore fiber or few-mode fiber, that have significant coupling between channels. Recent work has shown the potential of OAM to improve spectral efficiency and throughput, but practical applications require integrated devices that multiplex/demultiplex OAM modes onto/from multi-mode fibers or free-space and also interface with single-mode fiber (SMF) components (e.g., modulators, optical amplifiers, and receivers). As discussed in the previous sections, we have previously demonstrated an integrated OAM multiplexing device implemented as a silicon photonic integrated circuit (PIC). The silicon PIC generated OAM beams with a single polarization from a waveguide grating structure. Here, we described an integrateable OAM multiplexer based on hybrid integration of a silica planar lightwave circuit (PLC) with a silica 3-D PIC.

### II.B.3.a. Integrated silica OAM device concept

For review, Figure 15 shows the integratable OAM multiplexing device's operating principle which relies on converting linearly varying spatial phase to azimuthal variations [i.e.,  $\exp(iblx) \rightarrow \exp(i\ell\phi)$ , where  $b$  is the linear ( $x$ ) to azimuthal ( $\phi$ ) scaling factor]. To illustrate, Figure 15 shows a waveguide circuit where each single mode input (i.e.,  $\ell = -2, -1, 0, +1, +2$ ) will create a wavefront in the free-propagation region (FPR) with a different linear tilt. The phase-matched waveguides after the FPR sample the tilted phase front and maintain the phase tilt to the output apertures. Since the apertures are arranged in a circular pattern, they create a beam (coming out of the page) with azimuthally varying phase having topological charge  $\ell$ . If multiple inputs are illuminated, those inputs are multiplexed onto collinear OAM beams with  $\ell$ -numbers determined by the input position. By reciprocity, if an outside OAM beam illuminates the apertures, the sampled light will be focused in the FPR to a waveguide corresponding to the beam's  $\ell$ -number (i.e., an OAM demultiplexer).

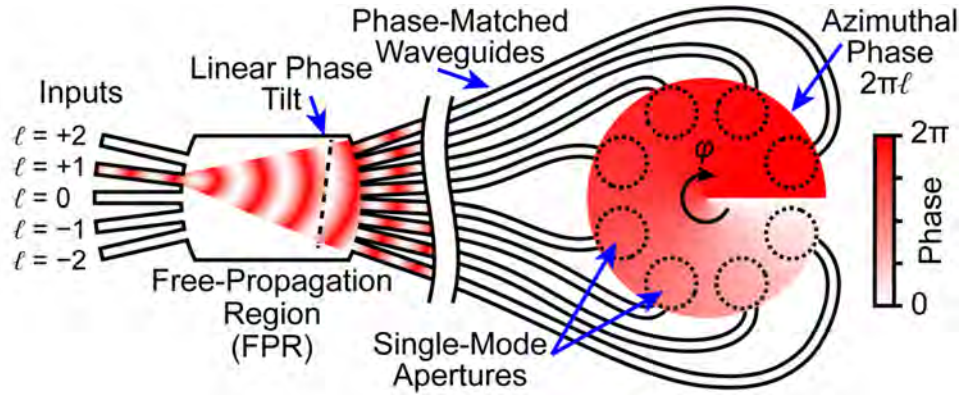


Figure 15. (a) Integratable OAM multiplexer/demultiplexer concept.

### II.B.3.b. 3D-Integrated Photonic Silica OAM device implementation

Direct laser writing of waveguides in dielectric material is an extremely powerful fabrication technique. It utilizes the multi-photon nonlinear absorption of sub-bandgap photons to create permanent structural changes (e.g., refractive index) in a material with dimensions comparable to the writing laser's wavelength (e.g.,  $\sim 1 \mu\text{m}^3$ ). The induced modifications from a sub-picosecond train of optical pulses are strongly localized in three dimensions to the high intensity region at the focus of a lens driven by a nonlinear absorption mechanism. This unique characteristic is what provides direct laser writing its biggest advantage over other waveguide fabrication techniques; the capability to freely form true 3-D structures. We take advantage of the 3-D capability to create the geometric transformation needed to convert linear phase tilt to azimuthal phase variation. Figure 16(a) shows how this concept is implemented using a silica PLC (to convert input position to a linear phase tilt) who's output is coupled to a 3-D PIC for geometric transformation.



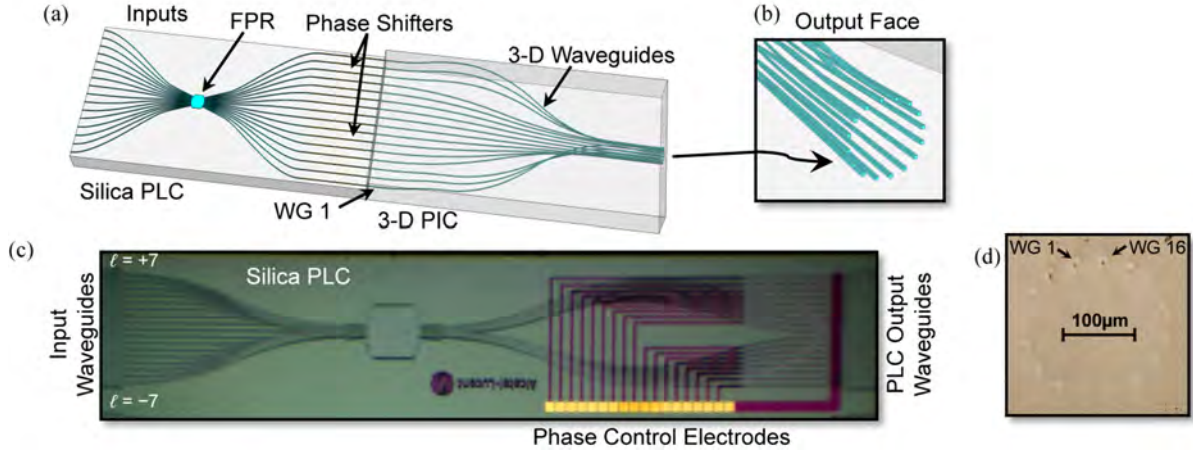


Figure 16. (a) Illustration of the silica PLC coupled to the 3-D PIC. (b) 3-D waveguide output face detail. (c) Photo of fabricated silica PLC. (d) Photo of unpolished 3-D PIC output face.

Using our design, the 3-D PIC was fabricated at a commercial foundry in bulk borosilicate glass and the waveguides had a  $\sim 10 \mu\text{m}$  mode field diameter (i.e., similar to SMF). Figure 16(b) presents a close view of the 3-D PIC output face showing the circular arrangement. Figure 16(c) shows a photo of the fabricated PLC. The waveguides on the silica PLC have a  $\Delta n$  of 2%. Electrical heaters on each output waveguide provide thermo-optic phase-error correction (PEC). This is used to phase match the waveguides between the FPR and the output face of the 3-D PIC. Both the PLC and the input of the 3-D PIC use a 127- $\mu\text{m}$  waveguide pitch. The hybrid device (i.e., PLC and 3-D PIC) is  $\sim 30\text{-mm}$  long and the waveguides on the output face form a 204  $\mu\text{m}$  diameter circle with a center-to-center spacing of 40  $\mu\text{m}$  (see Figure 16(d)).

### II.B.3.c. 3D-Integrated Photonic Silica OAM device characterization overview

Figure 17(a) shows the silica PLC had an average excess loss of 3.5 dB, while the 3-D PIC had an average excess loss of 1.7 dB. To characterize how well the hybrid device (PLC and 3-D PIC) created OAM modes, we imaged the device's output (i.e., near-field) onto an IR camera with a total magnification of  $\sim 50\times$  while illuminating only one PLC input at a time. The absolute phase (to within a constant) was measured using shearing interferometry. Figure 17(b) shows a false-color (linear scale) image of the near-field intensity and phase patterns when input  $\ell = 0$  is illuminated without PEC. Figure 17(c) shows the improvement with PEC (nearly same phase, correct for  $\ell = 0$ ). Figure 17(d) is a plot of the phase for each output waveguide to more clearly show the improvement with PEC. The output phase was then similarly measured for each device input ( $\ell = -7, \dots, 0, \dots, +7$ ) and the unwrapped phase is plotted in Figure 17(e). To estimate the OAM mode purity we can take the Fourier transform of the near-field amplitude and phase data for each of the device inputs. Figure 17(f) shows how well the device creates each OAM mode where the difference between a mode peak and the "noise" determines the OAM mode purity or crosstalk (below  $-12 \text{ dB}$ ). Figure 17(g-i) show the measured near-field pattern intensity and phase for several different example OAM modes (typical).



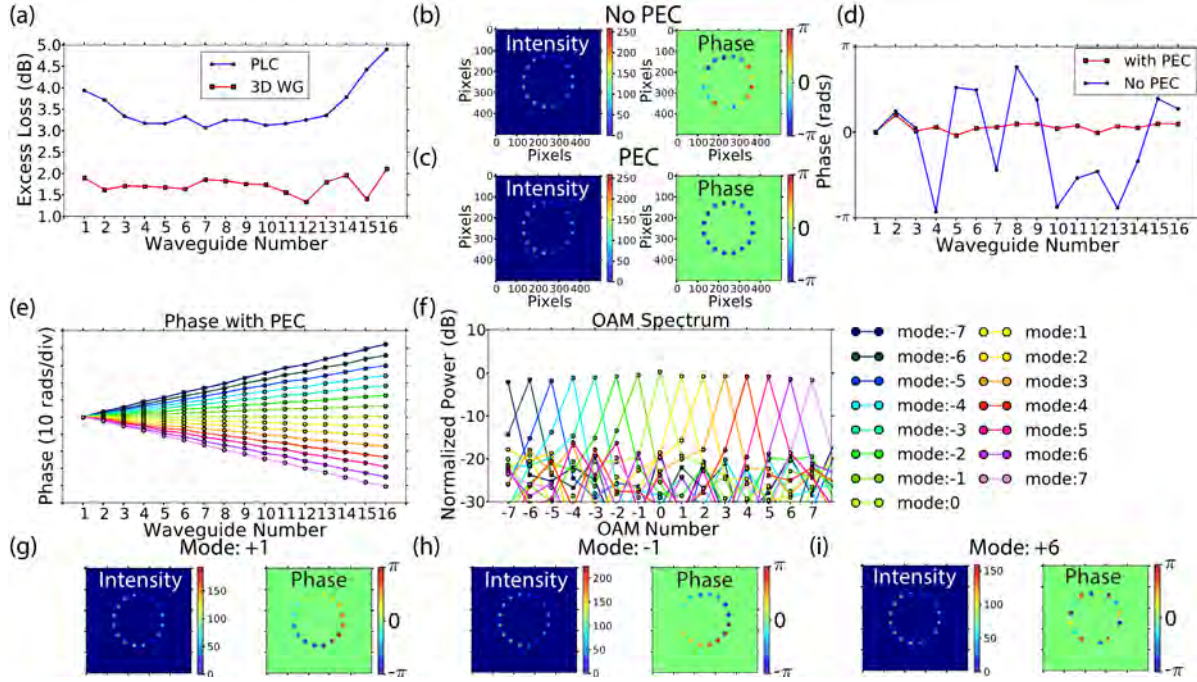


Figure 17. (a) Measured excess loss for the silica PLC and 3-D waveguides. (b) Measured intensity and phase of the device's output waveguides without PEC, (c) with PEC. (d) Measured average azimuthal phase at each output waveguide. (e) Unwrapped azimuthal phase for each OAM mode. (f) Calculated OAM mode purity. (g-i) The measured intensity and phase for three OAM modes ( $\ell = +1, -1, +6$ ).

Below (from Figure 18 to Figure 32) are the measured phases for each of the 15 OAM states for output waveguides of the hybrid silica OAM device. The left plot shows a color map of the phase and the right plot shows the line plot (easier to see exact phase value) of the phase for each waveguide output after phase-error correction. As the OAM mode changes we see that the azimuthal phase increase (or decrease) appropriately (i.e.,  $2\pi\ell$ ) for the mode number.

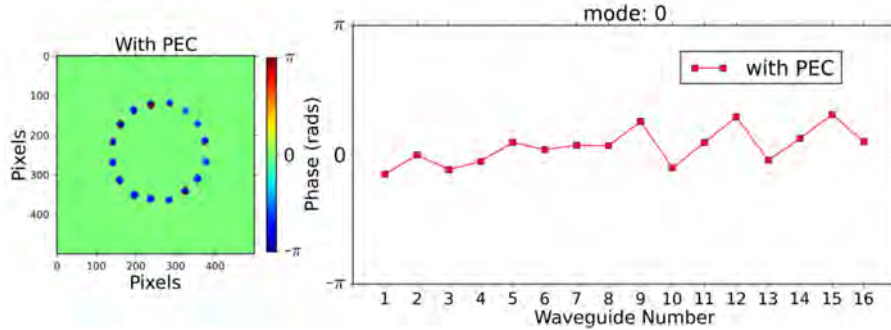


Figure 18. The measured phase for OAM mode  $\ell = 0$ .

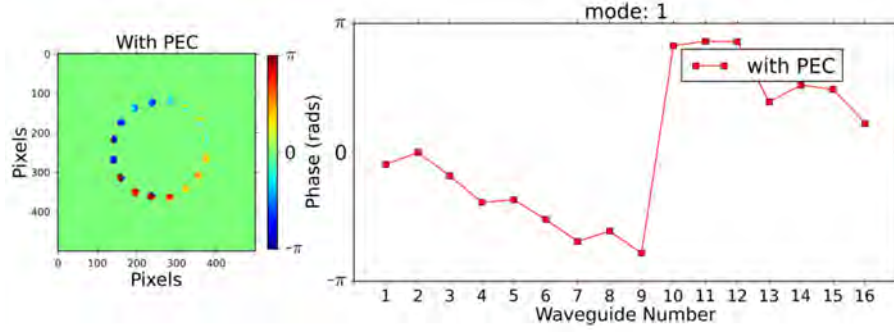


Figure 19. The measured phase for OAM mode  $\ell = 1$ .

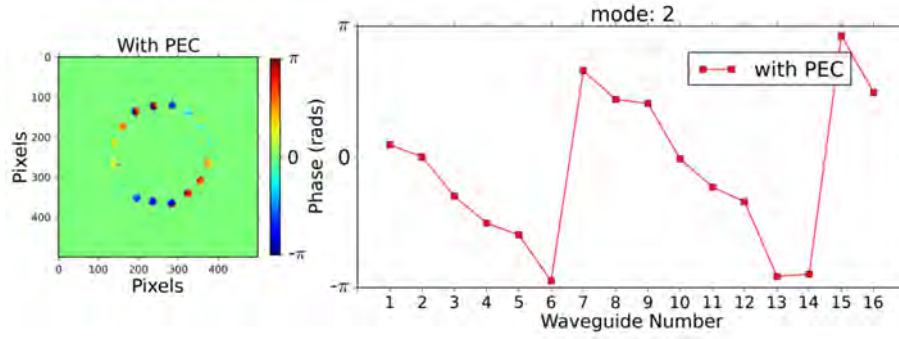


Figure 20. The measured phase for OAM mode  $\ell = 2$ .

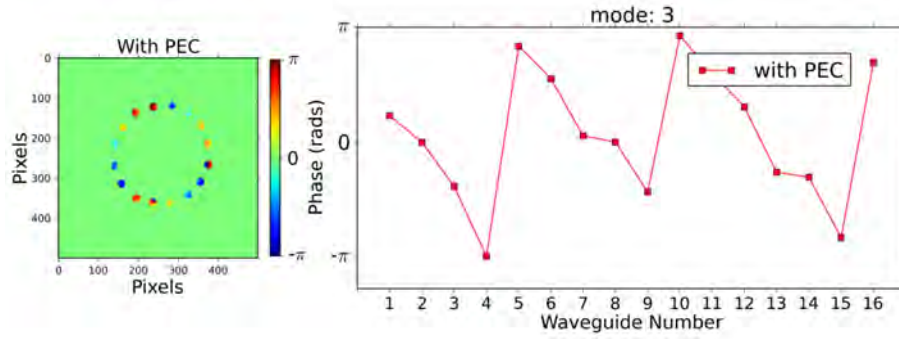


Figure 21. The measured phase for OAM mode  $\ell = 3$ .

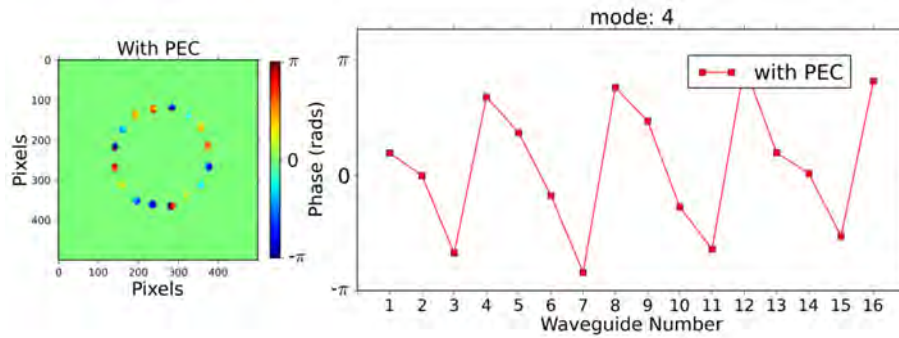


Figure 22. The measured phase for OAM mode  $\ell = 4$ .

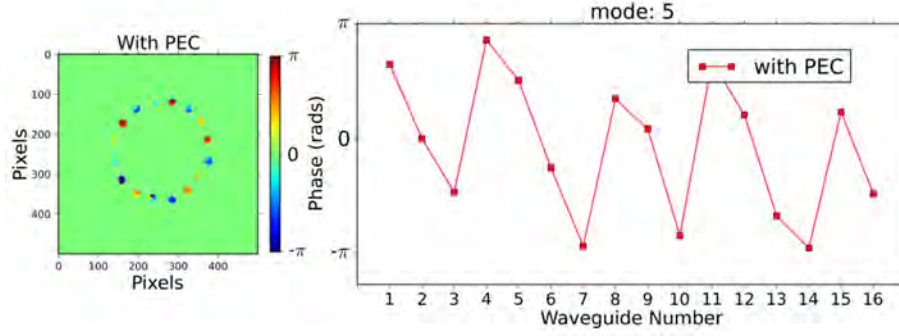


Figure 23. The measured phase for OAM mode  $\ell = 5$ .

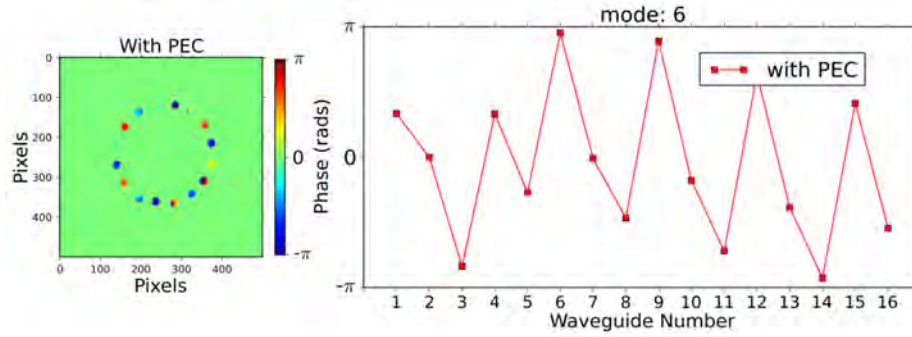


Figure 24. The measured intensity and phase for OAM mode  $\ell = 6$ .

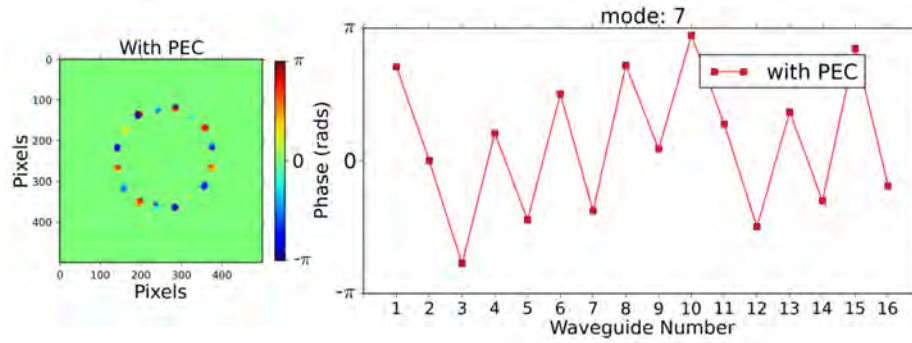


Figure 25. The measured phase for OAM mode  $\ell = 7$ .

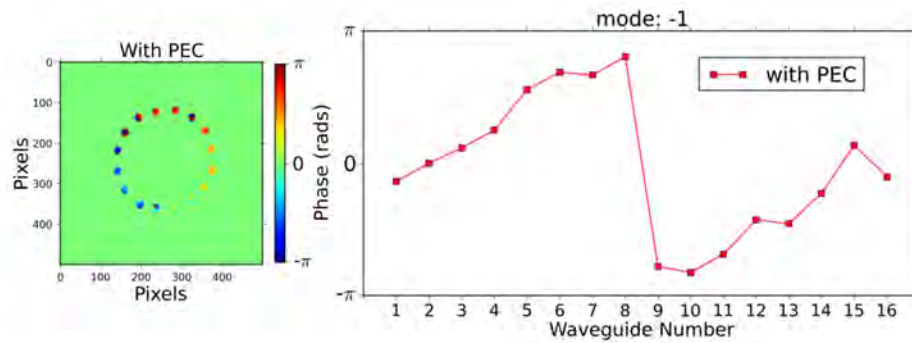


Figure 26. The measured phase for OAM mode  $\ell = -1$ .



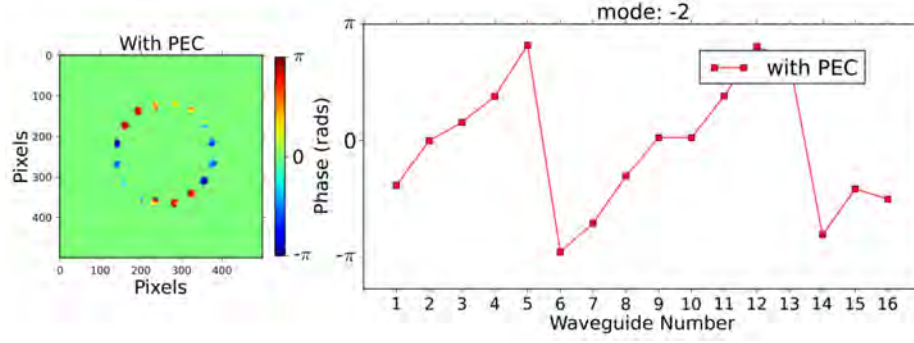


Figure 27. The measured phase for OAM mode  $\ell = -2$ .

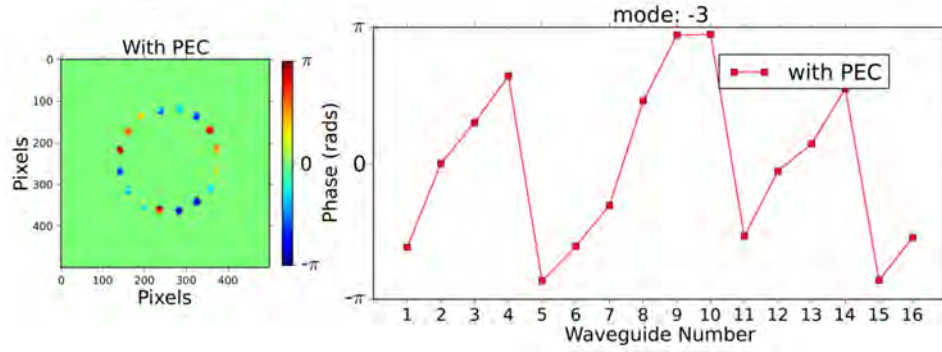


Figure 28. The measured phase for OAM mode  $\ell = -3$ .

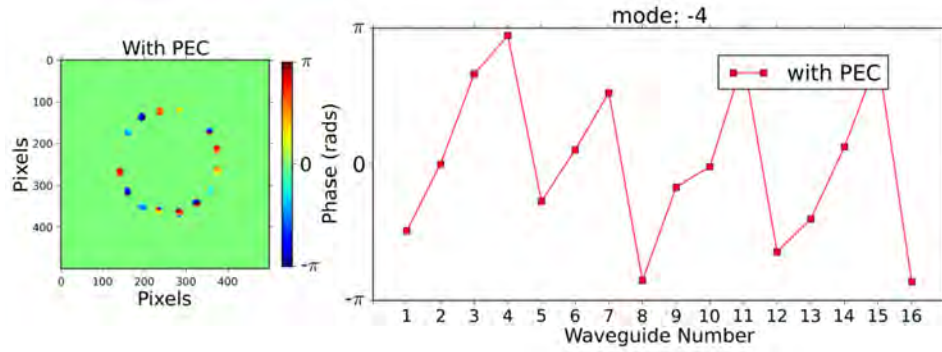


Figure 29. The measured phase for OAM mode  $\ell = -4$ .

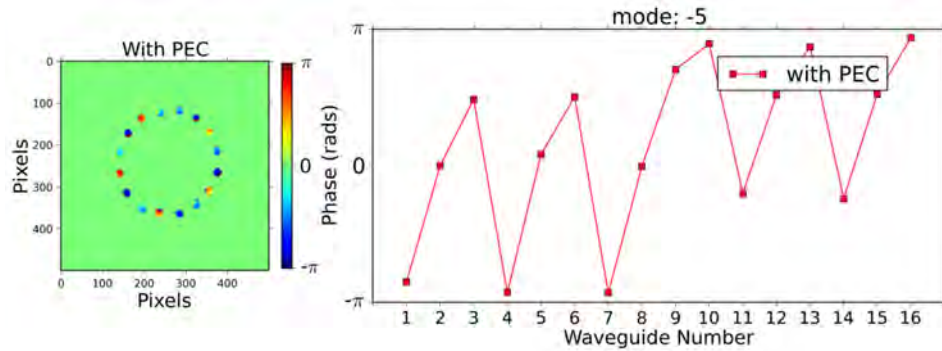


Figure 30. The measured phase for OAM mode  $\ell = -5$ .

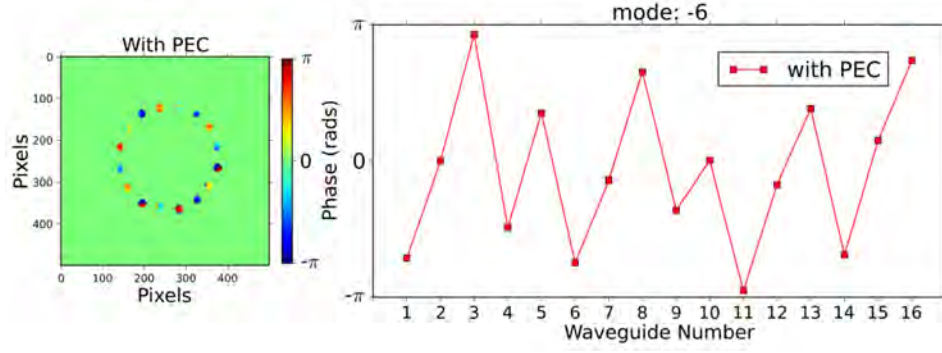


Figure 31. The measured phase for OAM mode  $\ell = -6$ .

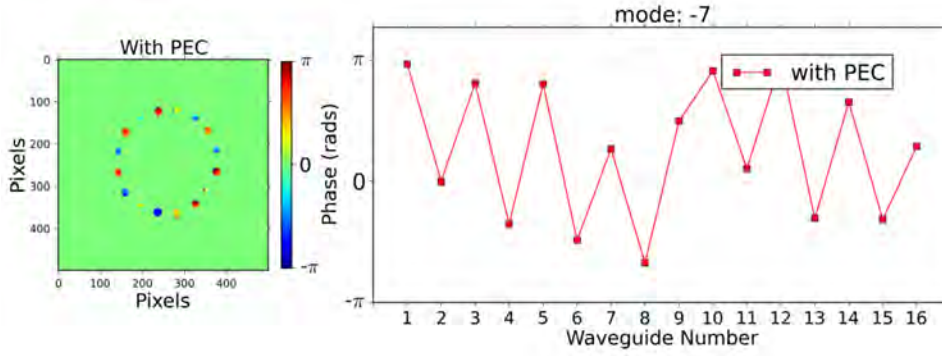


Figure 32. The measured phase for OAM mode  $\ell = -7$ .

Below (Figure 33 to Figure 48) is the measured amplitude and phase at the device output for each of the 15 OAM states for the hybrid silica OAM device. The left plot shows a color map of the intensity and the right plot shows a color map of the phase for each waveguide output after phase-error correction. As it should be, the intensity is nearly constant for each of the mode numbers. While the color phase maps show the azimuthal phase increasing or decreasing as appropriate for each mode number ( $2\pi\ell$ ).

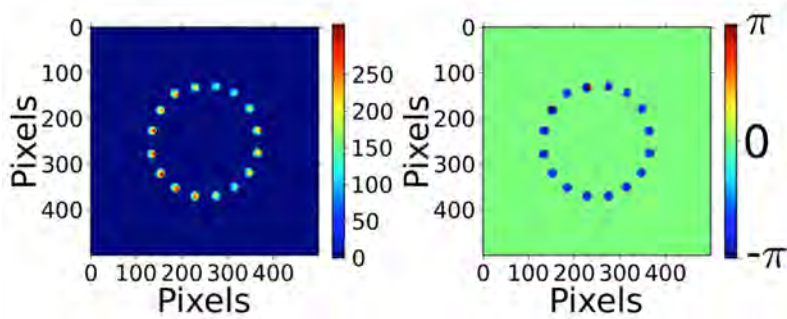


Figure 33. The measured intensity and phase for OAM mode  $\ell = 0$ .

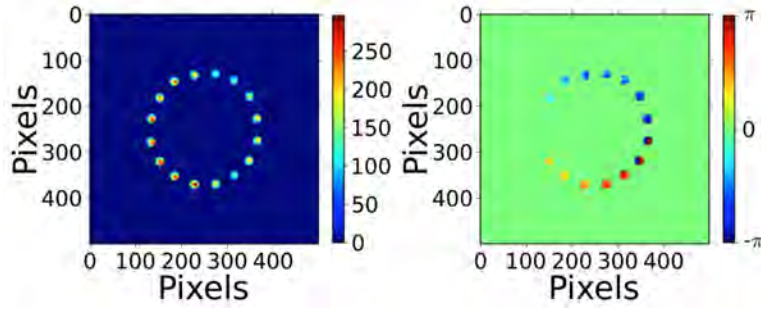


Figure 34. The measured intensity and phase for OAM mode  $\ell = -1$ .

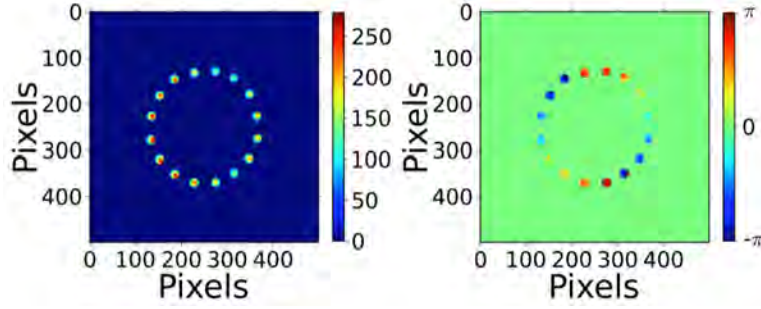


Figure 35. The measured intensity and phase for OAM mode  $\ell = -2$ .

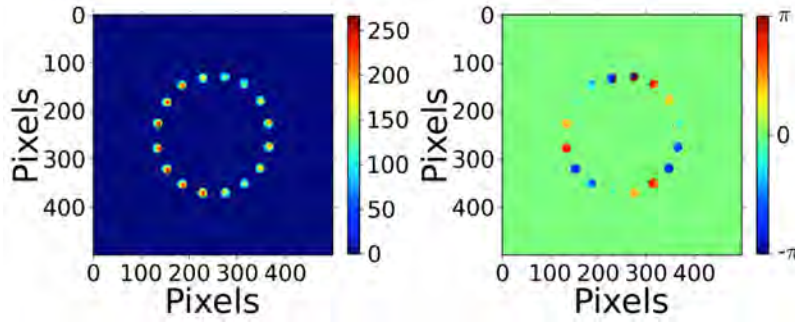


Figure 36. The measured intensity and phase for OAM mode  $\ell = -3$ .

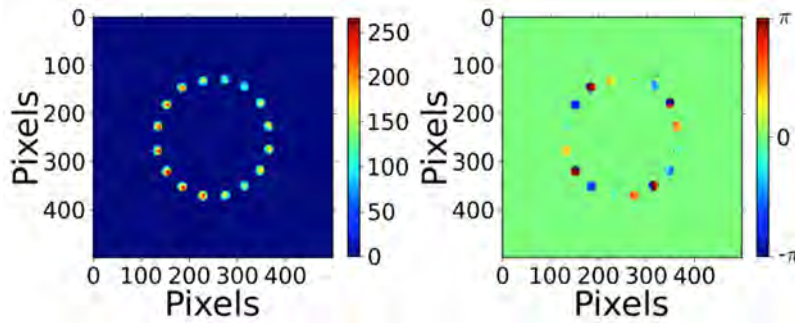


Figure 37. The measured intensity and phase for OAM mode  $\ell = -4$ .

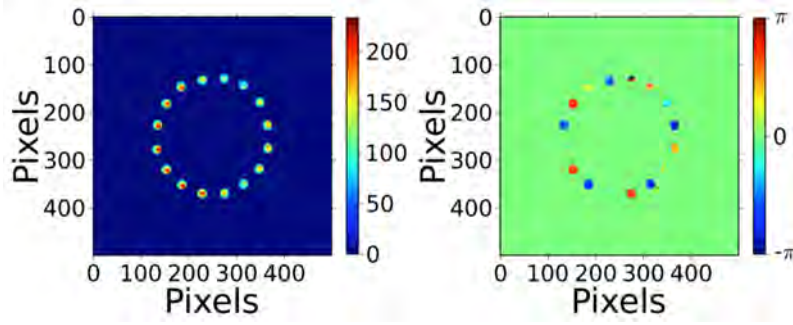


Figure 38. The measured intensity and phase for OAM mode  $\ell = -5$ .

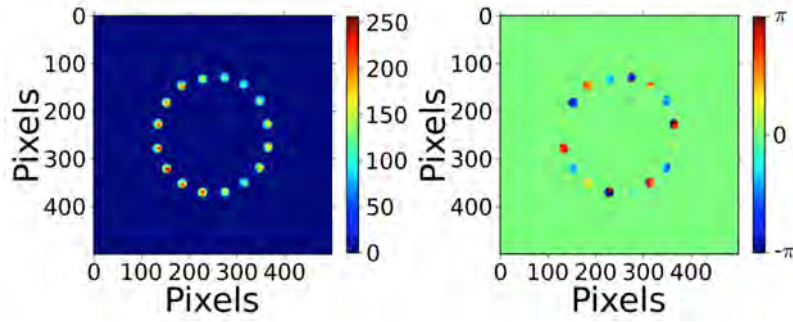


Figure 39. The measured intensity and phase for OAM mode  $\ell = -6$ .

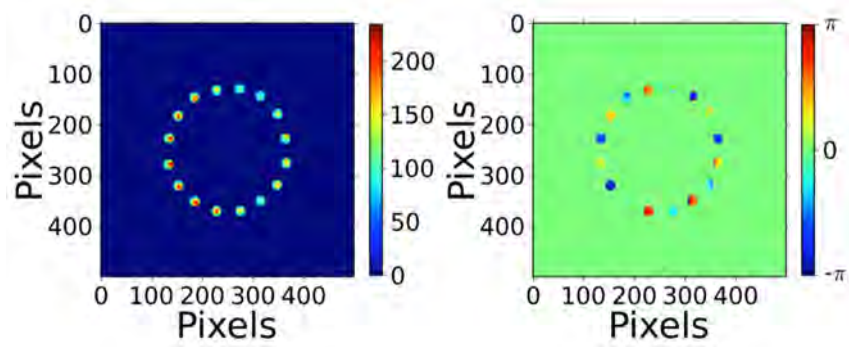


Figure 40. measured intensity and phase for OAM mode  $\ell = -7$ .

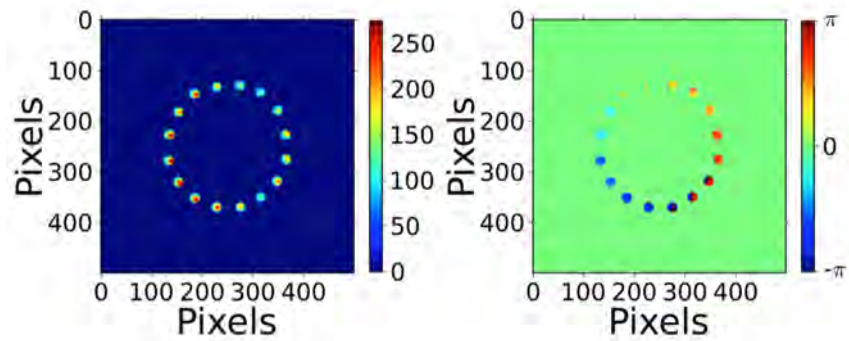


Figure 41. The measured intensity and phase for OAM mode  $\ell = 1$ .



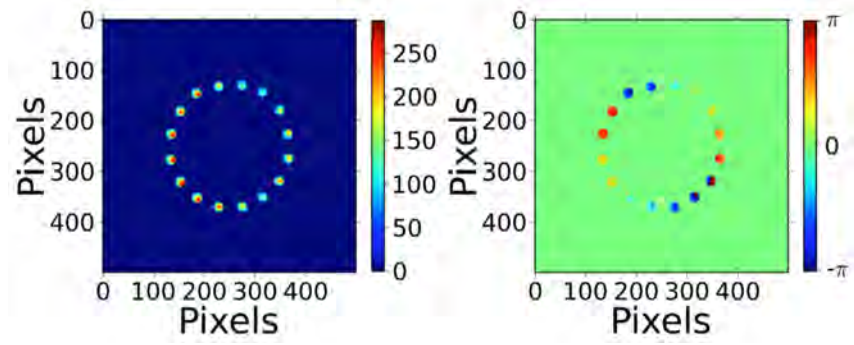


Figure 42. The measured intensity and phase for OAM mode  $\ell = 2$ .

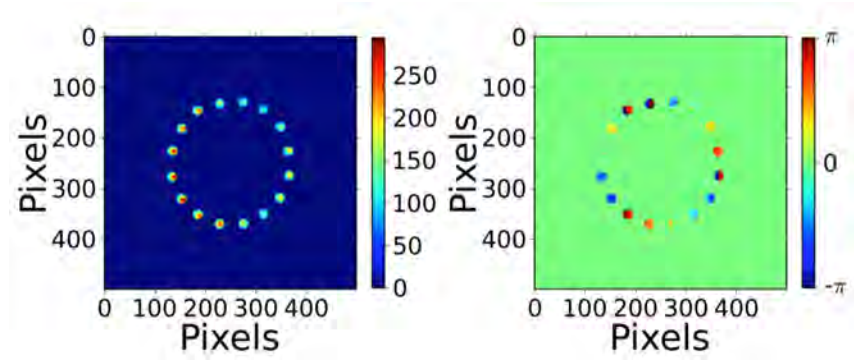


Figure 43. The measured intensity and phase for OAM mode  $\ell = 3$ .

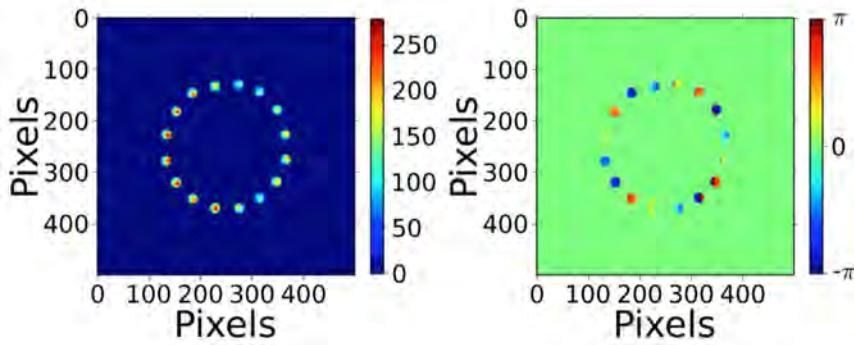


Figure 44. The measured intensity and phase for OAM mode  $\ell = 4$ .

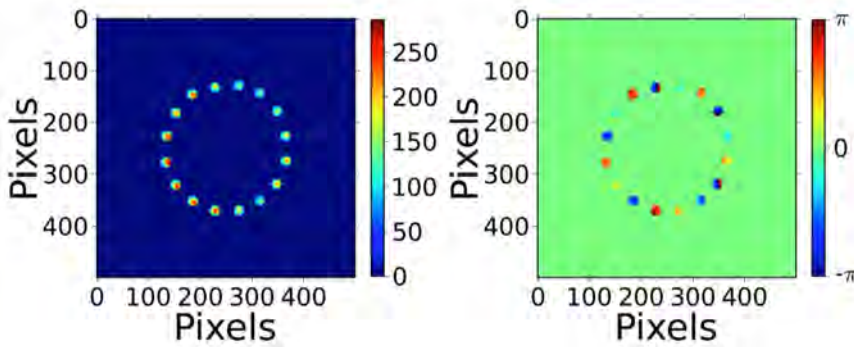


Figure 45. The measured intensity and phase for OAM mode  $\ell = 5$ .



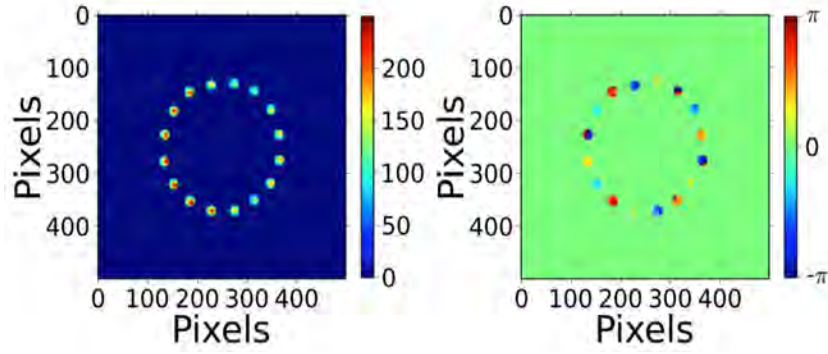


Figure 46. The measured intensity and phase for OAM mode  $\ell = 6$ .

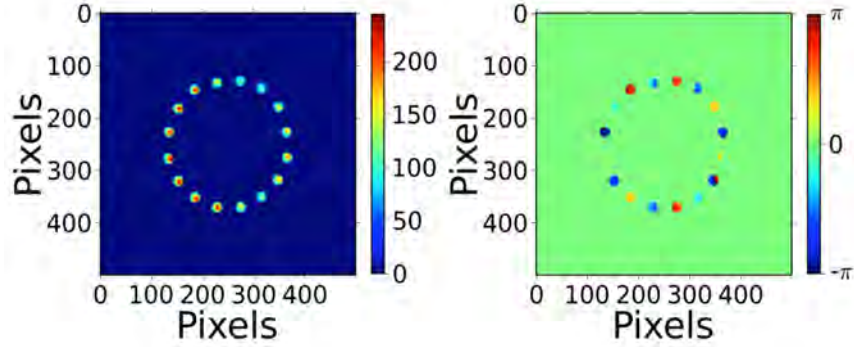


Figure 47. The measured intensity and phase for OAM mode  $\ell = 7$ .

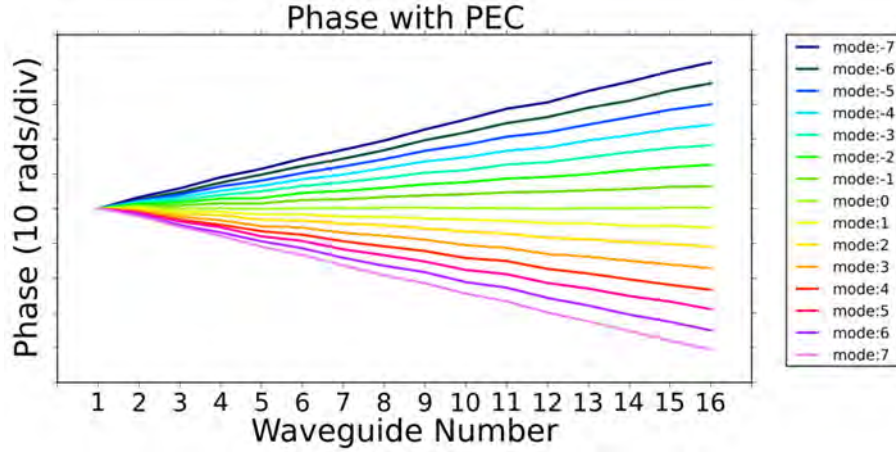


Figure 48. The measured unwrapped phase for OAM mode  $\ell = -7 \sim 7$ .

#### II.B.3.d. Phase characterization of the 3D-Integrated Photonic Silica OAM devices

We have further developed our spatial phase characterization system by pursuing two different methods of phase retrieval. The first method is based on shearing interferometry and the second method is based on scanning delay-line interferometry. Each method has its advantages which are pointed out in the descriptions below.

### II.B.3.d.i. *Spatial phase retrieval using shearing interferometry*

Figure 49 shows the shearing interferometry experiment arrangement. The output of the OAM device (chip) is relayed to the IR camera. At the camera, a magnified near-field image is formed. The reference beam from the collimator is combined with the near-field image of the OAM device output on the IR camera sensor. The interference of these two beams creates the light and dark fringes. Since a small amount of tilt is provided to the reference beam (i.e., shearing) fringes are always formed across the image on the camera (notice that each spot on the image in Figure 49 has a few fringes).

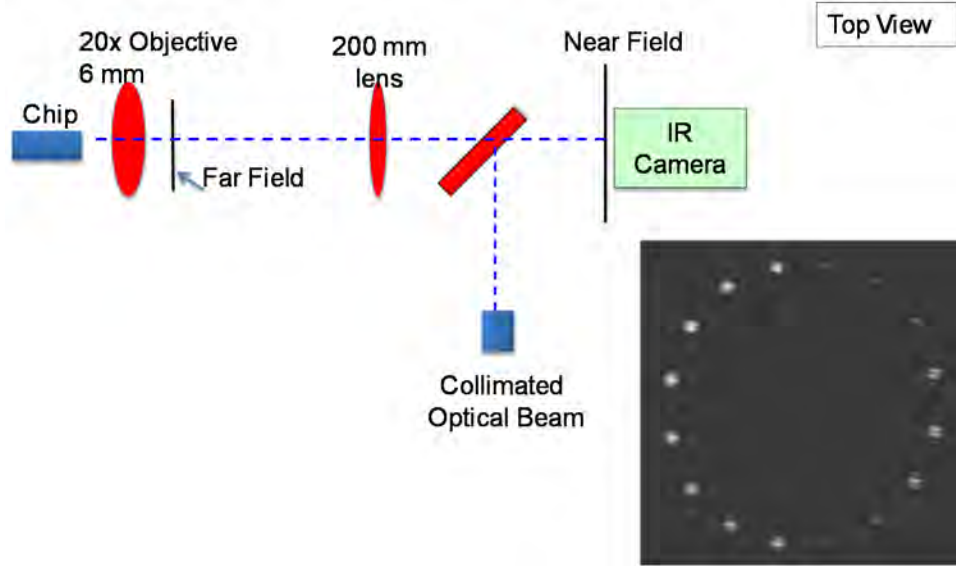


Figure 49. Shearing interferometry arrangement. The collimated beam is the reference.

Figure 50 shows a simulation of the phase retrieval process when making a shearing interferometry measurement of a simple Gaussian beam. Figure 50(a) is the amplitude of the spatial beam pattern (i.e., signal). Figure 50(b) shows the effect of interfering the signal with a tilted reference beam and the resulting fringes. If we record that interference pattern in (b) and take the fast Fourier transform (FFT), we get Figure 50(c). It is then filtered for one component to get to Figure 50(d). From Figure 50(d) we correct for the linear phase and retrieve the Figure 50(e) amplitude and Figure 50(f) phase of the measured signal. Thus, with a single intensity measurement of the fringe pattern, we are able to retrieve the amplitude and phase of our original signal.

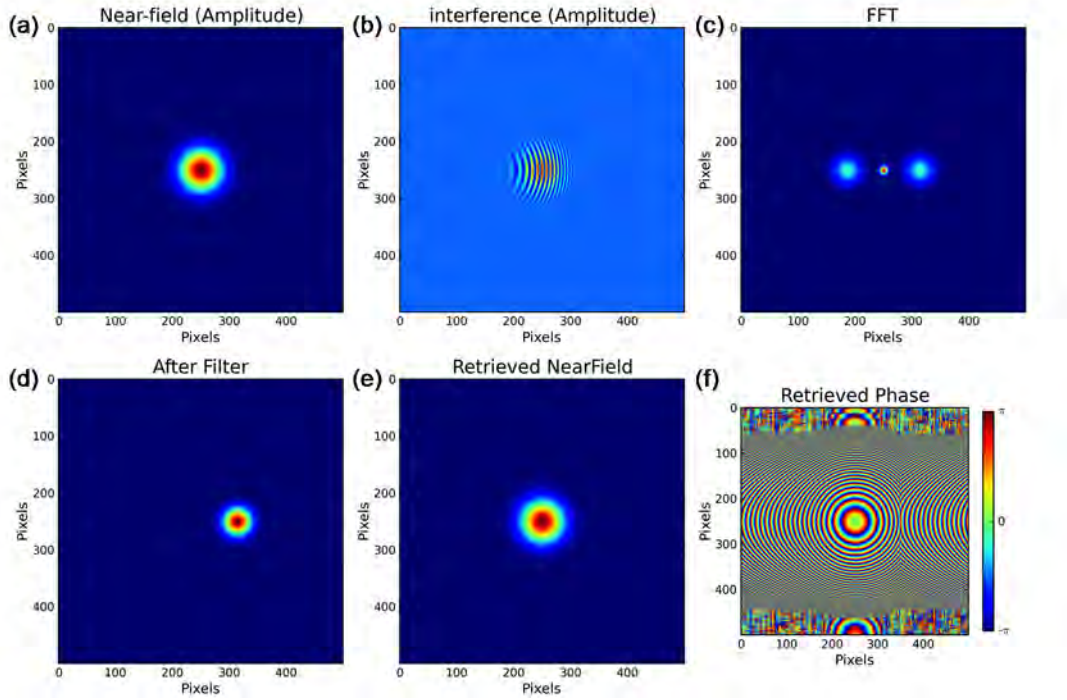


Figure 50. Simulation of shearing interferometry to show the process of phase retrieval.

Figure 51 shows a similar sequence for real data of the hybrid silica OAM device output. The retrieved amplitude is shown in (d) and the retrieved phase is shown in (f). There is no phase error correction applied in this case.

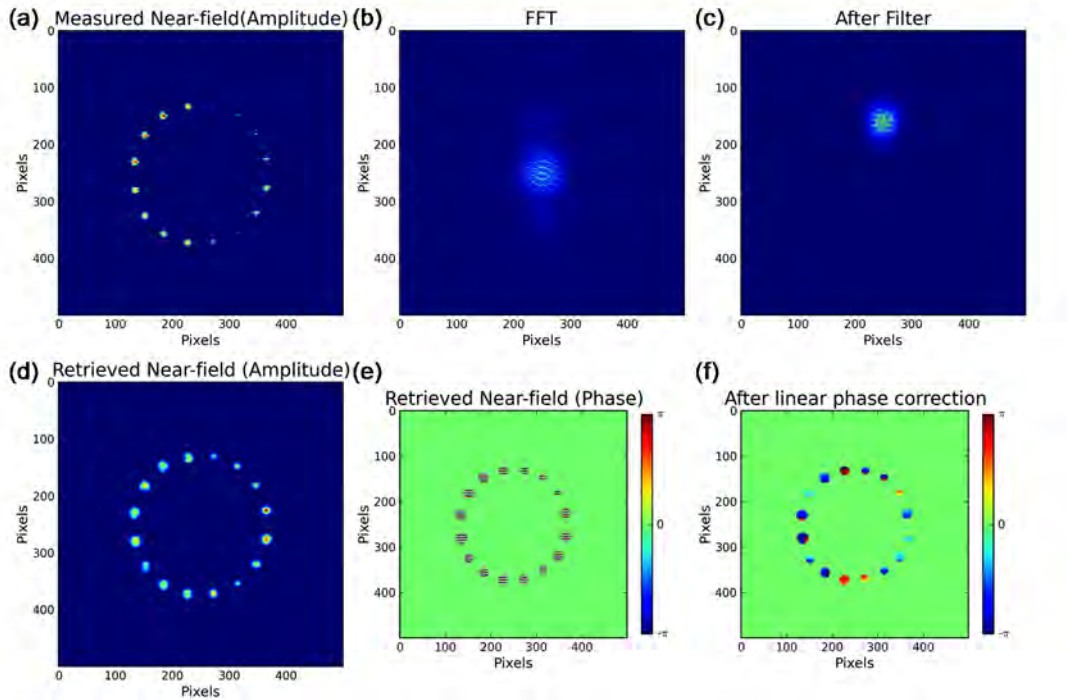


Figure 51. Shearing interferometry measurement results.

Figure 52 shows repeated measurements of the phase from the same device over a period of many tens of minutes. The constant phase relationship between the waveguide outputs (except for a phase offset) is a good indication of the measurement's repeatability.

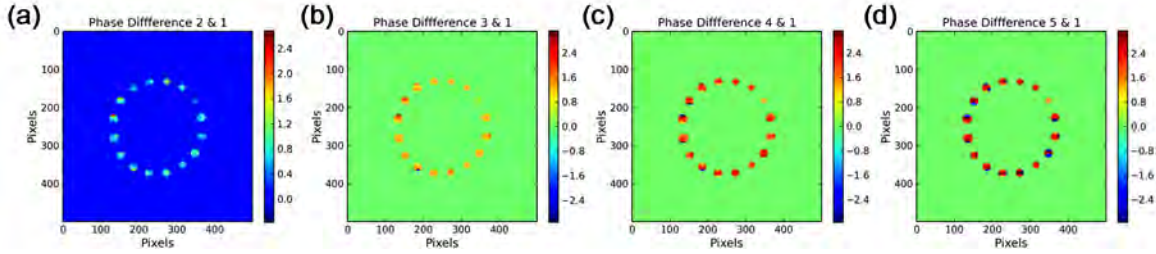


Figure 52. Verification of shearing interferometry method.

#### II.B.3.d.ii. *Spatial phase retrieval using scanning delay-line interferometry*

Figure 53 shows the arrangement used making scanning delay-line interferometry measurements. In this case, the reference beam (from collimator) and the magnified image of the near-field pattern from the device are collinearly combined (interfered) on the IR camera sensor. The collimator is then scanned in position to change the interference pattern. The interference pattern is recorded for 10-20 different collimator positions that correspond to path length changes of approximately  $\lambda/10$  each step. This provides fringe information for  $2\pi$  radian or more of relative phase difference between the signal and reference.

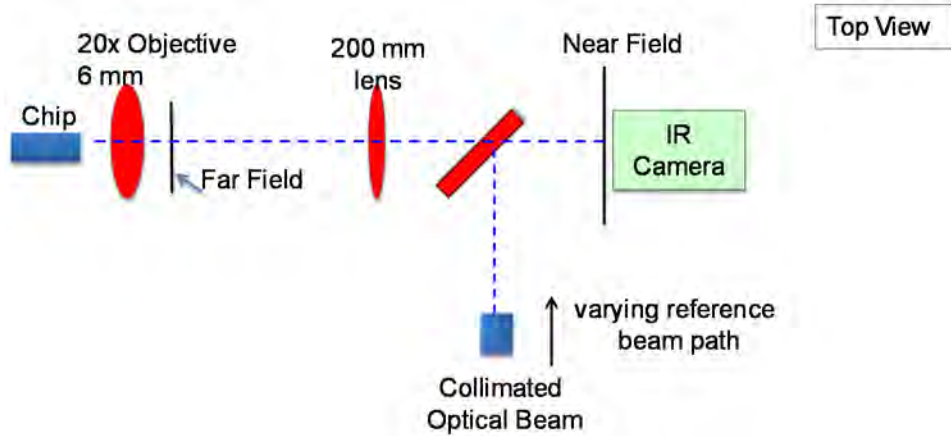


Figure 53. Scanning delay-line interferometry arrangement.

From the collected intensity measurements (of the fringes), we take the Fourier transform of each pixel and select the peak information (amplitude and phase for that pixel). From this information we can retrieve the complex far-field pattern and the complex near-field pattern. Figure 54 shows the retrieved data from one of the measurements.



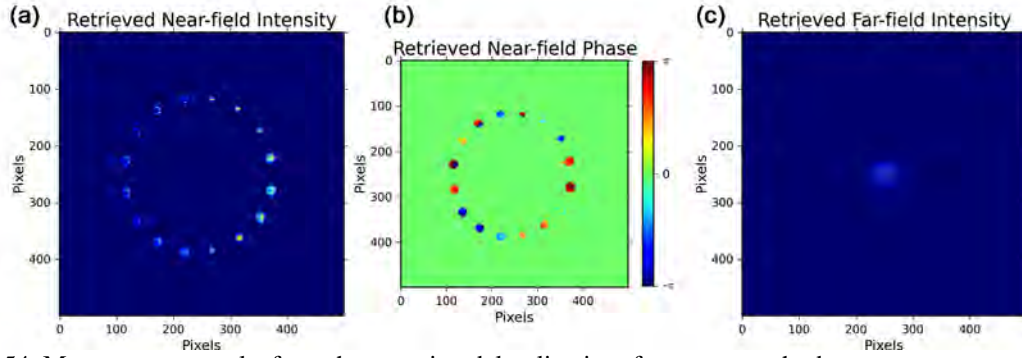


Figure 54. Measurement results from the scanning delay-line interferometer method.

Figure 55 shows repeated measurements of the phase from the same device over a period of many tens of minutes. The constant phase relationship between the waveguide outputs (except for a phase offset) is a good indication of the measurement's repeatability.

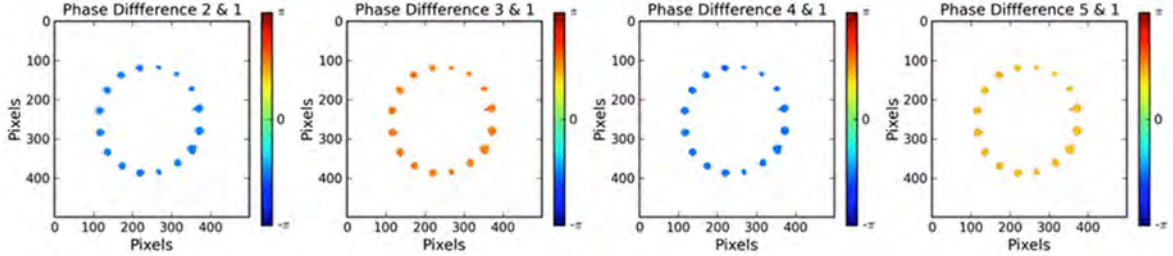


Figure 55. Verification of the scanning delay-line interferometry method.

Figure 56 shows a comparison of the two interferometry methods. Figure 56(b) shows the phase retrieved using shearing interferometry and Figure 56(c) shows the phase retrieved using scanning delay-line interferometry. Figure 56(d) shows the phase difference between (b) and (c) which is only different by a constant phase.

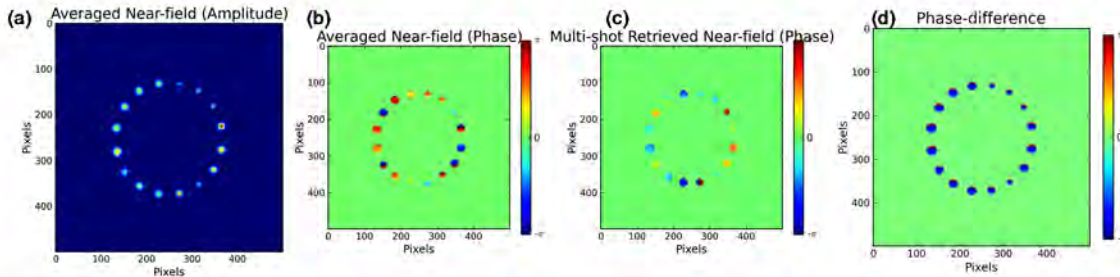


Figure 56. (a) Retrieved near-field pattern amplitude. Phase retrieval from (b) shearing interferometry and (c) scanning delay-line interferometry. (d) The difference in phase between (b) and (c).

Figure 57 shows the phase of the hybrid silica OAM device outputs before phase-error correction (PEC) has been applied and after PEC.

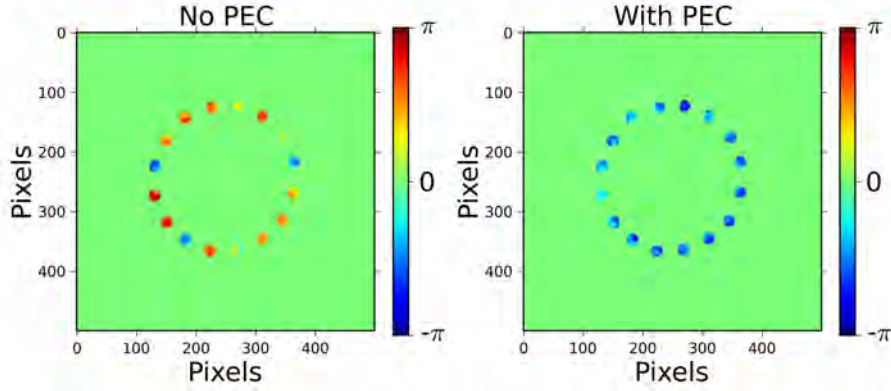


Figure 57. Retrieved phase of the hybrid silica OAM device without phase-error correction (PEC) and with PEC.

The most significant disadvantage of the scanning delay-line interferometry technique is the longer measurement time required when compared to shearing interferometry. The maximum image capture rate from the video output of the IR camera is 10 fps. Therefore it takes 1-2 seconds to record the necessary number of images. If there are any environmentally induced phase fluctuations during the recording, then it will cause errors in the phase retrieval. However, we are able to successfully use both phase measurement techniques in the lab environment.

### II.B.3.e. *Integrated 3D-Integrated Photonic Silica OAM device coherent transmission*

Figure 58 shows the experimental testbed for a SDM coherent optical communication link using a single hybrid OAM device as both an OAM multiplexer and demultiplexer. The coherent transmitter consists of a 100-kHz linewidth external cavity laser (ECL) centered at 1546 nm that has a data signal applied by an I/Q modulator. An electrical arbitrary waveform generator (eAWG) drives the modulator with a 10 GBd differential quadrature phase shift keyed (DQPSK) signal ( $2^7-1$  PRBS). The DQPSK signal is bandwidth limited in digital signal processing (DSP) by a Nyquist filter with a 3-dB bandwidth of 10 GHz for a single-channel spectral efficiency (SE) of 1.67 b/s/Hz. An erbium-doped fiber amplifier (EDFA) increases the optical power of the signal at the input of the hybrid OAM device to ~20 dBm.

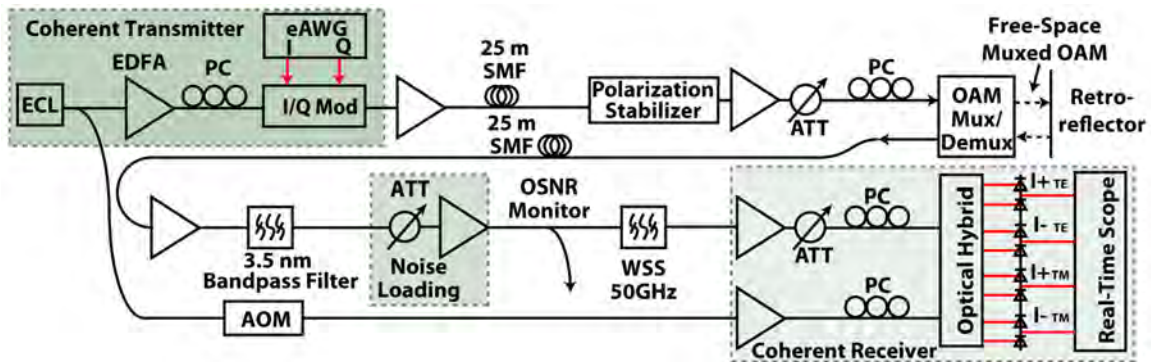


Figure 58. Schematic of the 10GBd QPSK OAM transmission experiment. (ECL: external cavity laser, PC: polarization controller, I/Q Mod: I/Q modulator, eAWG: electrical arbitrary waveform generator, ATT: optical attenuator, AOM: acousto-optic modulator, WSS: wavelength selective switch.)

Immediately following the OAM device is an EDFA and a 3.5 nm bandpass filter to minimize out-of-band noise. The optical signal-to-noise ratio (OSNR) is varied by noise loading from a second attenuator and EDFA. The signal enters the polarization diversified coherent receiver which uses a frequency shifted (35 MHz) sample of the transmitter's laser as its local oscillator (LO). We use offline DSP to process the

received data. The DSP first extracts the clock tone from Fourier transform of the magnitude-squared signal. Next, the waveform is resampled at twice the symbol rate. An adaptive equalizer is applied to the resampled waveform, which includes a 13-tap finite impulse response (FIR) filter adapted by a constant-modulus algorithm (CMA). Lastly, the DSP uses the power-of-four method for phase and frequency recovery.

The bit-error-rate (BER) performance for the 10 GBd DQPSK data were separately measured for OAM channels  $\ell = -7, -6, \dots, 6, 7$  (but not  $\ell = -2, \dots, +2$ ) by sending one input signal to the OAM device. Because of their close spacing, the low  $\ell$ -numbers input/output pairs were not simultaneously accessible by a pair of SMF fibers. Figure 59(a) shows that the implementation penalty is 3 dB at  $\text{BER} = 10^{-3}$  and the different OAM modes have less than 0.5 dB penalty variation. At  $\text{OSNR} > 16$  dB, all OAM modes were error free for the 379,960 bits tested. Figure 59(b) shows constellation diagrams corresponding to  $\text{OSNR} = 11$  dB and 25 dB.

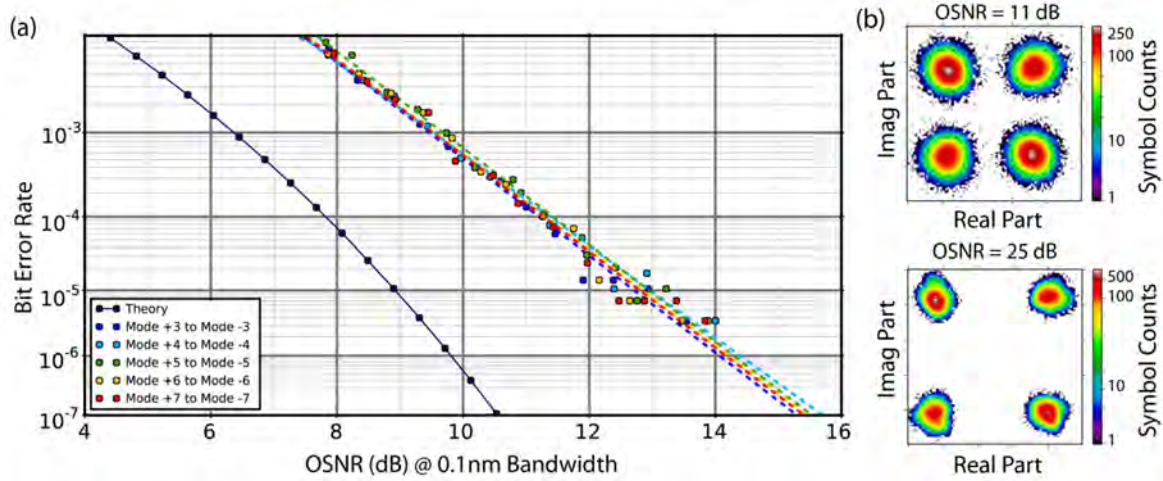


Figure 59. (a) BER performance of the different OAM modes for the hybrid OAM device (10 GBd DQPSK, SE = 1.67 b/s/Hz for a single channel). (b) DQPSK constellation at two different OSNRs.

### II.B.3.f. Packaging of Hybrid 3-D PIC and 2D Silica PLC

To implement more sophisticated multiple-OAM-device experiments; it is desirable to have the hybrid devices packaged as a single piece, thereby reducing the mounting and alignment complexities for each device and increasing long-term stability. Using adhesive materials to create mechanically rigid bonds between optical components and a substrate or carrier is one way to make such a package. The best adhesives for this work have a low refractive index, similar to that of glass, to reduce the Fresnel losses (return losses) of the light propagating across the bonded interfaces. In particular, ultraviolet (UV) curable epoxies are attractive since they cure within in 10s to 100s of seconds when exposed to modest amounts of UV radiation (i.e.,  $\sim 365$  nm wavelength and  $< 1$  W/cm<sup>2</sup>). To this end, Figure 60 shows the alignment and packaging station assembled at UC Davis. Figure 60(a) provides an overview showing input fiber in lower left corner, the 6-axis alignment stages in the center and IR imaging camera in upper right. In the upper left is a high resolution microscope used to help initial alignment of the individual devices. Figure 60(b) shows a closer view of the silica PLC and 3D waveguide block on an aluminum carrier (center of photo) before curing. The aluminum carrier is precision machined so that the waveguides of the silica PLC and the 3D waveguides are at nearly the same height (the 3D waveguides sit  $\sim 30$ - $40\mu\text{m}$  lower). UV-curing epoxy is applied to the facets of the devices and under the 3D waveguides for support. During the curing process the alignment is monitored using the IR imaging camera (inset photo) and optical vector network analyzer (OVNA) to counteract the misalignment caused by a small amount of epoxy shrinkage.



Initial tests with dummy devices (e.g., underperforming devices) show that the alignment is well maintained after a full cure of the epoxy (e.g., the output image does not change). Next, we will bond real devices and measure the loss performance of the packaged device.

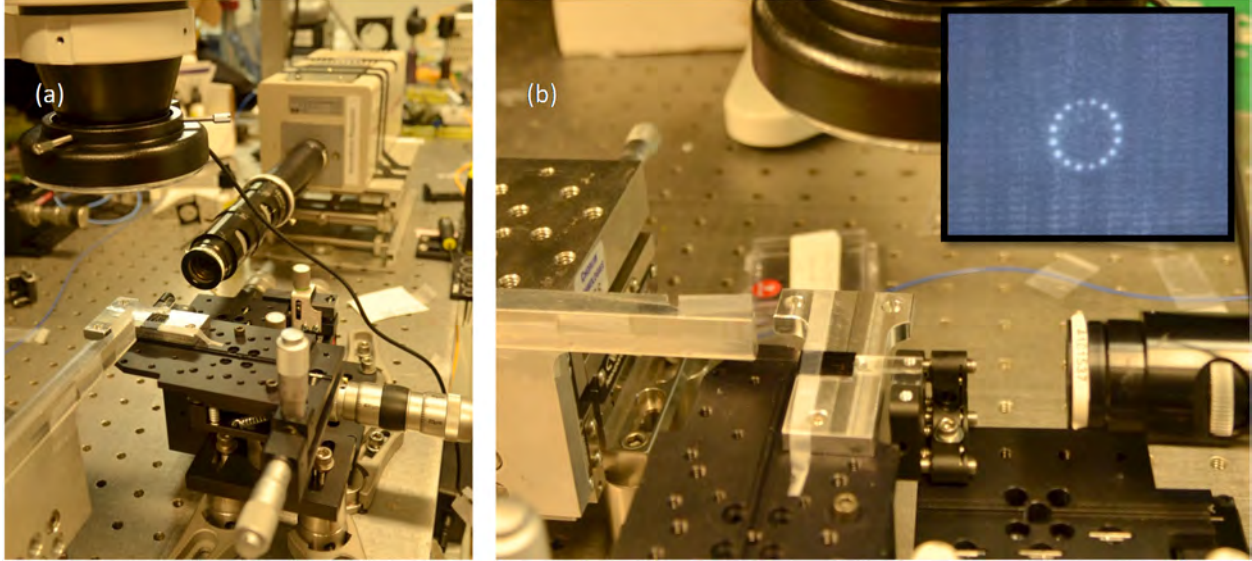


Figure 60. Photos of optical packaging station. (a) Overview of arrangement showing input fiber in lower left corner, 6-axis alignment stages in the center and IR imaging camera in upper right. Upper left is the high resolution microscope. (b) Photo showing silica PLC and 3D waveguide block on aluminum carrier (center of photo) before curing.

### ***II.B.3.g. Multi-device 15 OAM MUX/DEMUX + 20 Gb/s QPSK optical communication experimental arrangement***

We are currently implementing a new multi-device 15 OAM MUX/DEMUX experiment. Figure 61 shows a schematic of the experimental testbed for a SDM coherent optical communication link using two hybrid OAM devices, one as an OAM multiplexer and the other as an OAM demultiplexer. The coherent transmitter consists of a 100-kHz linewidth external cavity laser (ECL) centered at 1546 nm that has a data signal applied by an  $I/Q$  modulator. An electrical arbitrary waveform generator (eAWG) drives the modulator with a 10 GBd differential quadrature phase shift keyed (DQPSK) signal ( $2^7-1$  PRBS). The DQPSK signal is bandwidth limited in digital signal processing (DSP) by a Nyquist filter with a 3-dB bandwidth of 10 GHz for a single-channel spectral efficiency (SE) of 1.67 b/s/Hz. An erbium-doped fiber amplifier (EDFA) increases the optical power of the signal at the any single input of the hybrid OAM device to  $\sim 10$  dBm.

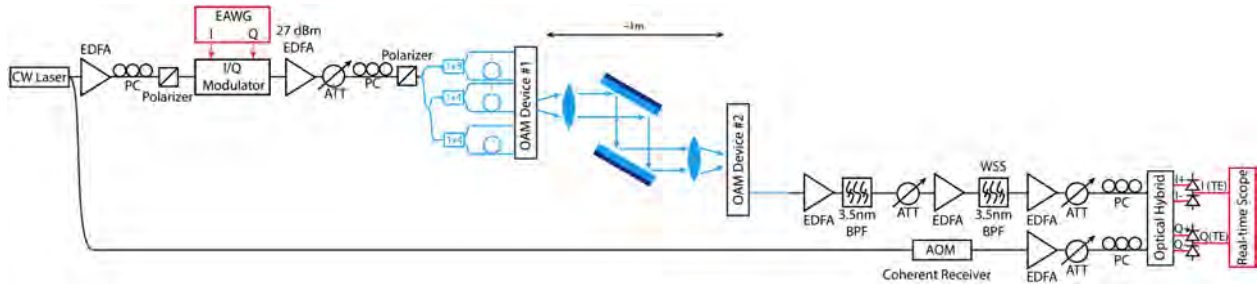


Figure 61. Schematic diagram of the multi-device 15 OAM MUX/DEMUX + 20 Gb/s DQPSK optical communication experimental arrangement.



Immediately following the OAM devices is an EDFA and a 3.5 nm bandpass filter to minimize out-of-band noise. The optical signal-to-noise ratio (OSNR) is varied by noise loading from a second attenuator and EDFA. The signal enters the polarization diversified coherent receiver which uses a frequency shifted (35 MHz) sample of the transmitter's laser as its local oscillator (LO). We will use offline DSP to process the received data.

Figure 62 shows a photo of the experimental arrangement in progress. The first OAM device (multiplexer) is in the foreground and the second OAM device (demultiplexer) is near the back of the photo. A camera is suspended above the devices to aid in optical alignment of the hybrid devices. Once the packaging of the devices is complete the camera won't be necessary.

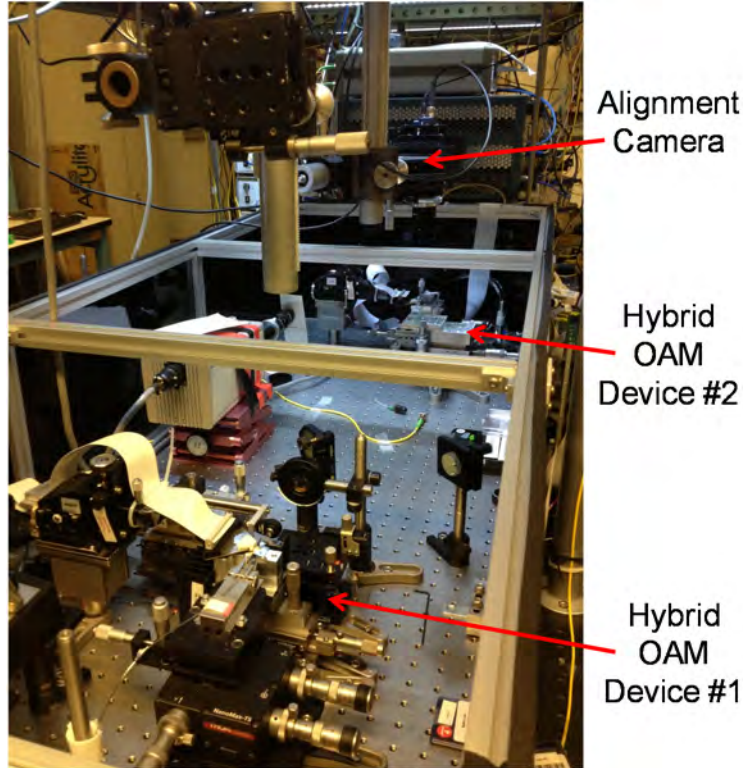


Figure 62. Photo of the multi-device 15 OAM MUX/DEMUX + 20 Gb/s DQPSK optical communication experimental arrangement. The first OAM device is shown in forefront and the second OAM device toward the back.

The above experiment has been upgraded and repeated by introducing fully packaged 2D-3D OAM devices as OAM MUX and DEMUX. Figure 63 again shows the upgraded experimental testbed for a multichannel OAM free-space coherent communication link, using two OAM hybrid devices as OAM multiplexer and demultiplexer, separately. The coherent transmitter consists of an external cavity laser (ECL) operated at 1550 nm with a linewidth of 100 kHz. An electrical arbitrary waveform generator applies a 10-GBd QPSK signal to the  $I/Q$  modulator, with a  $2^7-1$  pseudorandom bit sequence (PRBS). Offline digital signal processing (DSP) generates a pre-emphasized QPSK signal with a 10-GHz, 3-dB Nyquist bandwidth. As a result, the single channel spectral efficiency is 1.67 b/s/Hz. After multiplexing with the first hybrid OAM device, the spatially overlapped OAM beams are transmitted 81.8 cm using an  $8-f$  imaging system to a second OAM hybrid device where the OAM states are demultiplexed. After demultiplexing, the signal of interest is amplified by an EDFA and followed by a 3.5-nm bandpass filter to minimize out-of-band noise. The optical signal-to-noise ratio (OSNR) is varied by noise loading from the subsequent attenuator and EDFA. The signal, as well as the 35-MHz frequency offset reference, enters a polarization diversified coherent receiver. We apply offline DSP to the received data. The DSP extracts

the clock tone from Fourier transform of the magnitude-squared signal. After clock recovery, the data passes through an adaptive equalizer, which includes a 13-tap finite impulse response (FIR) filter. Lastly, the DSP uses power-of-four methods for phase and frequency recovery and differential decoding based bit error counting.

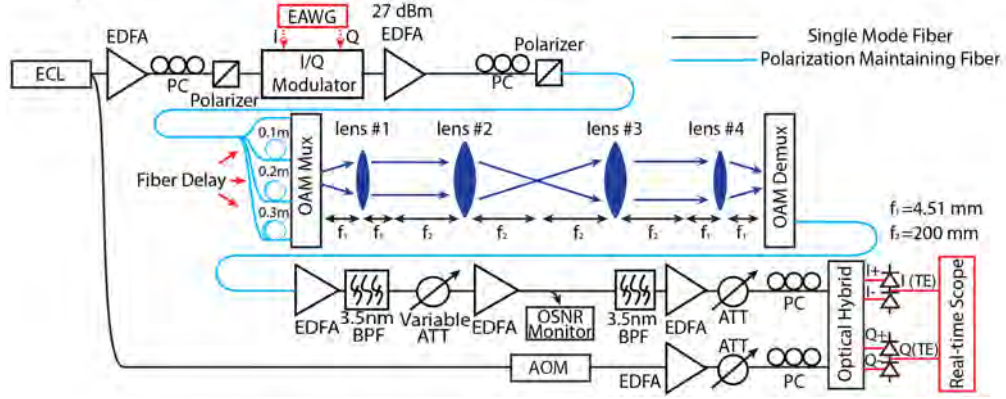


Figure 63. Experimental arrangement of the multichannel OAM free space coherent communication link testbed. ECL: external cavity laser. EDFA: erbium-doped fiber amplifier. PC: polarization controller. ATT: attenuator. BPF: bandpass filter. AOM: acousto-optic modulator.

The bit-error-rate (BER) performance for single channel (OAM state  $-7$  to  $+7$ ) and multichannel OAM states free-space coherent link transmission were measured separately. Figure 64(a) shows the BER performance for single channel OAM state transmission. At a  $\text{BER} = 10^{-3}$ , the implementation penalty is 2.7 dB and the penalty variation is less than 1.1 dB between different OAM states. The penalty is mainly from total insertion loss (30 dB) and residual phase errors of the OAM hybrid devices. At  $\text{OSNR} > 15$  dB, there were no errors recorded with 379,960 bits measured, which indicated error-free performance (i.e.,  $\text{BER} < 10^{-12}$ ) with hard decision forward-error correction (FEC) (e.g., RS(255,239) coding [1]). Figure 64(b) shows BER performance for the free-space coherent optical communication link while simultaneously multiplexing and demultiplexing two, three and four OAM states. In this experiment, we only take BER measurements for the OAM state  $-1$  output. The BER performance of OAM state  $-1$  with the interfering OAM state  $+3$ , or OAM states  $+3$  and  $-5$  together, registered no errors when the  $\text{OSNR} > 21$  dB. The measured crosstalk between OAM state  $-1$  and OAM states  $+3$ ,  $-5$ ,  $-7$  are  $-10.7$  dB,  $-17.9$  dB and  $-10.6$  dB, respectively. Therefore, the penalty for these two and three OAM states interfering is less than 0.1 dB. When the  $\text{OSNR} > 26$  dB, the BER for OAM state  $-1$  with the interfering OAM states  $+3$ ,  $-5$ ,  $-7$  is  $3 \times 10^{-4}$ , which also indicates error-free performance with hard decision FEC. Figure 64(c-f) show the examples of constellation plots for OAM state  $-1$  with or without interference from other OAM states. The reduced performance for four OAM states multiplexing is mainly due to the non-uniform amplitude distribution of the OAM beams and residual phase errors.

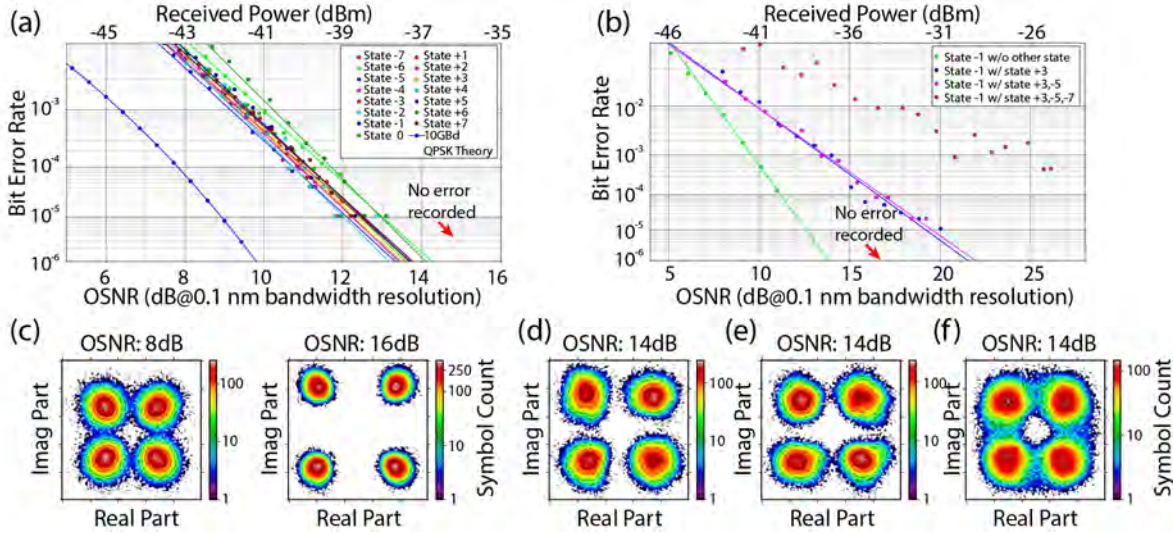


Figure 64. (a) BER performance for single channel OAM state transmission. (b) BER performance for multichannel OAM state transmission (OAM state  $-1$  with, and without other states (interferer) present). (c) Constellation plots at 8-dB and 16-dB OSNR for OAM state  $-1$  transmission without other states. Constellation plots at 14-dB OSNR for OAM state  $-1$  with (d) OAM state  $+3$  present, (e) OAM state  $+3, -5$  present and (f) OAM state  $+3, -5, -7$  present.

We have demonstrated a multichannel OAM free-space coherent communication link using two separate 3D photonic hybrid devices which can multiplex and demultiplex 15 OAM states. The optical coherent link with a 20-Gb/s QPSK signal showed the capability of error-free transmission at OSNR  $> 15$  dB for all the OAM states with hard decision FEC. Moreover, we showed scalability of transmit four OAM states simultaneously with the coherent link, achieving a 80-Gb/s QPSK and spectral efficiency of 6.67 b/s/Hz. Future work includes investigating crosstalk performance and performing link experiments with more OAM state multiplexing.

#### II.B.4. Arbitrary Spatial Waveform Generation and Detection including the Radial Component

One important aspect of Inpho should be to add a radial component waveform shaping in addition to the azimuthal (OAM) component to create a large number of orthogonal spatial states. We are currently investigating two methods as follows. First, under a new ONR project, we are currently setting up a new 3D waveguide inscribing capability using a newly purchased femtosecond laser. Second, we are investigating multi-layer method to the 2D integrated chip discussed earlier.

##### II.B.4.a. 3D waveguide writing to add a radial component

The 3D waveguide inscribing allows us to form waveguides propagating in arbitrary directions so long as effective bending radius is above its loss limit. Figure 65 shows an example of two groups of 3D waveguides overlaying on each other to be able to produce overlaid rectangular lattices. Similarly, the apertures can be arranged in cylindrical symmetry as illustrated in Figure 66. A group of the apertures on the same concentric ring will be driven by the same 2D waveguides in Figure 16, but multiple groups are driven by the same source to maintain spatial symmetry. The 3D waveguide writing system is being setup and we expect it to be ready in early June for writing such waveguides. At the same time, a coherent matrix of the 2D waveguide to drive this 3D waveguide block will also be designed and fabricated.

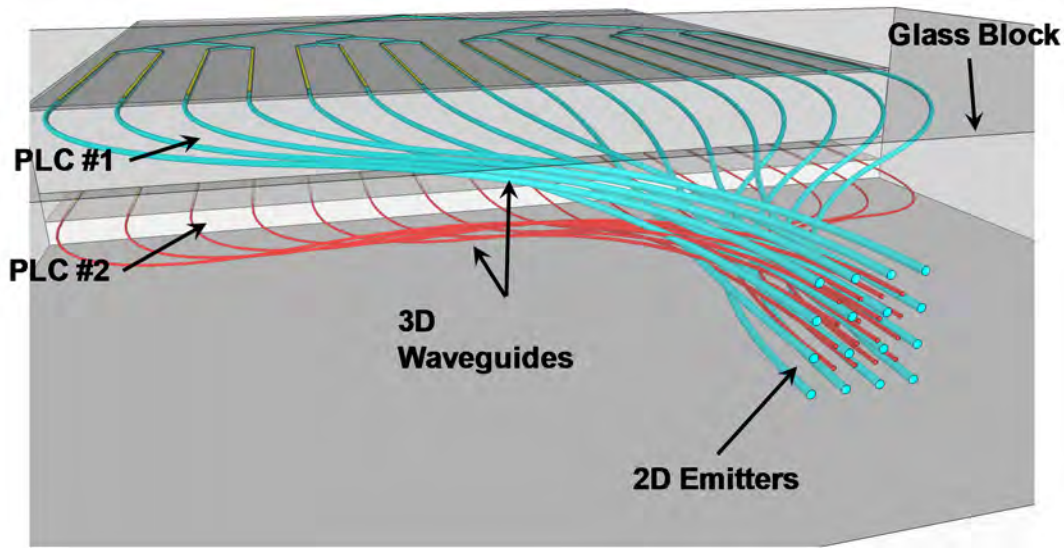


Figure 65. Arbitrary waveform shaper using 3D waveguide writing technique

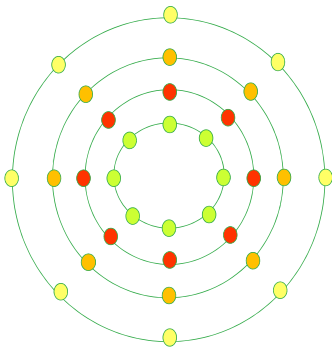
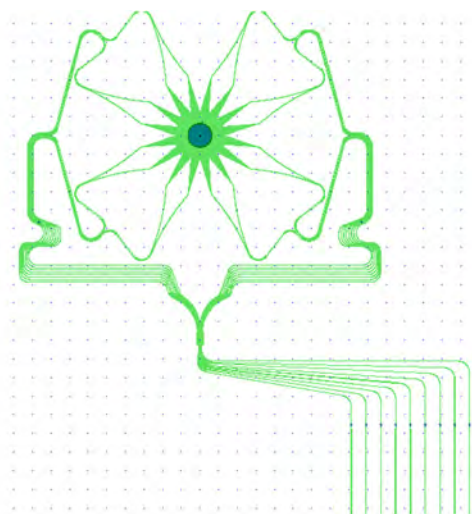


Figure 66. The apertures of the 3D waveguides arranged in concentric cylindrical symmetry.

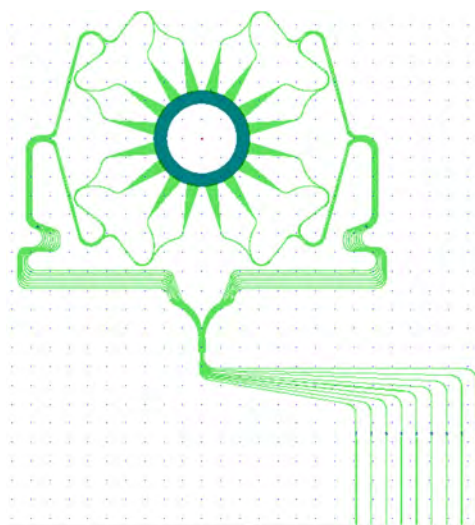
#### ***II.B.4.b. Multilayer 2D photonic integrated circuit***

Another way to achieve azimuthal and radial variations is to use stacking of multiple 2D layers as illustrated in Figure 67 (a)(b). Using silicon nitride 2D waveguide, one can design and implement multiple silicon nitride core layers on silica to achieve this goal. First, a 2D waveguide layer with a larger diameter grating aperture will be fabricated, and subsequently, a chemical-mechanical polishing and the second 2D waveguide layer fabrication will be pursued. The grating apertures of multiple layers will be appropriately coordinated in order to reduce loss and cross-coupling.

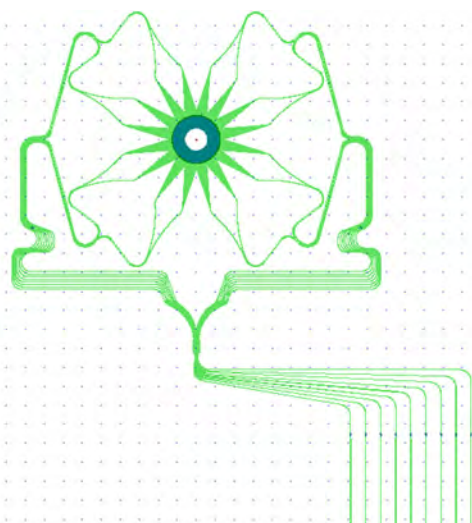




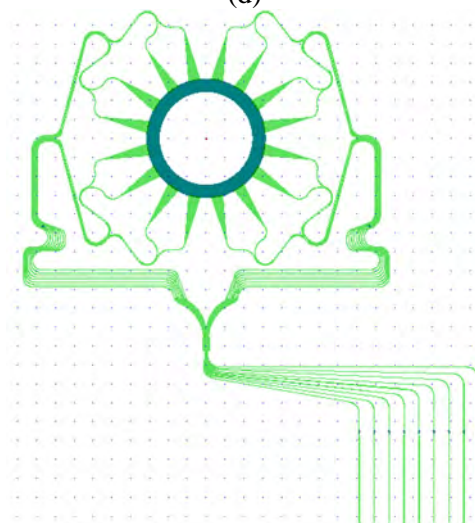
(a)



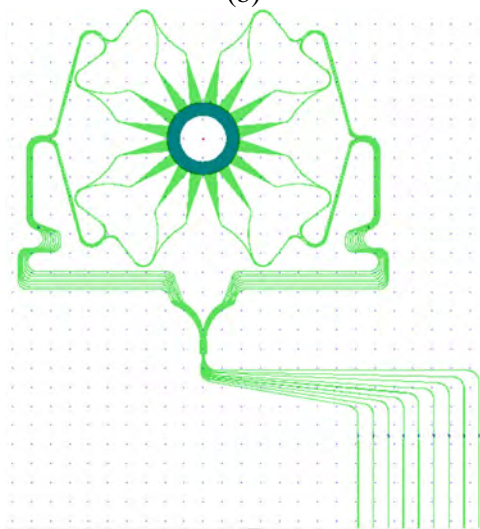
(d)



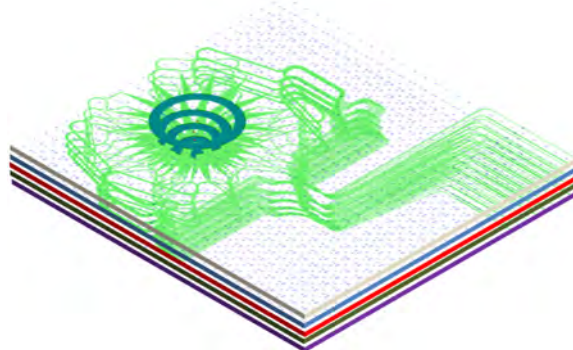
(b)



(e)



(c)



(f)

Figure 67. Stacking of multiple 2D layers for arbitrary waveform shaping. (a) Layer 1, (b) Layer 2, (c) Layer 3, (d) Layer 4, (e) Layer 5, and (f) stacked device consisting of Layer 1-5.

#### II.B.4.c. Grating simulation

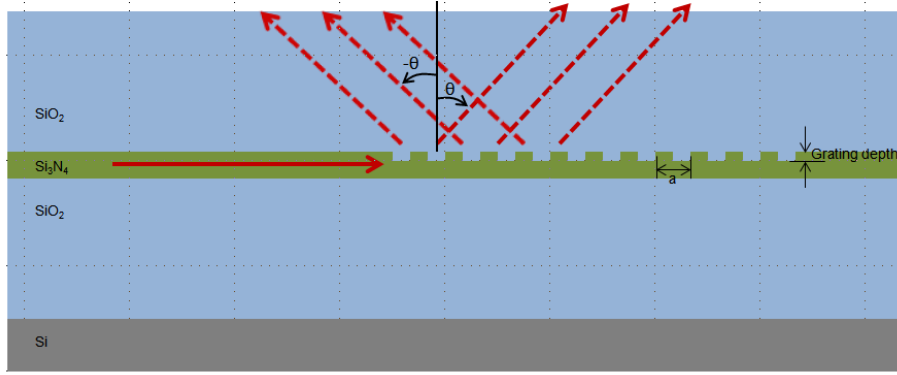


Figure 68 Schematic of grating coupler design

To design the multilayer silicon nitride OAM device, the first part is designing the grating structure. Figure 68 shows the schematic picture of the grating coupler. The core layer is 500nm thick  $\text{Si}_3\text{N}_4$ , with  $\text{SiO}_2$  as lower cladding and upper cladding. The core layer is etched to form grating with 50:50 duty circle.

The grating pitch is calculated using equation:

$$a = \frac{\lambda}{n_{\text{eff}} - (\sin \theta)n_{\text{cladding}}}$$

In the equation,  $a$  is the grating pitch,  $\lambda$  is the operating wavelength,  $n_{\text{eff}}$  is the waveguide effective index,  $n_{\text{cladding}}$  is the cladding index, and  $\theta$  is the launch angle. For  $\theta=0^\circ$  (vertical coupling), the grating pitch for different etch depth is calculated in Figure 69.

Si3N4 WG Thickness (nm)	Neff of the etched region	Neff of the whole grating	Etch Depth (nm)	Grating Pitch (a) (nm)
500	1.7875	1.7875	0	
300	1.6675	1.7275	200	897
280	1.6526	1.7201	220	901
260	1.6366	1.7121	240	905
240	1.6168	1.7022	260	911
220	1.5996	1.6936	280	915
200	1.5800	1.6838	300	921
180	1.5613	1.6744	320	926
160	1.5409	1.6642	340	931
140	1.5220	1.6547	360	937
120	1.5011	1.6443	380	943
100	1.4828	1.6351	400	948

Figure 69 Table for grating period for different grating etch depth

Figure 70 and Figure 71 shows the grating simulation using FDTD for two different etch depths and grating pitch. The light launches vertically from the grating. For the actual design, we are using 897nm and 923nm as the grating pitch.

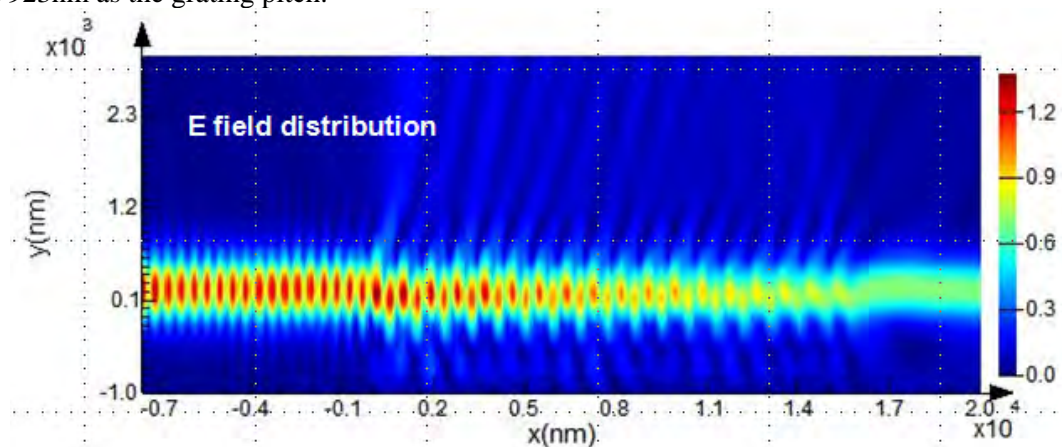


Figure 70 Grating simulation for grating pitch 0.897 $\mu$ m and etch depth 200nm

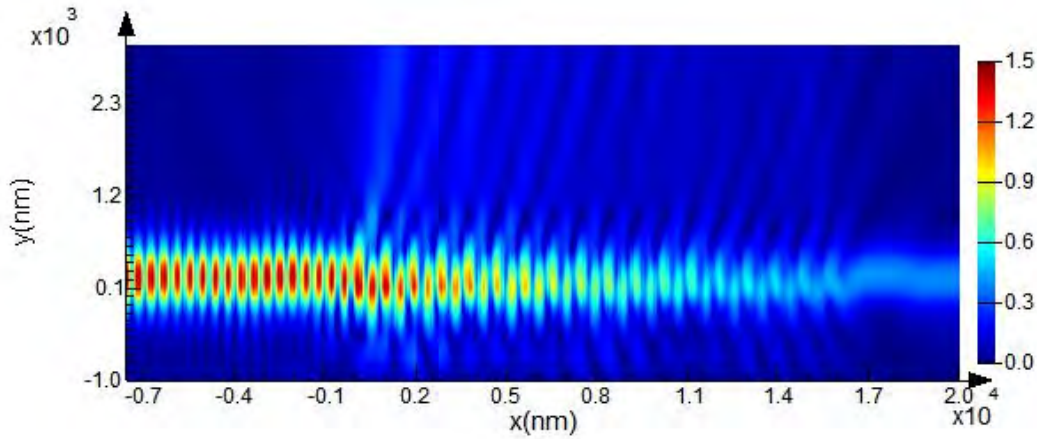


Figure 71 Grating simulation for grating pitch 0.923 $\mu\text{m}$  and etch depth 300nm

#### II.B.4.d. Coupling Simulation

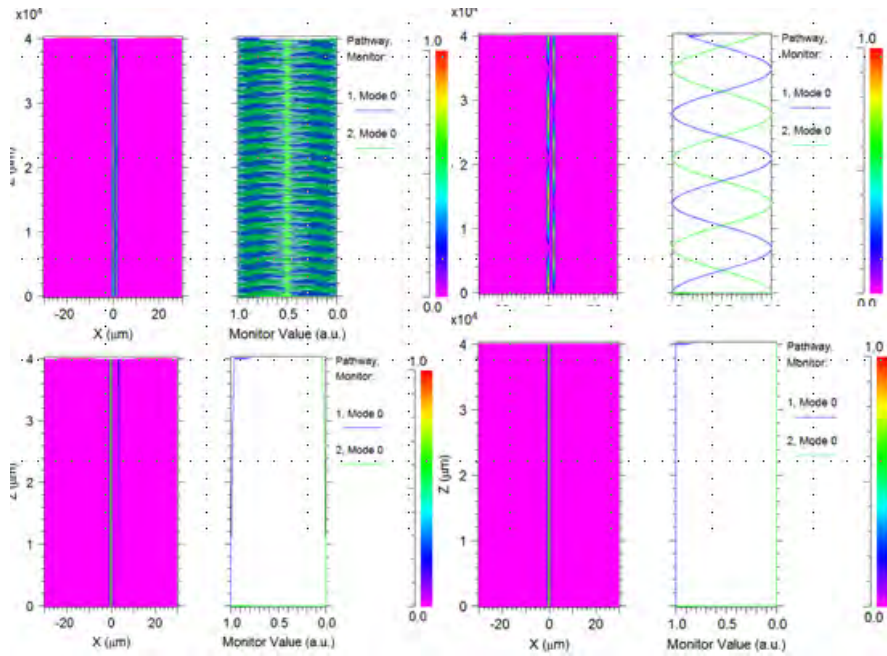


Figure 72 Coupling between different layer of SiN waveguide for layer gap of 1 $\mu\text{m}$ , 2 $\mu\text{m}$ , 3 $\mu\text{m}$ , 4 $\mu\text{m}$

Figure 72 shows the coupling between different layers of SiN waveguide for layer gap of 1~4 $\mu\text{m}$ . This is also an import design parameter for it determines the silica layer thickness during fabrication. Simulation indicates for layer gap of 1 $\mu\text{m}$ , the coupling length is smaller than 100 $\mu\text{m}$ . Layer gap of 2 $\mu\text{m}$ , coupling length is ~6mm. Layer gap of 3 $\mu\text{m}$  and 4 $\mu\text{m}$ , coupling length is  $\gg 40\text{mm}$ .

For our design, the array arm is about 6000 $\mu\text{m}$  long, so 3 $\mu\text{m}$  layer gap is enough. For future design with higher channel count (thus longer array arms), the layer gap may need to increase.

#### II.B.4.e. Mask layout



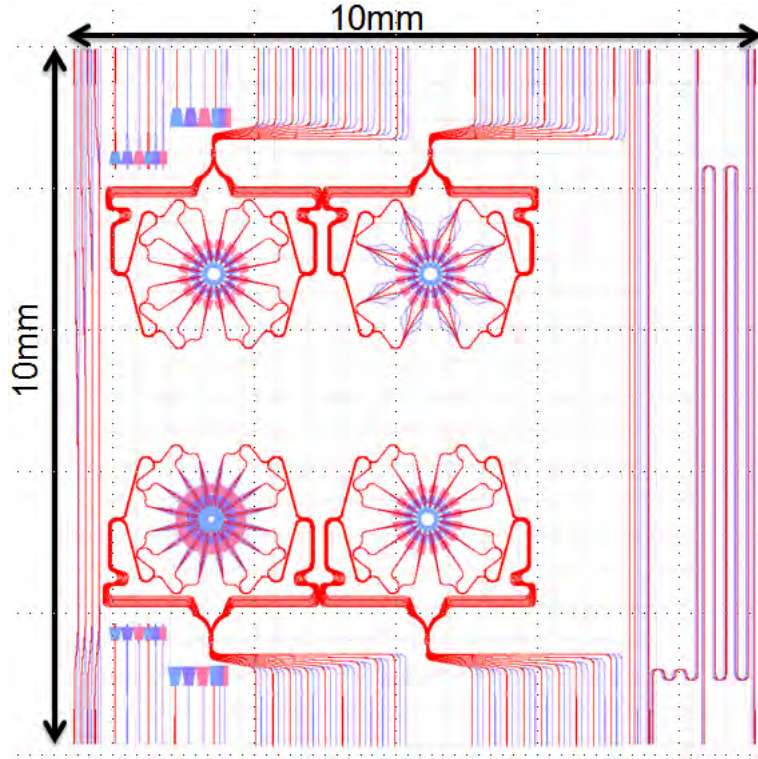


Figure 73 Overall layout of one die

Figure 73 shows the overall layout of the device. There are total of 6 layout layers in the design, top layer grating, top layer waveguide, middle layer grating, middle layer waveguide, bottom layer grating and bottom layer waveguide. The overall device is within 10mm x 10mm die size.

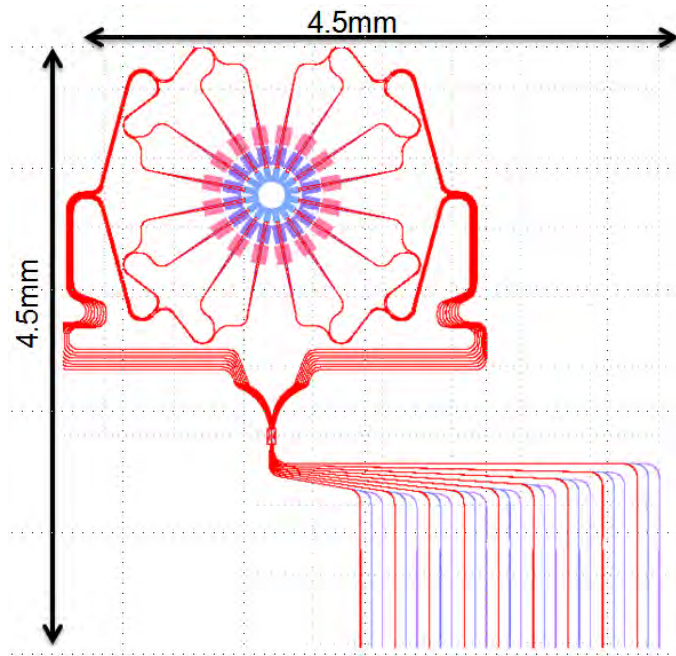


Figure 74 Triple layer 16 arm OAM device

Figure 74 shows the layout of the triple layer OAM device. Each layer of the device has 9 inputs and 16 arms. So there are total of  $16 \times 3 = 48$  apertures in the grating region. As in the single layer device, launching light from different input should generate output beam with different OAM charge.

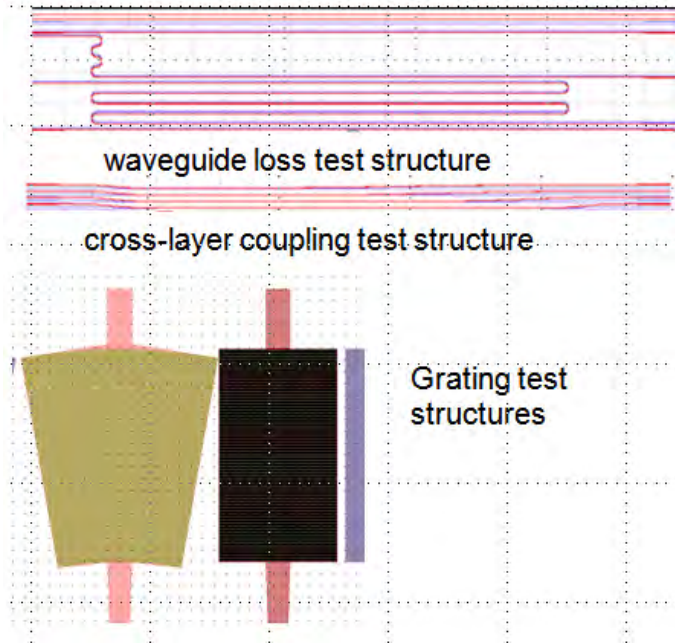


Figure 75 Test structures on the layout

Since this is our first attempt to make multi-layer device, a lot of test structure are included in the design. Figure 75 shows some of the test structures. Straight waveguide loss is measured as the difference in insertion loss for the waveguide structure with different length. Cross-layer coupler structure test coupling between different layers of waveguide. There are four couplers with coupling length 500  $\mu\text{m}$  ~ 6500  $\mu\text{m}$ . Grating test structure tests the grating launched light from all three grating layers.

### II.B.5. Multilayer SiN fabrication process

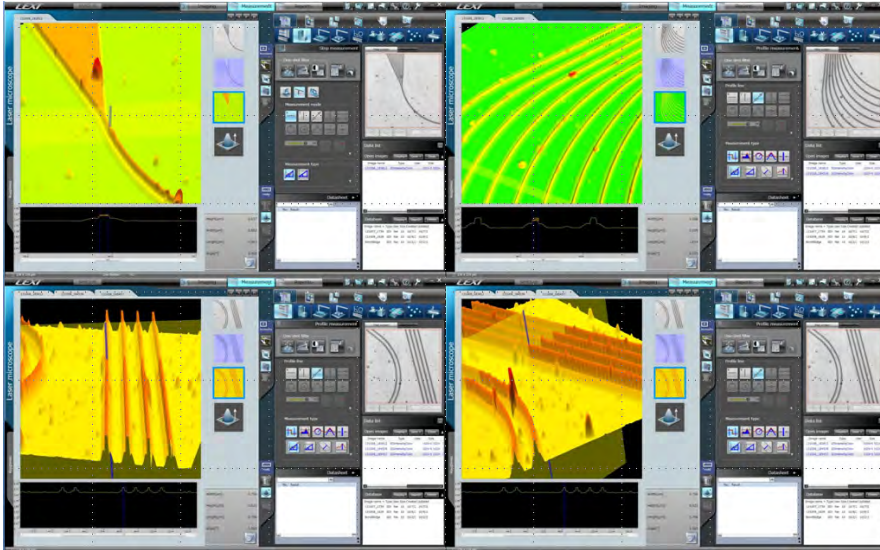


Figure 76 Microscope picture of the fabricated waveguide layer

We have tried fabrication of the multilayer device with test patterns. Figure 76 shows the 3D microscope picture of the first layer SiN waveguide.

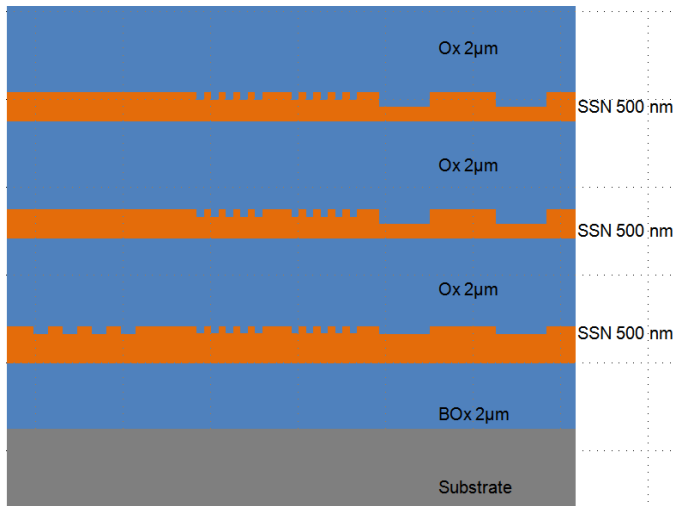


Figure 77 Cross Section of the triple layer SiN device

Figure 77 shows the intended pattern of the triple layer SiN device. In this test the SiN layer is 500nm thick, and the oxide layer in between is 2um thick.

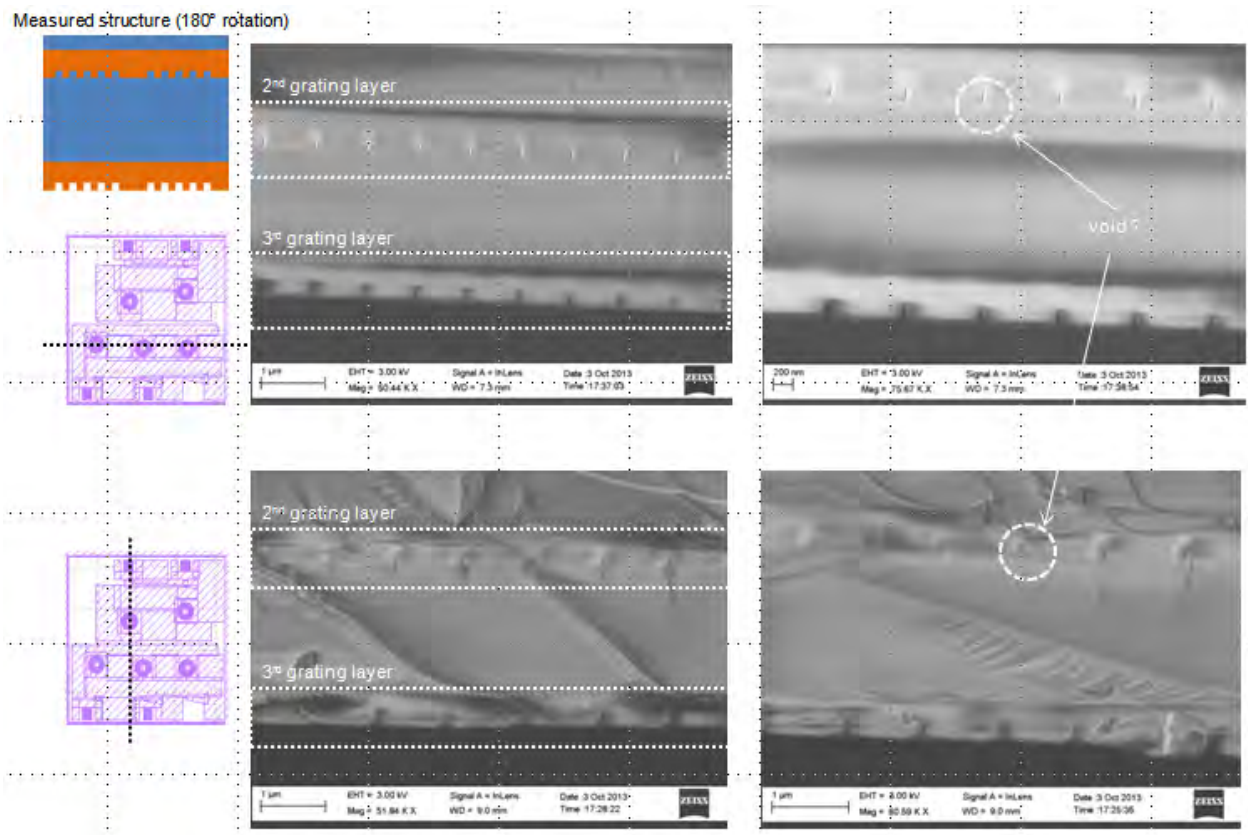


Figure 78 SEM picture of the fabricated triple layer device

Figure 78 shows the SEM picture of the fabricated triple layer device. We can see two layers of grating structure in the picture.

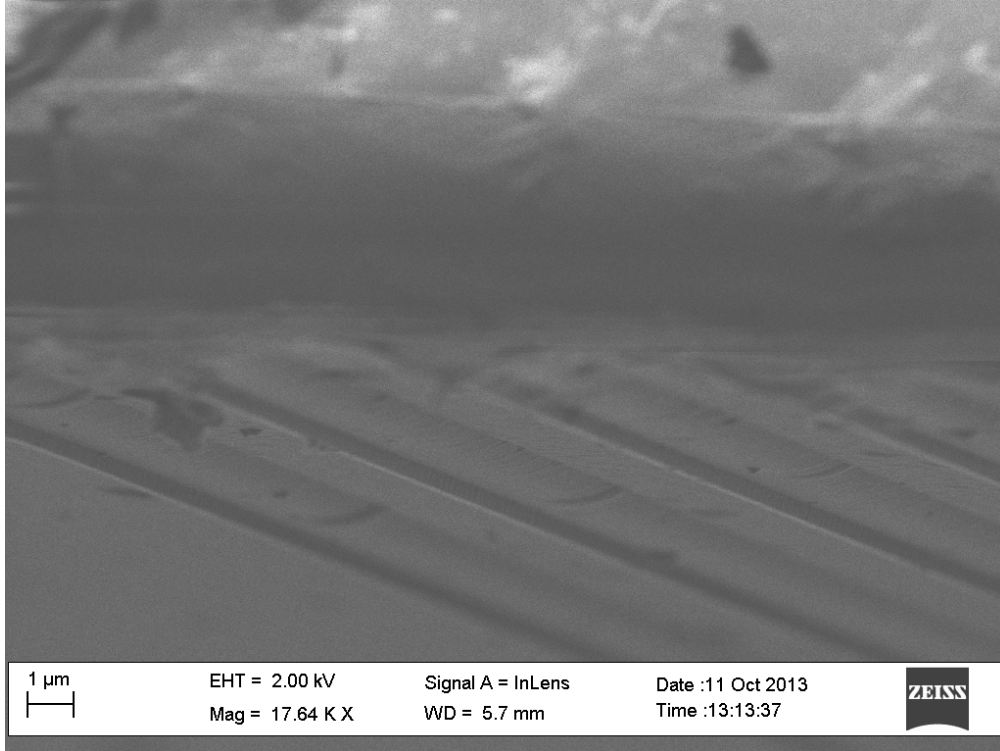


Figure 79 SEM picture of the waveguide side wall

Figure 79 shows the sidewall roughness of the waveguide under SEM.

### II.B.6. Arbitrary Spatial Waveform Transformer

So far, the designed and fabricated devices achieve multiplexing or demultiplexing of multiple OAM states simultaneously. In a functional diagram, the functional steps in Figure 80 can be expressed in the functional diagram in Figure 81 for multiplexing and in Figure 82 for demultiplexing. Further, the functional diagram can utilize arbitrary orthogonal states in Figure 83 for multiplexing and Figure 87 for demultiplexing. Extending the discussions to 2D orthogonal spatial modes with radial and azimuthal variations (e.g. LP modes), one can in principle generate arbitrary spatial waveforms. Conversely, any given arbitrary spatial waveform can constitute one of the eigenstates in the basis so that one can couple theoretically 100% output power with no loss of energy. This latter part of the discussion has been expanded in a recent publication by D. A. B. Miller in "Self-aligning universal beam coupler," Opt. Express 21, 6360-6370 (2013). In essence, the concept is fairly simple if steps in Figure 81, Figure 82, Figure 83 and Figure 87 are followed by generalizing for 2D waveform shaping and reconfigurable unitary matrix  $U$  between  $a$  and  $b$  basis sets.



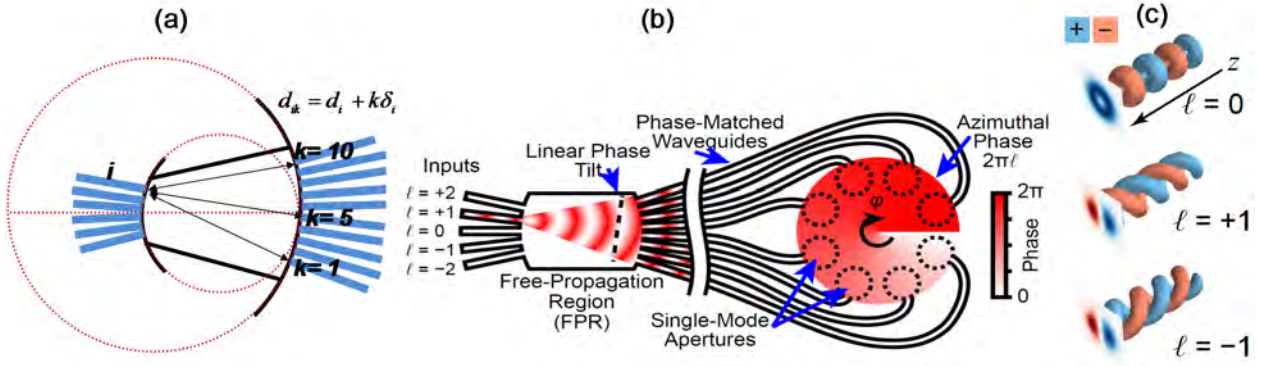
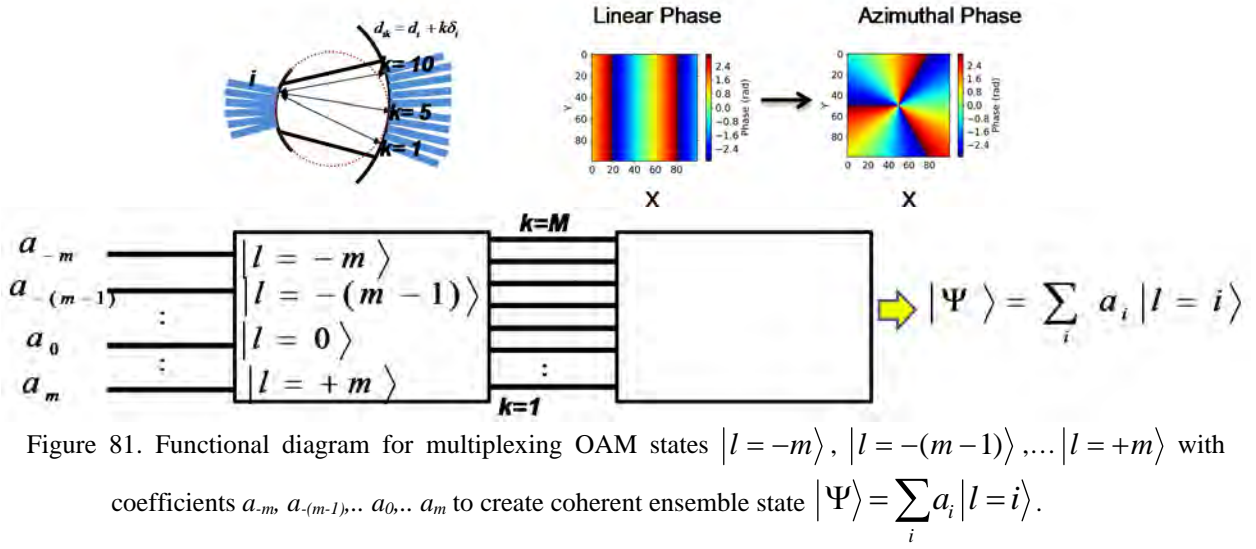


Figure 80. Functional steps for generating orbital angular momentum states starting with (a) linear phase variation, (b) conversion of linear phase variations to azimuthal phase variations to generate (c) OAM states.

### II.B.7. Arbitrary Waveform Shaping in Time, Space, Spectral Domain

Under DSO OAWG project, our team has developed optical arbitrary waveform generation and measurement techniques using coherent optical frequency combs. Figure 88 and Figure 89 describe these methods.



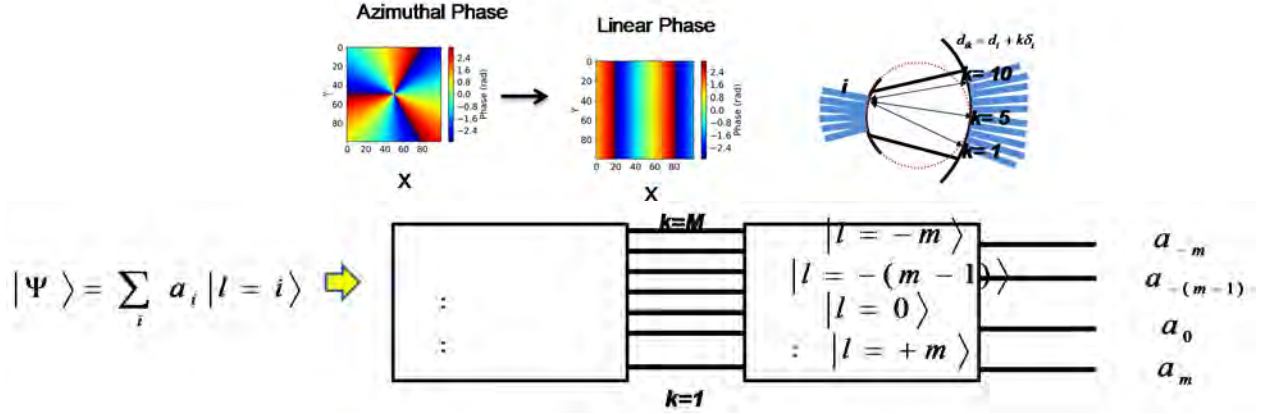


Figure 82. Reverse process of Figure 81 illustrating a functional diagram for demultiplexing the coherent ensemble state  $|\Psi\rangle = \sum_i a_i |l = i\rangle$  into OAM states  $|l = -m\rangle, |l = -(m-1)\rangle, \dots, |l = +m\rangle$  with coefficients  $a_{-m}, a_{-(m-1)}, \dots, a_0, \dots, a_m$ .

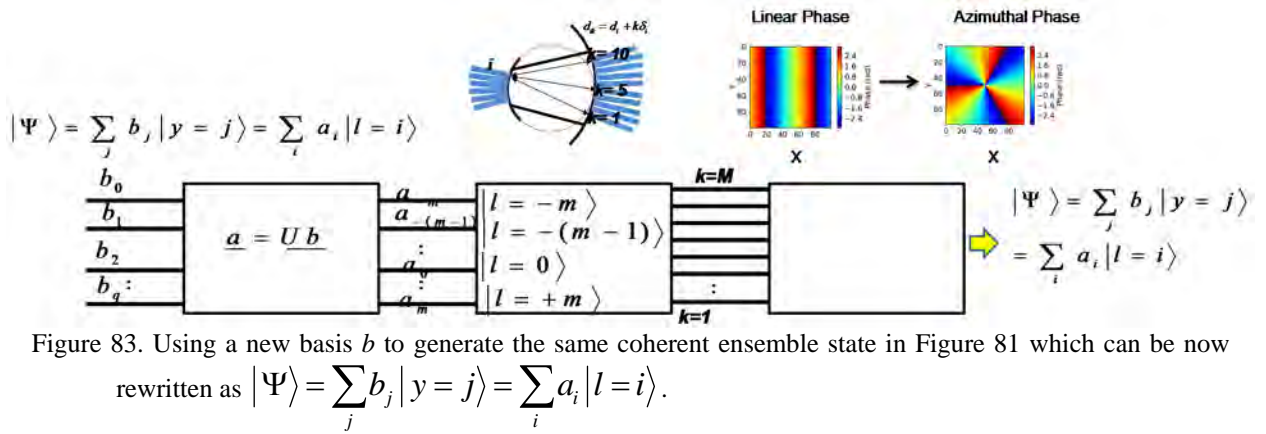


Figure 83. Using a new basis  $b$  to generate the same coherent ensemble state in Figure 81 which can be now rewritten as  $|\Psi\rangle = \sum_j b_j |y = j\rangle = \sum_i a_i |l = i\rangle$ .

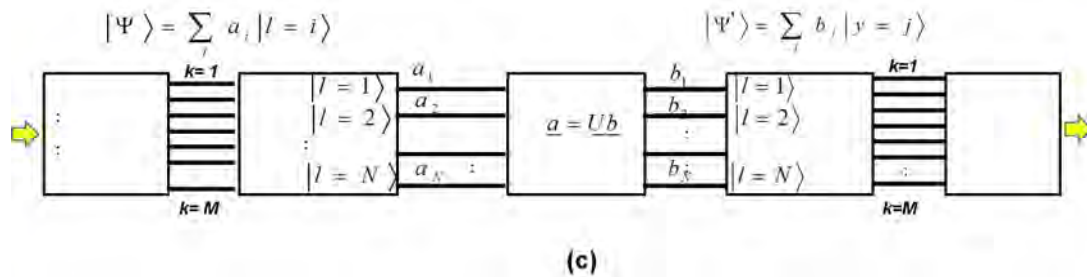


Figure 84. OAM state converter.

As Figure 84 indicates, OAM state converter consists of the OAM multiplexer and demultiplexer back to back with a reconfigurable optical switch in the middle. Ideally the reconfigurable optical switch is in fact a unitary matrix (loss less) that relates the demuxed coefficients to the new coefficients by a unitary matrix. The reconfiguration of the unitary matrix allows conversion of any input ensemble of the OAM states to any desired ensemble of the OAM states at the output.



In this paper, we will utilize a simple reconfigurable fiber switch for the unitary matrix and utilizes the OAM state converter (Figure 84 (c)) inserted in between the OAM state multiplexer as a transmitter (Figure 84(a)) and the OAM state demultiplexer as a receiver (Figure 84 (c)).

### II.B.7.a.i. OAM state conversion testbed

Figure 85 shows the OAM state conversion testbed with OAM multiplexing and demultiplexing devices including approximately 1.6 m free-space transmission. The CW laser with a 100 kHz linewidth has a wavelength at 1550 nm. The signal is modulated by an electrical arbitrary waveform generator (eAWG) driven in-phase quadrature-phase modulator (I/Q modulator) using 10GBd  $2^7-1$  pseudo-random bit sequence (PRBS) quadrature phase shift keying (QPSK) signal with a spectral efficiency of 1.67 b/s/Hz created by offline digital signal processing (DSP). A 27dBm erbium-doped amplifier amplifies the signal before the OAM devices. The signal goes into the OAM device #1 as OAM state -1 and comes out as OAM state -1. The free-space transmission includes an 8-f imaging system. The focus of lens #1 and #4 is 4.51mm and of lens #2 and #3 is 200mm. At the output of the OAM device #2 we switch the signal to OAM state -4 after an EDFA and 1nm bandpass filter which minimizes the out-of-band noise and send it back to the OAM device #2. The OAM device #1 would receive the signal as OAM state -4. The counter-propagating transmission reduces the crosstalk otherwise appears in co-propagating transmission (or loopback configuration). The signal goes through the noise loading part before it enters the coherent receiver that has a polarization diversified optical 90° hybrid and a real-time oscilloscope at 50GS/s. A local oscillator comes from the same laser with 35 MHz frequency offset shifted by an acousto-optic modulator (AOM). Offline DSP applies clock recovering, 13-tap finite impulse response (FIR) filter based equalizer and carrier phase estimation. In the end, the DSP calculated the bit-error-rate (BER).

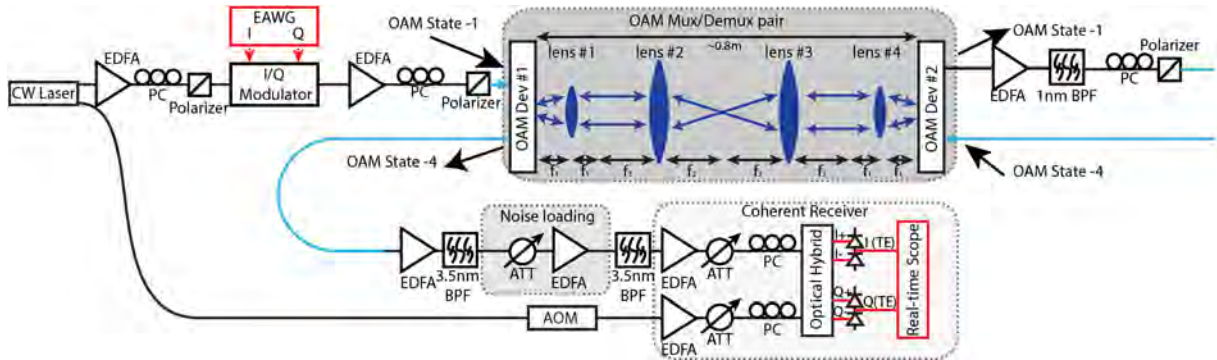


Figure 85. 10-GBd QPSK link experiment testbed for OAM state conversion using two OAM hybrid devices with ~1.6m round-trip free-space transmission. EDFA: erbium-doped fiber amplifier. PC: polarization controller. ATT: attenuator. BPF: bandpass filter. AOM: acousto-optic modulator.

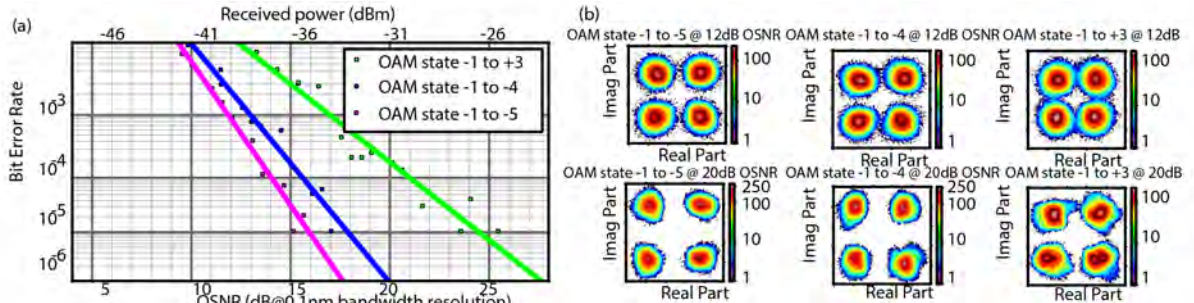


Figure 86. (a) BER performance for OAM state -1 as the input and switched to +3, -4 and -5. (b) Constellation plots for each case at OSNR of 12dB and 20dB.

Figure 86 (a) shows the BER performance with 379,960 bits tested for input OAM state -1 switched to OAM state -5, -4 and +3. Note that the BER is less than  $10^{-5}$  (no errors are recorded) when OSNR is more than 16dB for -1 to -5 conversion, 18dB and 25 dB for -1 to -4 and -1 to +3 respectively. Figure 86 (b) shows the constellation plots for

the three conversion cases in Figure 86 (a) at both 12dB and 20dB OSNR. We notice that the OAM state -1 to +3 has the worst BER performance in three and -1 to -5 has the best performance.

### II.B.7.a.ii. *Arbitrary waveform generation and detection in temporal, spectral, and spatial domains*

It is feasible to imagine arbitrary waveform generation and detection in time, space, and spectrum. In principle, OAWG and OAWM achieved time domain and spectral domain arbitrary waveform generation and detection so long as it is within the limit of Fourier transform limit. Incorporating OAWG and OAWM in the matrices in Figure 83 and Figure 87 can allow arbitrary waveform generation and detection in time, space, and spectral domains. However, the actual implementation can be extremely complicated. Much simpler implementation is possible by separating temporal/spectral shaping and spatial shaping by separating the variables, where in approximating the temporal, spectral, and spatial shaping processes. This assumption for approximation is qualitatively very good so long as the dispersion in the spatial shaper is small and the spatial shaper is nearly time-independent over the time scale of temporal variations (thus taking spatial shaping as spectrally and temporally invariant). Figure 90 and Figure 91 show the simplified generation and detection schemes of arbitrary waveforms in time, space, and spectral domains.

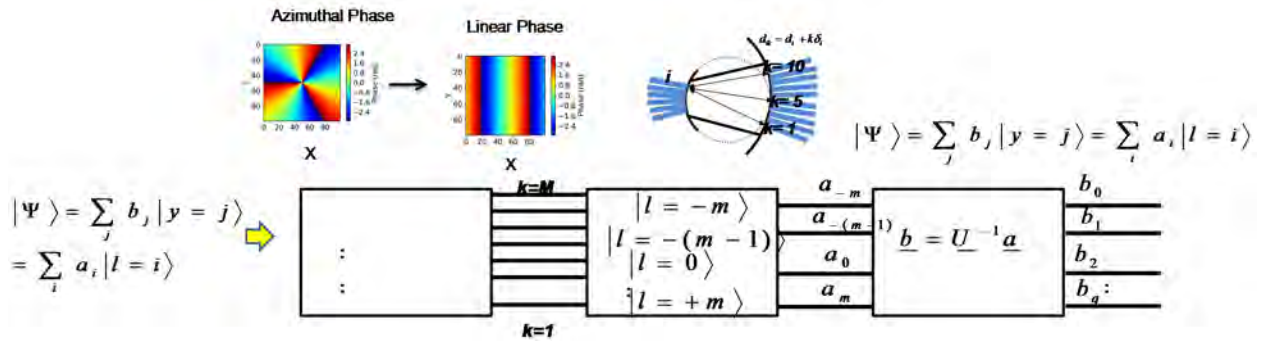


Figure 87 Similarly to Figure 83 and Figure 82, the demultiplexing can utilize the new basis

$$|\Psi\rangle = \sum_j b_j |y=j\rangle = \sum_i a_i |l=i\rangle.$$

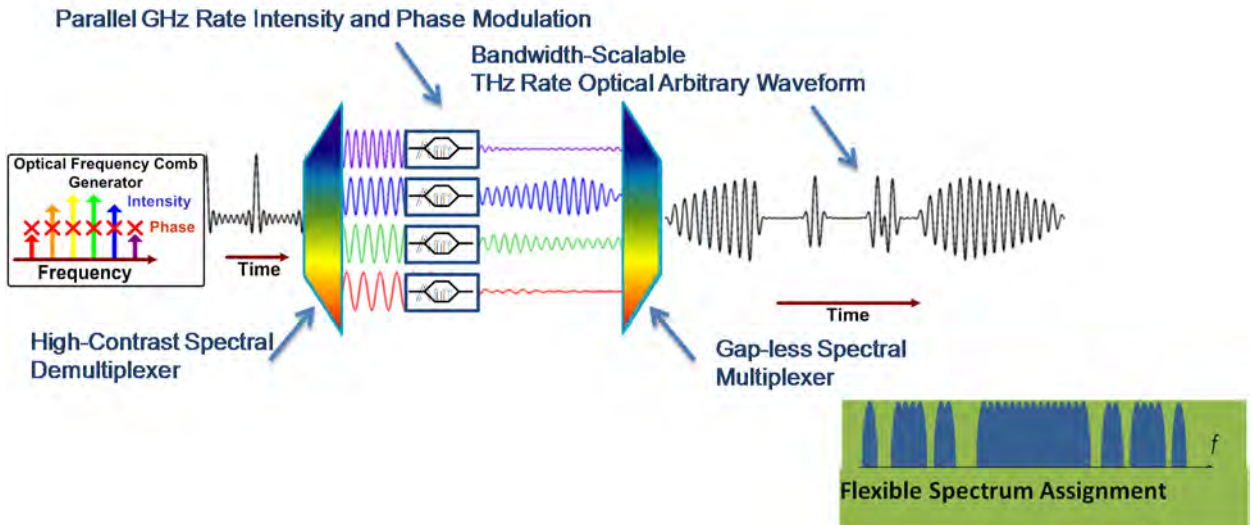


Figure 88. Dynamic optical arbitrary waveform generation techniques using coherent optical frequency combs.

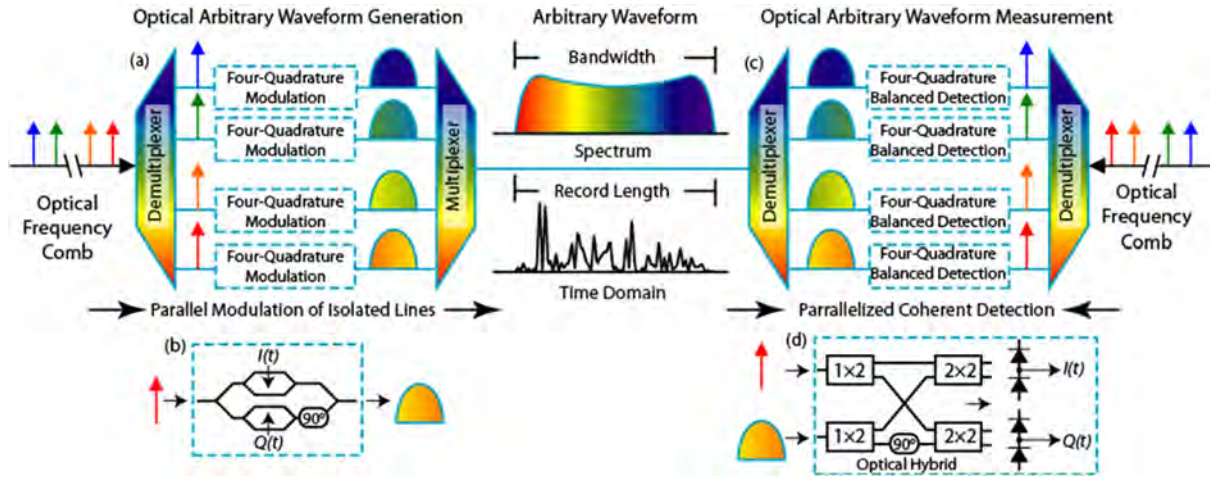


Figure 89. Dynamic optical arbitrary waveform generation and measurement schemes in symmetry.

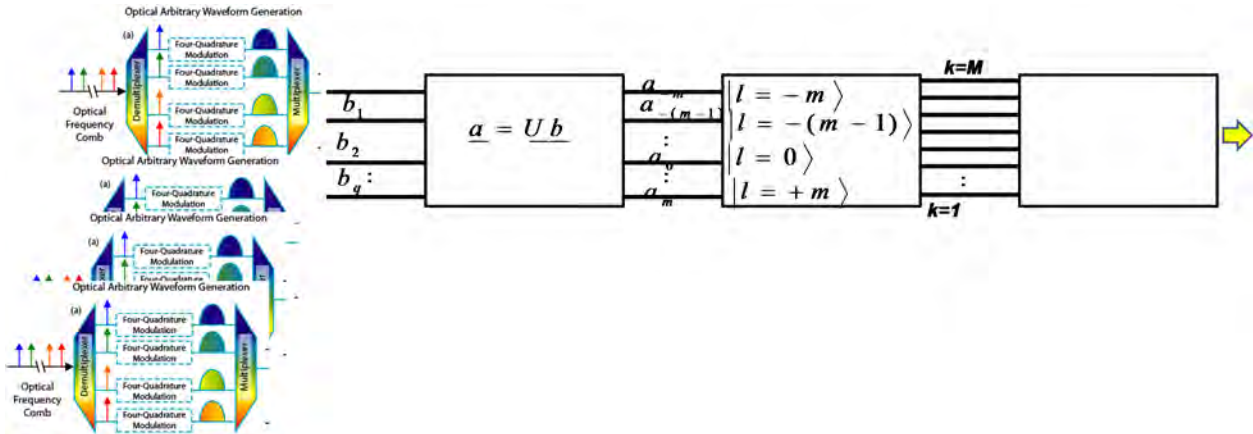


Figure 90. Simplified generation schemes of arbitrary waveforms in time, space, and spectral domains.

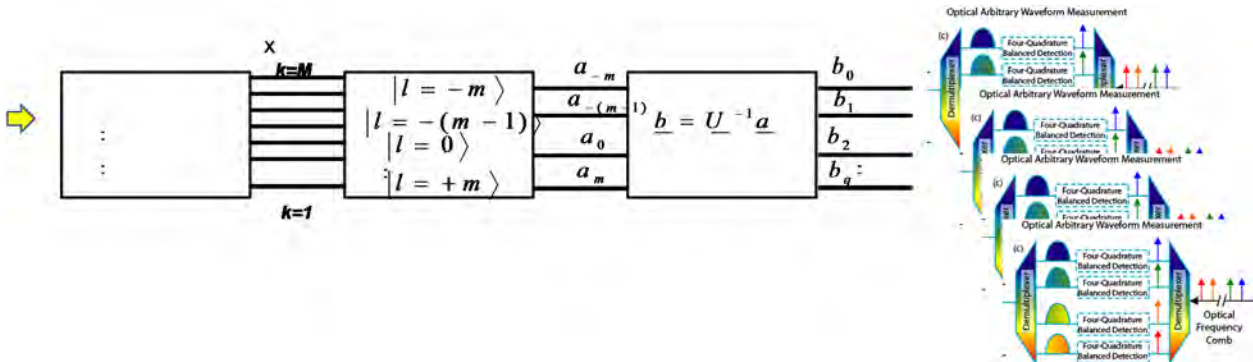


Figure 91. Simplified detection schemes of arbitrary waveforms in time, space, and spectral domains.



## II.B.8. Transmission and switching experiment based on OAM 3D-Integrated Photonic Silica OAM device

### II.B.8.a. OAM State Switching

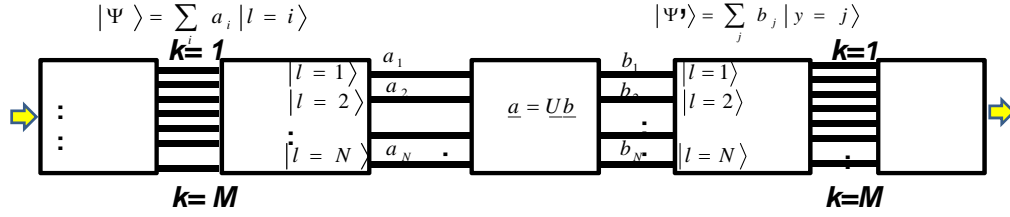


Figure 92. OAM state converter

As Figure 92 indicates, OAM state converter consists of the OAM multiplexer and demultiplexer back to back with a reconfigurable optical switch in the middle. Ideally the reconfigurable optical switch is in fact a unitary matrix (loss less) that relates the demuxed coefficients to the new coefficients by a unitary matrix. The reconfiguration of the unitary matrix allows conversion of any input ensemble of the OAM states to any desired ensemble of the OAM states at the output. In the experiments below, we will utilize a simple reconfigurable fiber switch for the unitary matrix and utilizes the OAM state converter inserted in between the OAM state multiplexer as a transmitter and the OAM state demultiplexer as a receiver. During this reporting period, we have further advanced the theory behind the OAM state MUX, DEMUX, conversion, and scalability limit due to coherent crosstalk.

### II.B.8.b. Crosstalk Reduction by Phase Error Correction (PEC)

Phase error correction (PEC) largely determines whether we will have good orthogonality between OAM modes or not. Hence PEC is essential for low crosstalk OAM experiments. As reported in the previous interim report, we achieved phase error measurements by using shearing interferometry and scanning delay-line interferometer methods. Figure 93 illustrates the shearing interferometry method where we repeated measurements of the phase from the same device over a period of many tens of minutes and checked constant phase relationship (except for a phase offset) between the waveguide outputs for different measurement pairs (2&1, 3&1, etc.) as a good indication of the measurement's repeatability. Figure 94 illustrates the scanning delay-line interferometer method where we again repeated measurements of the phase from the same device over a period of many tens of minutes and checked constant phase relationship (except for a phase offset) between the waveguide outputs for different measurement pairs (2&1, 3&1, etc.) as a good indication of the measurement's repeatability. Figure 95 shows the comparison of the two methods which resulted in the same phase error measurements.

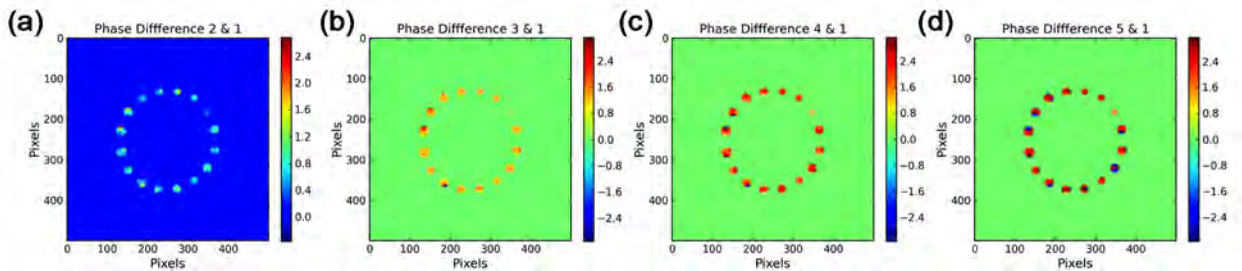


Figure 93. Verification of Shearing Interferometry Method for Phase Error Measurements

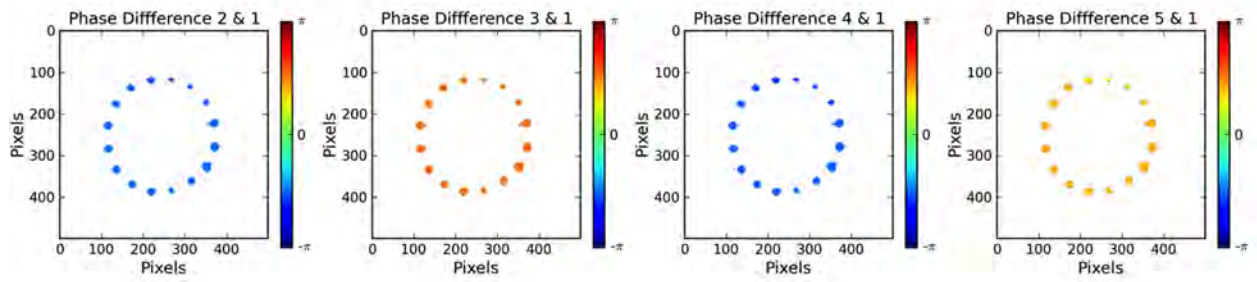


Figure 94. Verification of Scanning Delay-Line Interferometer Method for Phase Error Measurements

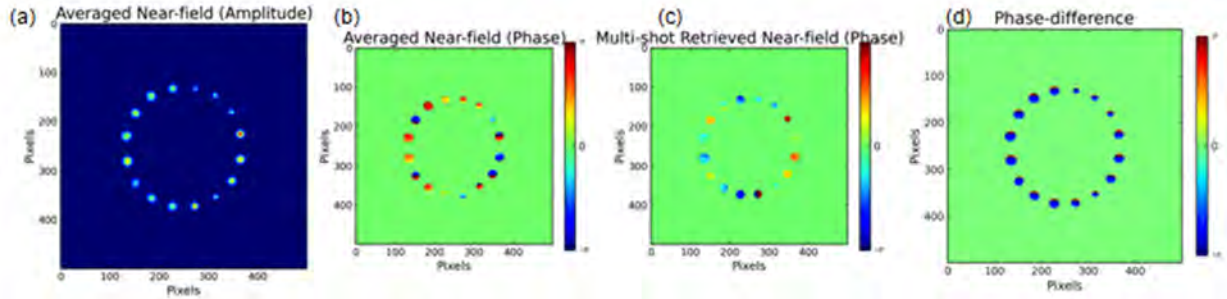


Figure 95. Comparison of Shearing Interferometry and Scanning Delay-Line Interferometer Methods.

#### II.B.8.b.i. *Phase Error Measurement of 3D OAM waveguides and PEC*

Figure 96 shows the setup of the PEC. The fibers need to be taped down and do not vibrate because any vibration after the PM one by two splitter will cause significant phase variation. The free space transmission distance of the reference beam should be short enough to maintain stability.

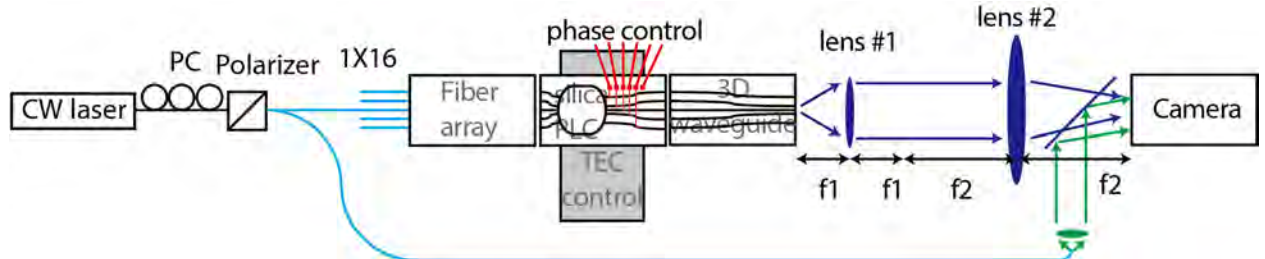


Figure 96 Phase error correction setup.

#### II.B.8.b.ii. *Fine tuning the PEC*

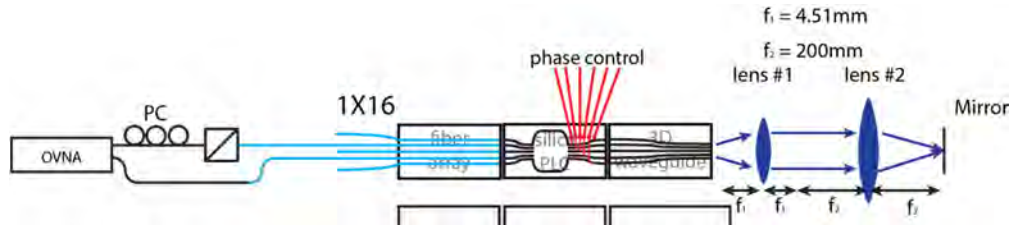


Figure 97 Setup for reflection measurement.

Once the PEC is done using the setup in Figure 96, we modified the setup as in Figure 97 to measure the crosstalk matrix. In this step, we can fine tune the PEC to minimize the loss from +1 to -1 state. The minimum loss for the reflection mode setup in Figure 97 should be  $\sim 15.6$  dB after the fine tuning.

### II.B.8.b.iii. Alignment for the free space and measure the crosstalk

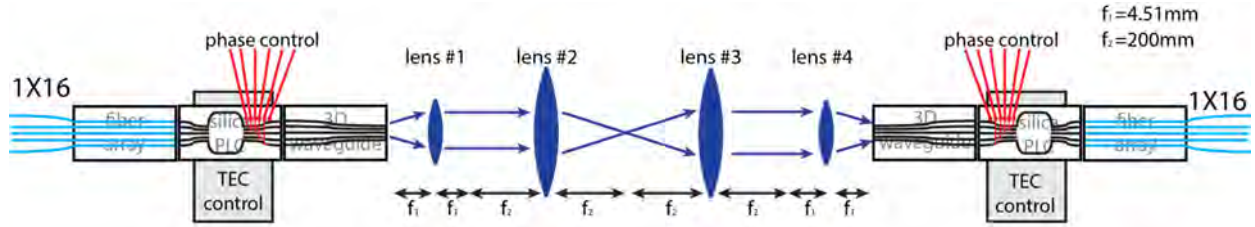


Figure 98. Chip to chip setup.

Figure 98 shows the chip to chip setup. After the retro-reflection setup, we need to put two 200mm focus lens in the middle and align the beam to shoot at each other from both sides. The minimum chip to chip loss should be  $\sim 15.5$  dB for center waveguides.

### II.B.8.c. Crosstalk measurement

With modulated data we measured the forward crosstalk and backward crosstalk. The reason we measured the backward crosstalk is that for OAM state switching experiment (see section II.B.8.d) the OAM states need to go through the mux/demux pair again.

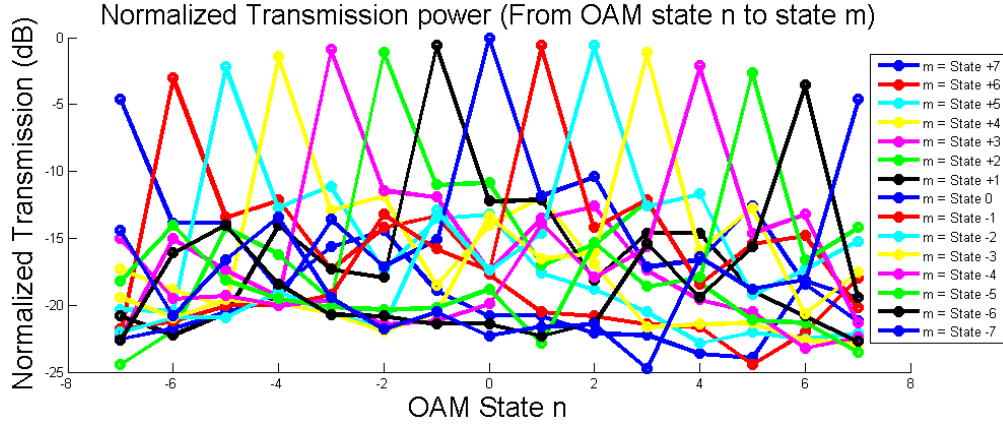


Figure 99. Forward crosstalk.



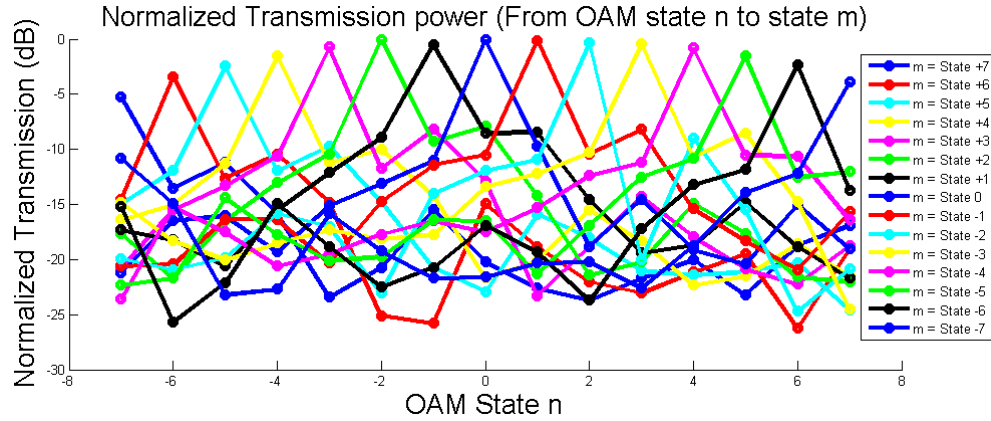


Figure 100. Backward crosstalk.

Figure 99 and Figure 100 show the forward and backward measured normalized transmission. This measurement provides information about the crosstalk between different OAM states. Given this information, we searched all possible combinations of OAM state switching and found the three states switching providing simultaneously the lowest crosstalk:

- $-5 \rightarrow -7$
- $+4 \rightarrow -3$
- $-2 \rightarrow +5$

#### II.B.8.d. Switching experiment setup and BER curve measurement

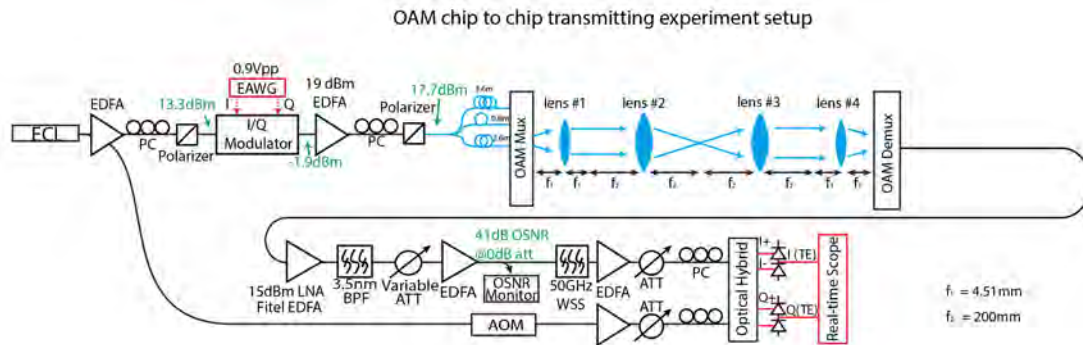


Figure 101. Transmission experiment setup.

Figure 102 shows the BER curves while three states are transmitted from OAM mux to demux. We used 10 GBd QPSK ( $2^{15}$ -1 PRBS). About 770,000 bits are tested to calculate BER for each curve. The "back2back" on the legend refers to the case where the signal goes into the coherent receiver right after the I/Q modulator". The "1channel\_att" refers to the case where an attenuator replaces the OAM chip-to-chip link while everything else remains the same.

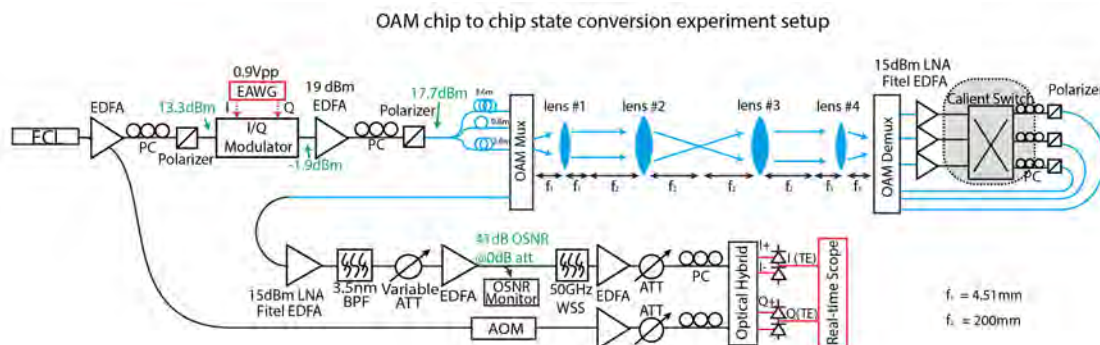


Figure 103. Switching experiment setup.

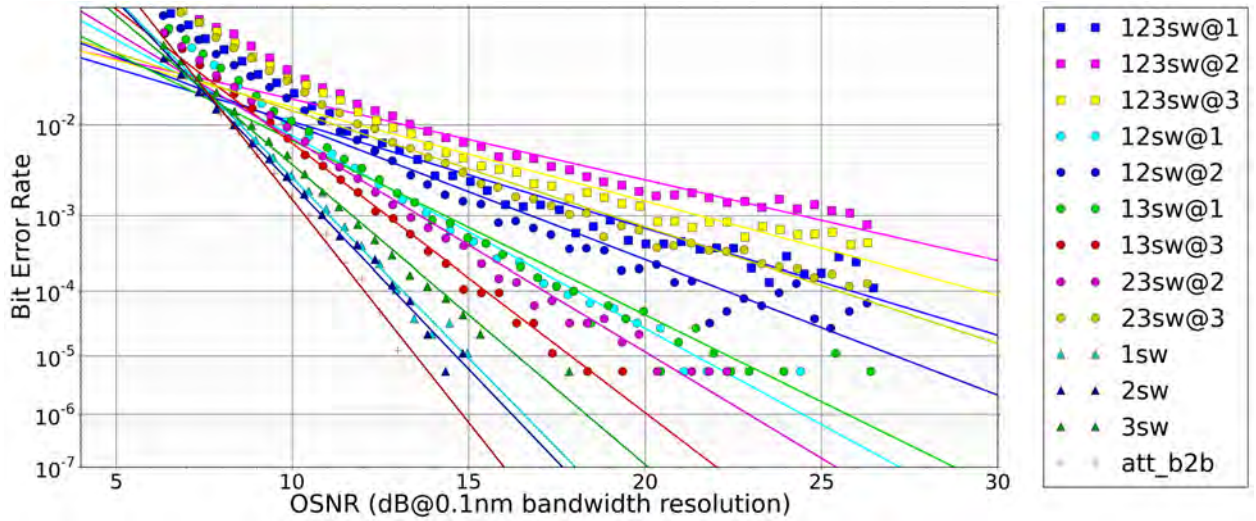


Figure 104. Switching experiment BER curves.

Figure 103 shows the switching experiment setup and Figure 104 shows the BER curves for switching. Same modulation format is used and number of bits tested for BER as in transmitting BER measurement. The crosstalk of transmission and switching are shown in Table 1 and Table 2 respectively. link  $x \rightarrow$  link  $y$  means when link  $x$  is present, what the power at the output of link  $y$  is. The calculated field sum adds two fields that has contribution to the crosstalk and is the worst case where two fields are completely coherent. If we consider the worst case, for transmission, the crosstalk from link 2 and link 3 to link 1 is 12.9 dB; from link 1 and link 3 to link 2 is 11.7 dB; from link 1 and link 2 to link 3 is 7.8 dB. For switching, the crosstalk from link 2 and link 3 to link 1 is 11.3 dB; from link 1 and link 3 to link 2 is 10.1 dB; from link 1 and link 2 to link 3 is 13.9 dB.

Table 1 Transmitting crosstalk values

Link1 $\rightarrow$ link1: -8.3dBm	link2 $\rightarrow$ link1: -28.5dBm	link3 $\rightarrow$ link 1: -26.2dBm	link 2 and 3 $\rightarrow$ link 1: -24.3dBm	Calc field sum: -21.2dBm
Link2 $\rightarrow$ link 2: -7.8dBm	Link1 $\rightarrow$ link2: -24.7dBm	Link3 $\rightarrow$ link2: -26.6dBm	Link 1 and 3 $\rightarrow$ link2: -22.6dBm	Calc field sum: -19.5dBm
Link3 $\rightarrow$ link3: -8.3dBm	Link1 $\rightarrow$ link3: -20.1dBm	Link2 $\rightarrow$ link3: -24.9dBm	Link1 and 2 $\rightarrow$ link3: -19.3dBm	Calc field sum: -16.1dBm

Table 2 Switching crosstalk values

Link1 $\rightarrow$ link1: -8.8dBm	link2 $\rightarrow$ link1: -24.8dBm	link3 $\rightarrow$ link 1: -27.8dBm	link 2 and 3 $\rightarrow$ link 1: -23.3dBm	Calc field sum: -20.1dBm
Link2 $\rightarrow$ link 2: -7.6dBm	Link1 $\rightarrow$ link2: -23.3dBm	Link3 $\rightarrow$ link2: -24.2dBm	Link 1 and 3 $\rightarrow$ link2: -20.9dBm	Calc field sum: -17.7dBm
Link3 $\rightarrow$ link3: -7.6dBm	Link1 $\rightarrow$ link3: -28.6dBm	Link2 $\rightarrow$ link3: -26.7dBm	Link1 and 2 $\rightarrow$ link3: -24.3dBm	Calc field sum: -21.5dBm

In summary, we have demonstrated three OAM states switching. All three states showed BER  $<10^{-3}$  at high OSNR value ( $>26\text{dB}$ ).

### II.B.9. OAM based High speed and high spectral efficiency WDM based DP-QPSK transmission experiment

In this experiment, we demonstrate a polarization diversified free-space OAM link with simultaneously three OAM states and 14 wavelength channels using two OAM hybrid devices as a OAM mux/demux pair. Each wavelength channel has 10-GBd, dual-polarization quadrature phase shift keying (DP-QPSK) data for an aggregate capacity of 1.68 Tb/s and spectral efficiency of 9.6 bits/s/Hz.

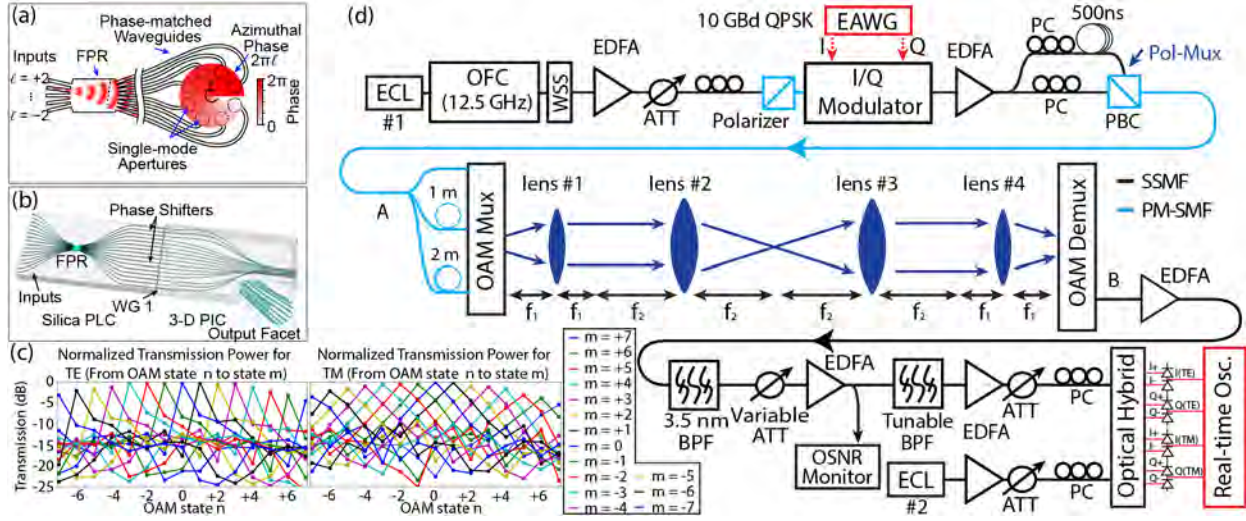


Figure 105 (a) Concept of the OAM photonic integrated circuit. (b) Conceptual view of the 2D-3D hybrid integrated device for OAM mux/demux. (c) Normalized transmission of the OAM mux/demux pair. (d) Experimental arrangement of the multichannel OAM polarization-diversified free-space communication link testbed. FPR: free-propagation region; ECL: external cavity laser; OFC: optical frequency comb; WSS: wavelength-selective switch; EDFA: erbium-doped fiber amplifier; ATT: attenuator; PC: polarization controller; PBC: polarization beam combiner; BPF: bandpass filter. EAWG: electrical arbitrary waveform generator.

Figure 105 (a) shows a conceptual diagram of a photonic integrated circuit (PIC) for OAM state multiplexing/demultiplexing. The free-propagation region (FPR) applies a linear phase tilt on the input light. The phase-matched waveguides sample the output of the FPR and transform the linear phase tilt to azimuthal phase variations at the output apertures. Illuminating multiple inputs simultaneously generates OAM states that spatially overlap at the output apertures, providing true OAM state multiplexing. Alternatively, when operated in reverse, the circular-patterned apertures sample and demultiplex spatially overlapped OAM states. Figure 105 (b) shows a drawing of the 2D-3D hybrid integrated device where the 2D silica PLC is mated with a 3D waveguide circuit fabricated by direct laser inscribing in borosilicate glass. Figure 105 (c) shows the normalized transmission from OAM mux input (A) to OAM demux output (B) for both polarizations. The total loss for OAM state 0 is 19.4 dB (device TE) and 19.3 dB (device TM). Figure 105 (d) shows the experimental arrangement where a 10-GBd QPSK signal ( $2^{15}$ -1 PRBS) is applied to all 14 WDM channels (12.5-GHz spacing). The modulated signal is polarization multiplexed with decorrelation of 500-ns between the two polarization states. After multiplexing up to three OAM states through the first hybrid device, the spatially overlapped beams are transmitted over a 81.8 cm free space link, demultiplexed by the second hybrid device and sent to the polarization diversified coherent receiver with offline DSP. The DSP uses an adaptive equalizer, which includes a 17-



tap finite impulse response (FIR) filter and power-of-four methods for phase and frequency recovery and direct-decision based bit-error counting.

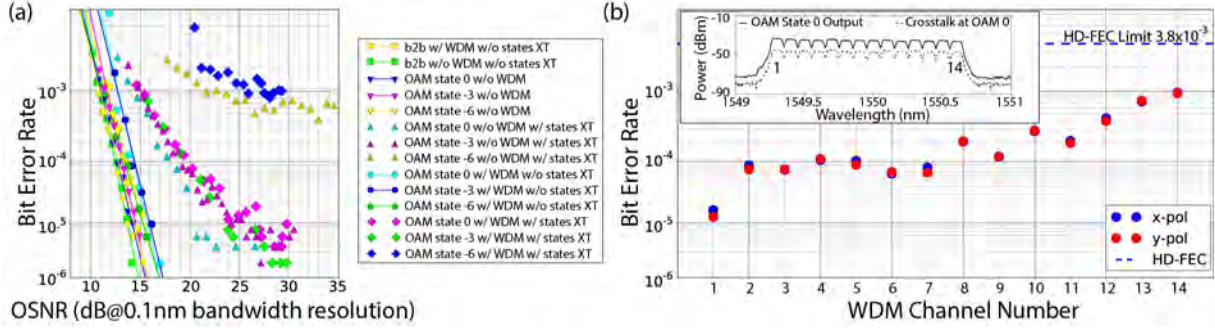


Figure 106. (a) BER performance for the multichannel OAM link with  $14 \times 10$ -GBd, DP-QPSK WDM channels. (b) Averaged BER for three OAM states (0, -3 and -6) for two received orthogonal polarizations (x-pol and y-pol not necessarily the same as device TE and TM).

The averaged bit-error-rate (BER) of two polarization states for a multichannel free space transmission link was measured. We use OAM states -6, -3 and 0 for the transmission link experiment. The measured crosstalk values at all three OAM states outputs are between -10.5 dB and -11.6 dB for TE, between -10.2 dB and -14.1 dB for TM. Figure 106 (a) shows the measured BER for the following cases: i) back to back transmission without WDM or OAM states crosstalk (XT); ii) back to back transmission with all the wavelength channels; iii) single OAM state and single wavelength channel transmission without crosstalk from other OAM states; iv) all three OAM states transmission with single wavelength channel; v) single OAM state with all the wavelength channels but without crosstalk from other OAM state; vi) all three OAM states transmission with all the wavelength channels. There is ~3dB OSNR penalty for OAM state 0 and -3 transmission with OAM states crosstalk. However, the OSNR penalty for OAM state -6 is much higher due to a joint effect of crosstalk and polarization dependent loss (PDL). In the future, the better phase error correction can further reduce the crosstalk. PDL is mainly from the misalignment in the device setup. Figure 106 (b) shows that the measured averaged BER values with all three OAM states at all wavelength channels are below HD-FEC limit of  $3.8 \times 10^{-3}$  (BCH(1020,988) super FEC code, 7% overhead).

In summary, we have demonstrated a multichannel OAM free-space coherent communication link using two separate photonic hybrid devices with polarization diversity. We transmitted  $14 \times 10$  GBd DP-QPSK signals simultaneously on three OAM states that shows the averaged BER of both polarization states for all three OAM states at all wavelength channels are below HD-FEC limit. Future work includes device packaging to improve device stability and device design changes to reduce crosstalk for additional OAM state multiplexing.

## II.B.10. Multi-ring hybrid 2D-3D OAM devices using multilayer silicon nitride PLCs and 3D waveguide blocks

For ultimate ‘Information in a photon’ with extremely high spectral efficiency, we would ideally like to generate arbitrary spatial waveforms of many orthogonal states spanning a high Fresnel number. Figure 107 shows targeted optical mode generations using multi-ring OAM MUX/DEMUXes: (a) Laguerre-Gaussian/Ince-Gaussian/Hermite Gaussian modes (b) Linear Polarization modes. LP modes may be particularly useful for step index cylindrically symmetric fiber transmissions.

### II.B.10.a. 3D Waveguide Device Design

Towards this goal, we have further developed our in-house automatic 3D waveguide routing program for multi-ring 3D waveguides. Figure 108 shows an *optical-path-length-matched* multi-ring 3D



waveguide design using the automatic 3D waveguide routing program. The multi-ring 3D waveguide is composed of 64 input waveguides and two circular output patterns, each with 32 waveguides.

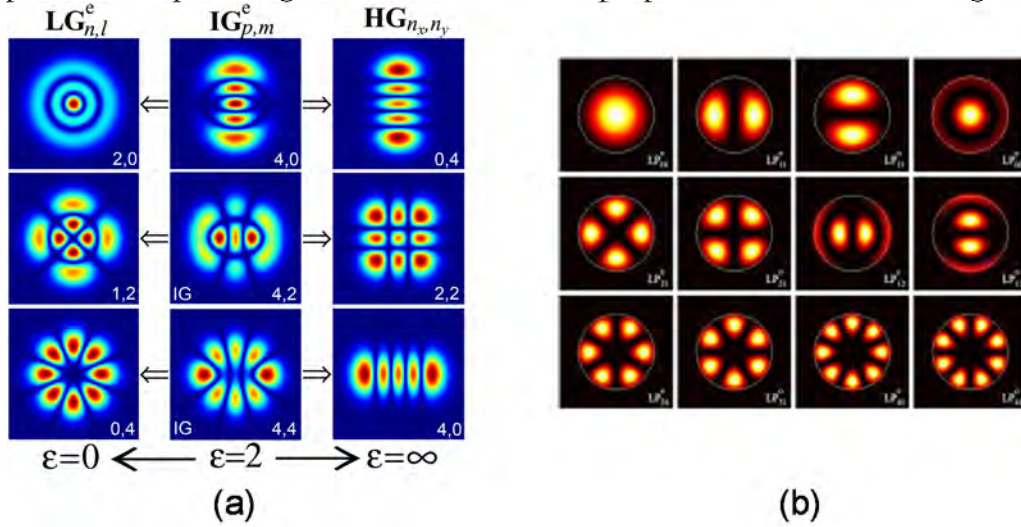


Figure 107. Targeted optical mode generations using multi-ring OAM MUX/DEMUXes. (a) Laguerre-Gaussian/Ince-Gaussian/Hermite Gaussian modes (figure courtesy of kb-en.radiantzemax.com). (b) Linear Polarization modes (figure courtesy of SPIE.org).

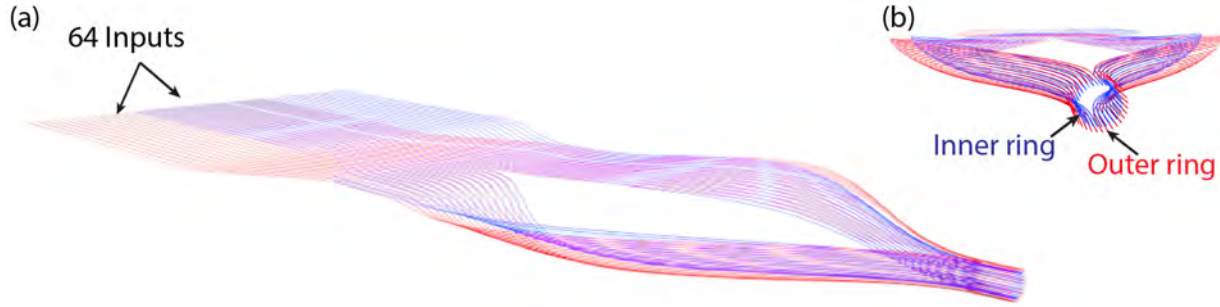


Figure 108. (a) Auto-routing and optical-path-length-matched multi-ring 3D waveguide design. (b) Output facet view.

In order to fabricate broadband 3D waveguides, we need to design *path-length-matched* waveguides in three-dimensions to reduce the accumulation of phase errors at different wavelengths among different optical paths. Figure 109 shows the flow chart for designing path-length-matched 3D waveguides. To start with, we need to know the input and output pattern in the Cartesian coordinate system. In our waveguide design algorithm, we normally use three types of waveguides: straight waveguides, cosine-curve bending waveguides and B-spline bending waveguides. B-spline bending waveguides have been mainly used for path-length matching because of their control point flexibility. We build up to  $N$  waveguides with a B-spline bending waveguide model. The starting point of each waveguide is one of the input patterns; the ending point is one of the output patterns. We use only one control knot (i.e., places where the pieces meet) in order to keep the design algorithm simple. To start with, we provide a set of parameters to initialize all of the waveguides. Second, we use a nonlinear optimizer to find out the optimum solution that can minimize the differences between desired waveguide length and each designed waveguide. The nonlinear optimizer will move the control knots (only in  $x$ -direction) to find out a global optimum solution. If the optimizer converges in the end, we can successfully design path-length matched waveguides. In our design algorithm, the path-length difference tolerance is set to be  $10^{-8}$   $\mu\text{m}$ , which is

much smaller than the fabrication error (0.1  $\mu\text{m}$  level). The nonlinear optimizer can also handle constraints such as minimum bending requirements, no crossings between waveguides, etc. Besides the nonlinear optimizer, we also built verification tools such as waveguide crossing check software. All of the designed tools are written at UC Davis, and based on open-source software.

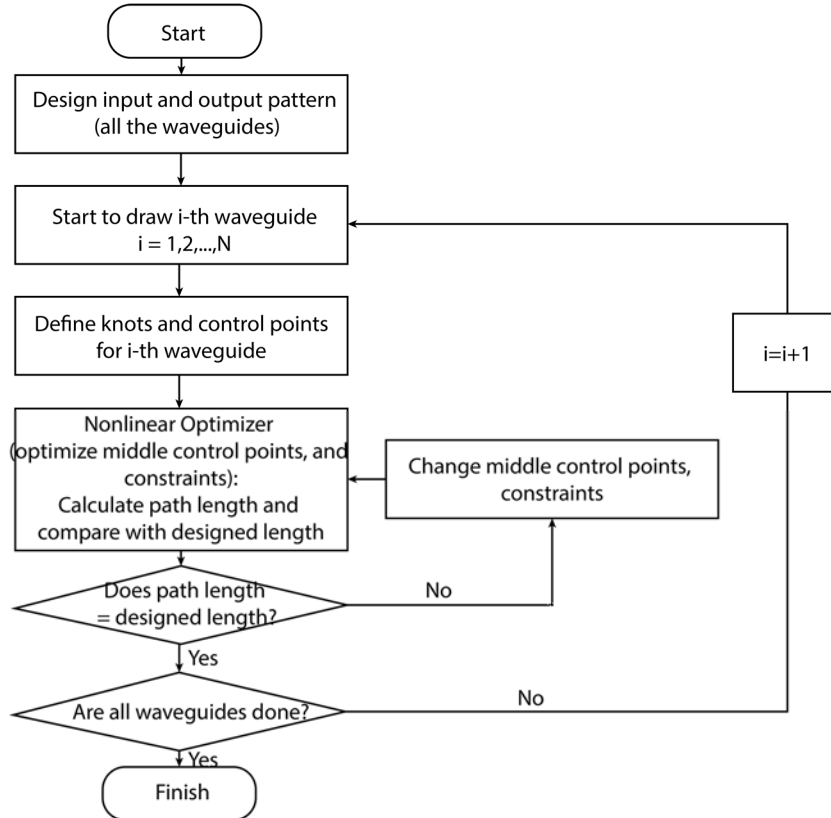


Figure 109. Path-length matched 3D waveguide design flow chart.

### II.B.10.b. 3D Waveguide Fabrication at UC Davis

Although our early 3D waveguide designs were fabricated by a commercial foundry (i.e., Optoscribe), we have recently built our own direct laser inscribing (DLI) facility at UC Davis for a project supported by the ONR. DLI 3D waveguide fabrication uses a femtosecond laser to make material modifications in transparent dielectric materials. Femtosecond laser writing on borosilicate glass or other transparent materials has attracted great interest in applications such as space division multiplexing, beam steering, etc. The technique does not require masks for waveguide fabrication, and also gives one more degree of freedom via the third dimension. As Figure 110 shows, the 300-fs pulses at 1037 nm are focused into a dielectric material with an objective lens. The high peak power of each pulse induces nonlinear absorption phenomena (e.g., multiphoton and avalanche ionizations). The nonlinear process causes a permanent refractive index modification (increase) due to the plasma effect and energy absorption. We use this technique to fabricate smooth refractive index profiles, by translating the substrate relative to the laser beam. There are usually two regimes for refractive index modification: low-repetition rate regime and high-repetition rate regime [2]. In the low-repetition rate regime, the time interval between pulses is large enough so that the thermal diffusion can transfer the heat from the beam focus to the surrounding material. Therefore, each pulse is acting relatively independently to modify the material. As a result, the written waveguide forms an index modification shape that is asymmetric. The asymmetry causes high coupling losses between the 3D waveguide mode and the standard single mode

fiber which is symmetrical [3]. On the other hand, the high-repetition rate regime shows heat accumulation inside the focal volume. Therefore, it is possible to fabricate cylindrically symmetric waveguides with low propagation loss and coupling loss [3].

We have successfully fabricated single mode waveguides at a 0.5 MHz and 1.5 MHz repetition rates, with 10-40 mm/s stage transition velocity and 135-325 mW average power. Figure 111 shows the mode profile of the fabricated waveguide with single-scan laser writing during our earliest work. The circularly polarized light is used to reduce the waveguide shape dependence on the stage's translation direction. In addition, the laser beam is focused  $\sim 200\text{ }\mu\text{m}$  underneath the device top surface, after an aspheric lens with 0.55 numerical aperture. The single scan written waveguide mode field diameter (MFD,  $1/e^2$ ) is measured as  $20.04\text{ }\mu\text{m}$  in  $x$  cross section and  $16.18\text{ }\mu\text{m}$  in  $y$  cross section. The large mode diameter is due to the small refractive index modification in the material. This has since been improved as discussed below.

To have a better control of the waveguide shape, we used a multi-scan laser writing technique to achieve a smaller mode diameter waveguide and provide for beam shape engineering. The multiscan technique is beneficial because it partially decouples the width of the waveguide from writing parameters such as repetition rate, pulse energy, and focused spot size. By scanning the sample through the laser focus multiple times in an overlapping fashion, the desired waveguide width is fabricated. In our latest work, we used a  $30\times$  objective lens ( $\text{NA} = 0.45$ ) and focused the circularly polarized light to a  $0.9\text{-}\mu\text{m}$  estimated spot size (radius) in Corning Eagle2000 glass. We worked in the heat accumulation regime with 135-180mW of laser power, 10 mm/s stage translation velocity, 11-13 times multi-scanning, and a repetition rate of 0.5 MHz. Figure 112(a) shows the results of the multi-scan laser writing for small MFD waveguides. Figure 112(b) shows that the fabricated waveguides can have a good mode match with standard single mode cleaved fiber (MFD =  $10.5\text{ }\mu\text{m}$ ). The smaller MFD shows that we have achieved higher index contrast (e.g., 0.6-0.7%), which is necessary for reducing the bending radius and waveguide separation.

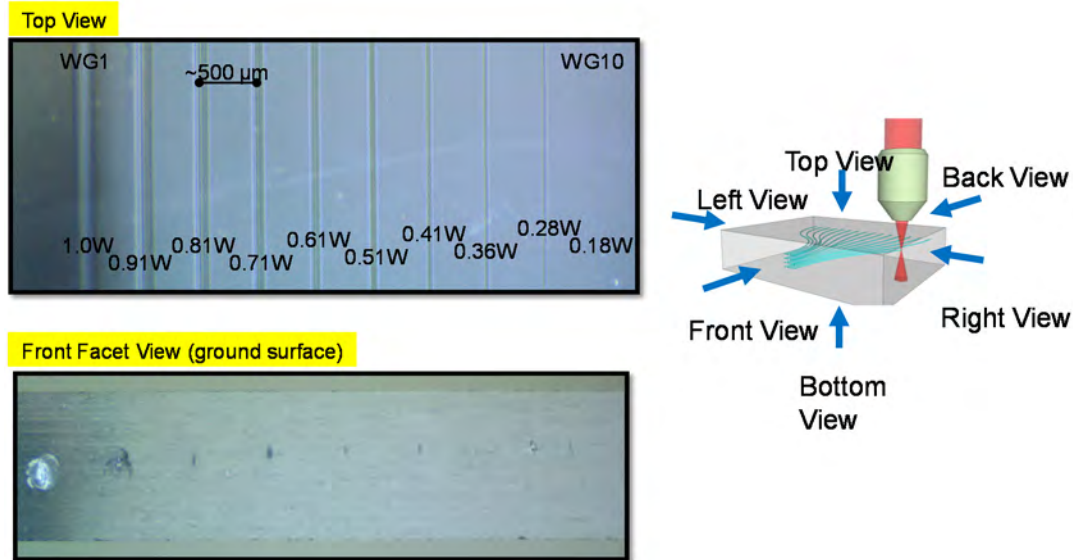


Figure 110. Optimization of 3D waveguide inscription technology by adjusting the femtosecond laser power and repetition rates.

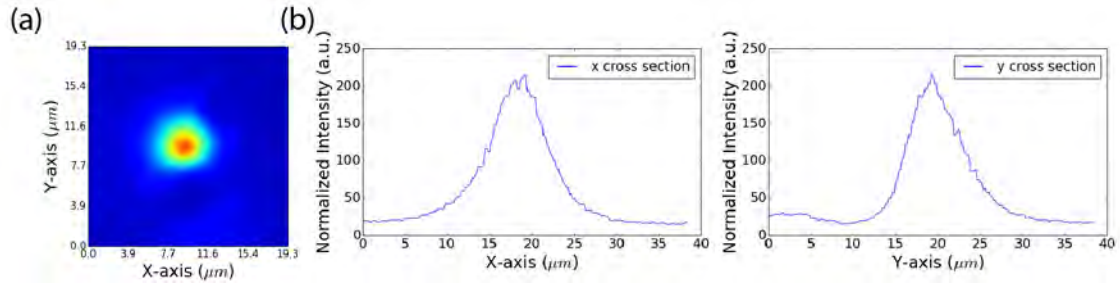


Figure 111. (a) Mode profile for a single scan waveguide. (b) x and y cross section for the mode profile.

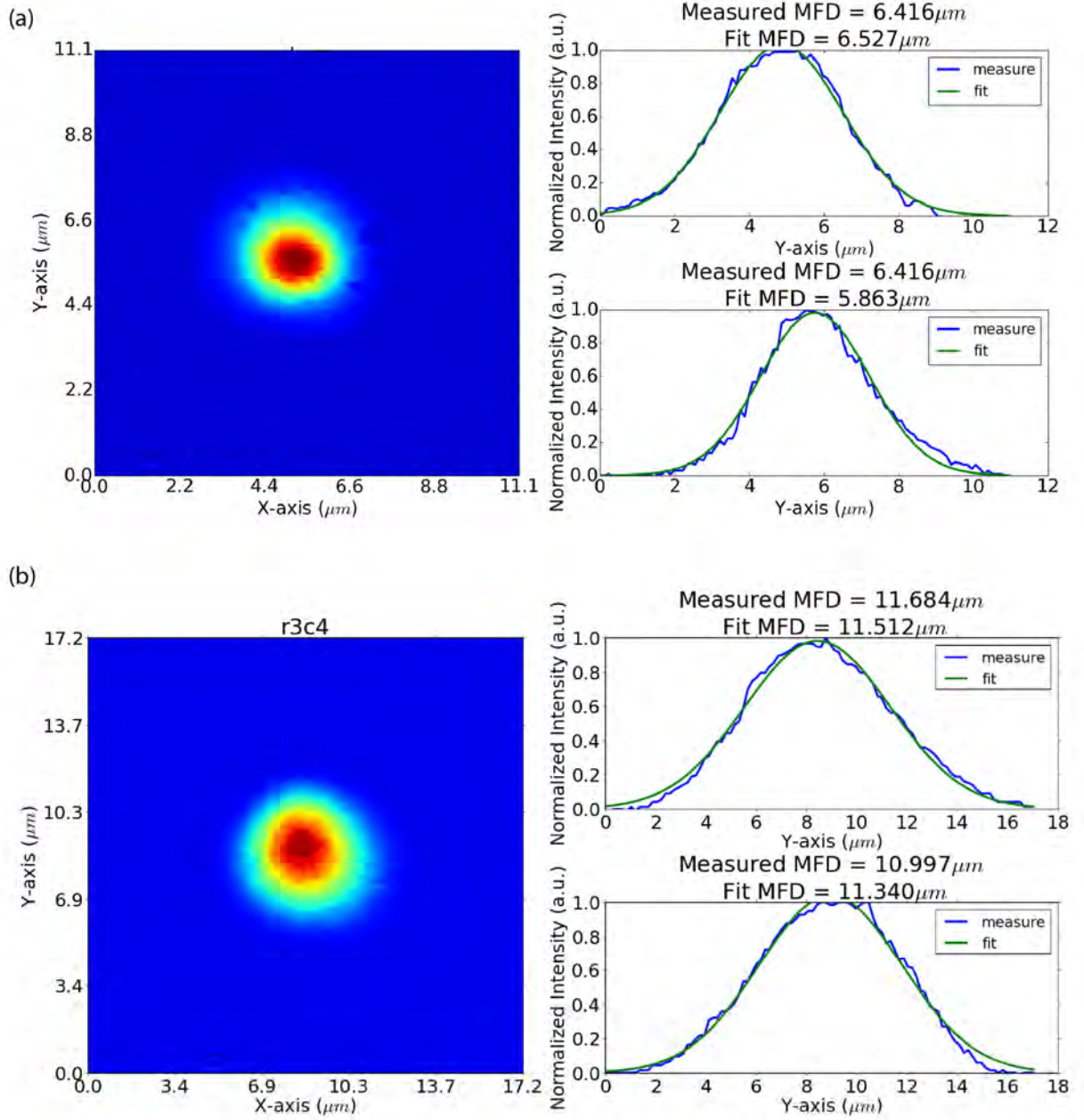


Figure 112. (a) Mode profile for small MFD waveguide (6.5  $\mu\text{m} \times 5.8 \mu\text{m}$ ). (b) Large MFD waveguide (11.5  $\mu\text{m} \times 11.34 \mu\text{m}$ ).



### II.B.10.c. Multilayer silicon nitride 2D PLC for multi-ring OAM

Recently, we have fabricated *two-layer*  $\text{Si}_3\text{N}_4$  2D PLCs to generating the linear phase tilt in the multi-ring hybrid 2D-3D OAM devices. We have also fabricated the 64 path-length matched 3D waveguides as described earlier for a multi-ring OAM device demonstration. We start with the description of the two-layer  $\text{Si}_3\text{N}_4$  device. Figure 113(a) shows the mask layout of the  $\text{Si}_3\text{N}_4$  device capable of 27 distinct OAM state with both azimuthal and radial indices. The device includes a lower layer and an upper layer with interlayer coupling capability. There are 27 inputs (i.e., for generating different OAM states) and 9 star couplers ( $5 \times 4$ ) on the input side (left). The two input waveguides of each star coupler maintains  $\pi$  phase shift, and they are sent to two different star couplers ( $11 \times 34$ ) for creating the appropriate linear tilted phase for each ring. As with the earlier hybrid 2D-3D OAM devices, we can butt-couple the 2D PLC to the 3D waveguides that geometrically convert the linear phase to azimuthal phase. Since each star coupler is on a different layer of the  $\text{Si}_3\text{N}_4$ , it can generate OAM states for both inner and outer rings of the 3D waveguide block. In addition, the  $\pi$  phase difference between two star couplers output waveguides are also maintained through the whole propagation. As a result, the inner and outer ring shows a constant  $\pi$  phase shift. We generate radial OAM mode based on this routine. Figure 113(b) shows the fabricated  $\text{Si}_3\text{N}_4$  device picture. Currently, we are working on characterizing the performance of the 2D  $\text{Si}_3\text{N}_4$  device.

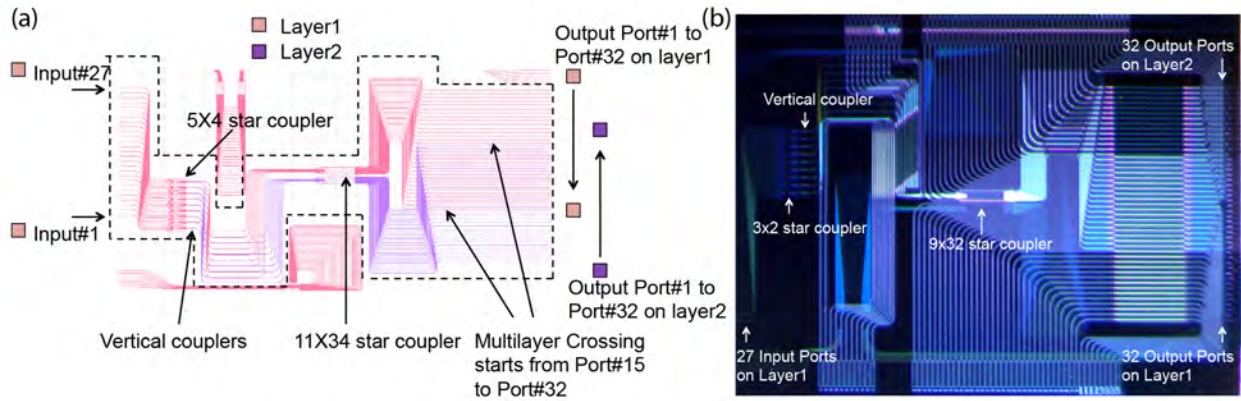


Figure 113. (a)  $\text{Si}_3\text{N}_4$  device mask layout. (b) Photo of fabricated azimuthal and radial index  $\text{Si}_3\text{N}_4$  OAM device.

### II.B.10.d. Multi-ring 3D Waveguide Block for Multi-ring OAM

Next, we fabricated the 64 path-length matched 3D waveguides for the multi-ring OAM device. Figure 114 shows photos the fabricated device's input and output facets. To match the 2D  $\text{Si}_3\text{N}_4$  device output, there are two-layers of input waveguides. Each layer is composed of 32 waveguides, and the height difference between the two layers is 400 nm. The waveguide pitch is 100  $\mu\text{m}$  within one layer. Since the two layers are interleaved, the horizontal waveguide to waveguide spacing is 50  $\mu\text{m}$  in the center section where the waveguides from the two layers overlap. Figure 114(a) shows the input facet view with two layers, and (b) shows the waveguides in detail. Figure 114(c) shows the output facet view for the multi-ring OAM circular pattern. In order to avoid coupling between waveguides, we choose 204  $\mu\text{m}$  (20- $\mu\text{m}$  waveguide to waveguide spacing) for inner ring diameter, and 255  $\mu\text{m}$  (25- $\mu\text{m}$  waveguide to waveguide spacing) for outer ring diameter. Based on our test structures, the coupling (crosstalk) between two waveguides with 20- $\mu\text{m}$  separation can be as low as -25 dB. Currently we are characterizing the device and then we will demonstrate multi-ring OAM multiplexing.



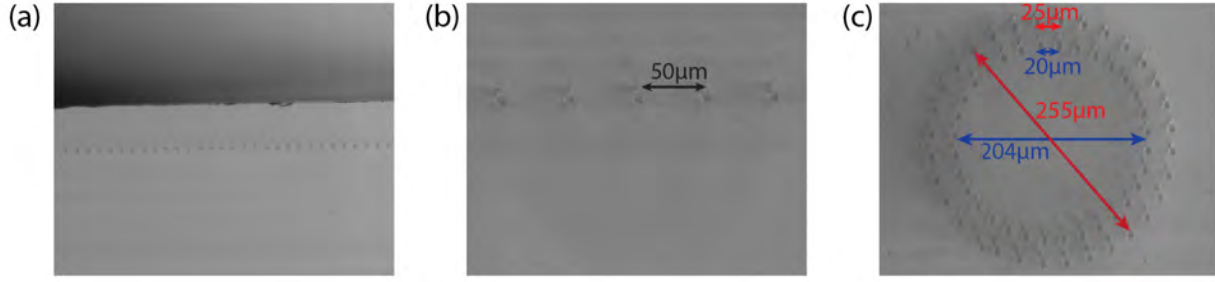


Figure 114. Fabricated 3D waveguide multi-ring OAM device. (a) Input facet view showing some of the 64 input waveguide array. (b) Close-up showing input waveguide separation in the center section where the upper and lower layers overlap. (c) Output facet view showing the two concentric output circular patterns (32 waveguides in each ring).

We continue to characterize the fabricated devices and we will demonstrate multi-ring OAM using the integrated devices.

### II.B.11. Multilayer Silicon Nitride Orbital Angular Momentum Devices

Towards the same goal of achieving arbitrary beam forming indicated in the previous section, we also develop multilayer silicon nitride OAM devices to generate LP and LG modes.

#### II.B.11.a. Multilayer orbital angular momentum (OAM) device fabrication

Fabrication of the multilayer OAM device starts with deposition of 3000-nm-thick silicon dioxide film by low pressure chemical vapor deposition (LPCVD) on silicon wafer. Then stoichiometric silicon nitride film of 500 nm thickness was also deposited by low pressure chemical vapor deposition (LPCVD) on the silicon dioxide. We first patterned ASML PM marks on the first silicon nitride layer because other layers have to be aligned with first layer. Then the grating and waveguide layers are patterned by desired depth, respectively. Features are defined using ASML<sup>TM</sup> PAS 5500/300 deep-UV lithography stepper technology and plasma etcher. We designed that the etch depth of the grating and waveguide are 200 nm and 250 nm, respectively.

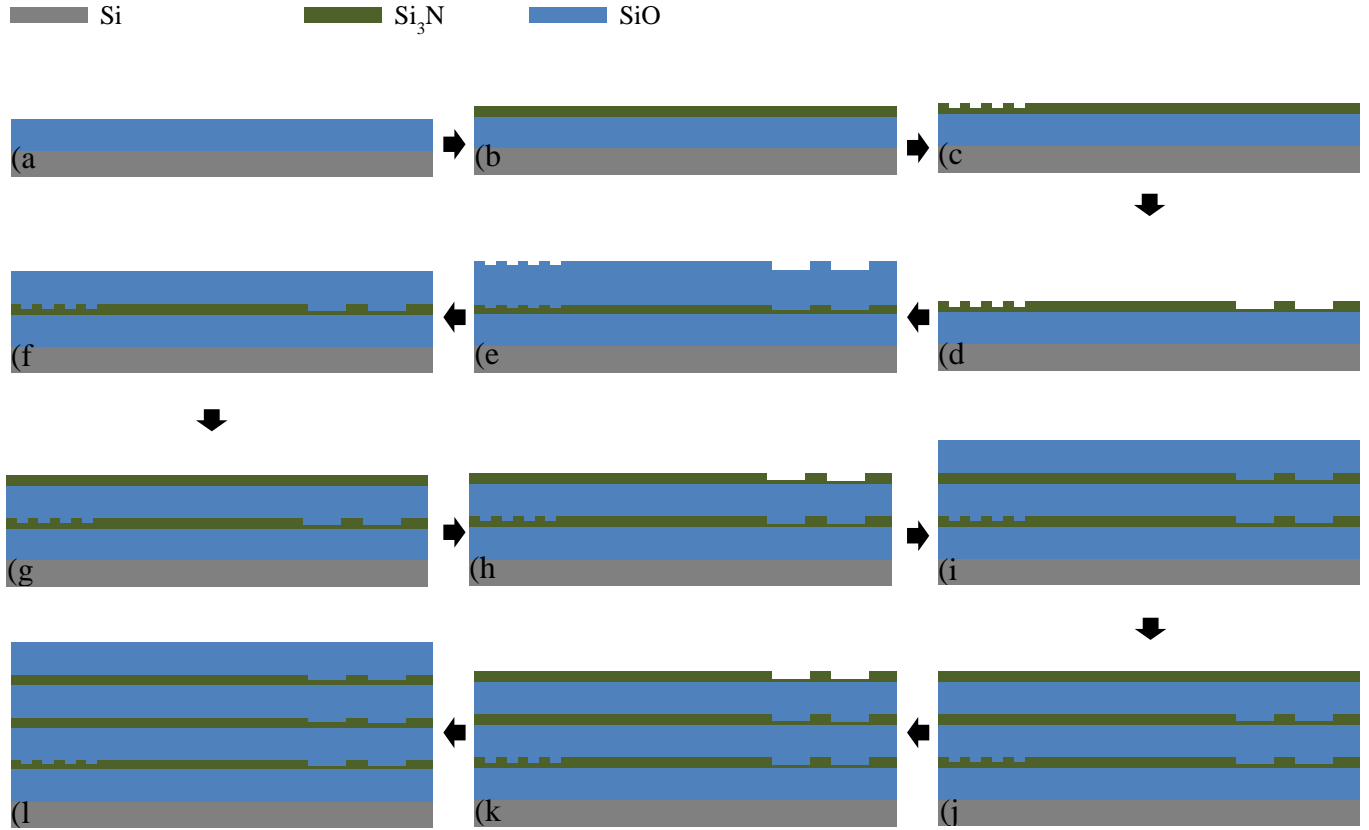


Figure 115. Fabrication process flow: a) silicon dioxide deposition b) first silicon nitride film deposition c) alignment mark patterning (photolithography and etch) d) grating and waveguide patterning of first layer e) silicon dioxide deposition f) chemical mechanical polishing for planarization g) second silicon nitride film deposition h) grating and waveguide patterning of second layer i) silicon dioxide deposition and chemical mechanical polishing for planarization j) third silicon nitride film deposition k) grating and waveguide patterning of third layer l) top silicon dioxide deposition. Each color describes the materials.

The period of the grating structure was optimized with the vertical emission angle. The silicon dioxide layer is used to make an intermediate cladding between each silicon nitride film. Once the silicon dioxide layer is deposited, it needs to planarization in order to deposit the planar silicon nitride film on the silicon dioxide cladding. Thus, we employed chemical mechanical planarization (CMP) process. Then we repeated the deposition, patterning, and CMP as shown in Figure 115.

Figure 116 shows scanning electron microscope (SEM) images of the cross section and the side wall of the silicon nitride features including grating and waveguide. We can see the well-defined etch depth (grating of 200 nm thickness and waveguide of 250 nm thickness) and the side. SEM images are obtained by means of LEO 1550 SEM tool.

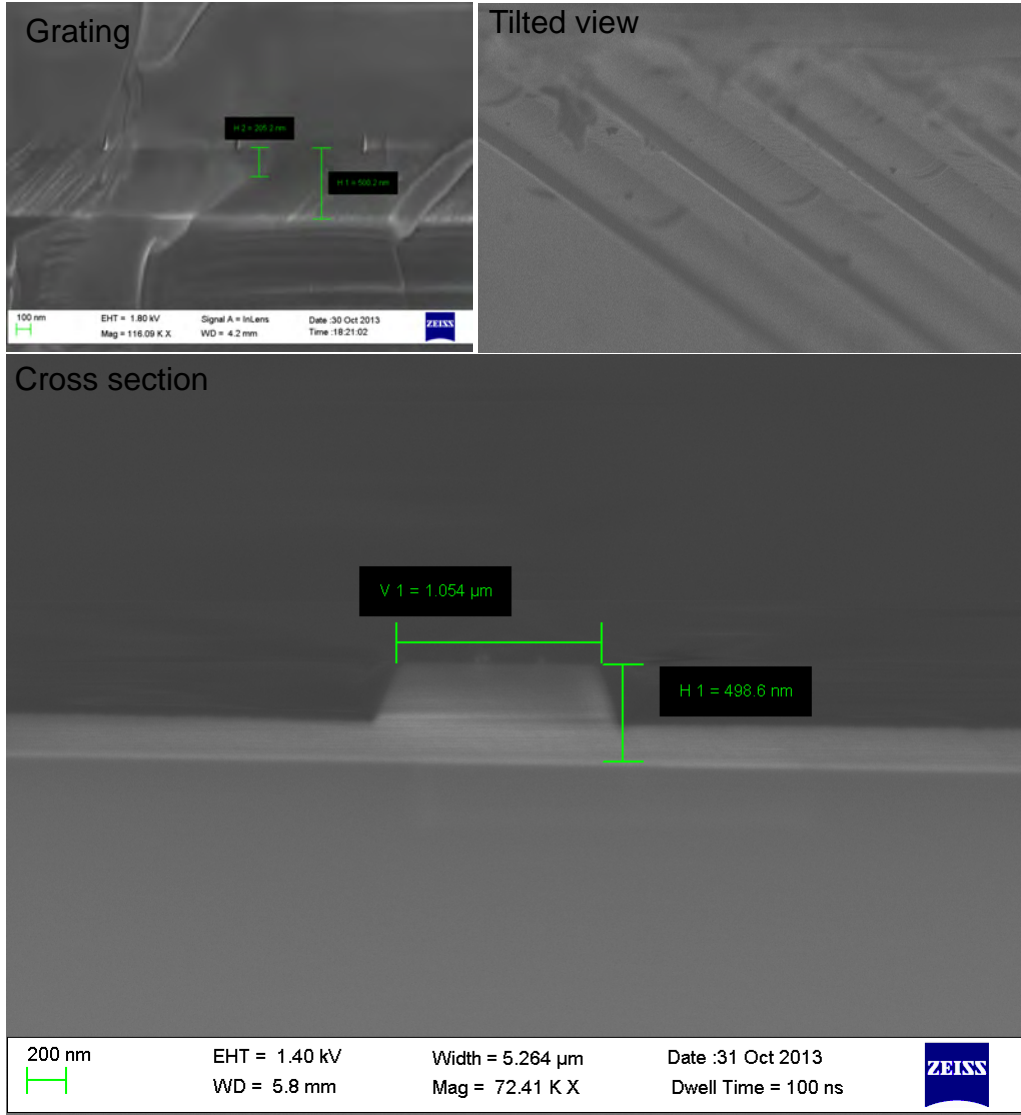


Figure 116. SEM images of grating and waveguide structures. They show the well-defined feature dimension.

Fabricated OAM devices are shown in Figure 117. We designed several grating structures according to grating shape. Centric, centric arcs, and parallel stripes are applied in this OAM devices (see Figure 117 (a) and (c), respectively). The widths of the tapered waveguides region, which link the waveguide and grating, are also designed differently since this is our first attempt to make multilayer devices as shown in Figure 117. Shown in the inset of Figure 117 is mask layout of the each grating. Figure 118 shows a mask layout and fabricated wafer.

Figure 119 shows stacking of multiple 2D layers for arbitrary waveform shaping, (a) stacked device consisting of Layer 1-5, and (b) fabricated three layer silicon nitride/silicon dioxide OAM device. Also shown are the images of the three layer silicon nitride/silicon dioxide OAM device when the (c) bottom (layer 1), (d) middle (layer 2), and (e) top (layer 3) are illuminated. When multiple layers are coherently excited, this device can create mode profile that can excite eigen modes of the multimode fibers.

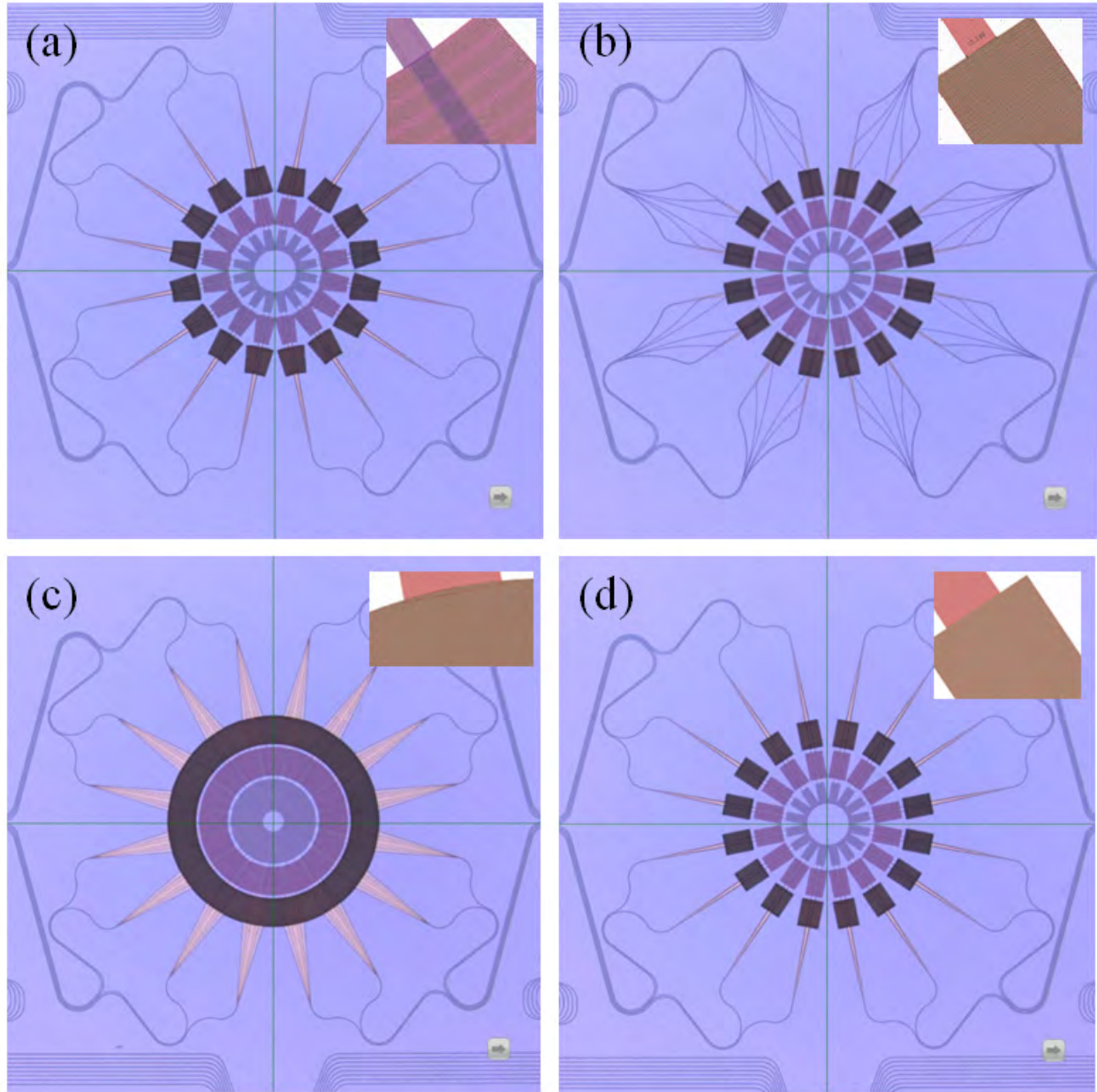


Figure 117. Microscope images of fabricated silicon nitride OAM devices. Gratings with different shape and various width of the tapered waveguide between waveguides and gratings are designed: a) centric arc b) parallel with narrow tapered waveguide c) centric ring gratings d) parallel with broad tapered waveguide. Mask layouts of gratings are shown in the inset.

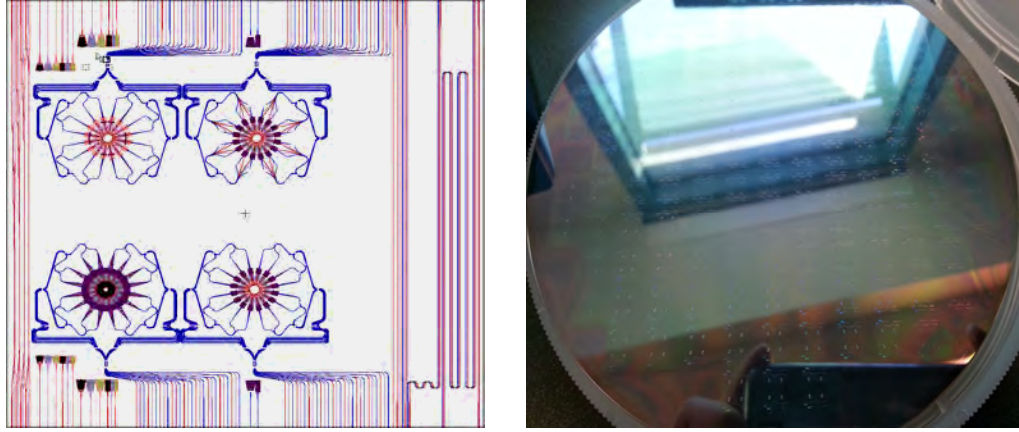


Figure 118. Mask layout (left) and fabricated wafer with silicon nitride devices (right).

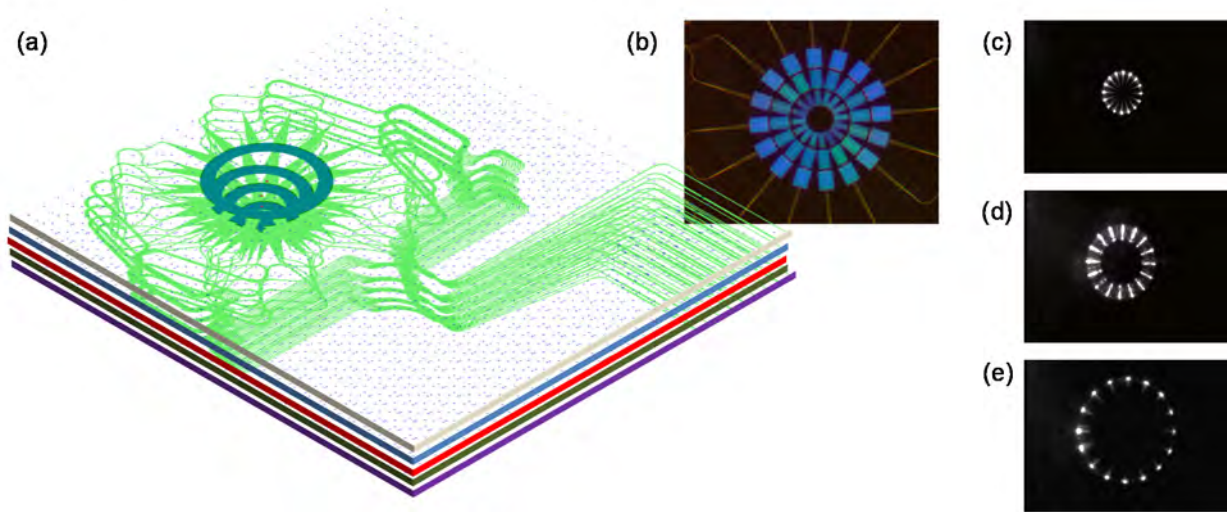


Figure 119. Stacking of multiple 2D layers for arbitrary waveform shaping. (a) Stacked device consisting of Layer 1-5. (b) Fabricated three layer silicon nitride/silicon dioxide OAM device. Image of the three layer silicon nitride/silicon dioxide OAM device when the (c) bottom (layer 1), (d) middle (layer 2), and (e) top (layer 3) are illuminated.

#### II.B.11.a.i. *Chemical mechanical polishing (CMP) for low loss multi-layer OAM devices*

Chemical mechanical polishing (CMP) processes are used to achieve flat silicon dioxide surface after cladding deposition. So we need to confirm for each surface in order to make sure the planar surface. Figure 120 shows CMP results. If we measure the height of the deposited silicon dioxide surface on top of silicon nitride waveguide, the surface has the same surface profile with silicon nitride waveguide as you can see Figure 120(b). However, if CMP is carried out, the surface has the flat profile as shown in Figure 120(c). We found the optimized minimum CMP time in order to avoid non-uniformity. The surface profile of the planarized silicon dioxide surface is plotted within  $\pm 13$  nm. We used the Strausbaugh CMP tool and Cabot D-7000 slurry. To obtain the surface profile, the Alpha-step IQ surface profiler is used.



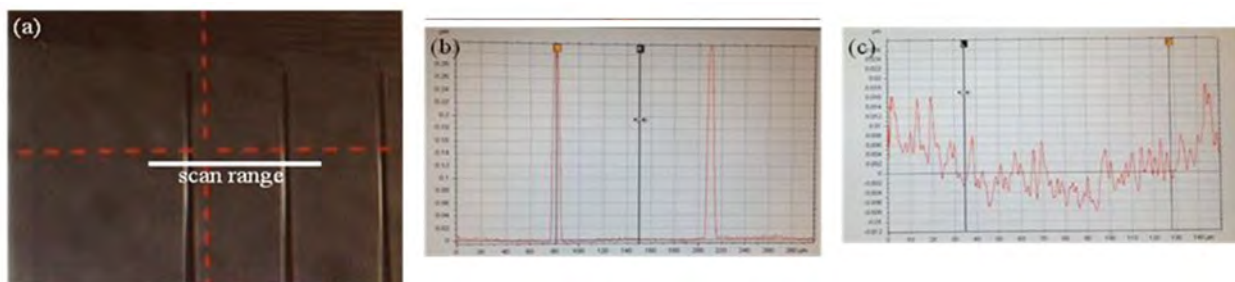


Figure 120. CMP results: a) scanned waveguide region b) surface profile before CMP c) surface profile after CMP.

### II.B.12. Multilayer Silicon Nitride Orbital Angular Momentum Device Fabrication

Towards the goal of achieving arbitrary beam forming indicated in the previous section, we further developed a multilayer silicon nitride waveguide process to generate improved OAM patterns. In particular, such devices can generate multiple concentric OAM patterns, each with a different OAM charge.

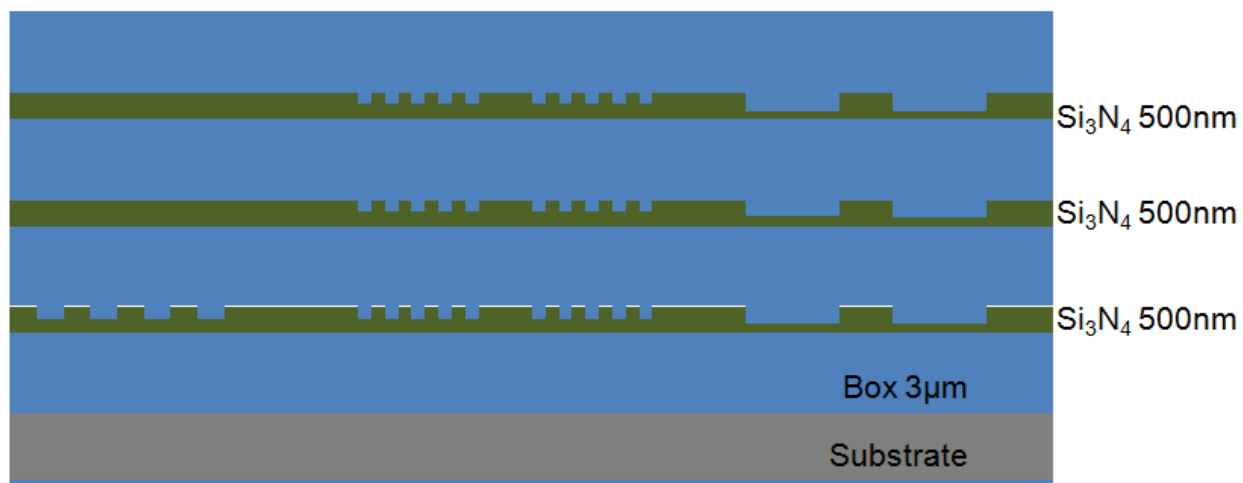


Figure 121. Integrated Multilayer silicon nitride OAM PLC cross section

Figure 121 shows the cross section of the multilayer OAM device. In this case, there are three silicon nitride layers, each 500 nm thick. We etched each silicon nitride layer to waveguides and vertical emitting gratings. In between the silicon nitride layers, there are 1  $\mu\text{m}$  thick silicon dioxide layers to form the cladding of the waveguides.

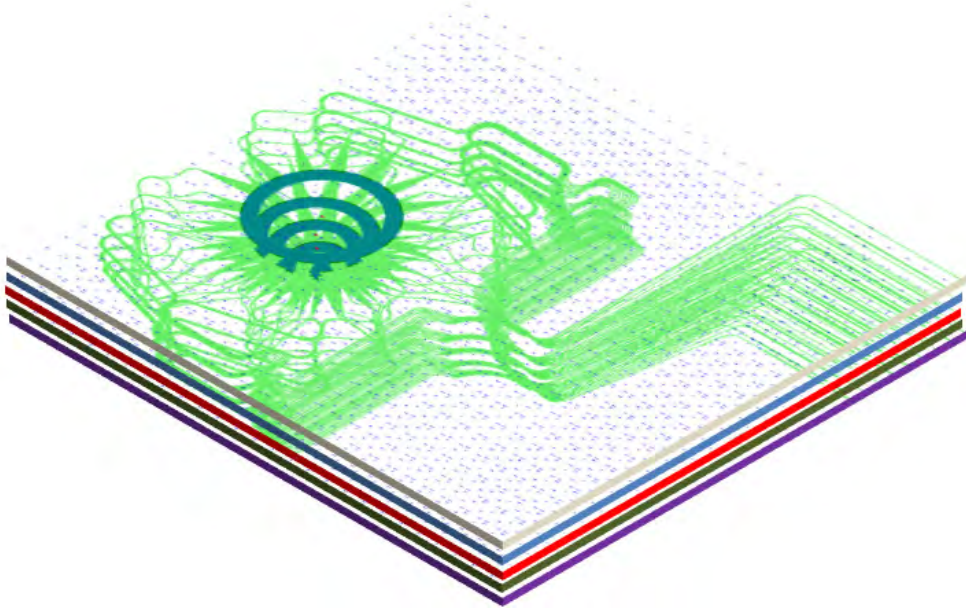


Figure 122. Schematic picture of the multilayer device

Figure 122 shows the schematic picture of a 5-layer device. Each layer generates an OAM beam with different size. The lowest layer generates the smallest OAM pattern, while the top layer generates largest OAM pattern.

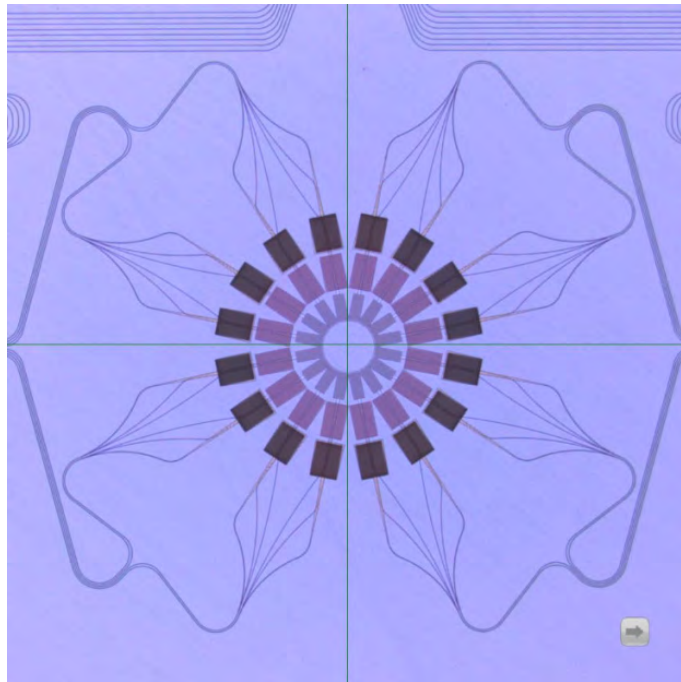


Figure 123 Top view of the fabricated device

The star coupler and path length matched waveguide design of the multilayer device is similar to the single layer OAM device. The main difference is in the three grating layer region. Figure 123 shows the top view of the fabricated OAM device. There are a total of 48 surface normal emission gratings, and the gratings are formed into three concentric groups. Each group has 16 gratings. The inner 16 gratings are on the lowest silicon nitride waveguide layer, while the outer 16 gratings are on the top silicon nitride waveguide layer. Using multiple waveguide layers makes the device much smaller in size, and avoids any waveguide crossings.

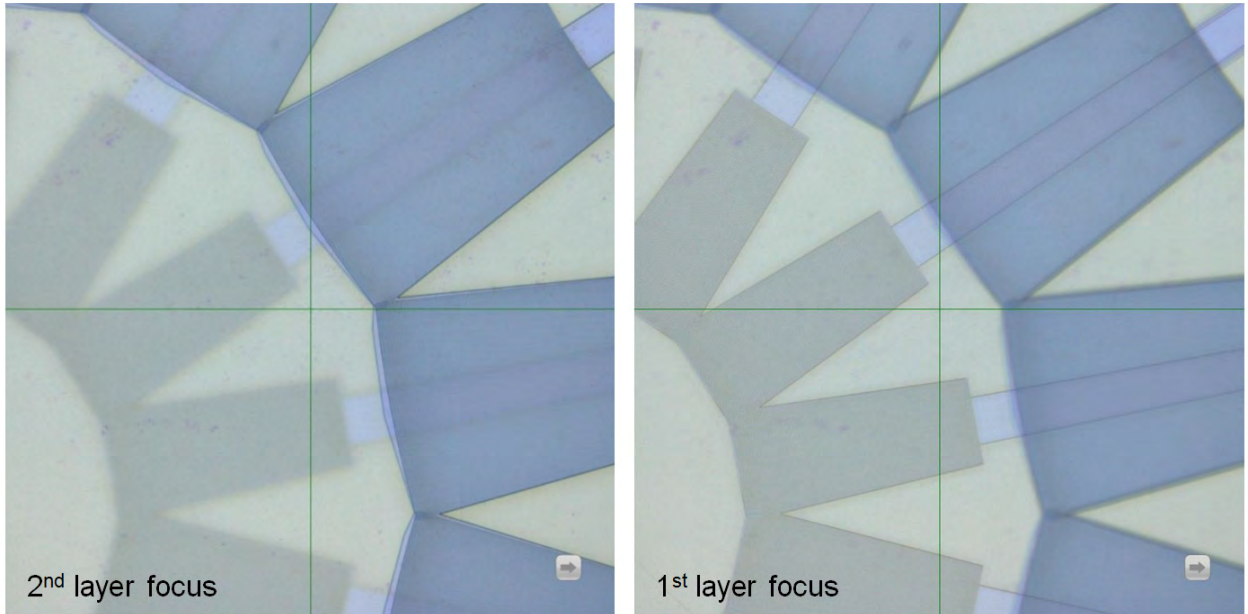


Figure 124. Microscope picture of the grating layers.

Figure 124 shows the close up picture of the grating layer. It is clear that the two grating layers are at different depths due to the change in focus.



Figure 125. Grating emission of a) lowest layer b) middle layer c) top layer

Figure 125 shows the grating emissions from the different silicon nitride layers. By changing different input ports, we can generate OAM beams with different radii.

### II.B.13. Multilayer Silicon Nitride Waveguide Coupler Design

A conventional directional coupler with two parallel waveguides is well understood. For 100% power coupling, it is required to have perfect optical impedance matching when the effective indices of the two waveguides are identical and the coupling length is exactly equal to the transfer distance at which 100% power coupling is complete. However, a  $\text{Si}_3\text{N}_4$  multi-layer coupling based on this conventional coupling design is not robust. Firstly the gap between the two layers is defined by the fabrication process. Secondly, fabrication of a multi-layer coupler requires multiple process steps which introduce variations in the dimensions of the waveguides at each level. These variations in waveguide dimension will cause a deviation in the effective index of the waveguide as well as coupling efficiency. Lastly, waveguide misalignment will change the effective coupling gap between the two waveguides. These problems can be overcome by using a coupler consisting of two vertically overlapped inverse tapers extending from the respective waveguides as shown in Figure 126.

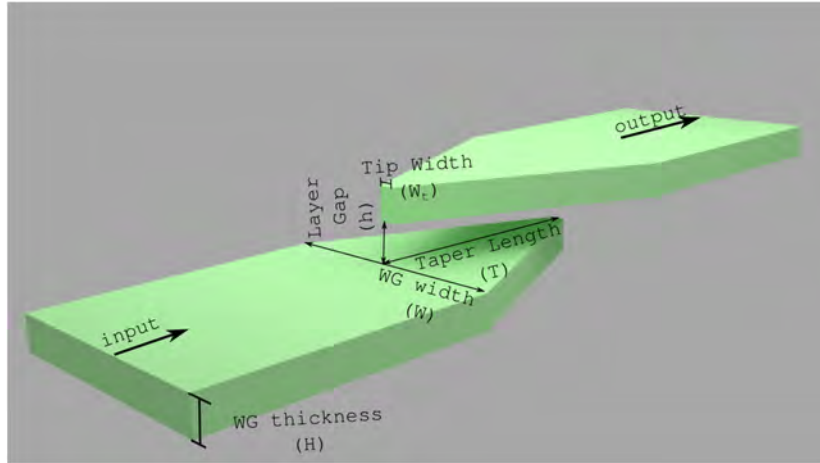


Figure 126. Schematic diagram of the multi-layer inverse taper coupling.

The inverse tapers have a shallow linear slope to ensure an adiabatic evolution of the optical mode. For proof of concept demonstration, the linear taper is the simplest design although nonlinear tapers may provide a more optimized coupling performance. The top and bottom  $\text{Si}_3\text{N}_4$  taper is designed to be centrally symmetric to the bottom SOI taper for simplicity.

#### II.B.13.a. Design and Simulation:

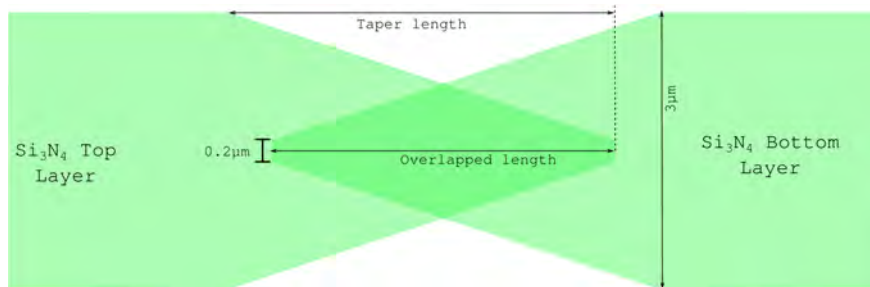


Figure 127: 2D top view of the multi-layer inverse taper coupling.

To design the multi-layer taper coupler we used two 200 nm thick  $\text{Si}_3\text{N}_4$  core layers separated by the 200 nm. The  $\text{SiO}_2$  is used as a cladding. A  $3\text{ }\mu\text{m}$  wide single mode waveguide is inversely tapered to the

200 nm width (the minimum size is limited by the fabrication). The taper length and the overlap length (as shown in Figure 127) need to be optimized in order to obtain low loss coupling.

We used 3D finite-difference time-domain (FDTD) to simulate this multi-layer coupling. In Figure 128 we can see the transferring of the mode-profile from the bottom layer to the top layer using three observation planes.

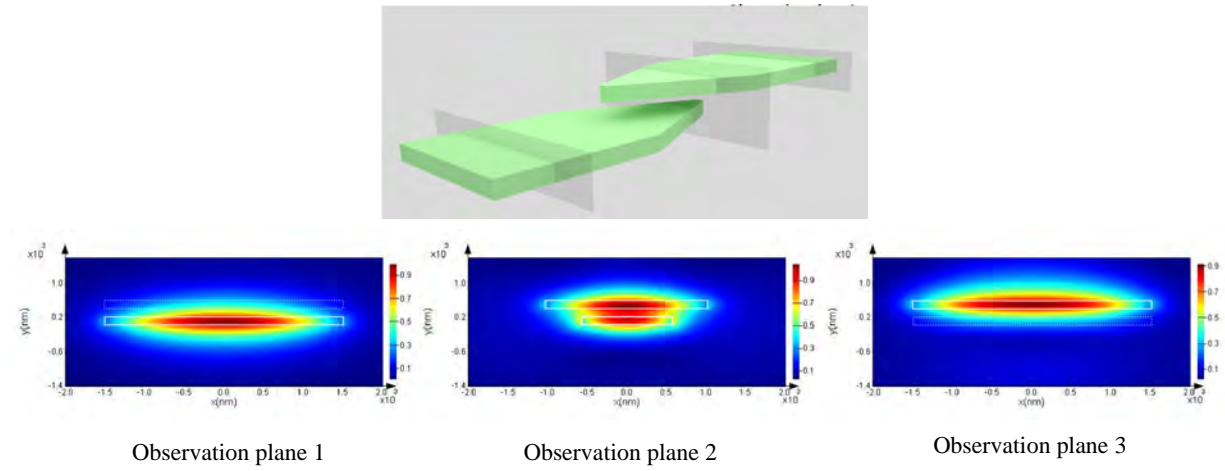


Figure 128. Simulated field profile of a multi-layer inverse taper coupling.

We varied the overlap length for a 10  $\mu\text{m}$  long taper in order to minimize the loss. Figure 129 shows the variation of the transmission (from bottom to top coupling) with the variation of the overlap length. With a 10  $\mu\text{m}$  long taper we reduced the loss to 5.7% for 7  $\mu\text{m}$  overlap length. As the overlap length decreases to 2  $\mu\text{m}$  the loss increases to 24% and the loss becomes 8% as the overlap length increases to 12  $\mu\text{m}$ . It is expected that if we increase the taper length the loss will be reduced but it will increase the coupler size. Therefore, Figure 130 shows the variation of the loss with the variation of the taper length. The overlap length is the same length of the taper length. From the simulation we can see that the loss become 1.0 % (approx.) when the taper length is 50  $\mu\text{m}$ , which represents a better balance between the loss and the device size.



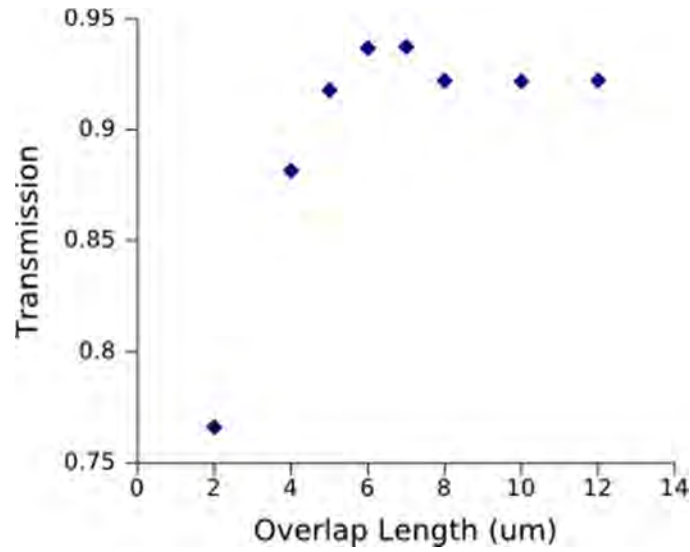


Figure 129. Variation of the simulated transmission with overlap length.

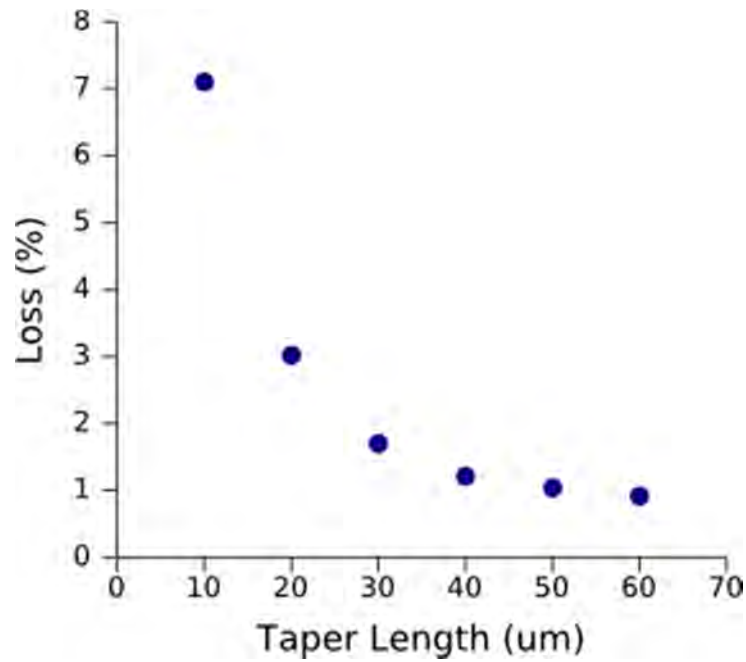


Figure 130. Variation of the simulated Loss with taper length.

One of the biggest challenges of the multi-layer waveguide fabrication is the misalignment between the layers. So we simulated the loss after misaligning the waveguides by 1  $\mu\text{m}$  along the waveguide width. The 1  $\mu\text{m}$  misalignment along the waveguide width increases the loss by 10 %. But in the fabrication the misalignment is expected to be well below 1  $\mu\text{m}$ .

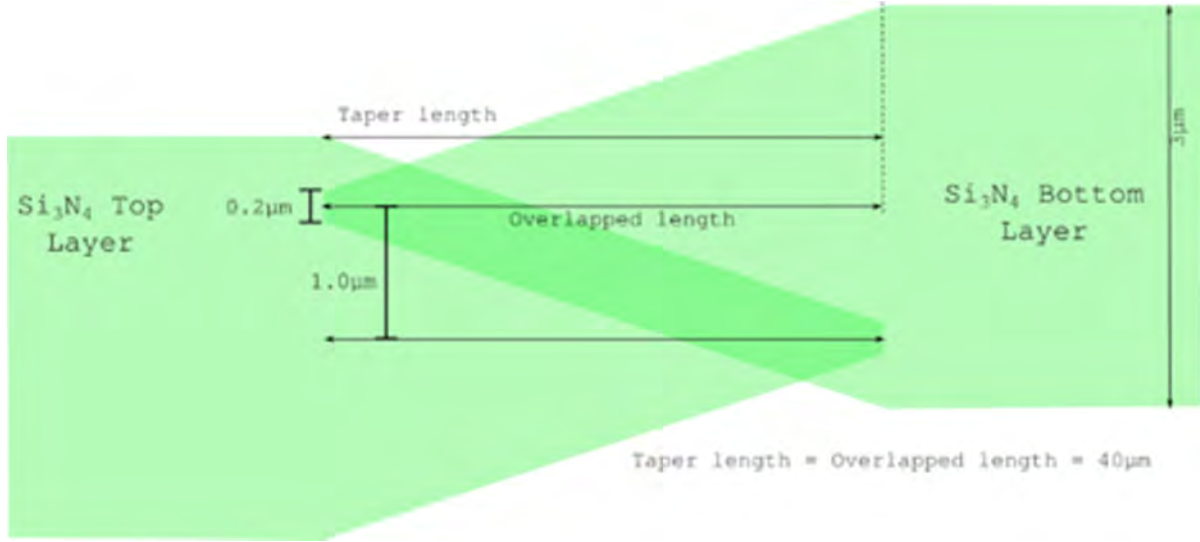


Figure 131. Misalignment between layers.

### II.B.13.b. Conclusion

The simulation results show that the 50  $\mu\text{m}$ -long inverse taper based multi-layer couplings can provide very promising results. However, in a fabricated device this long taper will have more scattering loss compared to the short taper. Therefore a tradeoff between the loss and taper-length need to be investigated for fabricated multi-layer couplers. From the simulation it's also clear that the fabrication misalignment between the waveguide along length or width of waveguide will not cause significant loss.

## II.B.14. Investigation of bonding of $\text{LiNbO}_3$ and $\text{SiO}_2$

So far, the 2D OAM devices and 3D OAM devices relied on silica or silicon nitride devices with thermo-optical tuning resulting in high power consumption or silicon photonics that required high losses during current injection. A new class of 2D and 3D OAM devices can be fabricated if we utilize waveguides with materials such as  $\text{LiNbO}_3$  with low loss and high electro-optical coefficients.

### II.B.14.a. $\text{LiNbO}_3$ material

$\text{LiNbO}_3$  is a crystal widely used in photonics, acoustics and acousto-optics. To achieve the requested device performance in applications, such as electro-optic modulation, nonlinear optical frequency conversion, electric-field sensing and surface acoustic wave filtering, it needs to be often combined with other materials. In this paper, we investigate direct bonding of  $\text{LiNbO}_3$  crystals with other dielectric materials, such as  $\text{SiO}_2$ , showing that surface chemical cleaning together with Ar or  $\text{O}_2$  plasma activation can be used to increase the surface free energy and achieve effective bonding at room temperature[4, 5]. Alternatively,  $\text{LiNbO}_3$  can be bonded by benzocyclobutene (BCB), a well known adhesive polymer, used for the realization of three dimensional semiconductor devices[6].

### II.B.14.b. Wafer bonding procedures

#### II.B.14.b.i. Hydrophilic bonding

It has been shown in [4], that surface cleaning and pre-treatments are essential steps that determine the quality of the final bonding. Precise knowledge of the effects of cleaning and surface pretreatments is crucial to control the surface free energy of the substrates to be bonded on order to obtain high strength adhesive joints. Moreover, an additional  $\text{O}_2$  plasma treatment increase the surface wettability with the advantage of leaving a smoother surface with compared to Ar treatment. Thus lead to bond a full 3 inch  $\text{LiNbO}_3$  to a 3 inch  $\text{SiO}_2$  substrate (Figure 132).

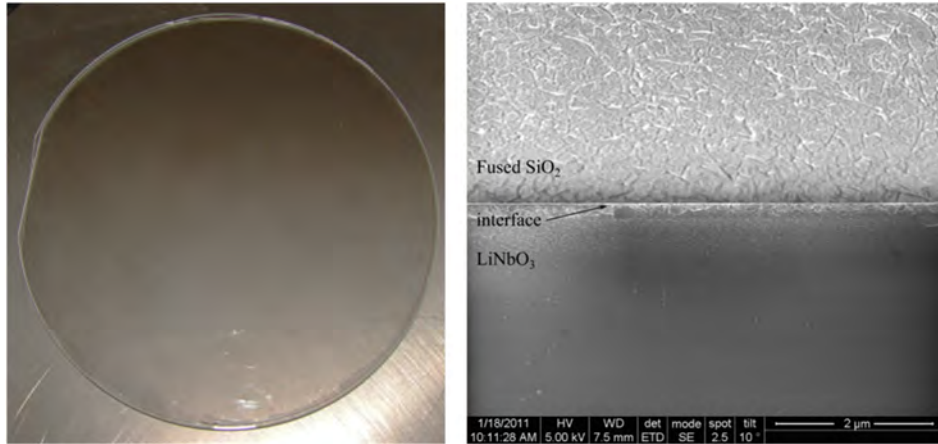


Figure 132 :left) Bonded 3 inches  $\text{LiNbO}_3$  wafer to a 3 inches  $\text{SiO}_2$  wafer [4]; right) SEM cross sectional image of the hybrid substrate.

#### II.B.14.b.ii. *BCB bonding*

BCB is a thermosetting polymer, commonly used in the electronics industry. It is developed by Dow Chemicals Company with a commercial name of Cyclotene® [7]. It is available in dry etch and photo-definable grades, commercially known as 3000 series and 4000 series resins, respectively. In our applications, we work with a dry etch Cyclotene 3022-57 resin, so we will focus exclusively to this type of BCB.

The use of BCB offers several advantages: its planarization and adhesion properties reduce the role of surface defects and greatly enhance the reproducibility and the size of the transferred films; optically, BCB has excellent transparency in the visible and infrared region, and as a substrate, provides a suitable optical confinement owing to its low refractive index ( $n=1.55$ )[6].

#### Spin coating and curing

As shown in Figure 133, our BCB 3022-57 formulation has a minimum achievable thickness of around  $5.7\mu\text{m}$  when spin coated on flat surface.

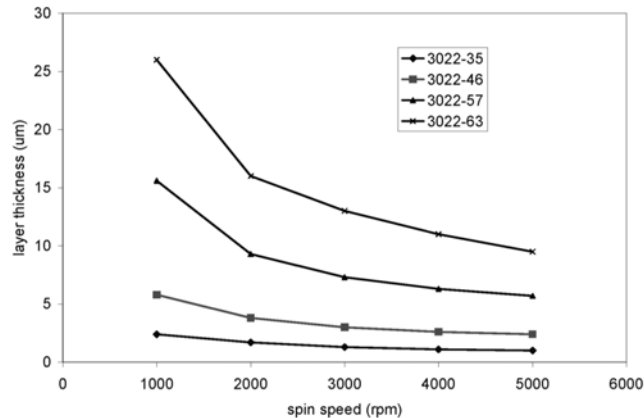


Figure 133 Spin curves for various commercially available BCB formulations.

For our applications, thinner BCB layers are required. To achieve this, custom BCB solutions are formulated by adding mesitylene[8].

During curing, BCB goes through chemical transformations at a rate which depends on the temperature used for curing. This is graphically represented in a time-temperature transformation

isothermal cure diagram, as shown in Figure 134. The main features of such a diagram are obtained by measuring the time needed for events to occur during isothermal cure at different temperatures.

Our BCB curing consists of four steps. In first step after spin-coating, BCB is baked on hotplate at temperature 90°C for 1 minute. In second step BCB is pre-cured at 100°C for 15 minutes. In third step BCB is pre-cured at 150°C for 15 minutes more. In the final step BCB is cured at 220°C for 120 minutes.

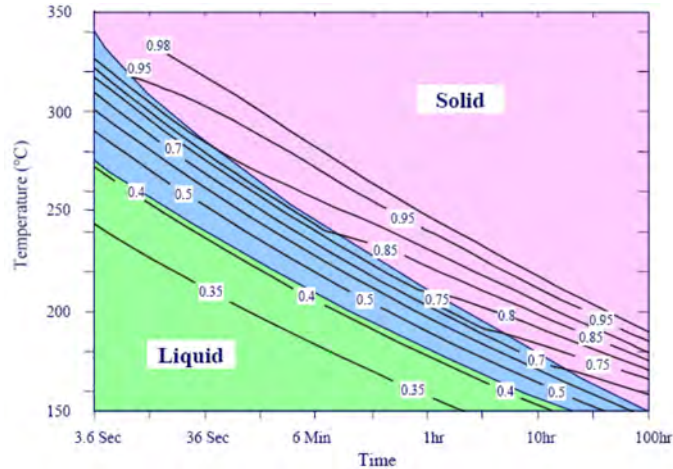


Figure 134 BCB degree of polymerization as a function of temperature and time.

### **Bonding experiment**

Several bonding test have been performed on Si and InP wafer in order to optimize the bonding process and to find the best settings and parameters. A result of these tests is shown in Figure 135.

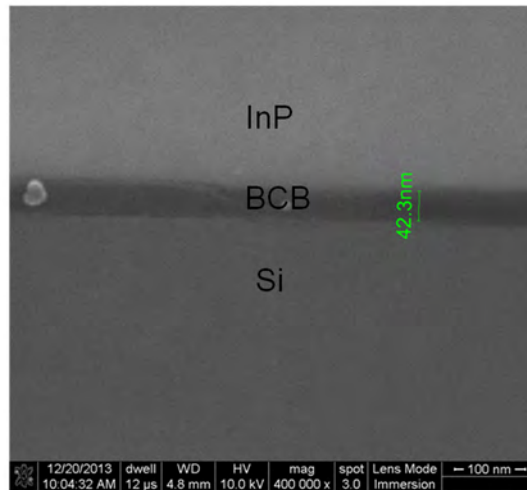


Figure 135 SEM image of ultra-thin BCB bonding layer between Si and InP wafers, obtained using 1:12 BCB: mesitylene solution.

BCB bonding offers an excellent alternative method to hydrophilic bonding and we believe that it can be successfully employed for the development of new  $\text{LiNbO}_3$ -on- $\text{SiO}_2$  integrated devices.



### II.B.15. OAM Silica PLC Design

Simulations of the components that make up the PIC have been performed to optimize their design and predict their performance. Figure 136(a-e) shows the simulated optical mode for the design core size of  $4.3\ \mu\text{m} \times 4.3\ \mu\text{m}$ .

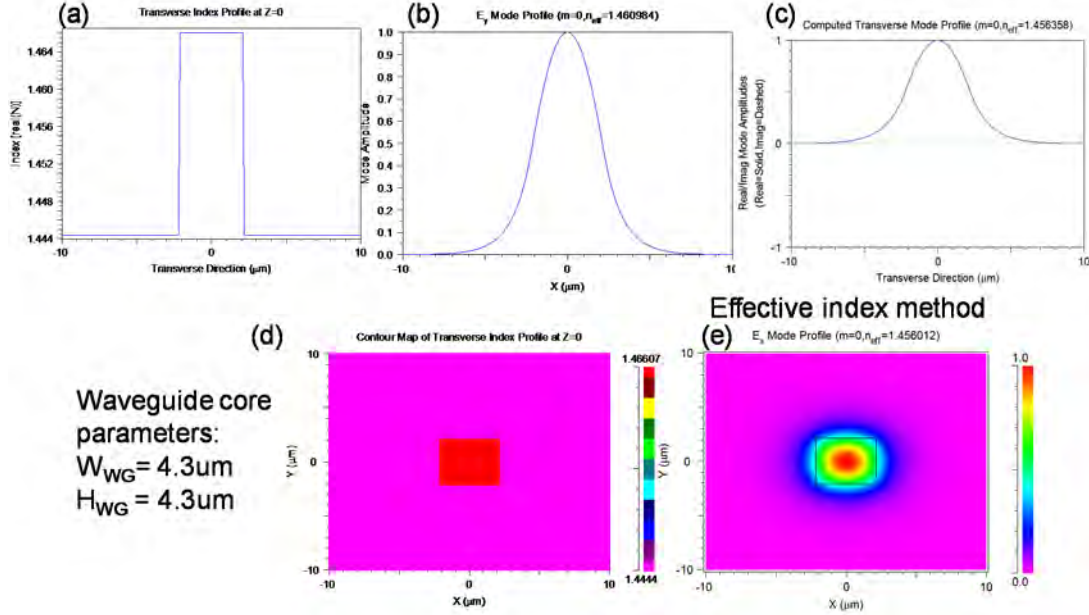


Figure 136. Waveguide mode design and simulation results. (a) Index profile (1.5% index contrast). (b) Calculated optical mode profile. (c). Optical mode profile computed using the effective index method. (d) Index contour map of waveguide and cladding. (e) Simulated optical mode profile.

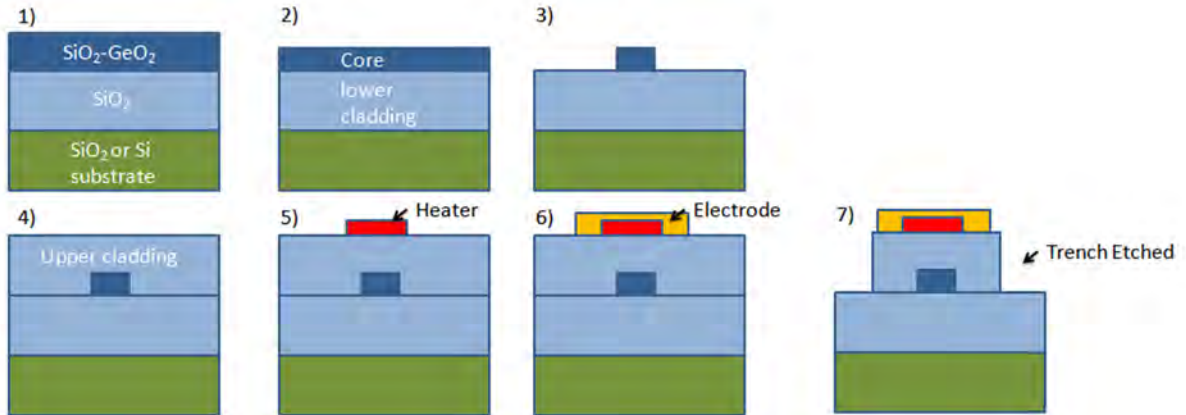


Figure 137. Fabrication process of the silica device.

To better understand the purpose of each layout layer, Figure 137 shows the fabrication process of PLCs using silica-based optical waveguides. The process starts with a silicon or silica substrate. Then, using a combination of flame hydrolysis deposition (FHD) and reactive ion etching, fine glass particles are produced in the oxyhydrogen flame and deposited on the host substrate (step 1). After under cladding and core glass layers are deposited, the wafer is heated to high temperature for consolidation (step 2). The circuit pattern is fabricated by means of photolithography and reactive ion etching (RIE), using the waveguide layer mask (step 3). Then, core ridge structures are covered with an over cladding layer and consolidated again (step 4). The heater layer is deposited and defined using the heater layer mask (step 5),

followed by the deposition and lift-off of the electrode layer (step 6). Finally, the trench layer is defined and etched (step 7).

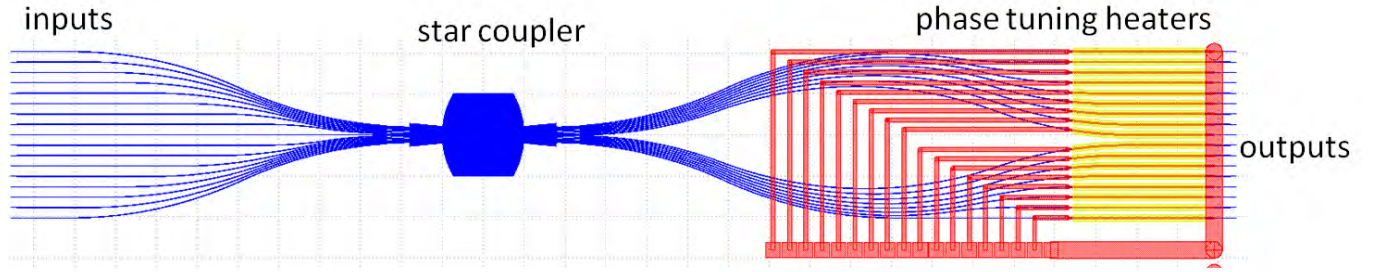


Figure 138 Layout of the OAM silica PLC

Figure 138 shows the layout of the OAM silica PLC. The blue lines are waveguides, the red blocks are electrodes, and yellow blocks are heaters.

In the measurements, we launch light from one of the 17 inputs on the left hand side. Light beam reaches the star coupler and expands as it propagate in the star coupler. Each of the 17 output waveguides at the other end of the star coupler capture a part of the input beam and guide the 17 beams to the output ports. Depending on which input is used, the star coupler gives 17 output beams a constant phase difference  $\Delta\theta$  between neighboring beams. The output waveguides are length matched so the phase differences  $\Delta\theta$  from star coupler are preserved at the output ports. The 17 phase tuning heaters utilize thermal optical effect to change the local refractive index in the waveguides, thus correct for any phase error due to fabrication variation.

#### II.B.16. Foundry fabricated 2D silica PLC chip loss characterization for both polarizations

In this section we report an experimental characterization of the loss of a 2D silica PLC chip both for x and y polarizations. Our commercial foundry partner, Enablence, fabricated the silica PLC.

Figure 139 shows the loss characterization setup for both polarizations. When we measured the loss for one polarization, the attenuator on the other polarization was set to maximum so that there was no power from the other polarization. The results in Figure 140 are obtained aligning the cleaved fiber with each output of the silica PLC, while the input is kept at a given central fiber array input. The results in Figure 141 are obtained for a given central fiber output while scanning the inputs of the fiber array.

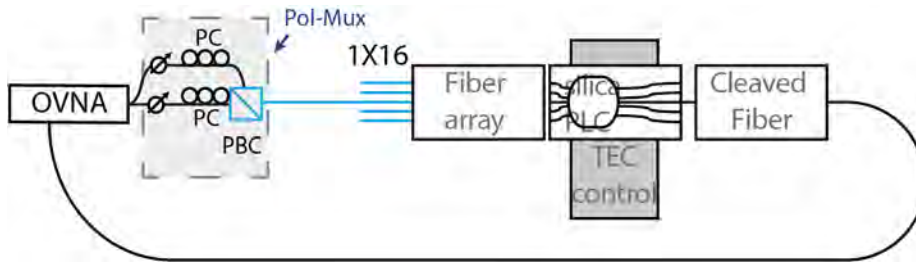


Figure 139. Loss characterization setup.

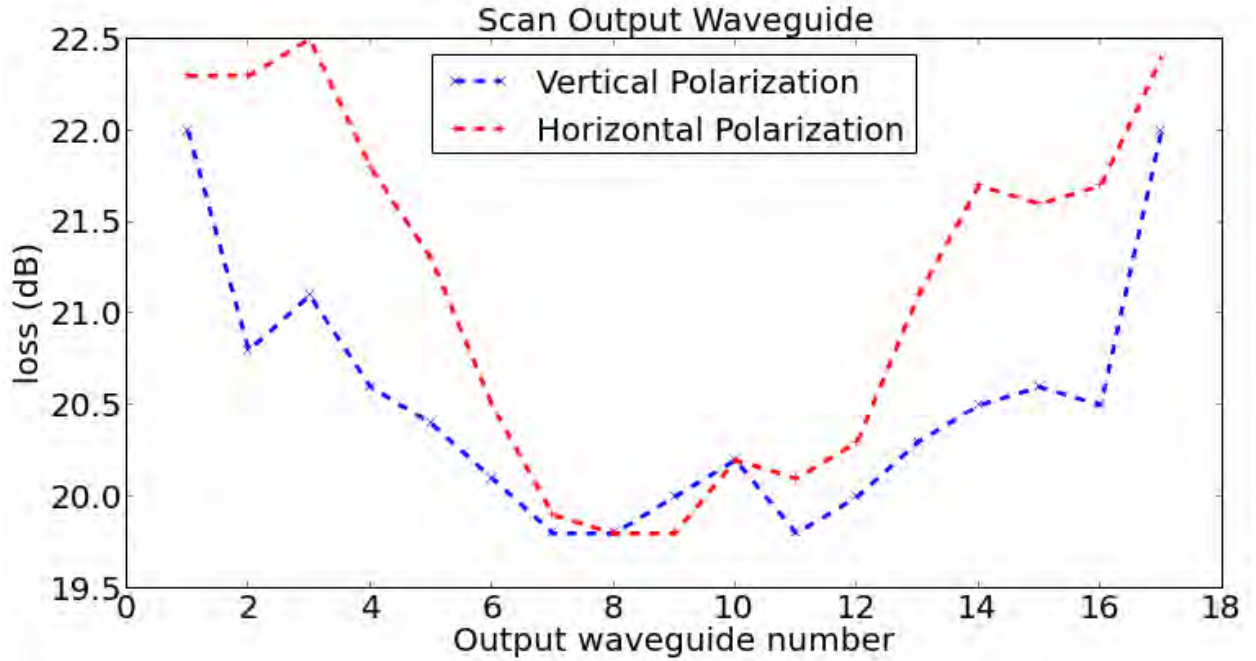


Figure 140. Loss measurement for a fixed central input and different outputs, for both polarizations.

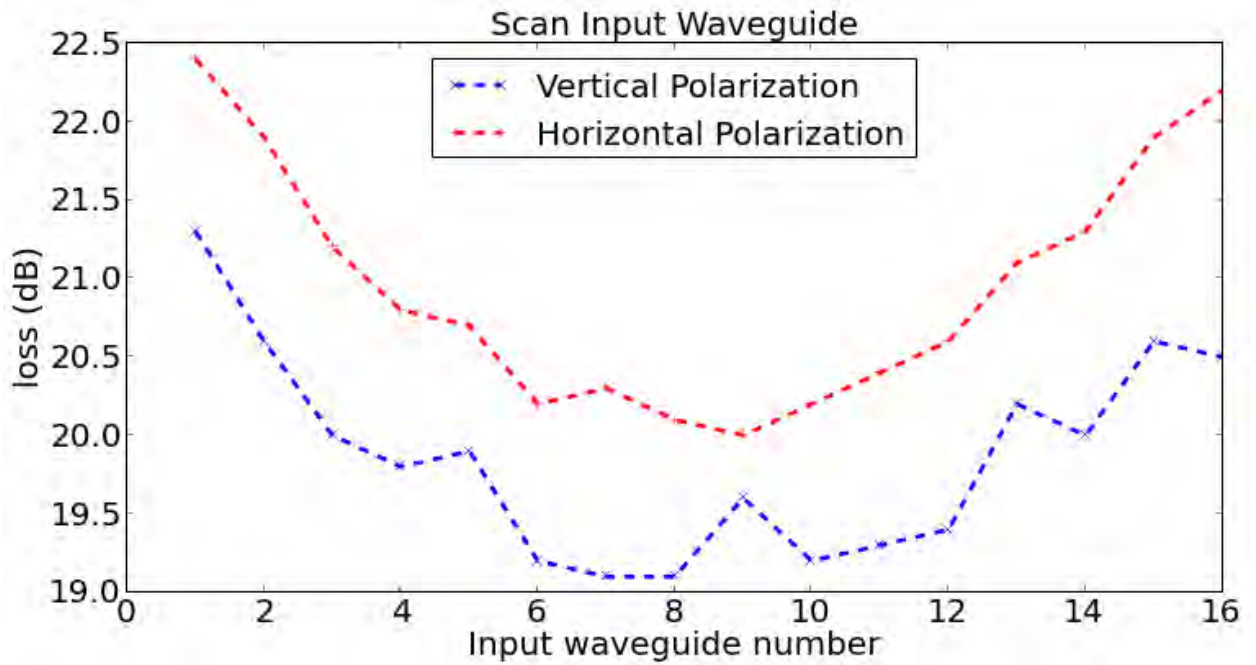


Figure 141. Loss measurement for a fixed central output and different inputs, for both polarizations.

From Figure 140 we can observe that the minimum loss of 19.5-20 dB for both polarizations. Output waveguides on the edge have ~2.5 dB of additional loss. From Figure 141 the minimum loss is 19 dB for a central input and vertical polarization. Horizontal polarization has ~1 dB of additional loss. The maximum loss is 22.5 dB for horizontal polarization, when an input on the edge is considered.

## II.B.17. Publications

- [1] Binbin Guan, Chuan Qin, Ryan P. Scott, Nicolas K. Fontaine, Tiehui Su, Roberto Proietti, and S.J.B. Yoo, "Polarization Diversified Integrated Circuits for Optical Angular Momentum Multiplexing," *submitted to IEEE Photonics Technology Letters, October, 2014.*
- [2] Ryan P. Scott and S. J. B. Yoo, "3D Waveguide Technologies for Generation, Detection, Multiplexing/Demultiplexing Orbital Angular Momentum Optical Waves," in *OptoElectronics and Communication Conference and Australian Conference on Optical Fibre Technology (OECC/ACOFT 2014) (Invited), Paper TH10F-5, July, 2014.*
- [3] Binbin Guan, Chuan Qin, Ryan P. Scott, Nicolas K. Fontaine, Tiehui Su, Roberto Proietti, and S. J. B. Yoo, "Polarization-Diversified, Multichannel Orbital Angular Momentum (OAM) Coherent Communication Link Demonstration using 2D-3D Hybrid Integrated Devices for Free-Space OAM Multiplexing and Demultiplexing," in *Conference on Lasers and Electro-Optics (CLEO), Paper STu1G.5, June, 2014.*
- [4] Chuan Qin, Binbin Guan, Ryan P. Scott, Roberto Proietti, Nicolas K. Fontaine, Tiehui Su, Carlo Ferrari, Mark Cappuzzo, Fred Klemens, Bob Keller, Mark Earnshaw, and S. J. B. Yoo, "Demonstration of orbital angular momentum state conversion using two hybrid 3D photonic integrated circuits," in *Optical Fiber Communication Conference (OFC), Paper Th4A.1, March, 2014.*
- [5] Binbin Guan, Ryan P. Scott, Chuan Qin, Nicolas K. Fontaine, Tiehui Su, Carlo Ferrari, Mark Cappuzzo, Fred Klemens, Bob Keller, Mark Earnshaw, and S. J. B. Yoo, "Free-Space Coherent Optical Communication with Orbital Angular Momentum Multiplexing/Demultiplexing Using a Hybrid 3D Photonic Integrated Circuit," in *Optics Express, Vol. 22, No. 1, pp. 145-156, January, 2014.*
- [6] Ryan P. Scott, Binbin Guan, Chuan Qin, Nicolas K. Fontaine, Tiehui Su, Carlo Ferrari, Mark Cappuzzo, Fred Klemens, Bob Keller, Mark Earnshaw, and S. J. B. Yoo, "Free-Space Coherent Optical Communication Demonstration using a 3D Photonic Integrated Circuit Device for Orbital Angular Momentum Multiplexing/Demultiplexing," in *European Conference on Optical Communications (ECOC), Paper Tu.3.B.2, September, 2013.*
- [7] Binbin Guan, Ryan P. Scott, Nicolas K. Fontaine, Tiehui Su, Carlo Ferrari, Mark Cappuzzo, Fred Klemens, Bob Keller, Mark Earnshaw, and S. J. B. Yoo, "Integrated Optical Orbital Angular Momentum Multiplexing Device using 3-D Waveguides and Silica PLC," in *Conference on Lasers and Electro-Optics (CLEO), Paper CTu1L.4, June, 2013.*

## II.B.18. References

- [1] T. Mizuochi, "Forward error correction," in *High Spectral Density Optical Communication Technologies*. vol. 6, M. Nakazawa, K. Kikuchi, and T. Miyazaki, Eds., ed: Springer, 2010, pp. 303-333.
- [2] S. M. Eaton, H. Zhang, M. L. Ng, J. Li, W.-J. Chen, S. Ho, *et al.*, "Transition from thermal diffusion to heat accumulation in high repetition rate femtosecond laser writing of buried optical waveguides," *Optics Express*, vol. 16, pp. 9443-9458, 2008/06/23 2008.
- [3] R. Ramponi, R. Osellame, and G. Cerullo, "Femtosecond Laser Micromachining."
- [4] D. Tulli, D. Janner, and V. Pruneri, "Room temperature direct bonding of LiNbO<sub>3</sub> crystal layers and its application to high-voltage optical sensing," *Journal of Micromechanics and Microengineering*, vol. 21, p. 085025, 2011.

- [5] I. Bakish, R. Califa, T. Ilovitsh, V. Artel, G. Winzer, K. Voigt, *et al.*, "Voltage-Induced Phase Shift in a Hybrid LiNbO<sub>3</sub>-on-Silicon Mach-Zehnder Interferometer," in *Advanced Photonics 2013*, Rio Grande, Puerto Rico, 2013, p. IW4A.2.
- [6] P. G. Guarino Andrea, Rezzonico Daniele, Degl'Innocenti Riccardo, Gunter Peter, "Electro-optically tunable microring resonators in lithium niobate," *Nat Photon*, vol. 1, 2007.
- [7] [http://www.dow.com/cyclotene/docs/cyclotene\\_3000\\_dry\\_etch.pdf](http://www.dow.com/cyclotene/docs/cyclotene_3000_dry_etch.pdf). (1/31/2014).
- [8] D. V. T. S. Stankovic, G. Roelkens, R. Jones, J. Heck, M. Sysak "Die-to-Die Adhesive Bonding for Evanescently-Coupled Photonic Devices," *ECS TRANSACTIONS*, vol. 33, p. 10, 2010.



# Free-space coherent optical communication with orbital angular, momentum multiplexing/demultiplexing using a hybrid 3D photonic integrated circuit

Binbin Guan,<sup>1</sup> Ryan P. Scott,<sup>1,\*</sup> Chuan Qin,<sup>1</sup> Nicolas K. Fontaine,<sup>2</sup> Tiehui Su,<sup>1</sup> Carlo Ferrari,<sup>3</sup> Mark Cappuzzo,<sup>3</sup> Fred Klemens,<sup>3</sup> Bob Keller,<sup>3</sup> Mark Earnshaw,<sup>3</sup> and S. J. B. Yoo<sup>1</sup>

<sup>1</sup>Department of Electrical and Computer Engineering, University of California, Davis, CA 95616, USA

<sup>2</sup>Bell Laboratories, Alcatel-Lucent, 791 Holmdel Rd, Holmdel, NJ 07733, USA

<sup>3</sup>Bell Laboratories, Alcatel-Lucent, 600 Mountain Ave, Murray Hill, NJ 07974, USA

\*[rpscott@ucdavis.edu](mailto:rpscott@ucdavis.edu)

**Abstract:** We demonstrate free-space space-division-multiplexing (SDM) with 15 orbital angular momentum (OAM) states using a three-dimensional (3D) photonic integrated circuit (PIC). The hybrid device consists of a silica planar lightwave circuit (PLC) coupled to a 3D waveguide circuit to multiplex/demultiplex OAM states. The low excess loss hybrid device is used in individual and two simultaneous OAM states multiplexing and demultiplexing link experiments with a 20 Gb/s, 1.67 b/s/Hz quadrature phase shift keyed (QPSK) signal, which shows error-free performance for 379,960 tested bits for all OAM states.

©2013 Optical Society of America

**OCIS codes:** (060.1660) Coherent communications; (050.4865) Optical vortices; (060.4230) Multiplexing; (130.2755) Glass waveguides.

---

## References and links

1. P. J. Winzer, "High-spectral-efficiency optical modulation formats," *J. Lightwave Technol.* **30**(24), 3824–3835 (2012).
2. R. Essiambre, G. Kramer, P. J. Winzer, G. J. Foschini, and B. Goebel, "Capacity limits of optical fiber networks," *J. Lightwave Technol.* **28**(4), 662–701 (2010).
3. L. Allen, M. W. Beijersbergen, R. J. C. Spreeuw, and J. P. Woerdman, "Orbital angular momentum of light and the transformation of Laguerre-Gaussian laser modes," *Phys. Rev. A* **45**(11), 8185–8189 (1992).
4. A. M. Yao and M. J. Padgett, "Orbital angular momentum: origins, behavior and applications," *Adv. Opt. Photonics* **3**(2), 161–204 (2011).
5. N. Bozinovic, Y. Yue, Y. Ren, M. Tur, P. Kristensen, H. Huang, A. E. Willner, and S. Ramachandran, "Terabit-scale orbital angular momentum mode division multiplexing in fibers," *Science* **340**(6140), 1545–1548 (2013).
6. M. W. Beijersbergen, R. P. C. Coerwinkel, M. Kristensen, and J. P. Woerdman, "Helical-wavefront laser beams produced with a spiral phaseplate," *Opt. Commun.* **112**(5–6), 321–327 (1994).
7. J. Wang, J.-Y. Yang, I. M. Fazal, N. Ahmed, Y. Yan, H. Huang, Y. Ren, Y. Yue, S. Dolinar, M. Tur, and A. E. Willner, "Terabit free-space data transmission employing orbital angular momentum multiplexing," *Nat. Photonics* **6**(7), 488–496 (2012).
8. J. Leach, M. J. Padgett, S. M. Barnett, S. Franke-Arnold, and J. Courtial, "Measuring the orbital angular momentum of a single photon," *Phys. Rev. Lett.* **88**(25), 257901 (2002).
9. T. Su, R. P. Scott, S. S. Djordjevic, N. K. Fontaine, D. J. Geisler, X. Cai, and S. J. B. Yoo, "Demonstration of free space coherent optical communication using integrated silicon photonic orbital angular momentum devices," *Opt. Express* **20**(9), 9396–9402 (2012).
10. N. K. Fontaine, C. R. Doerr, and L. Buhl, "Efficient multiplexing and demultiplexing of free-space orbital angular momentum using photonic integrated circuits," in *Optical Fiber Communication Conference, OSA Technical Digest* (Optical Society of America, 2012), OTu11.2.
11. J. Sun, E. Timurdogan, A. Yaacobi, E. S. Hosseini, and M. R. Watts, "Large-scale nanophotonic phased array," *Nature* **493**(7431), 195–199 (2013).
12. B. Guan, R. P. Scott, N. K. Fontaine, T. Su, C. Ferrari, M. Cappuzzo, F. Klemens, B. Keller, M. Earnshaw, and S. J. B. Yoo, "Integrated optical orbital angular momentum multiplexing device using 3-D waveguides and a silica PLC," in *CLEO: 2013, OSA Technical Digest* (online) (Optical Society of America, 2013), CTu1L.4.
13. R. P. Scott, B. Guan, C. Qin, N. K. Fontaine, T. Su, C. Ferrari, M. Cappuzzo, F. Klemens, B. Keller, M. Earnshaw, and S. J. B. Yoo, "Free-space coherent optical communication demonstration using a 3D photonic

- integrated circuit device for orbital angular momentum multiplexing/demultiplexing,” in *European Conference and Exhibition on Optical Communication (ECOC)*, OSA Technical Digest (Optical Society of America, 2013), Tu.3.B.2.
14. Y. Nasu, M. Kohtoku, and Y. Hibino, “Low-loss waveguides written with a femtosecond laser for flexible interconnection in a planar light-wave circuit,” *Opt. Lett.* **30**(7), 723–725 (2005).
  15. R. R. Thomson, H. T. Bookey, N. D. Psaila, A. Fender, S. Campbell, W. N. Macpherson, J. S. Barton, D. T. Reid, and A. K. Kar, “Ultrafast laser inscription of a three-dimensional fan-out device for multicore fiber coupling applications,” in *Quantum Electronics and Laser Science Conference* (Optical Society of America, 2008).
  16. A. V. Oppenheim, A. S. Willsky, and S. H. Nawab, *Signals and Systems* (Prentice-Hall, 1983), Vol. 2.
  17. A. Himeno, K. Kato, and T. Miya, “Silica-based planar lightwave circuits,” *IEEE J. Sel. Top. Quantum Electron.* **4**(6), 913–924 (1998).
  18. K. Okamoto, *Fundamentals of Optical Waveguides* (Elsevier, 2010).
  19. W. Steinchen and L. X. Yang, *Digital Shearography: Theory and Application of Digital Speckle Pattern Shearing Interferometry* (SPIE, 2003), Vol. 100.
  20. M. Kawachi, “Silica waveguides on silicon and their application to integrated-optic components,” *Opt. Quantum Electron.* **22**(5), 391–416 (1990).
  21. J. G. Proakis and M. Salehi, *Digital Communications*, 5th ed. (McGraw-Hill, 2008).
  22. I. Kaminow, T. Li, and A. E. Willner, *Optical Fiber Telecommunications VB: Systems and Networks* (Academic, 2010).
  23. S. J. Savory, “Digital filters for coherent optical receivers,” *Opt. Express* **16**(2), 804–817 (2008).
  24. A. Papoulis and S. U. Pillai, *Probability, Random Variables, and Stochastic Processes* (McGraw-Hill, 2002).
  25. D. Mitić, A. Lebl, and Ž. Markov, “Calculating the required number of bits in the function of confidence level and error probability estimation,” *Serbian J. Electr. Eng.* **9**(3), 361–375 (2012).
  26. T. Mizuochoi, “Forward error correction,” in *High Spectral Density Optical Communication Technologies*, M. Nakazawa, K. Kikuchi, and T. Miyazaki, eds. (Springer, 2010), pp. 303–333.

## 1. Introduction

The explosive growth of data traffic has transformed the landscape of modern telecommunication networks. Initially, the remarkable increases in capacity demands were successfully met by deployment of wavelength-division-multiplexing (WDM) technologies, which increased communication capacity from 10 Gb/s to multiple Tb/s on a single mode fiber. Recent optical networking advances have addressed optical communications with high spectral efficiency beyond 1–10 b/s/Hz employing advanced modulation formats. The steady increases in spectral efficiency reported for high capacity transmission systems, which has reached 100 Tb/s capacity and 10 b/s/Hz spectral efficiency [1]. However, it is extremely difficult to support such high spectral efficiency over a long distance due to the nonlinear Shannon limit [2] of the fiber-optic channel for even moderate (~500 km) transmission distances. Space-division-multiplexing (SDM) becomes an attractive and practical technique to provide an additional degree of freedom for increasing the spectral efficiency and communication capacity [1]. One such SDM method on orbital angular momentum (OAM) [3] has generated great interest because of its relative simple employment of cylindrically symmetric modes. The light beam carrying orbital angular momentum exhibits an azimuthal phase variation of  $\varphi(r, \phi) = \exp(i\ell\phi)$ , where  $\phi$  is the azimuthal angle and  $\ell$  the charge number or OAM state; a positive or negative integer. The handedness of this helical phase front is determined by the sign of the charge number  $\ell$  and a non-zero state OAM beam leads to a phase singularity on the beam axis [4]. Hence, the amplitude along the beam axis vanishes, and the center of the OAM beam is dark. Compared to a spin mode (i.e., polarization), the light beam can in principle support an infinite number of OAM states at the same time (subject to the limitation imposed by the signal to noise ratio). Therefore, OAM has the potential to significantly improve the spectral efficiency or photon efficiency of free-space and fiber optical communications [5]. In addition, the inherent orthogonality of the various OAM states may reduce crosstalk, resulting in reduced reliance on digital signal processing (DSP) compared to cases employing standard multiple-input and multiple-output (MIMO) methods. For instance, Bozinovic et al. [5] have recently demonstrated OAM transmission over 1.1-km of fiber for up to 10 OAM states without the use of MIMO.

The early work of Allen [3] on OAM was followed by a number of papers experimentally demonstrating OAM generation, sorting, multiplexing, and demultiplexing. Typical

approaches utilize holograms [6], spatial light modulators (SLMs) [7], dove prisms [8], and other bulk optics. However, practical SDM systems greatly benefit from integrated optics on a robust platform, especially when combined with coherent optical communications. Our group demonstrated silicon photonic OAM multiplexing and demultiplexing devices based on a free propagation region employing a Rowland circle and waveguide apertures with grating structures [9], and a number of other groups have also provided alternative integrated 2D photonic circuits for creating spatial modes [10, 11]. Such structures induce relatively large losses and polarization dependent losses that impede their broad use in transmission systems.

In this paper, we follow up on our first reports [12, 13] of a 3D photonic integrated circuit capable of multiplexing/de-multiplexing OAM states. The circuit supports up to 15 OAM states, with both TE and TM polarizations and relatively low loss performance at 1.55  $\mu\text{m}$ . The compact design and single-mode interface easily connect with other high speed optical components for future on-chip integration. This paper is organized as follows, Section 2 discusses the device's design and operating principles, Section 3 provides device characterization results, Section 4 and 5 present free-space transmission demonstration results, and Section 6 is the conclusion.

## 2. Orbital angular momentum device design and operating principle

Figure 1 shows a conceptual diagram of a photonic integrated circuit (PIC) for OAM beam generation and multiplexing. On the left side, each single-mode waveguide input corresponds to an OAM state ( $\ell = -2$  through  $+2$  shown). The input light beams pass through the free-propagation region (FPR) employing the Rowland circle, where they laterally expand and the wavefronts acquire a linear phase tilt based on the input waveguide position. At the output side of the FPR, the phase-matched waveguides sample the wavefront and maintain the phase relationship. A geometrical transformation is then necessary for conversion of the linear phase tilt to azimuthal phase variations at the output apertures. If multiple inputs are illuminated simultaneously, the OAM states are multiplexed, and they overlap spatially at the output apertures. On the other hand, when operated in reverse, the 3D waveguides' circular-patterned apertures can sample and retrieve spatially overlapped OAM states, and as a result, the demultiplexed signal can be detected at different output waveguides of the silica PLC.

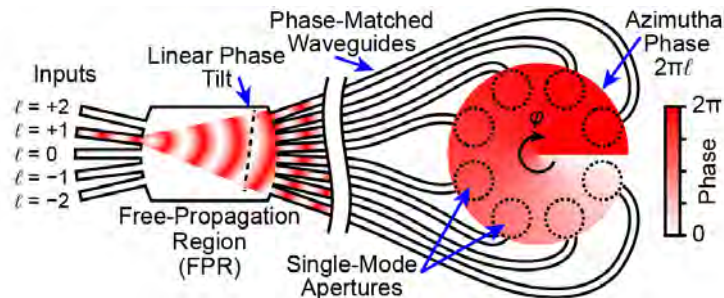


Fig. 1. Concept of the OAM photonic integrated circuit for multiplexing or demultiplexing free-space OAM beams.

In this work, laser inscribed 3D waveguides [14, 15] perform the geometrical conversion, and at the output of the 3D waveguide apertures, we have a discretely sampled optical beam with the correct azimuthal phase for each of the OAM states. OAM states can be fully recovered if the sampling of the OAM state azimuthal phase distribution satisfies Nyquist sampling theory [16]. Referring to Fig. 1, if we consider each output aperture as a spatial beam sample and those samples are evenly distributed around the azimuthal coordinate, the number of supported OAM states depends on the number of beam samples (i.e., apertures or waveguides). Therefore, at least  $2N$  waveguides are required for the generation of  $2N$  OAM states (e.g., from  $\ell = -N + 1$  to  $\ell = +N$ , including  $\ell = 0$ ). Since this multiplexing technique does not suffer from  $1 \times N$  splitting/combining losses, with photonic integration, scaling the

number of the waveguides and increasing the number of supported OAM states to very large numbers without large losses is straightforward. However, OAM state crosstalk emerges as the practical limit for device implementation.

Figure 2 shows a conceptual drawing of our implementation of Fig. 1, where the OAM hybrid integrated device is composed of a silica PLC and a 3D waveguide circuit. The silica PLC has 17 waveguide inputs where 15 are used to create linearly tilted wavefronts that correspond to unique OAM states (i.e., from  $\ell = -7$  to  $\ell = +7$ ), and the additional 2 input waveguides are used for device characterization. The FPR is implemented as a star coupler and performs a Fourier transform so that the unique angle of the input waveguide creates a wavefront with a specific linear phase tilt. The FPR has 17 waveguide outputs that sample the wavefront, but only the first 16 waveguides are used to create the OAM beam (the 17th waveguide's phase is always the same as the first waveguide and is used for characterization). There are electrical heaters on each output waveguide after the FPR to provide the phase error correction (PEC) necessary for correcting the unintended phase variations rising from both fabrication errors and length variations in the 3D waveguides. Here we define the path length differences between 3D waveguides as length variations. The waveguides on the silica PLC use a  $\Delta n$  of 2% [17]. Figure 3(a) shows a photo of the fabricated PLC which is 15-mm long and it has a 127- $\mu\text{m}$  pitch for both the input and the output waveguides. Figure 3(b) shows the output light beam intensities captured by an infrared camera.

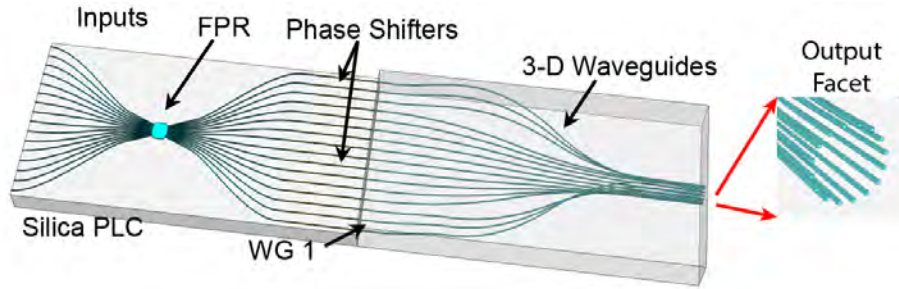


Fig. 2. Conceptual view of the hybrid photonic integrated device for OAM state multiplexing and demultiplexing.

The right part of Fig. 2 shows a conceptual drawing of the 3D waveguide circuit with a magnified view of output facet. 3D waveguide circuit was fabricated at a commercial foundry by direct laser writing of the optical waveguides in a borosilicate glass. The fabrication technique uses focused femtosecond laser pulses to permanently increase the refractive index via multi-photon absorption, which occurs directly inside a transparent dielectric material. Three-axis variation of the substrate during the laser writing enables an accurate fabrication of the 3D waveguides. Figure 3(c) shows a photo of the 3D waveguide circuit's output facet before polishing so that the 16 waveguides are visible. The mode field diameter of each output is  $\sim 10\ \mu\text{m}$  (numerical aperture (NA) = 0.1). The center-to-center spacing between neighboring outputs is kept at  $40\ \mu\text{m}$  to minimize coupling between adjacent waveguides. The circular pattern diameter is  $204\ \mu\text{m}$  and the length of the 3D waveguide is 19 mm. Over this distance, the 2D-array waveguides can carefully transit to their 3D circular geometry while keeping bending losses negligible. The waveguides are pathlength matched to within  $40\ \mu\text{m}$ , which provides an operating bandwidth of  $\sim 9\ \text{nm}$  when the heaters on the silica PLC phase match the output waveguides (assuming two identical devices and  $< -10\text{-dB}$  crosstalk). The operating bandwidth is defined as the maximum wavelength range at which the crosstalk for each OAM state is less than  $-10\ \text{dB}$ . The operating bandwidth is based on a simulation of the OAM state crosstalk that uses the wavelength dependent phase errors that arise from the path length difference,  $\phi_{\text{error}} = 2\pi n_{\text{eff}} \Delta L / \lambda$ , where  $n_{\text{eff}}$  is 1.49. Figure 3(d) shows the measured output intensities of the 3D waveguides. The variation in the intensity distribution occurs mainly within the silica PLC where the illumination of the outer-most FPR output

waveguides is less than the center waveguides. The input power from any one of the  $N$  input waveguides is radiated to the FPR and it is received by the output waveguide array. The radiation pattern at the output side of the FPR is the Fraunhofer pattern (Fourier transform) of the field profile at the input side FPR-array interface. The FPR parameters, such as the aperture angle, radius of the FPR region and input/output waveguide taper shapes, were optimized by using beam propagation method (BPM) simulations to concurrently try to maximize the output power, splitting uniformity, and desired phase conditions [18]. Since OAM state crosstalk arises from the combination of phase errors and amplitude (or intensity) variations from each waveguide in the hybrid device, variations in the intensity distribution may decrease the performance of the hybrid devices. Further investigations are needed to reduce the variations in intensity distribution, as well as the excess loss in future silica PLC designs.

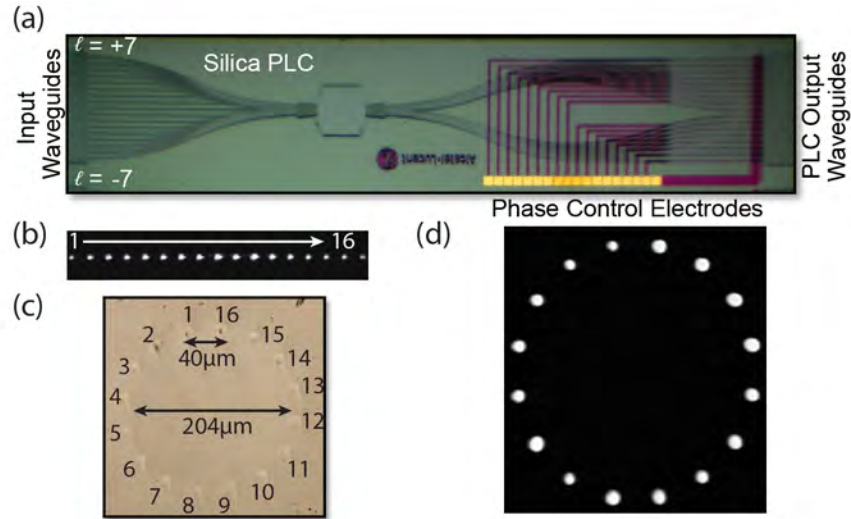


Fig. 3. Integrated device details. (a) Silica PLC image. (b) Measured mode profile of the silica PLC output waveguides (17 outputs). (c) 3D waveguide output facet image before polishing. (d) Measured mode profile of the light beams at the output of the 3D waveguides.

### 3. Device characterization

Figure 4(a) shows the simulated loss of the silica PLC due to the FPR region design and the measured total loss of the silica PLC with input OAM state 0. The measured loss shows less variation than the simulation predicts, possibly due to fabrication errors. Figure 4(b) presents the excess loss for the silica PLC using the OAM state 0 input and the insertion loss for the 3D waveguides. The measurements were made using cleaved single mode fibers and index matching fluid and the PLC's excess loss does not include the simulated splitting loss. Excess loss is defined as the difference between the measured loss and expected (simulated) loss. The excess loss of the silica PLC is  $\sim 3.5$  dB and mainly arises from fabrication errors and mode mismatch between the single mode fibers and PLC waveguide (i.e., to avoid risk of damage, there was always a gap between the fiber and facet). As mentioned previously, the silica PLC loss [Fig. 4(a)] is highest for the outer-most waveguides (i.e., lowest and highest waveguide numbers) due to the FPR design, while the 3D waveguides' loss variation is much smaller at  $< 0.6$  dB. The measured total excess loss of the hybrid device is  $\sim 7.5$  dB with a variation of 1.5 dB across all inputs.



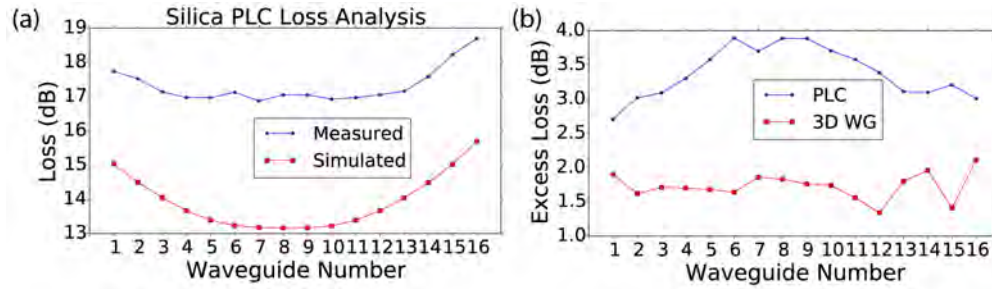


Fig. 4. (a) Measured and simulated loss distribution for the output waveguides of the silica PLC (OAM state 0 as input). (b) Measured excess loss for the silica PLC and insertion loss of the 3D waveguides.

To characterize the phase of the OAM hybrid device outputs, we used a technique based on spatial shearing interferometry [19] where a tilted reference beam with flat spatial phase is interfered with a signal beam that has a known spatial intensity but unknown spatial phase. Separately measuring the signal beam, reference beam, and their resulting interferogram, allows retrieval of the unknown spatial phase. Figure 5(a) shows the measurement arrangement where the output of the hybrid device is imaged onto an infrared camera with a magnifying lens ( $f_1 = 4.51$  mm and  $f_2 = 100$  mm) arrangement when only one input of the silica PLC was illuminated at a time. We used polarization-maintaining (PM) fiber after the polarizer to insure TE polarization at the device input and reference beam output. The magnified image of hybrid device output interfered with the linear tilted reference beam, resulting in the generation of an interference pattern on the infrared camera. We used offline digital signal processing of the images to retrieve both the amplitude and the phase (modulo  $2\pi$  rad) of each waveguide output with a measurement update rate of  $\sim 0.5$  Hz.

Using the fast updating spatial phase measurements, we proceeded to correct the phase errors of the hybrid device. The upper color maps in Fig. 5(b) show the measured near-field pattern (intensity and phase of the waveguide outputs) for OAM state 0 before any PEC was applied. The phase of each waveguide output is random due to the phase errors from both the silica PLC and the 3D waveguides. After applying voltages to the electrical heaters [20], the lower color maps in Fig. 5(b) show that we could correct all of the phase errors and equalize the phases of the waveguide outputs (OAM state 0 has no azimuthal phase variation). The measured electrical power for a  $\pi$  rad phase shift (i.e.,  $P_\pi$ ) was  $\sim 400$  mW (no heat isolating trenches were used [18]). The silica PLC was set on an aluminum block that was temperature stabilized to  $30^\circ\text{C}$  and the PLC was held in place by the pressure of the multiprobe used to access the electrical connections. Although the temperature stabilization of the aluminum block worked well with or without the PEC applied, we suspect that varying air currents across the device's surface may impact the local temperatures of the PLC heater regions and limit the phase stability. A fully packaged device may further improve its phase stability. Figure 5(c) shows a line plot of the phase data in Fig. 5(b) for easy comparison. The measured result with PEC matches the theoretical phase distribution of OAM state 0 well.

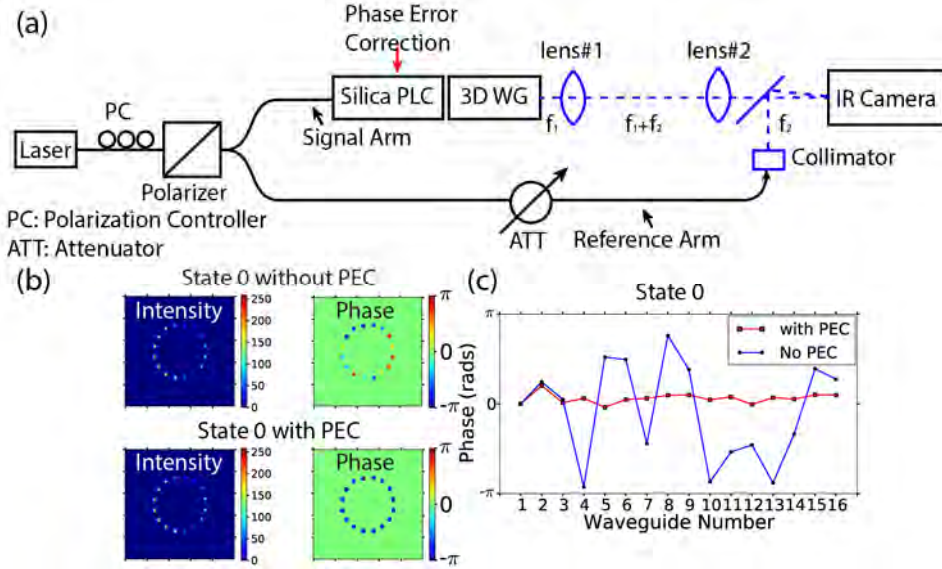


Fig. 5. (a) Experimental arrangement for OAM device intensity and phase characterization. (b) Near-field intensity and phase before and after phase-error correction is applied for OAM state 0 (flat phase). (c) Line plot of the measured near-field phase shown in (b).

The near-field output phase was then measured in a similar way for all of the OAM states through the illumination of one input waveguide of the silica PLC at a time (from  $\ell = -7$  to  $\ell = +7$ ). Figure 6(a) summarizes the results for all of the OAM states where PEC adjustments were made only for OAM state 0. OAM states with opposite sign show the correct change in azimuthal phase rotation. For OAM states  $+7$  and  $-7$ , the phase is sampled by nearly a factor of 2 as a result of the 16 waveguides. Therefore, it is approaching the Nyquist sampling theory limitation which occurs for OAM states  $+8$  and  $-8$  where each waveguide has a relative phase of 0 or  $\pi$  and it is not possible to unambiguously determine the OAM state. Figure 6(c) shows the unwrapped phase plot versus waveguide output number for all of the OAM states. The result shows clearly that, for each OAM state, the phase is the product of  $2\pi$  and the OAM charge number  $\ell$ .

The characterization results demonstrate that the hybrid device can be used for OAM state multiplexing/demultiplexing, with low excess loss and repeatable performance. Since this multiplexing technique does not suffer from  $1 \times N$  splitting/combining losses, with photonic integration, scaling the number of the waveguides and increasing the number of supported OAM states to very large numbers without large losses is straightforward.

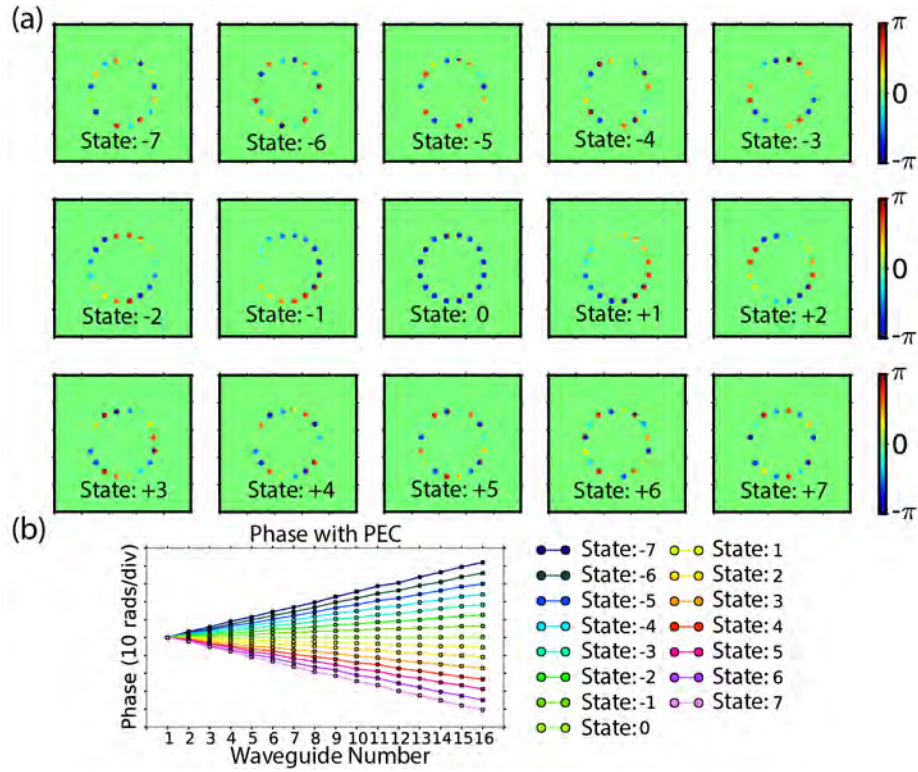


Fig. 6. Integrated photonic circuit OAM state characterization results. (a) OAM state near-field phase pattern as a color map. (b) Line plots of the measured and unwrapped phase for each OAM state.

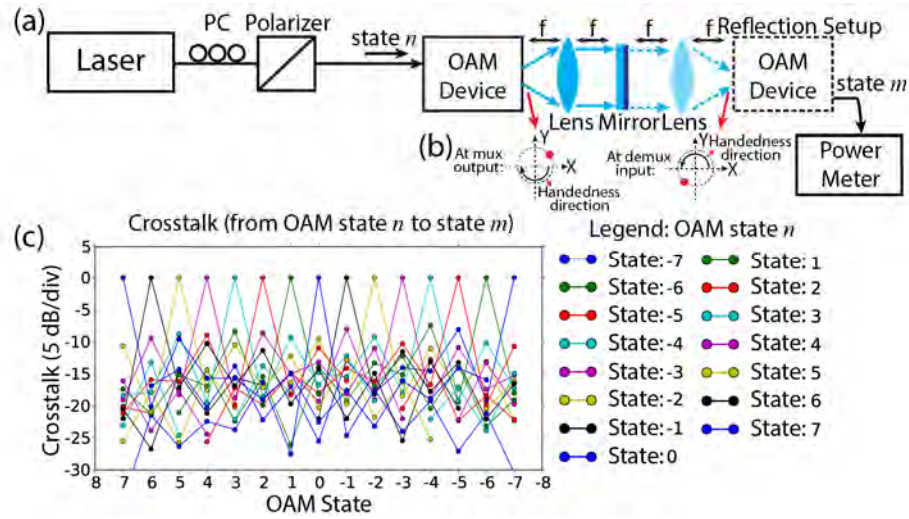


Fig. 7. (a) Crosstalk experimental setup. (b) An example of how the lens and mirror reflection change the beam pattern. (c) Measured crosstalk for OAM state  $n$  to  $m$ .

To measure the crosstalk between one OAM state and all other states, we used a single hybrid device for multiplexing and demultiplexing. Figure 7(a) shows the retro-reflection based setup used to measure the crosstalk. The retro-reflection setup builds a 4- $f$  imaging system with one aspheric lens ( $f = 4.51$  mm) and one mirror. In this particular arrangement,

light at the  $+\ell$  input of the silica PLC (OAM state  $+\ell$ ) comes out at the  $-\ell$  output of the silica PLC, because the mirror reverses the propagation direction for the OAM beam. As Fig. 7(b) illustrates, the lens and mirror also rearrange the beam to different 3D waveguides while changing the handedness of the azimuthal phase. Therefore, when we illuminated input +1 of the silica PLC, we expected to receive a peak value at input -1 on the same silica PLC. This behavior is verified by Fig. 7(c) which shows measurements for the crosstalk between one OAM state and all other states. The crosstalk was measured as the normalized fiber-to-fiber loss from input  $n$  to output  $m$  ( $n \neq m$ ) for the multiplexer/demultiplexer pair. The maximum measured crosstalk is approximately -8 dB which is somewhat worse when compared to the measured OAM spectrum (mode purity) of a single pass through the device (Fig. 2(f) of [12]).

#### 4. Free-space coherent optical communication link experiment

We performed an OAM state link experiment with a 10-GBd quadrature phase shift keyed (QPSK) signal. Figure 8 shows the experimental testbed schematic which includes the free-space coherent SDM link of 1.8 cm that is based on a retro-reflecting 4- $f$  imaging system. In the setup, we used one hybrid OAM device as both the OAM multiplexer and demultiplexer. The transmitter used an external cavity laser (ECL) with a linewidth of 100 kHz and tuned to 1546 nm. A portion of the laser output was sent to the receiver after an acousto-optic modulator (AOM) frequency shifted the carrier by 35 MHz. An electrical arbitrary waveform generator (EAWG) drove the I/Q modulator to generate a 10-GBd QPSK signal, with a  $2^7-1$  pseudorandom bit sequence (PRBS). Offline digital signal processing (DSP) created a pre-emphasized (shaped) QPSK signal with a 10-GHz, 6-dB bandwidth Nyquist filter (roll-off factor is 0.2) [21]. As a result, the single channel spectral efficiency was 1.67 b/s/Hz [2]. We included an erbium-doped fiber amplifier (EDFA) to increase the output signal power from the I/Q modulator to 15 dBm. Since the transmitter, noise loader, and receiver were located in a room separate from the OAM device, a 25-m fiber, polarization stabilizer, and EDFA were used between the transmitter and OAM device. An attenuator before the OAM device was used to optimize the input power and a 2-m fiber temporally decorrelated the signal patterns on the two inputs when we transmitted two OAM states simultaneously.

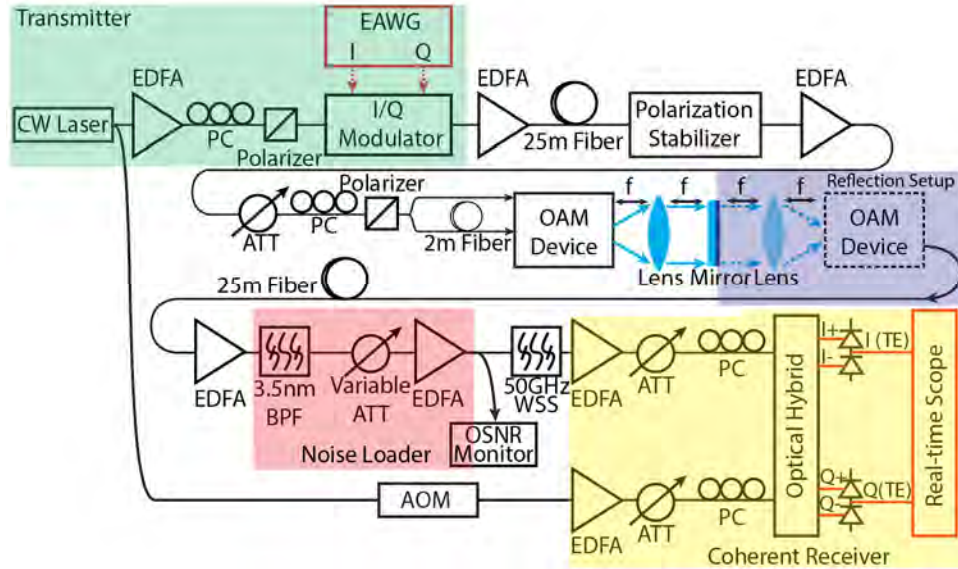


Fig. 8. 10-GBd QPSK link experimental arrangement using a retro-reflecting free-space link. EAWG: electrical arbitrary waveform generator. EDFA: erbium-doped fiber amplifier. PC: polarization controller. ATT: attenuator. BPF: bandpass filter. AOM: acousto-optic modulator. WSS: wavelength selective switch.



After demultiplexing, the signal passed through 25 m of fiber before it was amplified by an EDFA with a 3.5-nm bandpass filter (BPF) to minimize the out-of-band noise. We varied the optical signal-to-noise ratio (OSNR) by using a variable optical attenuator and an EDFA directly after the BPF. On the receiver side, the signal, as well as a 35-MHz frequency shifted local oscillator (LO), enters a polarization diversity optical hybrid. Both the real and the imaginary parts of the coherently detected signal were collected by a 50 GS/s real-time oscilloscope (16-GHz, 3-dB bandwidth).

We applied offline DSP to evaluate bit-error-rate (BER) performance for the received data using the following steps. The DSP first extracted the clock tone from the Fourier transform of the received magnitude-squared signal in the time domain [22]. Next, the data were resampled to 20 GS/s. A 13-tap finite impulse response (FIR) filter adapted by a constant modulus algorithm [23] constituted an adaptive equalizer, which was applied to the resampled waveform. Lastly, carrier phase recovery used the power-of-four average method [22].

Figure 9(a) shows the individual BER performance for OAM states from  $\ell = +1, +2, \dots, +7$  to  $\ell = -1, -2, \dots, -7$  measured by varying the OSNR. The blue curve on the left side in Fig. 9(a) shows the theoretical QPSK BER performance with differential decoding based error counting [21]. The green curve shows the back-to-back (b2b) BER performance which has an OSNR implementation penalty of  $\sim 2$  dB at  $\text{BER} = 10^{-3}$ . In our experiment, the back-to-back arrangement directly connects the modulator output to the noise loader and coherent receiver in Fig. 8. For OAM states  $+1, +2, \dots, +7$ , there is a 0.5-dB OSNR penalty when measured at  $\text{BER} = 10^{-3}$ . This small penalty is mainly due to the differences in EDFAs used compared to the back-to-back case. The BER measurement registered no errors detected when the OSNR  $> 14$  dB (received power  $> -36.9$  dBm) with the measured 379,960 bits. This indicates the upper-bound of the BER value to be  $< 10^{-5}$  with 97.7% confidence level [24, 25].

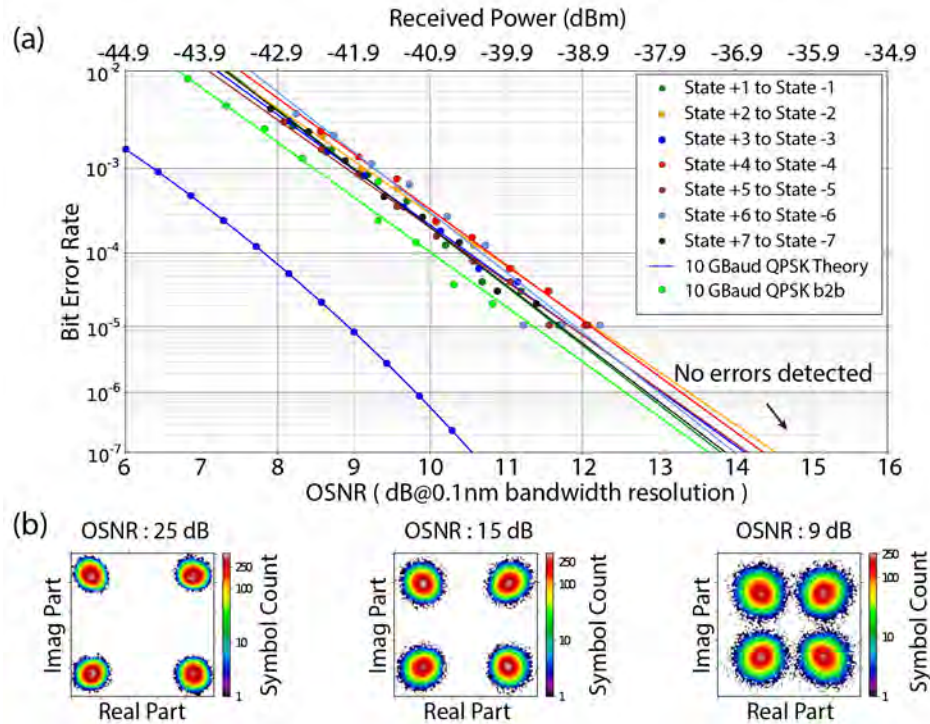


Fig. 9. Link performance for a single transmitted OAM state. (a) BER performance for a 10-GBd QPSK link using OAM states  $+1, +2, \dots, +7$ . (b) Constellation plots at 25 dB, 15 dB and 9 dB OSNR.



We note that hard decision forward-error correction (FEC) such as Reed Solomon method with RS(255,239) coding [26] can bring the raw data with  $\text{BER} < 1.4 \times 10^{-4}$  to error-free performance (i.e.,  $\text{BER} < 10^{-12}$ ). Figure 9(b) shows the constellations for OAM state  $\ell = +1$  at OSNRs of 25 dB, 15 dB and 9 dB, respectively. The slightly non-circular nature of the constellation points arises mainly from the imperfect waveform generation at the transmitter and is not due to the hybrid OAM device since it is present in the back-to-back case as well. Again, when the OSNR is larger than 14 dB, the constellation points are well isolated, which supports the measured error-free performance.

## 5. Two-OAM-state, free-space coherent optical communication link experiment

In the next step, we demonstrated the free-space coherent optical communication link while multiplexing and demultiplexing two simultaneous OAM states. The experimental arrangement is the same as shown in Fig. 8, with the addition of a second illuminated input on the silica PLC. To illustrate performance for various cases, we used the crosstalk measurements in Fig. 7 and chose additional (interfering) states that represented the highest, lowest and average crosstalk scenarios for the OAM states +1 and +3.

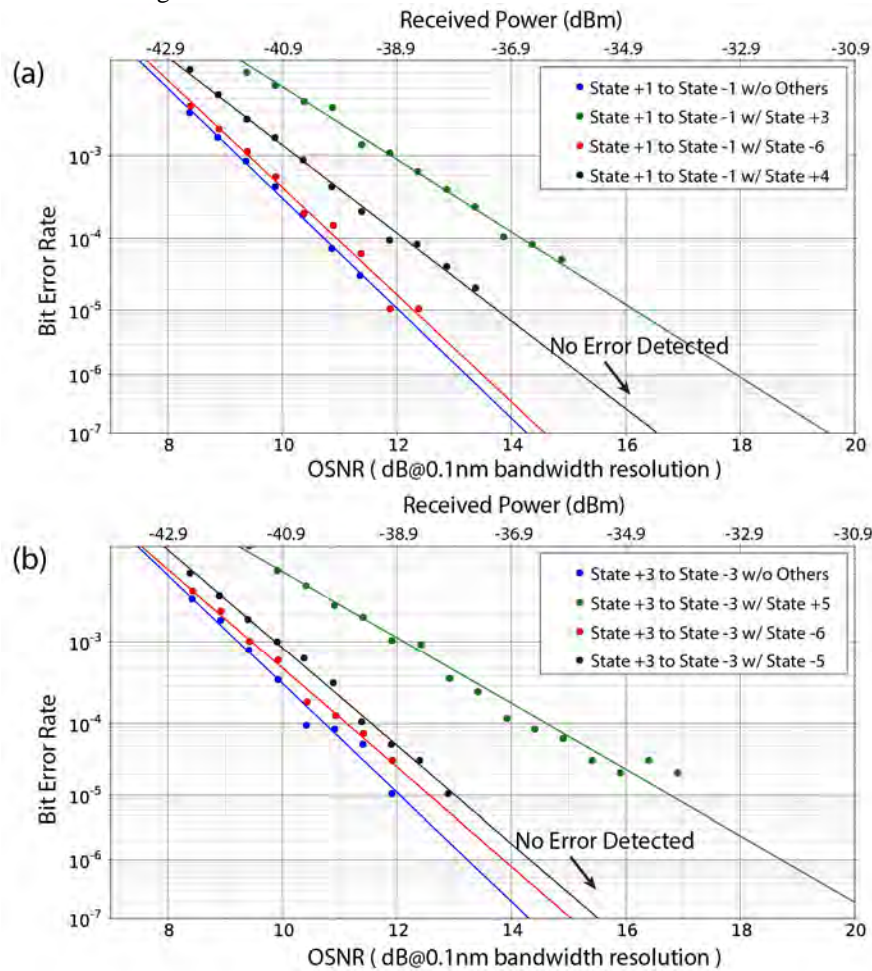


Fig. 10. Link performance for two simultaneous OAM states with varying amounts of crosstalk. (a) BER performance for a 10-GBd QPSK link using OAM state +1 to -1 with, and without, other states (interferer) present. (b) BER performance for a 10-GBd QPSK link using OAM state +3 to -3 with, and without, other states (interferer) present.

Figure 10(a) shows the BER performance (379,960 bits tested) for OAM state + 1, with or without the interfering OAM states of + 3, -6, or + 4. At OSNR > 18 dB (or received power > -32.9 dBm), no errors were recorded with the interfering OAM states. Therefore, error-free performance can be easily achieved with hard decision FEC. The crosstalk between OAM state + 1 and + 3 is -8.38 dB (highest). The crosstalk between OAM state + 1 and -6 is -23.19 dB (lowest). The crosstalk between OAM state + 1 and + 4 is -16.93 dB (average). From the BER performance, the worst case interference (highest crosstalk) between OAM state + 1 and + 3 induces a 2.7-dB OSNR penalty ( $\text{BER} = 10^{-3}$ ) compared to the single state case, while the average and best cases have less than 1-dB OSNR penalty.

Figure 10(b) shows the BER performance for the OAM state + 3, with or without the interfering OAM states + 5, -6, or -5. The crosstalk between OAM state + 3 and + 5 is -8.79 dB (highest). The crosstalk between OAM state + 3 and -6 is -23.87 dB (lowest). The crosstalk between OAM state + 3 and -5 is -17.09 dB (average). Again, the BER performance for the highest case crosstalk (OAM state + 3 and + 5) shows a 2.7-dB OSNR penalty measured at  $\text{BER} = 10^{-3}$  when compared to the case without interfering OAM states. The channels with average or lower crosstalk display less than 1-dB OSNR penalty. Again, at OSNR > 18 dB (or received power > -32.9 dBm), no errors were recorded, which indicates that error-free performance would be easily achieved with hard decision FEC. A fully packaged device with smaller phase errors and better phase stability is expected to reduce the crosstalk and improve the BER performance with multiple OAM states.

## 6. Conclusion

We have demonstrated a hybrid photonic integrated circuit composed of a silica PLC and 3D waveguide PIC which multiplexes and demultiplexes 15 OAM states. Spatial shearing interferometry provided near-field phase characterization to verify that the hybrid OAM produced the correct azimuthal phase for all 15 OAM states. In a retro-reflection arrangement for multiplexing/demultiplexing, the average device crosstalk was -17 dB and the maximum crosstalk was -8 dB. A free-space SDM coherent optical transmission link experiment with a 20-Gb/s QPSK signal and individual OAM beam multiplexing/demultiplexing showed the capability for error-free transmission at OSNR > 14 dB for all of the OAM states, and similar error-free transmission was demonstrated with two simultaneous OAM states for OSNR > 18 dB if hard decision FEC were employed. Future work includes investigating packaging techniques for hybrid device integration with better alignment and phase stability, as well as using multiple devices to perform link experiments with the multiplexing of additional states.

## Acknowledgments

This work was supported in part by DARPA DSO under the contracts HR0011-11-1-0005 and W911NF-12-1-0311.

# Demonstration of Orbital Angular Momentum State Conversion using Two Hybrid 3D Photonic Integrated Circuits

Chuan Qin,<sup>1</sup> Binbin Guan,<sup>1</sup> Ryan Scott,<sup>1</sup> Roberto Proietti,<sup>1</sup> Nicolas K. Fontaine,<sup>2</sup> Tiehui Su,<sup>1</sup> Carlo Ferrari,<sup>3</sup> Mark Cappuzzo,<sup>3</sup> Fred Klemens,<sup>3</sup> Bob Keller,<sup>3</sup> Mark Earnshaw,<sup>3</sup> and S. J. B. Yoo<sup>1\*</sup>

<sup>1</sup>Department of Electrical and Computer Engineering, University of California, Davis, CA 95616, USA

<sup>2</sup>Bell Laboratories, Alcatel-Lucent, 791 Holmdel Rd, Holmdel, NJ 07733, USA

<sup>3</sup>Bell Laboratories, Alcatel-Lucent, 600 Mountain Ave, Murray Hill, NJ 07974, USA

\*sbyoo@ucdavis.edu

**Abstract:** We demonstrate orbital angular momentum state conversion using two 3D photonic integrated circuits for free-space communication of 20-Gb/s QPSK signals. Different combinations of OAM states show error-free performance with 379,960 bits tested.

**OCIS codes:** (060.1810) Buffers, couplers, routers, switches and multiplexers; (050.4865) Optical vortices; (060.4230) Multiplexing

## 1. Introduction

Recent optical networks start to employ space-division multiplexing (SDM) to support the increasing capacity needs while maintaining high spectral efficiency. One such SDM method, orbital angular momentum (OAM) has the advantage of using relatively simple cylindrically symmetric modes. The OAM beam shows an azimuthal phase change of  $\varphi(r, \phi) = \exp(i\ell\phi)$  where  $\phi$  is the azimuthal angle and  $\ell$  the charge number of OAM state. The early work of Allen [1] on OAM was followed by a number of papers experimentally demonstrating OAM generation, sorting, multiplexing, and demultiplexing. Typical approaches utilize holograms [2], spatial light modulators (SLMs) [3], dove prisms [4], and other bulk optics. OAM state conversion can also be achieved in techniques involving the holograms, SLMs or bulk optics. However, practical SDM systems greatly benefit from integrated optics on a robust platform, especially if it can achieve arbitrary and simultaneous conversion of multiple OAM channels for future reconfigurable OAM networks. Recently, our group demonstrated silicon photonic OAM multiplexing and demultiplexing devices based on a free propagation region employing a Roland circle and waveguide apertures with grating structures [5] and silica based integrated 3D waveguides [6, 7].

In this paper, we will discuss OAM state conversion using a pair of integrated 3D OAM multiplexing/demultiplexing devices and a non-blocking reconfigurable fiber switch.

## 2. Orbital angular moment device design and operating principle

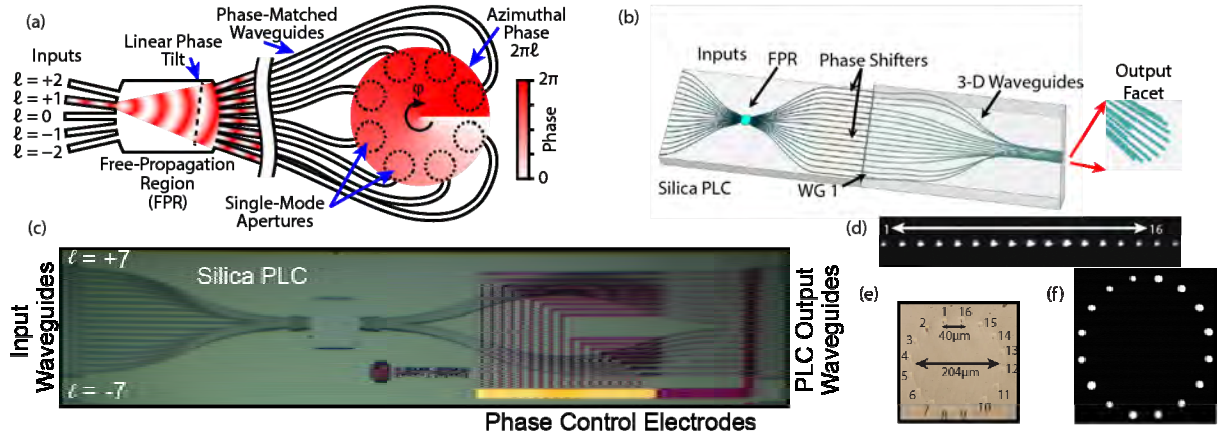
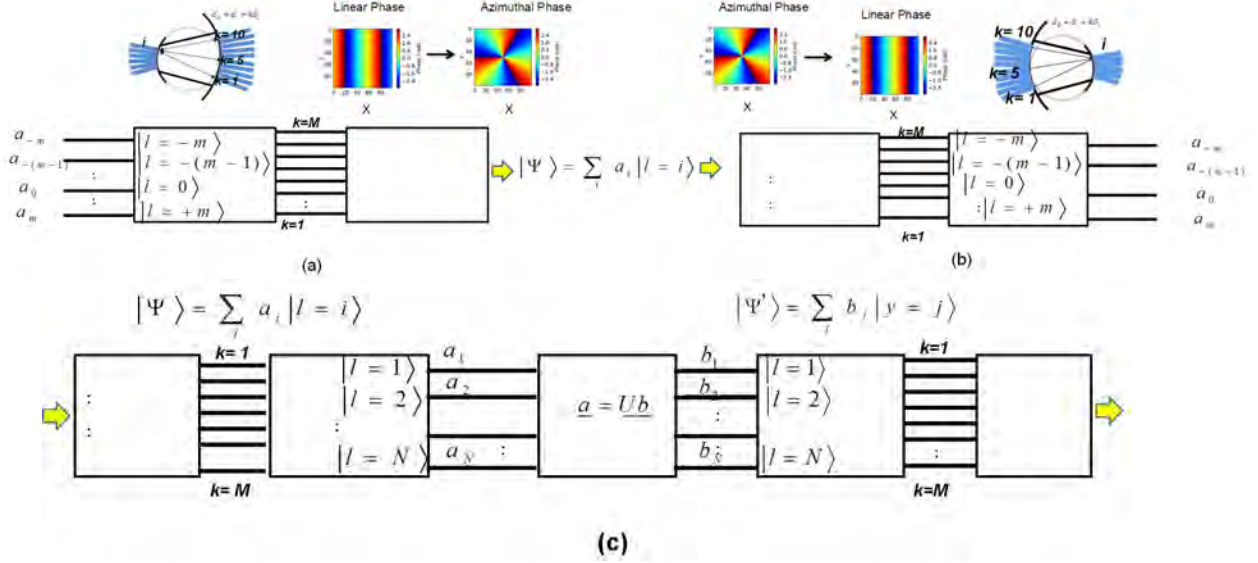
Figure 1(a) shows OAM multiplexer consisting of the 2D photonic integrated circuit (PIC) containing a free-propagation region (FPR) employing the Roland circle, where they laterally expand and the wavefronts acquire a linear phase tilt based on the input waveguide position, and the 3D integrated photonic waveguides with circular-patterned apertures that can emit the superposition of OAM states weighted by the coefficients  $a_m$ ,  $a_{-(m-1)}$ , ..  $a_m$ . Figure 1 (b) shows the OAM demultiplexer that shows the inverse process.

As Figure 1 (c) indicates, OAM state converter consists of the OAM multiplexer and demultiplexer back to back with a reconfigurable optical switch in the middle. Ideally the reconfigurable optical switch is in fact a unitary matrix (loss less) that relates the demuxed coefficients to the new coefficients by a unitary matrix. The reconfiguration of the unitary matrix allows conversion of any input ensemble of the OAM states to any desired ensemble of the OAM states at the output.

In this paper, we will utilize a simple reconfigurable fiber switch for the unitary matrix and utilizes the OAM state converter (Figure 1 (c)) inserted in between the OAM state multiplexer as a transmitter (Figure 1(a)) and the OAM state demultiplexer as a receiver (Figure 1 (c)).

Figure 2 (a) shows a conceptual diagram of photonic integrated circuit based OAM beam generation and multiplexing. The inputs on the left side corresponds to different OAM states ( $\ell = -2$  through  $+2$  shown). The illuminated signal goes through free propagation region (FPR), and its wavefront is linearly tilted. The output of FPR connects with path length matched waveguides. A geometry transformation can convert the linear phase to azimuthal phase variations at the output apertures. When multiple inputs are illuminated simultaneously, the OAM states are multiplexed and overlapped spatially at the output. In opposite, spatially overlapped OAM states can be sampled by circular patterned apertures and retrieved, separately. Therefore, the same device can be used as OAM states demultiplexer. Figure 2 (b) shows the conceptual implementation of Figure 2 (a). The hybrid device consists

of a silica PLC and a 3D waveguide circuit. The silica PLC applies linear tilted phase on different inputs through FPR. The 3D waveguide circuit converts the linear phase to azimuthal phase geometrically. There are electrical heaters on each output waveguides of the silica PLC to provide necessary phase error corrections. Figure 2 (c) shows an image of the real silica PLC device and Figure 2 (e) shows the image of the output facet of 3D waveguide. Figure 2 (d) and (f) shows the output mode profile from silica PLC and 3D waveguide respectively.



### 3. OAM state conversion testbed

Figure 3 shows the OAM state conversion testbed with OAM multiplexing and demultiplexing devices including approximately 1.6 m free-space transmission. The CW laser with a 100 kHz linewidth has a wavelength at 1550 nm. The signal is modulated by an electrical arbitrary waveform generator (eAWG) driven in-phase quadrature-phase modulator (I/Q modulator) using 10GBd  $2^7-1$  pseudo-random bit sequence (PRBS) quadrature phase shift keying (QPSK) signal with a spectral efficiency of 1.67 b/s/Hz created by offline digital signal processing (DSP). A 27dBm erbium-doped amplifier amplifies the signal before the OAM devices. The signal goes into the OAM device #1 as OAM state -1 and comes out as OAM state -1. The free-space transmission includes an 8-f imaging system. The focus of lens #1 and #4 is 4.51mm and of lens #2 and #3 is 200mm. At the output of the OAM device #2 we switch the signal to OAM state -4 after an EDFA and 1nm bandpass filter which minimizes the out-of-band noise and send it back to the OAM device #2. The OAM device #1 would receive the signal as OAM state -4. The counter-propagating transmission reduces the crosstalk otherwise appears in co-propagating transmission (or loopback



configuration). The signal goes through the noise loading part before it enters the coherent receiver that has a polarization diversified optical 90° hybrid and a real-time oscilloscope at 50GS/s. A local oscillator comes from the same laser with 35 MHz frequency offset shifted by an acousto-optic modulator (AOM). Offline DSP applies clock recovering, 13-tap finite impulse response (FIR) filter based equalizer and carrier phase estimation. In the end, the DSP calculated the bit-error-rate (BER).

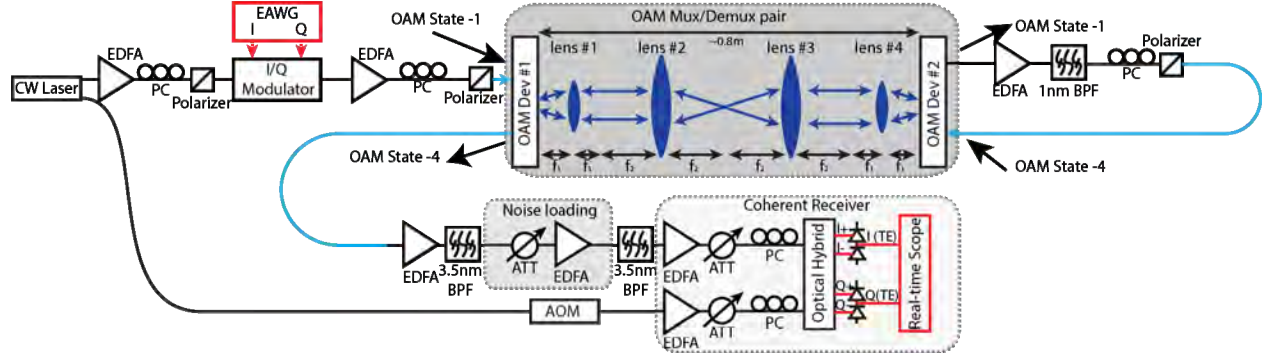


Figure 3. 10-Gb/s QPSK link experiment tested for OAM state conversion using two OAM hybrid devices with ~1.6m round-trip free-space transmission. EDFA: erbium-doped fiber amplifier. PC: polarization controller. ATT: attenuator. BPF: bandpass filter. AOM: acousto-optic modulator.

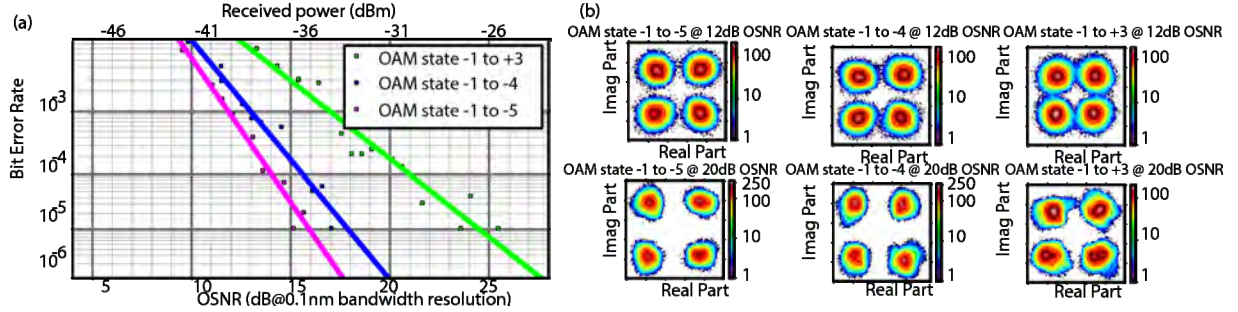


Figure 4. (a) BER performance for OAM state -1 as the input and switched to +3, -4 and -5. (b) Constellation plots for each case at OSNR of 12dB and 20dB.

#### 4. Experimental results and BER performance

Figure 4 (a) shows the BER performance with 379,960 bits tested for input OAM state -1 switched to OAM state -5, -4 and +3. Note that the BER is less than  $10^{-5}$  (no errors are recorded) when OSNR is more than 16dB for -1 to -5 conversion, 18dB and 25 dB for -1 to -4 and -1 to +3 respectively. Figure 4 (b) shows the constellation plots for the three conversion cases in Figure 4 (a) at both 12dB and 20dB OSNR. We notice that the OAM state -1 to +3 has the worst BER performance in three and -1 to -5 has the best performance.

#### 5. Summary

This paper discusses OAM state conversion using a pair of integrated 3D OAM multiplexing/demultiplexing devices and a non-blocking reconfigurable fiber switch. 10GBaud QPSK signal is transmitted and BER shows error-free performance with hard decision FEC for three conversion cases we tested. Future work includes simultaneous multiple OAM state conversion by improving the crosstalk and loss from the device.

#### 6. References

- [1] L. Allen, *et al.*, *Physical Review A*, **45**, 8185-8189 (1992).
- [2] M. W. Beijersbergen, *et al.*, *Optics Communications*, **112**, 321-327 (1994).
- [3] J. Wang, *et al.*, *Nature Photonics*, **6**, 488-496 (2012).
- [4] J. Leach, *et al.*, *Physical Review Letters*, **88**, 257901 (2002).
- [5] T. Su, *et al.*, *Optics Express*, **20**, 9396-9402 (2012).
- [6] B. Guan, *et al.*, in *CLEO: 2013*, CTu1L.4 (2013).
- [7] R. P. Scott, *et al.*, in *European Conference and Exhibition on Optical Communication (ECOC)*, Tu.3.B.2 (2013).

This work was supported in part by DARPA DSO under the contracts HR0011-11-1-0005 and W911NF-12-1-0311.



# Integrated Optical Orbital Angular Momentum Multiplexing Device using 3-D Waveguides and a Silica PLC

Binbin Guan,<sup>1</sup> Ryan P. Scott,<sup>1</sup> Nicolas K. Fontaine,<sup>2</sup> Tiehui Su,<sup>1</sup> Carlo Ferrari,<sup>3</sup> Mark Cappuzzo,<sup>3</sup> Fred Klemens,<sup>3</sup> Bob Keller,<sup>3</sup> Mark Earnshaw,<sup>3</sup> and S. J. B. Yoo<sup>1</sup>

<sup>1</sup>Department of Electrical and Computer Engineering, University of California, Davis, CA 95616, USA

<sup>2</sup>Bell Laboratories, Alcatel-Lucent, 791 Holmdel Rd, Holmdel, NJ 07733, USA

<sup>3</sup>Bell Laboratories, Alcatel-Lucent, 600 Mountain Ave, Murray Hill, NJ 07974, USA  
sbyoo@ucdavis.edu

**Abstract:** We demonstrate a low-loss hybrid-integrated device based on a silica planar lightwave circuit (PLC) coupled to a 3-D photonic circuit that efficiently generates and multiplexes 15 optical orbital angular momentum (OAM) modes in free space.

**OCIS codes:** (050.4865) Optical vortices; (060.4230) Multiplexing; (050.6875) Three-dimensional fabrication

There is significant interest in utilizing space-division multiplexing (SDM), like time-division multiplexing and wavelength-division multiplexing, to increase the photon efficiency or spectral efficiency of free-space and fiber-optic links. SDM includes using optical orbital angular momentum (OAM) modes [1] (e.g., beams with azimuthally varying optical phase) to provide orthogonal information channels. Practical applications require integrated devices that multiplex and demultiplex OAM modes onto/from multi-mode fibers or free-space and also interface with single-mode fiber (SMF) components such as modulators and coherent receivers. Previously, our group and others have demonstrated OAM multiplexing using silicon photonic integrated circuits (PICs) [2, 3] that generate OAM beams with a single polarization from a waveguide grating structure. Here, we demonstrate an integratable OAM multiplexer based on hybrid integration of a silica planar lightwave circuit (PLC) with a silica 3-D PIC that supports up to 15 OAM modes, both TE and TM polarizations, and shows relatively low optical loss at 1.55  $\mu\text{m}$ .

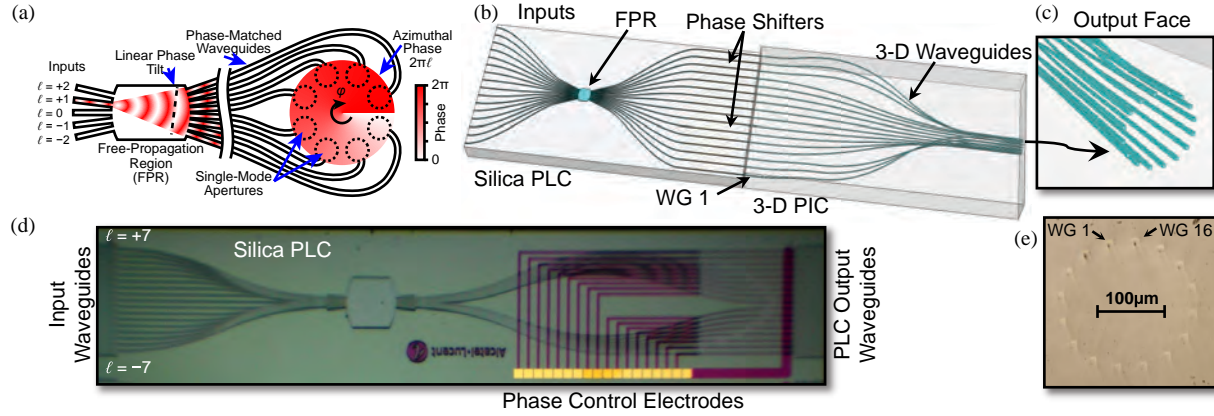


Fig. 1. (a) Device concept. (b) Illustration of the silica PLC coupled to the 3-D PIC. (c) Detail of output face of 3-D waveguides. (d) Photo of fabricated silica PLC. (e) Photo of 3-D PIC output face before polishing.

Fig. 1(a) shows the device's operating principle is based on converting linearly varying spatial phase to azimuthal variations [i.e.,  $\exp(iblx) \rightarrow \exp(il\phi)$ , where  $b$  is the linear ( $x$ ) to azimuthal ( $\phi$ ) scaling factor]. Each single mode input (i.e.,  $l = -2, -1, 0, +1, +2$ ) will create a wavefront in the free-propagation region (FRR) with a different linear tilt. The phase tilt is maintained while propagating through the phase-matched waveguides to the corresponding output apertures which are arranged in a circular pattern to create a beam with azimuthally varying phase having topological charge  $l$ . Multiple inputs can be illuminated to multiplex OAM beams. By reciprocity, if an outside OAM beam illuminates the apertures, the sampled light will be focused in the FPR to a waveguide corresponding to the beam's  $l$ -number. As Fig. 1(b) shows, this concept is implemented by a silica PLC which converts input position to a linear phase tilt coupled to a 3-D PIC that geometrically converts the linear phase tilt to an azimuthal phase variation. Fig. 1(c) presents the output face detail of the 3-D waveguides.

The waveguides on the silica PLC have a  $\Delta n$  of 2%. Fig. 1(d) is a photo of the fabricated PLC. Electrical heaters on each output waveguide provide thermo-optic based phase-error correction (PEC) to correct for path-length (phase) variations in the 3-D PIC. Fig. 2(a) (circles) shows the measured excess loss for the silica PLC when coupling to/from SMF with index matching fluid (3.5 dB average).

Using our design, the 3-D PIC was fabricated at a commercial foundry by direct laser writing of the optical waveguides in bulk fused silica. The technique uses focused femtosecond laser pulses to increase the refractive index via multi-photon absorption directly inside a transparent dielectric material [4]. Three-axis translation of the material during writing enables the 3-D characteristics of the waveguides. The 3-D waveguide had a  $\sim 10\text{-}\mu\text{m}$  mode field diameter (i.e., similar to SMF). The input waveguides of the 3-D PIC had a  $127\text{-}\mu\text{m}$  pitch to match the PLC. The 3-D PIC was  $15\text{-mm}$  long and, over that distance, the waveguides carefully transition from the linear array to a  $204\text{-}\mu\text{m}$  diameter circle on the output face [Fig. 1(e)]. The output waveguide center-to-center spacing is  $40\text{ }\mu\text{m}$ . Fig. 2(a) (squares) shows the measured 3-D waveguide loss ( $1.7\text{ dB}$  average), including coupling loss.

To characterize the hybrid device (PLC and 3-D PIC), we imaged the device's output (i.e., near-field) onto an IR camera with a total magnification of  $\sim 50\times$  while illuminating only one PLC input at a time. The absolute phase (to within a constant) was measured using shearing interferometry. Fig. 2(b) shows a false-color (linear scale) image of the near-field intensity and phase patterns when input  $\ell = 0$  is illuminated without PEC. Fig. 2(c) shows the improvement with PEC (nearly same phase, correct for  $\ell = 0$ ). Fig. 2(d) is a plot of the phase for each output waveguide to more clearly show the improvement with PEC. The output phase was then similarly measured for each device input ( $\ell = -7, \dots, 0, \dots, +7$ ) and the unwrapped phase is plotted in Fig. 2(e). To estimate the OAM mode purity we can take the Fourier transform of the near-field amplitude and phase data for each of the device inputs. Fig. 2(f) shows how well the device creates each OAM mode where the difference between a mode peak and the "noise" determines the OAM mode crosstalk (below  $-12\text{ dB}$ ). Fig. 2(g-i) show the measured near-field pattern intensity and phase for several different example OAM modes (typical).

We have demonstrated multiplexing of OAM states using a silica PLC and 3-D PIC that supports 15 modes. By increasing the number of waveguides, it is straightforward to expand the number of modes well beyond 50. This work shows an integratable device that supports both polarizations and is a lower loss alternative to silicon PICs.

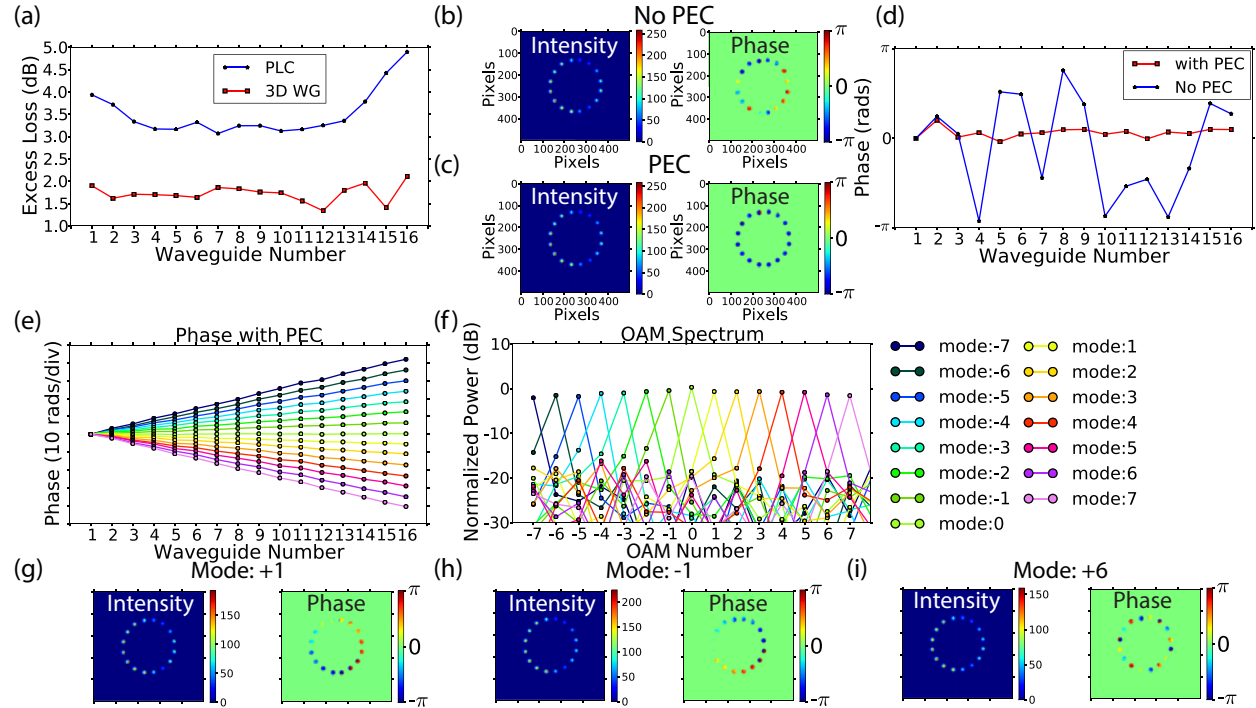


Fig. 2. (a) Measured excess loss for the silica PLC and 3-D waveguides. (b) Measured intensity and phase of the device's output waveguides without PEC, (c) with PEC. (d) Measured average azimuthal phase at each output waveguide. (e) Unwrapped azimuthal phase for each OAM mode. (f) Calculated OAM mode purity. (g-i) The measured intensity and phase for three OAM modes ( $\ell = +1, -1, +6$ ).

- [1] L. Allen, *et al.*, "Orbital angular momentum of light and the transformation of Laguerre-Gaussian laser modes," *Phys. Rev. A*, **45**, 8185-8189 (1992).
- [2] T. Su, *et al.*, "Demonstration of free space coherent optical communication using integrated silicon photonic orbital angular momentum devices," *Opt. Express*, **20**, 9396-9402 (2012).
- [3] N. K. Fontaine, *et al.*, "Efficient multiplexing and demultiplexing of free-space orbital angular momentum using photonic integrated circuits," in *OFC/NFOEC*, Paper OTu11.2 (2012).
- [4] Y. Nasu, *et al.*, "Low-loss waveguides written with a femtosecond laser for flexible interconnection in a planar light-wave circuit," *Opt. Lett.*, **30**, 723-725 (2005).

This work was supported in part by DARPA DSO under the contract HR0011-11-1-0005.

# Polarization-Diversified, Multichannel Orbital Angular Momentum (OAM) Coherent Communication Link Demonstration using 2D-3D Hybrid Integrated Devices for Free-Space OAM Multiplexing and Demultiplexing

Binbin Guan,<sup>1</sup> Chuan Qin,<sup>1</sup> Ryan P. Scott,<sup>1</sup> Nicolas K. Fontaine,<sup>2</sup> Tiehui Su,<sup>1</sup> Roberto Proietti,<sup>1</sup> and S. J. B. Yoo<sup>1,\*</sup>

<sup>1</sup>Department of Electrical and Computer Engineering, University of California, Davis, CA 95616, USA

<sup>2</sup>Bell Laboratories, Alcatel-Lucent, 791 Holmdel Rd, Holmdel, NJ 07733, USA

\*sbyoo@ucdavis.edu

**Abstract:** We present dual-polarization QPSK link transmission performance below the FEC limit with simultaneous transmission of three OAM states carrying 14×10-GBd WDM channels using silica 2D-3D hybrid integrated devices for OAM state multiplexing/demultiplexing capacity of 1.68 Tb/s.

**OCIS codes:** (060.1660) Coherent communications; (050.4865) Optical vortices; (060.4230) Multiplexing

Currently, space-division multiplexing (SDM) has generated great interest as a means to increase the spectral efficiency and communication capacity of free-space and telecommunications networks [1]. In particular, SDM based on orbital angular momentum (OAM) is attractive due to the natural orthogonality of the OAM states and the potential compatibility of the cylindrically symmetric beams with various types of multimode fiber (e.g., ring core, etc.). Light beams carrying OAM show an azimuthal phase variation of  $\varphi(r, \phi) = \exp(i\ell\phi)$  where  $\phi$  is the azimuthal angle, integer  $\ell$  is the charge number or OAM state [2], and  $\varphi(r, \phi)$  is the phase of the wavefront. Multiple demonstrations of OAM links based on bulk-optic OAM beam generators and sorters have been previously reported [3]. However, practical implementations would greatly benefit from integrated, polarization-diversified OAM state multiplexers and demultiplexers. Our group [4] and others [5] have recently demonstrated OAM mux/demux devices based on 2D (planar) photonic integrated circuits in silicon that utilize grating structures that are polarization dependent. More recently, we reported the single-polarization performance of a OAM mux/demux device based on hybrid integration of a silica planar lightwave circuit (PLC) and a direct laser inscribed 3-D waveguide structure [6]. Here, we significantly extend that work and demonstrate a polarization diversified free-space OAM link with simultaneously three OAM states and 14 wavelength channels using two OAM hybrid devices as an OAM mux/demux pair. Each wavelength channel has 10-GBd, dual-polarization quadrature phase shift keying (DP-QPSK) data for an aggregate capacity of 1.68 Tb/s and spectral efficiency of 9.6 bits/s/Hz.

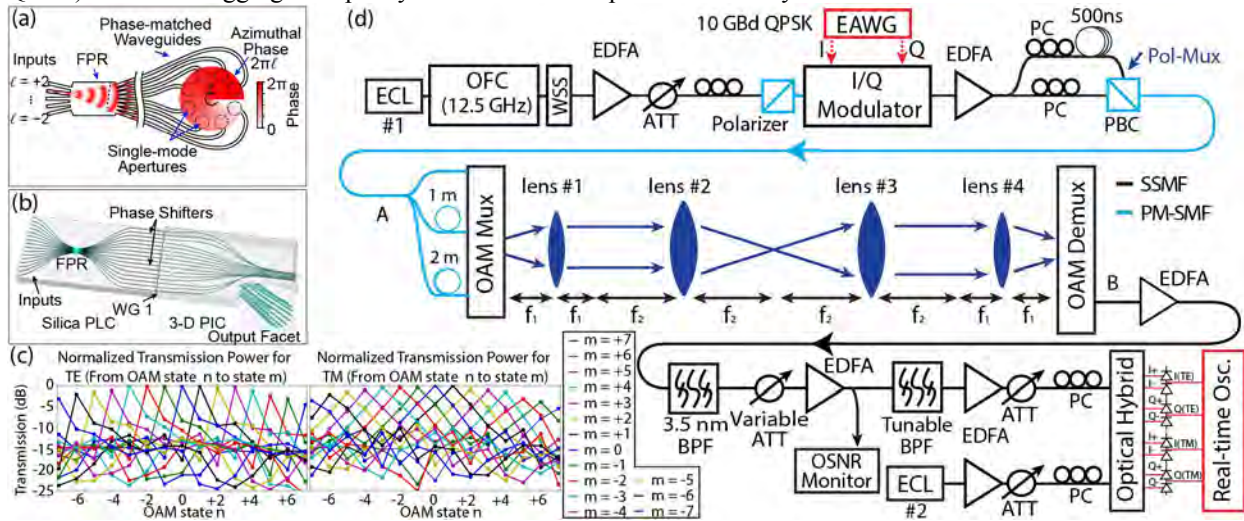


Fig. 1. (a) Concept of the OAM photonic integrated circuit. (b) Conceptual view of the 2D-3D hybrid integrated device for OAM mux/demux. (c) Normalized transmission of the OAM mux/demux pair for each polarization. (d) Experimental arrangement of the multichannel OAM polarization-diversified free-space communication link testbed. FPR: free-propagation region; ECL: external cavity laser; OFC: optical frequency comb; WSS: wavelength-selective switch; EDFA: erbium-doped fiber amplifier; ATT: attenuator; PC: polarization controller; PBC: polarization beam combiner; BPF: bandpass filter. EAWG: electrical arbitrary waveform generator.



Fig. 1(a) shows a conceptual diagram of a photonic integrated circuit (PIC) for OAM state multiplexing/demultiplexing. The free-propagation region (FPR) applies a linear phase tilt on the input light. The phase-matched waveguides sample the output of the FPR and transform the linear phase tilt to azimuthal phase variations at the output apertures. Illuminating multiple inputs simultaneously generates OAM states that spatially overlap at the output apertures, providing true OAM state multiplexing. Alternatively, when operated in reverse, the circular-patterned apertures sample and demultiplex spatially overlapped OAM states [6]. Fig. 1(b) shows a drawing of the 2D-3D hybrid integrated device where the 2D silica PLC is mated with a 3D waveguide circuit fabricated by direct laser inscribing in borosilicate glass (further device details are in [6]). Fig. 1(c) shows the normalized transmission from OAM mux input (A) to OAM demux output (B) for both polarizations. The total loss for OAM state 0 is 19.4 dB (device TE) and 19.3 dB (device TM). Fig. 1(d) shows the experimental arrangement where a 10-GBd QPSK signal ( $2^{15}$ -1 PRBS) is applied to all 14 WDM channels (12.5-GHz spacing). The modulated signal is polarization multiplexed with a decorrelation of 500-ns between the two polarization states. After multiplexing up to three OAM states through the first hybrid device, the spatially overlapped beams are transmitted over a 81.8 cm free-space link, demultiplexed by the second hybrid device and sent to the polarization diversified coherent receiver with offline DSP. The DSP uses an adaptive equalizer, which includes a 17-tap finite impulse response (FIR) filter and power-of-four methods for phase and frequency recovery and direct-decision based bit-error counting.

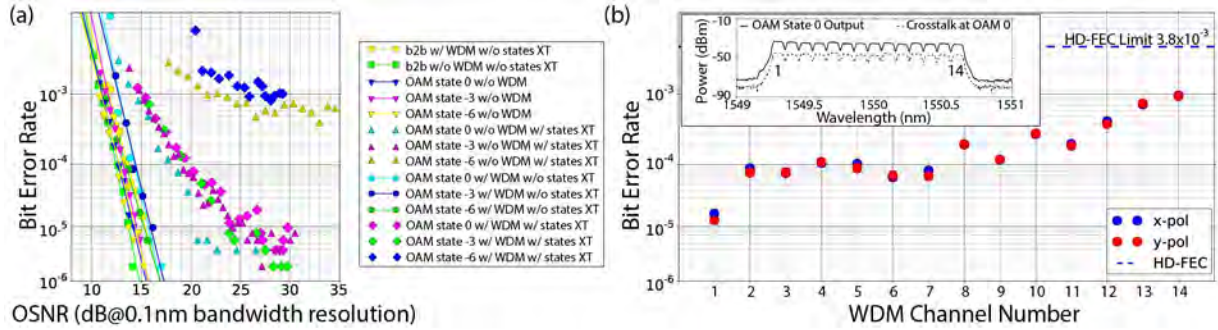


Fig. 2. (a) BER performance for the multichannel OAM link with  $14 \times 10$ -GBd, DP-QPSK WDM channels. (b) Averaged BER for three OAM states (0, -3 and -6) for two received orthogonal polarizations (x-pol and y-pol not necessarily the same as device TE and TM).

The averaged bit-error-rate (BER) of two polarization states for a multichannel free space transmission link was measured. We use OAM states -6, -3 and 0 for the transmission link experiment. The measured crosstalk values at all three OAM states outputs are between -10.5 dB and -11.6 dB for TE, between -10.2 dB and -14.1 dB for TM. Fig. 2(a) shows the measured BER for the following cases: i) back to back transmission without WDM or OAM state crosstalk (XT); ii) back to back transmission with all the wavelength channels; iii) single OAM state and single wavelength channel transmission without crosstalk from other OAM states; iv) all three OAM states transmission with a single wavelength channel; v) single OAM state with all the wavelength channels but without crosstalk from other OAM state; vi) all three OAM states transmission with all the wavelength channels. There is ~3-dB OSNR penalty for OAM state 0 and -3 transmission with OAM states crosstalk. However, the OSNR penalty for OAM state -6 is much higher due to a joint effect of crosstalk and polarization dependent loss (PDL). In the future, more precise phase error correction can further reduce the crosstalk. PDL is mainly from the submicron misalignment in the device setup. Fig. 2(b) shows that the measured averaged BER values with three OAM states and all wavelength channels are below HD-FEC limit of  $3.8 \times 10^{-3}$  (BCH(1020,988) super FEC code, 7% overhead) [7].

In summary, we have demonstrated a multichannel OAM free-space coherent communication link using two separate photonic hybrid devices with polarization diversity. We transmitted  $14 \times 10$  GBd DP-QPSK signals simultaneously on three OAM states that shows the averaged BER of both polarization states for all three OAM states at all wavelength channels are below HD-FEC limit. Future work includes device packaging to improve device stability and device design changes to reduce crosstalk for additional OAM state multiplexing.

- [1] P. J. Winzer, *IEEE Photon. J.*, **4**, 647-651 (2012).
- [2] L. Allen, *et al.*, *Phys. Rev. A*, **45**, 8185-8189 (1992).
- [3] J. Wang, *et al.*, *Nature Photon.*, **6**, 488-496 (2012).
- [4] T. Su, *et al.*, *Opt. Express*, **20**, 9396-9402 (2012).
- [5] N. K. Fontaine, *et al.*, in *OFC/NFOEC*, (2012).
- [6] B. Guan, *et al.*, *Opt. Express*, **22**, 145-156 (2014).
- [7] ITU-T, in *G.975.1 : Forward error correction for high bit-rate DWDM submarine systems, Appendix I.9*, (2004).

This work was supported in part by DARPA DSO under the contracts HR0011-11-1-0005 and W911NF-12-1-0311.

# 3D Waveguide Technologies for Generation, Detection, Multiplexing/Demultiplexing Orbital Angular Momentum Optical Waves

R. P. Scott<sup>1</sup>, S. J. B. Yoo<sup>1</sup>

<sup>1</sup>Department of Electrical and Computer Engineering, University of California, Davis, California 95616, U.S.A.

## Paper Summary

*We will discuss 3D photonic integrated circuits for arbitrary beam forming and spatial division multiplexing using orbital angular momentum states (OAM). We will demonstrate free-space communication and signal processing utilizing OAM Mux/Demux and switching.*

## Introduction

Rapid and exponential increases in data communications are continuing to drive the complexity of our computing, networking, and sensing systems. High degrees of integration is essential in scalable, practical, and cost-effective microsystems. In electronics, high-density 2D integration has naturally evolved towards 3D integration by stacking of memory and processor chips with through-silicon-vias. In photonics, too, we anticipate high-degrees of 3D integration of photonic components to become a prevailing method in realizing future microsystems for information and communication technologies. However, compared to electronics, photonic 3D integration face a number of challenges. This paper will discuss 3D photonic integration and its future applications.

## Orbital Angular Momentum Mux/Demux

**Figure 1(a)** shows the integratable orbital angular momentum multiplexing device's operating principle which relies on converting linearly varying spatial phase to azimuthal variations [i.e.,  $\exp(iblx) \rightarrow \exp(i\ell\phi)$ , where  $b$  is the linear ( $x$ ) to azimuthal ( $\phi$ ) scaling factor]. To illustrate, **Figure 1(a)** shows a waveguide circuit where each single mode input (i.e.,  $\ell = -2, -1, 0, +1, +2$ ) will create a wavefront in the free-propagation region (FPR) with a different linear tilt. The phase-matched waveguides after the FPR sample the tilted phase front and maintain the phase tilt to the output apertures. Since the apertures are arranged in a circular pattern, they create a beam (coming out of the page) with azimuthally varying phase having topological charge  $\ell$ . If multiple inputs are illuminated, those inputs are multiplexed onto collinear OAM beams with  $\ell$ -numbers determined by the input position. By reciprocity, if an outside OAM beam illuminates the apertures, the sampled light will be focused in the FPR to a waveguide corresponding to the beam's  $\ell$ -number (i.e., an OAM demultiplexer). Working as a demux (i.e., OAM state decoder), **Figure 1(b)** shows how a circular array of waveguide grating couplers are used to sample areas (dashed circles) of an incoming

beam encoded with an OAM state (e.g.,  $\ell = 1$ ) into a corresponding array of single-mode waveguides. Careful waveguide layout ensures that they have identical optical path lengths. Thus, at the input of the free-propagation region (FPR), the azimuthally varying phase of the OAM state is converted into a linear phase front with a tilt angle determined by the incoming beam's topological charge, as indicated in **Figure 1(a)**. The circular placement of the array waveguides at the input of the FPR focuses the light, and the tilt of the linear phase front directs it to a corresponding output. Using the PIC as a mux is as simple as reversing the light's propagation direction. This paper demonstrates a full coherent optical communication link including a pair of silicon photonic OAM mux/demux devices.

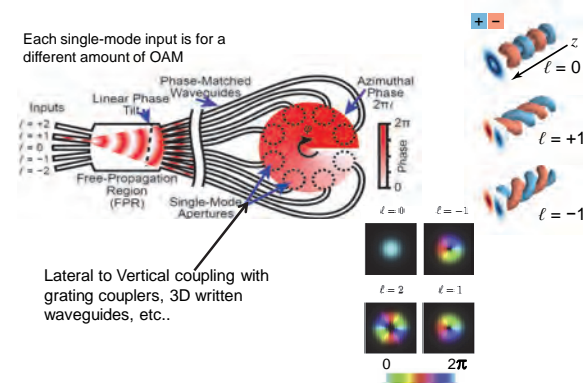


Figure 1. (a) Visualization of the electric field of OAM beams. (b) Illustration showing how a beam encoded with an OAM state is sampled and demultiplexed by a circular arrangement of apertures, length-matched waveguides and a star coupler.

## 3D inscription by femtosecond lasers

Direct laser writing of waveguides in dielectric material is an extremely powerful fabrication technique [1]. It utilizes the multi-photon nonlinear absorption of sub-bandgap photons to create permanent structural changes in a material with dimensions comparable to the writing laser's wavelength (e.g.,  $\sim 1 \mu\text{m}^3$ ). The induced modifications from a sub-picosecond train of optical pulses are strongly localized in three dimensions to the high intensity region at the focus of a lens driven by a nonlinear absorption mechanism. This unique characteristic is what provides direct laser writing its biggest advantage over other waveguide fabrication techniques; the capability to freely form true three dimensional structures[2]. Direct laser writing has been widely demonstrated in many types of materials



including amorphous glasses and crystals with measured losses as low as 0.1 dB/cm (Optoscribe, Ltd specification) [3, 4] in fused silica, and, as an initial demonstration, 0.65 dB/cm [5] in gallium lanthanum sulphide (GLS). This value is expected to go down to 0.1 dB/cm~0.2 dB/cm with writing process optimizations (bulk absorption loss for GLS is less than 0.045 dB/cm). **Figure 2(a)** illustrates the direct laser writing process that will be used to write the emitter waveguides into the 3D block. For visible and near infrared applications, fused silica is widely used for 3D waveguide inscription. **Figure 2(b)** shows a fabricated 3D waveguide fan-out device composed of directly laser writing butt coupled to a 2D waveguide block for orbital angular momentum applications [6-10].

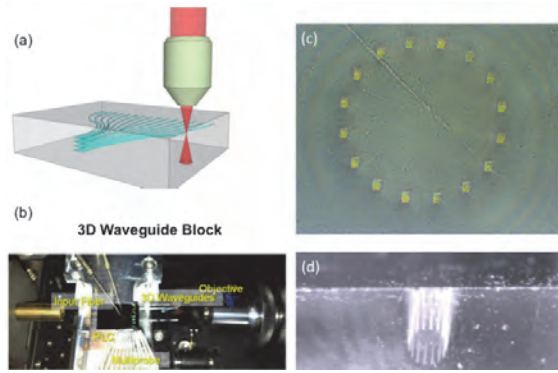


Figure 2. (a) Illustration of 3D waveguide fabrication by direct laser writing using a focused femtosecond laser. (b) Illustration of a 3D waveguide butt coupled to 2D waveguide for orbital angular momentum applications [11] (c-d) OAM waveguides inscribed by fs lasers at UC Davis.

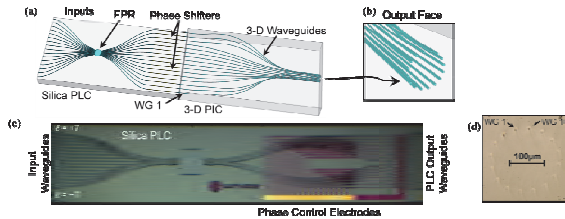


Figure 3. (a) Illustration of the silica PLC coupled to the 3-D PIC. (b) 3-D waveguide output face detail. (c) Photo of fabricated silica PLC. (d) Photo of unpolished 3-D PIC output face [7, 10].

Using our design [7, 10], the 3-D PIC was fabricated at a commercial foundry in bulk borosilicate glass and the waveguides had a  $\sim 10 \mu\text{m}$  mode field diameter (i.e., similar to SMF). **Figure 2(c-d)** presents a close view of the 3-D PIC output face showing the circular arrangement. **Figure 3(c)** shows a photo of the fabricated PLC. The waveguides on the silica PLC have a  $\Delta n$  of 2%. Electrical heaters on each output waveguide provide thermo-optic phase-error correction (PEC). This is used to phase match the waveguides between the FPR and the output face of the 3-D PIC. Both the PLC and the input of the 3-D PIC use a 127- $\mu\text{m}$  waveguide pitch. The

hybrid device (i.e., PLC and 3-D PIC) is  $\sim 30\text{-mm}$  long and the waveguides on the output face form a  $204 \mu\text{m}$  diameter circle with a center-to-center spacing of  $40 \mu\text{m}$  (see **Figure 3(d)**).

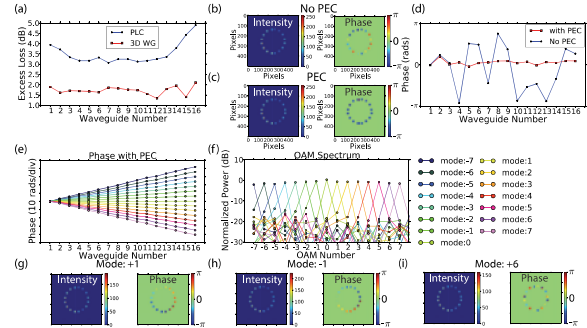


Figure 4. (a) Measured excess loss for the silica PLC and 3-D waveguides. (b) Measured intensity and phase of the device's output waveguides without PEC, (c) with PEC. (d) Measured average azimuthal phase at each output waveguide. (e) Unwrapped azimuthal phase for each OAM mode. (f) Calculated OAM mode purity. (g-i) The measured intensity and phase for three OAM modes ( $\ell = +1, -1, +6$ ).

Figure 4(a) shows the silica PLC had an average excess loss of 3.5 dB[7, 10], while the 3-D PIC had an average excess loss of 1.7 dB. To characterize the how well the hybrid device (PLC and 3-D PIC) created OAM modes, we imaged the device's output (i.e., near-field) onto an IR camera with a total magnification of  $\sim 50\times$  while illuminating only one PLC input at a time. The absolute phase (to within a constant) was measured using shearing interferometry. Figure 4(b) shows a false-color (linear scale) image of the near-field intensity and phase patterns when input  $\ell = 0$  is illuminated without PEC. Figure 4(c) shows the improvement with PEC (nearly same phase, correct for  $\ell = 0$ ). Figure 4(d) is a plot of the phase for each output waveguide to more clearly show the improvement with PEC. The output phase was then similarly measured for each device input ( $\ell = -7, \dots, 0, \dots, +7$ ) and the unwrapped phase is plotted in Figure 4(e). To estimate the OAM mode purity we can take the Fourier transform of the near-field amplitude and phase data for each of the device inputs. Figure 4(f) shows how well the device creates each OAM mode where the difference between a mode peak and the "noise" determines the OAM mode purity or crosstalk (below  $-12 \text{ dB}$ ). Figure 4(g-i) show the measured near-field pattern intensity and phase for several different example OAM modes (typical).

#### OAM Mux/Demux, Conversion, FSO Communication

Figure 5 shows the OAM state conversion tested with OAM multiplexing and demultiplexing devices including approximately 1.6 m free-space transmission. The CW laser with a 100 kHz linewidth has a wavelength at 1550 nm. The signal is modulated by an electrical arbitrary waveform generator (eAWG) driven in-phase quadrature-phase modulator (I/Q modulator) using

[illegible]

## Experimental results and BER performance

Figure 10 consists of two parts, (a) and (b). Part (a) is a log-linear plot of Bit Error Rate (BER) versus SNR (dBm) for three different OAM state combinations. The x-axis ranges from -46 dBm to -26 dBm, and the y-axis ranges from  $10^3$  to  $10^6$ . The legend indicates: OAM state -1 to +3 (green line with circles), OAM state -1 to -4 (blue line with circles), and OAM state -1 to -5 (magenta line with circles). All three curves show a linear decrease in BER as SNR increases. Part (b) shows six 2D plots of the Real Part and Imag Part of the received signal for the same three OAM state combinations. Each plot shows a 2D distribution of the signal components, with color bars indicating the magnitude of the Real Part (1 to 100) and Imag Part (1 to 100). The plots are arranged in a 2x3 grid, with the top row showing the Real Part and the bottom row showing the Imag Part for each state combination.

## Conclusion

## Acknowledgments

## References

- [1] S. Eaton, *et al.*, in *Femtosecond Laser Micromachining*, (2012), pp. 3-18.
- [2] R. R. Thomson, *et al.*, *Optics Express*, **15**, 11691-11697 (2007).
- [3] Y. Nasu, *et al.*, *Optics Letters*, **30**, 723-725 (2005).
- [4] Y. Nasu, *et al.*, *Lightwave Technology, Journal of*, **27**, 4033-4039 (2009).
- [5] B. McMillen, *et al.*, *Optics Letters*, **37**, 1418-1420 (2012).
- [6] T. H. Su, *et al.*, *Optics Express*, **20**(2012).
- [7] B. Guan, *et al.*, in *CLEO: 2013*, CTu1L.4 (2013).
- [8] R. P. Scott, *et al.*, in *ECOC 2013*, 1-3 (2013).
- [9] R. P. Scott, *et al.*, in *European Conference and Exhibition on Optical Communication (ECOC)*, (2013).
- [10] B. Guan, *et al.*, *Optics Express*, **22**, 145-156 (2014).
- [11] R. R. Thomson, *et al.*, *arXiv:1203.4584*, (2012).

# Free-Space Coherent Optical Communication Demonstration using a 3D Photonic Integrated Circuit Device for Orbital Angular Momentum Multiplexing/Demultiplexing

Ryan P. Scott<sup>(1)</sup>, Binbin Guan<sup>(1)</sup>, Chuan Qin<sup>(1)</sup>, Nicolas K. Fontaine<sup>(2)</sup>, Tiehui Su<sup>(1)</sup>, Carlo Ferrari<sup>(3)</sup>, Mark Cappuzzo<sup>(3)</sup>, Fred Klemens<sup>(3)</sup>, Bob Keller<sup>(3)</sup>, Mark Earnshaw<sup>(3)</sup>, and S. J. B. Yoo<sup>(1)</sup>

<sup>(1)</sup> Department of Electrical and Computer Engineering, University of California, Davis, CA 95616, USA, [rpscott@ucdavis.edu](mailto:rpscott@ucdavis.edu)

<sup>(2)</sup> Bell Laboratories, Alcatel-Lucent, 791 Holmdel Rd, Holmdel, NJ 07733, USA

<sup>(3)</sup> Bell Laboratories, Alcatel-Lucent, 600 Mountain Ave, Murray Hill, NJ 07974, USA

**Abstract** We show error-free 10 GBd QPSK data transmission performance using orbital angular momentum (OAM) modes that are multiplexed and demultiplexed by a low-loss, hybrid-integrated device based on a silica planar lightwave circuit (PLC) coupled to a 3-D photonic integrated circuit.

## Introduction

Space-division multiplexing (SDM) has recently generated significant interest because, like polarization-division multiplexing and wavelength-division multiplexing, it may be used to increase the photon efficiency or spectral efficiency of free-space and fiber-optic links. Although there are many approaches to SDM we focus on using optical orbital angular momentum (OAM) modes<sup>1</sup> (e.g., beams with azimuthally varying optical phase) to provide orthogonal information channels. The inherent orthogonality of OAM modes is attractive since it may require less digital signal processing (e.g., MIMO) when compared to other SDM approaches that have significant coupling between channels. Recent work<sup>2</sup> has shown the potential of OAM to improve spectral efficiency and throughput, but practical applications require integrated devices that multiplex/demultiplex OAM modes onto/from multi-mode fibers or free-space and also interface with single-mode fiber (SMF) components (e.g., modulators, optical amplifiers, and receivers). Our group and others<sup>3, 4</sup> have previously demonstrated an integrated OAM multiplexing device implemented as a silicon photonic integrated circuit (PIC). The silicon PIC generated OAM beams with a single polarization from a waveguide grating structure. Recently, we described an integratable OAM multiplexer based on hybrid integration of a silica planar lightwave circuit (PLC) with a silica 3-D PIC. Our initial device characterization was presented in a previous paper<sup>5</sup> which showed that it supports up to 15 OAM modes, both TE and TM polarizations, and had relatively low optical loss at 1.55  $\mu\text{m}$ . Here, we demonstrate the performance of the silica device as a both an OAM mode multiplexer and demultiplexer in a

free-space coherent transmission link.

## Device Concept

Fig. 1 shows the integratable OAM multiplexing device's operating principle which relies on converting linearly varying spatial phase to azimuthal variations [i.e.,  $\exp(ibx) \rightarrow \exp(i\ell\phi)$ , where  $b$  is the linear ( $x$ ) to azimuthal ( $\phi$ ) scaling factor]. To illustrate, Fig. 1 shows a waveguide circuit where each single mode input (i.e.,  $\ell = -2, -1, 0, +1, +2$ ) will create a wavefront in the free-propagation region (FPR) with a different linear tilt. The phase-matched waveguides after the FPR sample the tilted phase front and maintain the phase tilt to the output apertures. Since the apertures are arranged in a circular pattern, they create a beam (coming out of the page) with azimuthally varying phase having topological charge  $\ell$ . If multiple inputs are illuminated, those inputs are multiplexed onto colinear OAM beams with  $\ell$ -numbers determined by the input position. By reciprocity, if an outside OAM beam illuminates the apertures, the sampled light will be focused in the FPR to a waveguide corresponding to the beam's  $\ell$ -number (i.e., an OAM demultiplexer).

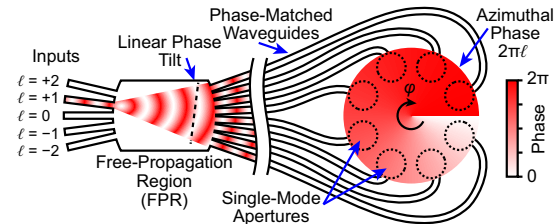
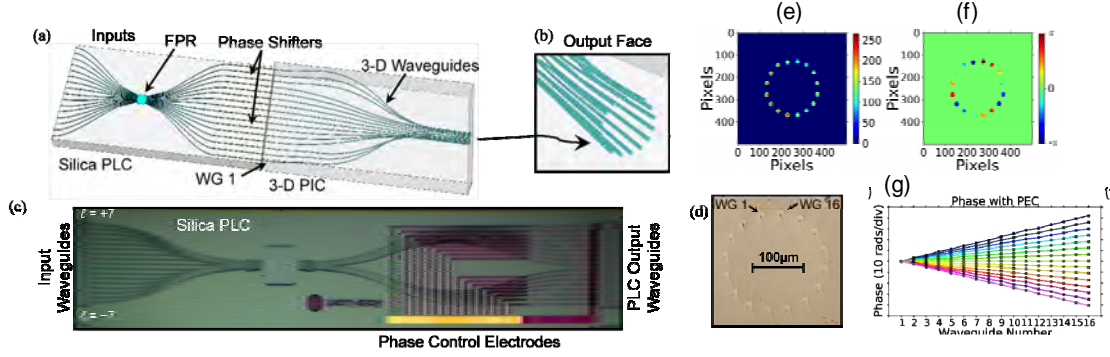


Fig. 1: Integratable OAM device concept.

## Device Implementation

Direct laser writing of waveguides in dielectric material is an extremely powerful fabrication technique<sup>6</sup>. It utilizes the multi-photon nonlinear





**Fig. 2:** (a) Illustration of the silica PLC coupled to the 3-D PIC. (b) 3-D waveguide output face detail. (c) Photo of fabricated silica PLC. (d) Photo of unpolished 3-D PIC output face. (e) amplitude pattern and (f) phase pattern of the generated OAM state  $l=-3$ . (g) phase control accuracy of the silican PLC.

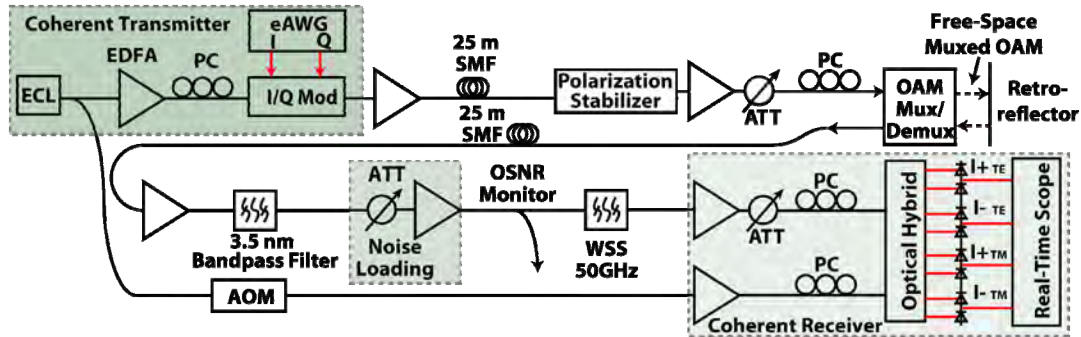
absorption of sub-bandgap photons to create permanent structural changes (e.g., refractive index) in a material with dimensions comparable to the writing laser's wavelength (e.g.,  $\sim 1 \mu\text{m}^3$ ). The induced modifications from a sub-picosecond train of optical pulses are strongly localized in three dimensions to the high intensity region at the focus of a lens driven by a nonlinear absorption mechanism. This unique characteristic is what provides direct laser writing its biggest advantage over other waveguide fabrication techniques; the capability to freely form true 3-D structures. We take advantage of the 3-D capability to create the geometric transformation needed to convert linear phase tilt to azimuthal phase variation. Fig. 2(a) shows how this concept is implemented using a silica PLC (to convert input position to a linear phase tilt) who's output is coupled to a 3-D PIC for geometric transformation.

Using our design, the 3-D PIC was fabricated at a commercial foundry in bulk fused silica and the waveguides had a  $\sim 10 \mu\text{m}$  mode field diameter (i.e., similar to SMF). Fig. 2(b) presents a close view of the 3-D PIC output face showing the circular arrangement. Fig. 2(c) shows a photo of the fabricated PLC (3.5 dB average

excess loss). Electrical heaters on each output waveguide provide thermo-optic phase-error correction (PEC). This is used to phase match the waveguides between the FPR and the output face of the 3-D PIC. Both the PLC and the input of the 3-D PIC use a 127- $\mu\text{m}$  waveguide pitch. The hybrid device (i.e., PLC and 3-D PIC) is  $\sim 30\text{-mm}$  long and the waveguides on the output face form a 204- $\mu\text{m}$  diameter circle with a pitch of 40  $\mu\text{m}$ .

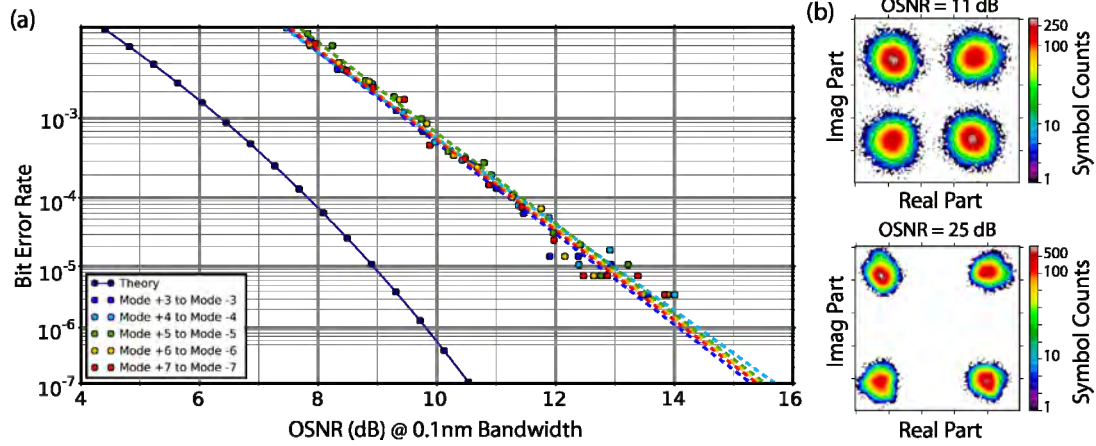
### OAM Coherent Transmission Testbed

Fig. 3 shows the experimental testbed for a SDM coherent optical communication link using a single hybrid OAM device as both an OAM multiplexer and demultiplexer. The coherent transmitter consists of a 100-kHz linewidth external cavity laser (ECL) centered at 1546 nm that has a data signal applied by an I/Q modulator. An electrical arbitrary waveform generator (eAWG) drives the modulator with a 10 GBd quadrature phase shift keyed (QPSK) signal ( $2^7-1$  PRBS). The QPSK signal is bandwidth limited in digital signal processing (DSP) by a Nyquist filter with a 3-dB bandwidth of 10 GHz for a single-channel spectral efficiency (SE) of 1.67 b/s/Hz. An erbium-doped fiber amplifier (EDFA) increases the optical power of the signal at the input of the hybrid



**Fig. 3:** Schematic of the 10GBd QPSK OAM transmission experiment. (ECL: external cavity laser, EDFA: erbium-doped fiber amplifier, SMF: single-mode fiber, PC: polarization controller, I/Q Mod: I/Q modulator, eAWG: electrical arbitrary waveform generator, ATT: optical attenuator, AOM: acousto-optic modulator, WSS: wavelength selective switch.)





**Fig. 4:** (a) BER performance of the different OAM modes for the hybrid OAM device (10 GBd QPSK, SE = 1.67 b/s/Hz for a single channel). (b) QPSK constellation at two different OSNRs.

OAM device to ~20 dBm.

To use a single hybrid OAM device as the multiplexer and demultiplexer simultaneously, a retroreflecting mirror is placed near the output face of the OAM device. Upon reflection, the  $\ell$ -number of the received OAM beam flips sign (i.e.,  $+3 \rightarrow -3$ ). Thus, a received OAM mode that has been correctly demultiplexed after retroreflection appears at the output with the opposite sign  $\ell$ -number from the input.

Immediately following the OAM device is an EDFA and a 3.5-nm bandpass filter to minimize out-of-band noise. The optical signal-to-noise ratio (OSNR) is varied by noise loading from a second attenuator and EDFA. The signal enters the polarization diversified coherent receiver which uses a frequency shifted (35 MHz) sample of the transmitter's laser as its local oscillator (LO). We use offline DSP to process the received data. The DSP first extracts the clock tone from Fourier transform of the magnitude-squared signal. Next, the waveform is resampled at twice the symbol rate. An adaptive equalizer is applied to the resampled waveform, which includes a 13-tap finite impulse response (FIR) filter adapted by a constant-modulus algorithm (CMA). Lastly, the DSP uses the power-of-four method for phase and frequency recovery.

The bit-error-rate (BER) performance for the 10 GBd QPSK data were separately measured for OAM channels  $\ell = -7, -6, \dots, 6, 7$  (but not  $\ell = -2, \dots, +2$ ) by sending one input signal to the OAM device. Because of their close spacing, the low  $\ell$ -numbers input/output pairs were not simultaneously accessible by a pair of SMF fibers. Fig. 4(a) shows that the implementation penalty is 3 dB at  $\text{BER} = 10^{-3}$  and the different OAM modes have less than 0.5 dB penalty

variation. At  $\text{OSNR} > 16$  dB, all OAM modes were error free for the 379,960 bits tested. Fig. 4(b) shows constellation diagrams corresponding to  $\text{OSNR} = 11$  dB and 25 dB.

### Conclusions

We have demonstrated free-space SDM coherent optical transmission using OAM state multiplexing and demultiplexing by a hybrid silica OAM device. The device design allows operation as either an OAM multiplexer or demultiplexer for an  $\ell$ -number range of  $-7$  to  $+7$  and easily interfaces with fiber-pigtailed components. The single-channel BER statistics for 20-Gb/s QPSK data indicated similar performance for all  $\ell$ -numbers. In all cases, the BER was error-free for the 379,960 bits tested. Future work includes bonding a fiber array to the PLC so that all inputs are simultaneously accessible and using multiple devices to investigate the performance of longer links.

### Acknowledgements

This work was supported in part by DARPA DSO under contract HR0011-11-1-0005 and W911NF-12-1-0311.

### References

- [1] L. Allen, *et al.*, *Phys. Rev. A*, **45**, 8185-8189 (1992).
- [2] N. Bozinovic, *et al.*, in *ECOC*, Paper Th.3.C.6 (2012).
- [3] T. Su, *et al.*, *Opt. Express*, **20**, 9396-9402 (2012).
- [4] N. K. Fontaine, *et al.*, in *OFC/NFOEC*, Paper OTu11.2 (2012).
- [5] B. Guan, *et al.*, in *CLEO*, Paper CTu1L.4 (2013).
- [6] Y. Nasu, *et al.*, *Opt. Lett.*, **30**, 723-725 (2005).

# 3D Waveguide Technologies for Generation, Detection, Multiplexing/Demultiplexing Orbital Angular Momentum Optical Waves

R. P. Scott<sup>1</sup>, S. J. B. Yoo<sup>1</sup>

<sup>1</sup>Department of Electrical and Computer Engineering, University of California, Davis, California 95616, U.S.A.

## Paper Summary

*We will discuss 3D photonic integrated circuits for arbitrary beam forming and spatial division multiplexing using orbital angular momentum states (OAM). We will demonstrate free-space communication and signal processing utilizing OAM Mux/Demux and switching.*

## Introduction

Rapid and exponential increases in data communications are continuing to drive the complexity of our computing, networking, and sensing systems. High degrees of integration is essential in scalable, practical, and cost-effective microsystems. In electronics, high-density 2D integration has naturally evolved towards 3D integration by stacking of memory and processor chips with through-silicon-vias. In photonics, too, we anticipate high-degrees of 3D integration of photonic components to become a prevailing method in realizing future microsystems for information and communication technologies. However, compared to electronics, photonic 3D integration face a number of challenges. This paper will discuss 3D photonic integration and its future applications.

## Orbital Angular Momentum Mux/Demux

**Figure 1(a)** shows the integratable orbital angular momentum multiplexing device's operating principle which relies on converting linearly varying spatial phase to azimuthal variations [i.e.,  $\exp(iblx) \rightarrow \exp(i\ell\phi)$ , where  $b$  is the linear ( $x$ ) to azimuthal ( $\phi$ ) scaling factor]. To illustrate, **Figure 1(a)** shows a waveguide circuit where each single mode input (i.e.,  $\ell = -2, -1, 0, +1, +2$ ) will create a wavefront in the free-propagation region (FPR) with a different linear tilt. The phase-matched waveguides after the FPR sample the tilted phase front and maintain the phase tilt to the output apertures. Since the apertures are arranged in a circular pattern, they create a beam (coming out of the page) with azimuthally varying phase having topological charge  $\ell$ . If multiple inputs are illuminated, those inputs are multiplexed onto collinear OAM beams with  $\ell$ -numbers determined by the input position. By reciprocity, if an outside OAM beam illuminates the apertures, the sampled light will be focused in the FPR to a waveguide corresponding to the beam's  $\ell$ -number (i.e., an OAM demultiplexer). Working as a demux (i.e., OAM state decoder), **Figure 1(b)** shows how a circular array of waveguide grating couplers are used to sample areas (dashed circles) of an incoming

beam encoded with an OAM state (e.g.,  $\ell = 1$ ) into a corresponding array of single-mode waveguides. Careful waveguide layout ensures that they have identical optical path lengths. Thus, at the input of the free-propagation region (FPR), the azimuthally varying phase of the OAM state is converted into a linear phase front with a tilt angle determined by the incoming beam's topological charge, as indicated in **Figure 1(a)**. The circular placement of the array waveguides at the input of the FPR focuses the light, and the tilt of the linear phase front directs it to a corresponding output. Using the PIC as a mux is as simple as reversing the light's propagation direction. This paper demonstrates a full coherent optical communication link including a pair of silicon photonic OAM mux/demux devices.

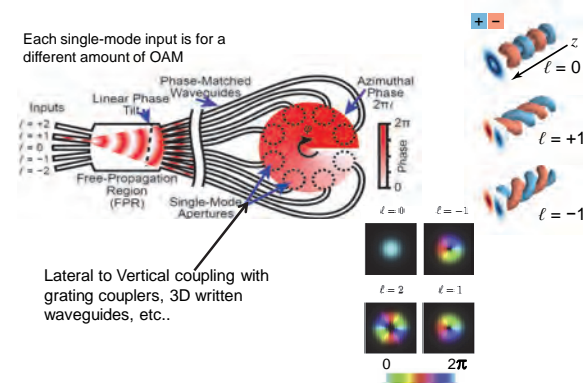


Figure 1. (a) Visualization of the electric field of OAM beams. (b) Illustration showing how a beam encoded with an OAM state is sampled and demultiplexed by a circular arrangement of apertures, length-matched waveguides and a star coupler.

## 3D inscription by femtosecond lasers

Direct laser writing of waveguides in dielectric material is an extremely powerful fabrication technique [1]. It utilizes the multi-photon nonlinear absorption of sub-bandgap photons to create permanent structural changes in a material with dimensions comparable to the writing laser's wavelength (e.g.,  $\sim 1 \mu\text{m}^3$ ). The induced modifications from a sub-picosecond train of optical pulses are strongly localized in three dimensions to the high intensity region at the focus of a lens driven by a nonlinear absorption mechanism. This unique characteristic is what provides direct laser writing its biggest advantage over other waveguide fabrication techniques; the capability to freely form true three dimensional structures[2]. Direct laser writing has been widely demonstrated in many types of materials

including amorphous glasses and crystals with measured losses as low as 0.1 dB/cm (Optoscribe, Ltd specification) [3, 4] in fused silica, and, as an initial demonstration, 0.65 dB/cm [5] in gallium lanthanum sulphide (GLS). This value is expected to go down to 0.1 dB/cm~0.2 dB/cm with writing process optimizations (bulk absorption loss for GLS is less than 0.045 dB/cm). **Figure 2(a)** illustrates the direct laser writing process that will be used to write the emitter waveguides into the 3D block. For visible and near infrared applications, fused silica is widely used for 3D waveguide inscription. **Figure 2(b)** shows a fabricated 3D waveguide fan-out device composed of directly laser writing butt coupled to a 2D waveguide block for orbital angular momentum applications [6-10].

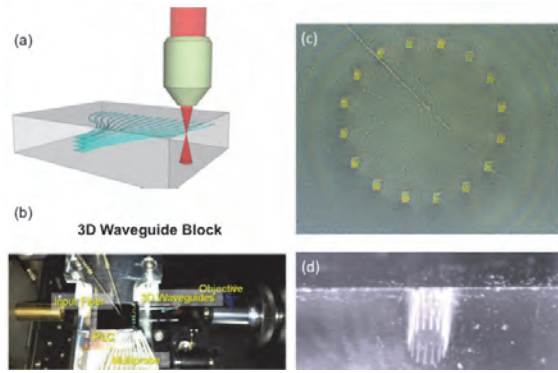


Figure 2. (a) Illustration of 3D waveguide fabrication by direct laser writing using a focused femtosecond laser. (b) Illustration of a 3D waveguide butt coupled to 2D waveguide for orbital angular momentum applications [11] (c-d) OAM waveguides inscribed by fs lasers at UC Davis.

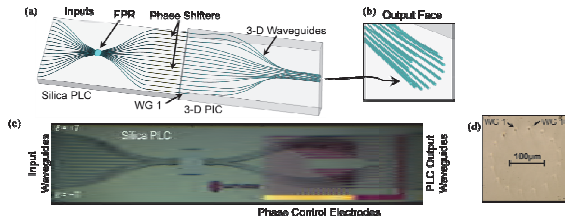


Figure 3. (a) Illustration of the silica PLC coupled to the 3-D PIC. (b) 3-D waveguide output face detail. (c) Photo of fabricated silica PLC. (d) Photo of unpolished 3-D PIC output face [7, 10].

Using our design [7, 10], the 3-D PIC was fabricated at a commercial foundry in bulk borosilicate glass and the waveguides had a  $\sim 10 \mu\text{m}$  mode field diameter (i.e., similar to SMF). **Figure 2(c-d)** presents a close view of the 3-D PIC output face showing the circular arrangement. **Figure 3(c)** shows a photo of the fabricated PLC. The waveguides on the silica PLC have a  $\Delta n$  of 2%. Electrical heaters on each output waveguide provide thermo-optic phase-error correction (PEC). This is used to phase match the waveguides between the FPR and the output face of the 3-D PIC. Both the PLC and the input of the 3-D PIC use a 127- $\mu\text{m}$  waveguide pitch. The

hybrid device (i.e., PLC and 3-D PIC) is  $\sim 30\text{-mm}$  long and the waveguides on the output face form a  $204 \mu\text{m}$  diameter circle with a center-to-center spacing of  $40 \mu\text{m}$  (see **Figure 3(d)**).

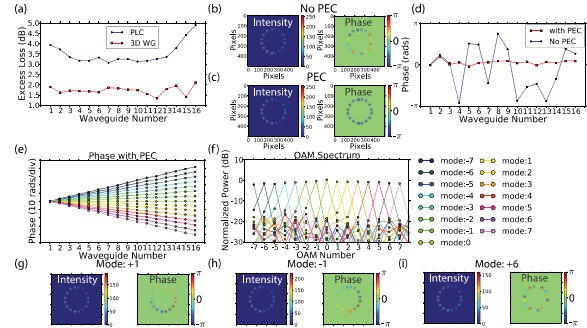


Figure 4. (a) Measured excess loss for the silica PLC and 3-D waveguides. (b) Measured intensity and phase of the device's output waveguides without PEC, (c) with PEC. (d) Measured average azimuthal phase at each output waveguide. (e) Unwrapped azimuthal phase for each OAM mode. (f) Calculated OAM mode purity. (g-i) The measured intensity and phase for three OAM modes ( $\ell = +1, -1, +6$ ).

Figure 4(a) shows the silica PLC had an average excess loss of 3.5 dB[7, 10], while the 3-D PIC had an average excess loss of 1.7 dB. To characterize the how well the hybrid device (PLC and 3-D PIC) created OAM modes, we imaged the device's output (i.e., near-field) onto an IR camera with a total magnification of  $\sim 50\times$  while illuminating only one PLC input at a time. The absolute phase (to within a constant) was measured using shearing interferometry. Figure 4(b) shows a false-color (linear scale) image of the near-field intensity and phase patterns when input  $\ell = 0$  is illuminated without PEC. Figure 4(c) shows the improvement with PEC (nearly same phase, correct for  $\ell = 0$ ). Figure 4(d) is a plot of the phase for each output waveguide to more clearly show the improvement with PEC. The output phase was then similarly measured for each device input ( $\ell = -7, \dots, 0, \dots, +7$ ) and the unwrapped phase is plotted in Figure 4(e). To estimate the OAM mode purity we can take the Fourier transform of the near-field amplitude and phase data for each of the device inputs. Figure 4(f) shows how well the device creates each OAM mode where the difference between a mode peak and the "noise" determines the OAM mode purity or crosstalk (below  $-12 \text{ dB}$ ). Figure 4(g-i) show the measured near-field pattern intensity and phase for several different example OAM modes (typical).

#### OAM Mux/Demux, Conversion, FSO Communication

Figure 5 shows the OAM state conversion tested with OAM multiplexing and demultiplexing devices including approximately 1.6 m free-space transmission. The CW laser with a 100 kHz linewidth has a wavelength at 1550 nm. The signal is modulated by an electrical arbitrary waveform generator (eAWG) driven in-phase quadrature-phase modulator (I/Q modulator) using



Figure 5. 10-Gbd QPSK link experiment testbed for OAM state conversion using two OAM hybrid devices with  $\sim 1.6\text{m}$  round-trip free-space transmission. EDFA: erbium-doped fiber amplifier. PC: polarization controller. ATT: attenuator. BPF: bandpass filter. AOM: acousto-optic modulator.

## Experimental results and BER performance

Figure 6 (a) shows the BER performance with 379,960 bits tested for input OAM state -1 switched to OAM state -5, -4 and +3. Note that the BER is less than  $10^{-5}$  (no errors are recorded) when OSNR is more than 16dB for -1 to -5 conversion, 18dB and 25 dB for -1 to -4 and -1 to +3 respectively. Figure 6 (b) shows the constellation plots for the three conversion cases in Figure 6 (a) at both 12dB and 20dB OSNR. We notice that the OAM state -1 to +3 has the worst BER performance in three and -1 to -5 has the best performance.

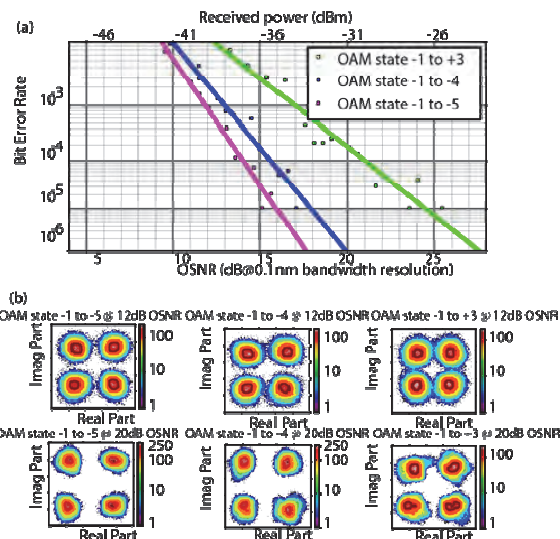


Figure 6. (a) BER performance for OAM state -1 as the input and switched to +3, -4 and -5. (b) Constellation plots for each case at OSNR of 12dB and 20dB.

## Conclusion

3D photonic integration emerges as a powerful new dimension to the current photonic integration platform. Laser inscribing provides a free-form method to create arbitrary shape embedded waveguides in 3D and also offers a method to achieve photonic wirebonding. Multilayer stacking facilitates creation of 3D photonic integrated circuits by using conventional lithography and deposition methods. 2D/3D heterogeneous photonic integration is essential for future computing, networking, and imaging systems aiming at scalability, high-performance, and cost effectiveness.

## Acknowledgments

The authors are grateful for the work from the Next Generation Networking Systems Group at UC Davis. The author acknowledges support in part by DARPA/ARL under Inpho program under grant W911NF-12-1-0311, under ONR grant N00014-13-1-0158, under NSF ECCS 1028729 grant, under NSF CNS-1302719 grant.

## References

- [1] S. Eaton, *et al.*, in *Femtosecond Laser Micromachining*, (2012), pp. 3-18.
- [2] R. R. Thomson, *et al.*, *Optics Express*, **15**, 11691-11697 (2007).
- [3] Y. Nasu, *et al.*, *Optics Letters*, **30**, 723-725 (2005).
- [4] Y. Nasu, *et al.*, *Lightwave Technology, Journal of*, **27**, 4033-4039 (2009).
- [5] B. McMillen, *et al.*, *Optics Letters*, **37**, 1418-1420 (2012).
- [6] T. H. Su, *et al.*, *Optics Express*, **20**(2012).
- [7] B. Guan, *et al.*, in *CLEO: 2013*, CTu1L.4 (2013).
- [8] R. P. Scott, *et al.*, in *ECOC 2013*, 1-3 (2013).
- [9] R. P. Scott, *et al.*, in *European Conference and Exhibition on Optical Communication (ECOC)*, (2013).
- [10] B. Guan, *et al.*, *Optics Express*, **22**, 145-156 (2014).
- [11] R. R. Thomson, *et al.*, *arXiv:1203.4584*, (2012).



# Polarization Diversified Integrated Circuits for Orbital Angular Momentum Multiplexing

Binbin Guan, Chuan Qin, Ryan P. Scott, *Member, IEEE*, Nicolas K. Fontaine, *Member, IEEE*, Tiehui Su, *Student Member, IEEE*, Roberto Proietti, and S. J. B. Yoo, *Fellow, IEEE*

**Abstract**—We present a free-space coherent communication link employing orbital angular momentum (OAM) multiplexing using polarization diversified 2D-3D hybrid photonic integrated circuits (PICs). The PICs support multiplexing/demultiplexing of up to 15OAM states with dual polarizations. We characterize the hybrid device including phase errors and crosstalk performance and we then use two hybrid PICs for a free-space coherent communication link demonstration utilizing polarization, frequency, quadrature and space dimensions to achieve a 1.68 Tb/s link bandwidth and a 9.6 b/s/Hz spectral efficiency.

**Index Terms**— Coherent communications; Optical vortices; Multiplexing; Glass waveguides, Orbital angular momentum.

## I. INTRODUCTION

The network capacity of optical communication systems has grown incredibly in the last several decades. After the mid-1990s, the deployment of the wavelength-division-multiplexing (WDM) technique has increased the single-fiber capacity from 10 Gb/s to multiple Tb/s. In addition, use of advanced modulation formats has raised spectral efficiency above 10 b/s/Hz, further increasing the optical fiber network capacity. One relatively recent report shows that the network traffic growth rate is 2 dB per year [1]. As a result, we would expect that a 100 times larger network capacity will be required in 10 years. However, the network capacity is already approaching the nonlinear Shannon limit [2] so we must look for new ways to increase capacity.

There are five physical dimensions available to carry optical data in the contemporary world [3]. In the last several decades, network capacity has been increased by employing four of them: time, frequency, polarization and quadrature dimensions. Space-division multiplexing (SDM) becomes attractive since it provides an addition dimension to support the needed aggregate network capacity growth rate and

increases to spectral efficiency. Orbital angular momentum (OAM) is one subset of SDM methods [4]. It has generated great interest recently due to its use of cylindrically symmetric modes. In addition, it only uses one degree of freedom to determine the mode orthogonality. Therefore, OAM has been considered as an emerging technique for SDM to potentially increase the network capacity both in free space and optical fiber communication systems.

A light beam carrying OAM shows an azimuthal phase variation of  $\phi(r, \phi) = \exp(i\ell\phi)$ , where  $\phi$  is the azimuthal angle and  $\ell$  is the OAM state or charge number [5]. The sign of  $\ell$  determines the rotation direction of the azimuthal phase front. Following the early work of Allen [4], several research groups have shown OAM state generation and sorting, and a few have shown OAM state multiplexing and demultiplexing. Many approaches rely on free space bulk-optic components, such as holograms, spatial light modulators, or dove prisms. However, it is necessary to integrate the OAM state emitter and multiplexer with other devices for large-scale system design and applications. Photonic integrated circuits (PICs) provide compact and robust platforms for such OAM components. Both Doerr, et al. [6] and Su et al. [7], have previously demonstrated such an integrated device for OAM state multiplexing and demultiplexing based on engineered star coupler regions and waveguide grating structures. Another integrated OAM emitter structure reported by Cai, et al. [8] utilizes grating structures on whispering gallery mode ring resonators. Since these devices use polarization dependent grating structures, simple polarization diversified designs are particularly challenging.

In this Letter, we significantly expand on our previous work [9, 10] by utilizing two separate 2D-3D hybrid PICs to demonstrate free-space links with dual-polarization OAM state multiplexing and demultiplexing of dual-polarization, wavelength division multiplexing (WDM), quadrature phase-shift keying (QPSK) light signals. Section II discusses the hybrid device's working principle and design. Then, Section III presents the device characterization results and Section IV describes the free-space coherent communication link arrangement and performance that uses two separate hybrid devices. Finally, Section V summarizes the work.

## II. DEVICE WORKING PRINCIPLE AND DESIGN

**Error! Reference source not found.**(a) shows the

Manuscript received Month 1, 2014; revised September 08, 2011; accepted Month 1, 2014. Date of publication Month 1, 2014; date of current version Month 1, 2014. This work was supported in part by DARPA DSO under contracts HR0011-11-1-0005 and W911NF-12-1-0311.

B. Guan, C. Qin, R. P. Scott, T. Su, R. Proietti and S. J. B. Yoo, are with the University of California, Davis, CA 95616 USA (corresponding author e-mail: sbyoo@ucdavis.edu)

N. K. Fontaine is with Alcatel-Lucent Bell Laboratories, Holmdel, NJ 07733 USA.

Color versions of one or more of the figures in this letter are available online at <http://ieeexplore.ieee.org>.

Digital Object Identifier 00.0000/LPT.2014.000000

conceptual diagram of the device when acting as an OAM state generator and multiplexer. The single mode waveguide inputs are on the left side and each input corresponds to a unique OAM state (e.g.,  $\ell = -2$  through  $+2$  shown in the figure). The phase fronts for each input light beam acquire a specific linear phase tilt after propagating through the free-propagation region (FPR). The phase tilt angle depends on the spatial location of the input port and the phase-matched waveguides sample and maintains the linear phase relationship (tilt) to the output apertures. **Error! Reference source not found.**(b) shows the 2D-3D hybrid device that consists of a silica planar lightwave circuit (PLC) and a 3D waveguide block. The silica PLC and 3D waveguides were designed to support both TE and TM polarizations. On the PLC, there are thermo-optic based phase shifters on each output waveguide to provide phase-error correction (PEC) on the hybrid device so that all waveguides are phase matched (i.e., phase tilt from FPR is maintained). The 3D waveguides block geometrically converts the linear phase tilts to azimuthal phase variations. The 3D waveguides were fabricated by directly writing waveguides in a borosilicate glass using a femtosecond laser writing technique [11]. Our previous publication [9] provides additional details of the silica PLC and 3D waveguides block.

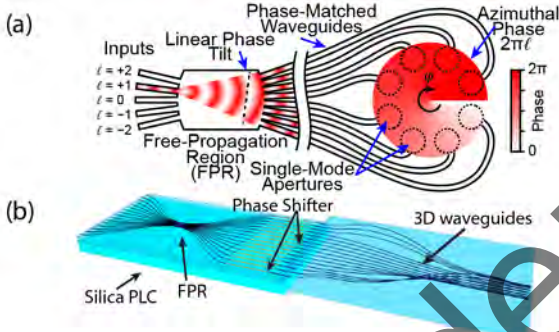


Fig. 1. (a) Hybrid device concept and operating principle. (b) 3D illustration of the hybrid integrated device.

The hybrid device generates 15 unique OAM states ( $\ell = -7$  to  $+7$  in our case). If multiple silica PLC inputs are illuminated at the same time, the hybrid device spatially multiplexes the OAM states. Alternatively, if we operate the hybrid device in reverse, the 3D waveguide block's circular-patterned apertures spatially sample overlapped OAM states. Hence, the silica PLC will retrieve individual OAM states by focusing the light to its corresponding output port. Since the output apertures spatially sample the OAM beam, Nyquist sampling theory [12] suggests that  $2N$  samples (waveguide apertures) can support the generation of  $2N$  states ( $\ell = -N + 1$  to  $+N$ ). As a result, we can generate and multiplex 16 OAM states ( $\ell = -7$  to  $+8$ ). However, for the case of OAM state  $+8$ , the phase on each waveguide (sampler) is either  $0$  or  $\pi$ . Therefore, we cannot unambiguously recover OAM state  $+8$  because its sampled phase will appear the same as OAM state  $-8$ . Since the multiplexing technique does not suffer from the  $1 \times N$  splitting/combining losses, it is straightforward to scale to support a larger number of OAM states with low loss.

However, as discussed in Section III, crosstalk between OAM states will limit the maximum number of supported states.

If the waveguides between the FRP and the output apertures are not path-length matched, but are only phase matched for a particular wavelength, then we expect that there will be phase errors when the device is operated at different wavelengths. These phase errors lead to azimuthal phase errors and cause crosstalk between OAM states. In our device, although the PLC waveguides are path-length matched to  $< 0.5 \mu\text{m}$ , the 3D waveguides are path-length matched to  $< 40 \mu\text{m}$ . **Error! Reference source not found.** shows simulation results for the worst-case crosstalk caused by the path-length mismatch of our device. Here, worst-case crosstalk is the maximum crosstalk from any other OAM state (i.e.,  $-7$  to  $+7$ ) to OAM state  $+1$ . If we define the maximum acceptable crosstalk at  $-10$  dB, our hybrid device has a  $\sim 9$ -nm operating bandwidth. If the path-length difference between the waveguides is kept to  $< 9.2 \mu\text{m}$ , the operating bandwidth of the device easily covers the C-band ( $1530$ – $1565$  nm) in fiber optics communications. We are currently developing new 3D design and fabrication techniques for sub-micron path-length matching.

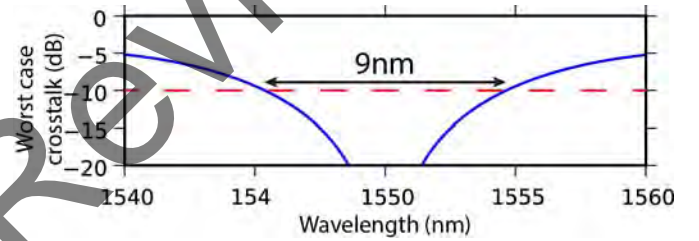


Fig. 2. Simulation of the worst-case crosstalk to OAM state  $+1$  from any other state for the 15-state hybrid OAM devices with waveguides path-length matched to  $< 40 \mu\text{m}$  and phase matched at  $1550$  nm.

### III. HYBRID DEVICE CHARACTERIZATION

The typical excess loss of a single hybrid device is  $\sim 7.5$  dB. Details of the device loss measurements were previously described in [9]. Correct azimuthal phase for each of the OAM states is critical to the performance of the devices. **Error! Reference source not found.**(a) shows the spatial shearing interferometry arrangement for phase characterization of the hybrid OAM device output [13]. A Gaussian reference beam with a relatively flat spatial phase is tilted with respect to the magnified OAM beam (16 beam samples) and the two beams create an interference pattern on the infrared camera's detector array. Using standard interferometric processing techniques [13], we retrieved the unknown spatial phase of the OAM beam by measuring the intensities of the OAM beam, reference beam and interference pattern separately. In our experiment, we characterized the phase for transverse-electric (TE) polarization and applied phase-error correction (PEC) to the hybrid device at  $1550$  nm.

**Error! Reference source not found.**(b) shows the near-field phase measurement results for OAM state  $0$  without and with PEC. The thermo-optic phase shifters require  $\sim 400$  mW for a  $\pi$  rad phase shift (there are no heat isolation trenches between waveguides [14]). **Error! Reference source not found.**(c) shows the unwrapped near-field phase

characterization for all OAM states ( $\ell = -7$  to  $+7$ ). The phase was measured by illuminating one input of the hybrid OAM device at a time. The slope of each line in **Error! Reference source not found.**(c) matches the product of  $2\pi$  and the OAM charge number  $\ell$ .

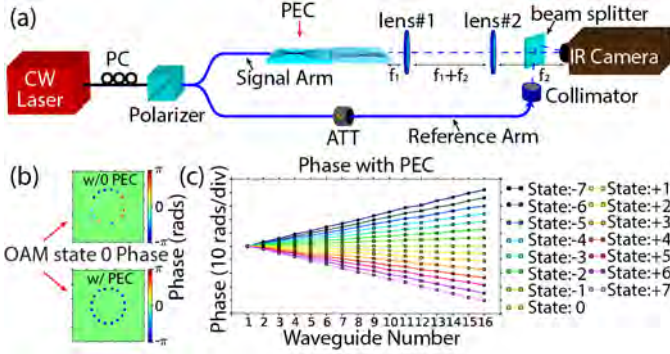


Fig. 3. (a) OAM hybrid device phase characterization arrangement. (b) Near-field phase comparison before and after applying PEC (OAM state 0). (c) Near-field phase measurements with PEC.

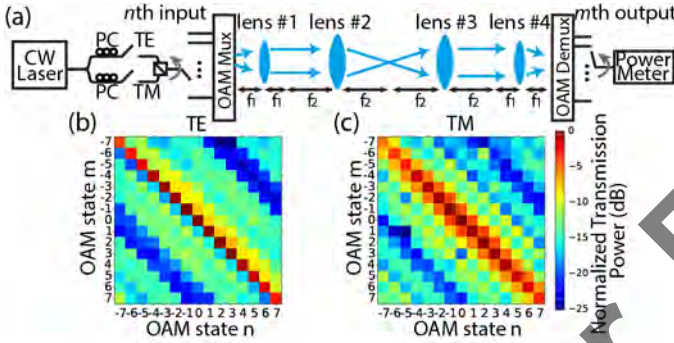


Fig. 4. (a) OAM state crosstalk measurement arrangement. OAM state crosstalk measurement for (b) TE and (c) TM polarizations. PC: polarization controller; TE: transverse-electric signal; TM: transverse-magnetic signal; Mux: multiplexer; Demux: demultiplexer.

Since the hybrid OAM devices function as spatial mode multiplexers and demultiplexers, it is important to characterize their crosstalk performance. The mode crosstalk determines the maximum number of OAM states that can be transmitted simultaneously without requiring space-time coding (e.g., multiple-input and multiple-output (MIMO) coding). Fig. 4(a) shows the experimental arrangement for measuring the crosstalk performance for both polarizations. Using polarization-maintaining (PM) fibers, either a TE or TM polarized 1550-nm signal beam is launched into the one of the  $n$ -inputs ( $n = -7$  to  $+7$ ) of the first hybrid OAM device (i.e., OAM multiplexer). As a result, the device generates an OAM beam with state  $n$ . The generated OAM beam propagates through an 81.8-cm free-space link that uses an  $8-f$  lens

configuration. A second hybrid OAM device demultiplexes the free-space beam to its  $m$  outputs ( $m = -7$  to  $+7$ ) where an optical power meter measures the signal power at each output. These measurements are taken for each polarization separately and repeated for all  $n$  inputs. Fig. 4(b) displays the normalized transmission matrix for TE polarization as a color map (normalized to state 0). As expected, the peak transmission occurs when  $n = m$  with all off-diagonal elements having lower transmission. Fig. 4(c) shows the performance for the TM polarization that uses the same PEC determined by the TE polarization. The measurement results show that the worst-case crosstalk for a single OAM state is approximately  $-8$  dB for the TE polarization and approximately  $-6$  dB for the TM polarization. If we use OAM state 0 (TE) as an example, the crosstalk is below  $-10$  dB from OAM state 0 to 13 other OAM states, and it is below  $-15$  dB from OAM state 0 to six other OAM states. The crosstalk performance is similar for TM, indicating that PEC using TE polarization works reasonable well for both polarizations. Several factors could affect overall crosstalk performance. It includes imperfect phase error correction, uneven power distribution across the output waveguides of the FPR, side lobe distribution due to limited number of waveguides around the FPR, aberrations and misalignments of the free space optics. Further improvement on any of these factors can reduce the crosstalk.

#### IV. FREE-SPACE COHERENT COMMUNICATION LINK

Two hybrid OAM devices were employed to demonstrate increases in the link capacity and spectral efficiency by simultaneously using frequency, quadrature, polarization and space dimensions. Fig. 5 shows the experimental arrangement of the demonstration. The WDM transmitter included 14-wavelength channels and each carried a 10-GBd QPSK signal with a  $2^{15}-1$  pseudorandom bit sequence (PRBS) data. The WDM signals were polarization multiplexed and divided into three branches, each with a different relative delay. The first hybrid device generated and multiplexed three OAM states simultaneously (OAM states 0,  $-3$  and  $-6$ ). The spatially overlapped OAM states propagated through the free-space region and were received by the second hybrid OAM device. This spatially demultiplexed the OAM states to separate outputs where a coherent receiver detected one OAM state at a time. As a result, the total link capacity is 1.68 Tb/s (14 wavelength channels  $\times$  20 Gb/s  $\times$  2 polarizations  $\times$  3 OAM states), and the spectral efficiency is 9.6 b/s/Hz.

We used offline digital signal processing (DSP) for evaluating bit-error-rate (BER) performance. First, DSP extracted the clock tone from the Fourier transform of the time

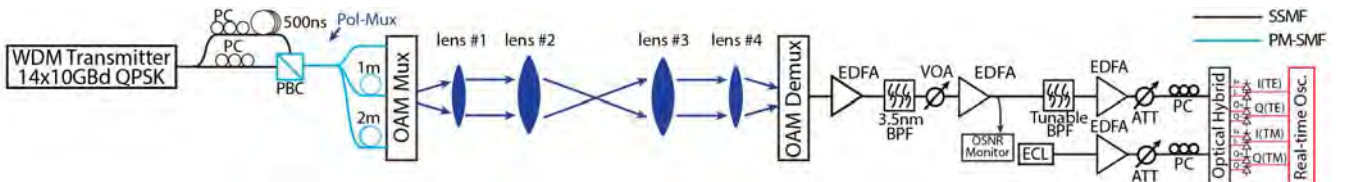


Fig. 5. Free-space coherent communication link experimental setup. WDM: wavelength-division-multiplexing; PC: Polarization controller; Pol-Mux: Polarization multiplexer; OAM Mux: OAM state multiplexer; OAM Demux: OAM state de-multiplexer; EDFA: Erbium doped fiber amplifier; BPF: Bandpass filter; VOA: Variable optical attenuator; ATT: Attenuator.



domain using the magnitude-squared method. After clock recovery, the signal was resampled at twice of the symbol rate. Then the DSP applied a 17-tap finite impulse response (FIR) filter and power-of-four frequency and phase recovery on the resampled signal to retrieve the constellation. Finally, a direct-decision based bit-error counting method was used to calculate the BER performance.

TABLE I. Measured crosstalk between OAM states 0, -3 and -6.

	TE (dB)	TM (dB)
OAM state 0 and -3	-12.9	-13.8
OAM state 0 and -6	-14.2	-14.5
OAM state -3 and -6	-14.1	-13.7

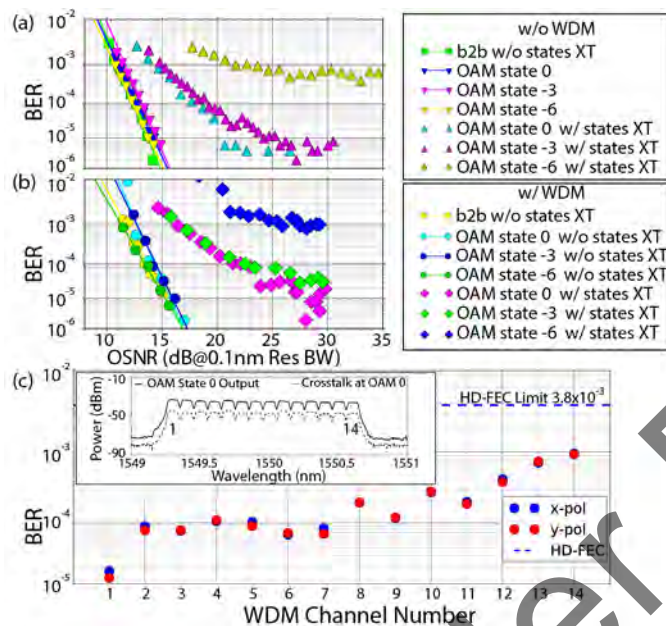


Fig. 6. Bit-error-rate (BER) measurement results (a) without WDM and (b) with WDM. (c) BER for each WDM channel.

Table 1 lists the measured crosstalk between each OAM state used in the experiment. These crosstalk values are near the median of measured crosstalk values for the experimental arrangement. **Error! Reference source not found.** (a, b) shows the average BER performance of the two polarization states. There are five scenarios in **Error! Reference source not found.** (a, b): i) back-to-back transmission of a single wavelength channel and with 14 WDM channels; ii) single OAM state transmission with single wavelength channel; iii) single OAM state transmission with all WDM channels; iv) three OAM state transmission simultaneously with a single wavelength channel; v) three OAM state transmission with all WDM channels. There is no observed optical signal-to-noise ratio (OSNR) penalty between the first two scenarios. In the third scenario, there are 1.5-dB to 2-dB OSNR penalties due to the WDM crosstalk. The fourth scenario shows that there was a 3-dB OSNR penalty for OAM states 0 and -3, and 9-dB OSNR penalty for OAM state -6 between single OAM state transmission and three OAM state transmission. We believe the higher OSNR penalty is due to a joint effect of crosstalk and polarization dependent loss (PDL). **Error! Reference**

**source not found.** (c) shows the measured average BER values of three OAM states at each WDM channel. The blue and red dots present the two orthogonal polarizations (e.g., x and y) independently. It shows that all measured BER values are below the hard-decision forward-error correction (HD-FEC) limit of  $3.8 \times 10^{-3}$  (e.g., BCH(1020,988) super FEC code, 7% overhead) [15].

## V. SUMMARY

In this Letter, we presented hybrid PICs composed of a silica PLC and 3D waveguides. The devices support up to 15 OAM states and both polarizations. We used two of these devices in a free-space communication link experiment which employs frequency, polarization, quadrature and space dimensions to achieve a 1.68 Tb/s link bandwidth with a spectral efficiency of 9.6 b/s/Hz. The experiment implies that OAM based SDM communication can potentially increase the network capacity and spectral efficiency. The future work includes an improved design for the silica PLC to minimize the crosstalk, investigating implementations that utilize optical fibers which support OAM states [16], and device packaging to improve PEC stability and long term performance.

## REFERENCES

- [1] R. W. Tkach, "Network traffic and system capacity: Scaling for the future," in *ECOC*, pp. 1-22, 2010.
- [2] R. Essiambre, G. Kramer, P. J. Winzer, G. J. Foschini, and B. Goebel, "Capacity Limits of Optical Fiber Networks," *J. Lightwave Technol.*, vol. 28, pp. 662-701, 2010.
- [3] P. J. Winzer, "Making spatial multiplexing a reality," *Nature Photon.*, vol. 8, pp. 345-348, 2014.
- [4] L. Allen, M. W. Beijersbergen, R. J. C. Spreeuw, and J. P. Woerdman, "Orbital angular momentum of light and the transformation of Laguerre-Gaussian laser modes," *Phys. Rev. A*, vol. 45, pp. 8185-8189, 1992.
- [5] A. M. Yao and M. J. Padgett, "Orbital angular momentum: origins, behavior and applications," *Adv. Opt. Photon.*, vol. 3, pp. 161-204, 2011.
- [6] C. R. Doerr and L. L. Buhl, "Circular grating coupler for creating focused azimuthally and radially polarized beams," *Opt. Lett.*, vol. 36, pp. 1209-1211, 2011.
- [7] T. Su, *et al.*, "Demonstration of free space coherent optical communication using integrated silicon photonic orbital angular momentum devices," *Opt. Express*, vol. 20, pp. 9396-9402, 2012.
- [8] X. Cai, *et al.*, "Integrated Compact Optical Vortex Beam Emitters," *Science*, vol. 338, pp. 363-366, 2012.
- [9] B. Guan, *et al.*, "Free-space coherent optical communication with orbital angular, momentum multiplexing/demultiplexing using a hybrid 3D photonic integrated circuit," *Opt. Express*, vol. 22, pp. 145-156, 2014.
- [10] B. Guan, *et al.*, "Polarization-Diversified, Multichannel Orbital Angular Momentum (OAM) Coherent Communication Link Demonstration using 2D-3D Hybrid Integrated Devices for Free-Space OAM Multiplexing and Demultiplexing," in *CLEO: 2014*, San Jose, California, p. STu1G.5, 2014.
- [11] Y. Nasu, M. Kohtoku, and Y. Hibino, "Low-loss waveguides written with a femtosecond laser for flexible interconnection in a planar light-wave circuit," *Opt. Lett.*, vol. 30, pp. 723-725, 2005.
- [12] A. V. Oppenheim, A. S. Willsky, and S. H. Nawab, *Signals and systems* vol. 2: Prentice-Hall Englewood Cliffs, NJ, 1983.
- [13] W. Steinchen and L. X. Yang, *Digital shearography: theory and application of digital speckle pattern shearing interferometry* vol. 100: SPIE, 2003.
- [14] K. Okamoto, *Fundamentals of optical waveguides*: Access Online via Elsevier, 2010.
- [15] ITU-T, in *Recommendations G.975.1 : Forward error correction for high bit-rate DWDM submarine systems*, Appendix I.9, 2004.



- [16] P. Gregg, *et al.*, “Stable Transmission of 12 OAM States in Air-Core Fiber,” in *CLEO: 2013*, San Jose, California, p. CTu2K.2, 2013.

Under Review